AD-A229 025

(1)

Proceedings of the 9th Annual DARPA/AFGL Seismic
Research Symposium, 15-18 June 1987

DTIC FILE COPY

Editors:
JAMES F. LEWKOW1CZ
JEANNE M. McPHETRES

DTIC
ELECTE
NOV 20 1990
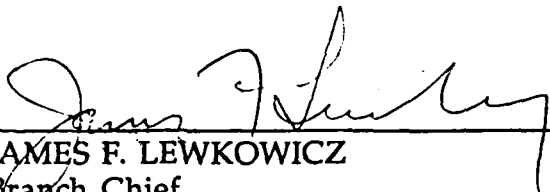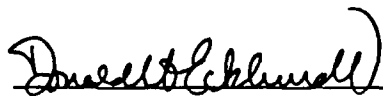**S** **B** **D**

6 November 1990

EARTH SCIENCES DIVISION   PROJECT 2309
GEOPHYSICS LABORATORY
HANSCOM AFB, MA 01731-5000

90 11 19 228

"This technical report has been reviewed and is approved for publication."

FOR THE COMMANDER

JAMES F. LEWKOWICZ
Branch Chief
Solid Earth Geophysics Branch
Earth Sciences Division

DONALD H. ECKHARDT
Director
Earth Sciences Division

REPORT DOCUMENTATION PAGE

4. TITLE AND SUBTITLE

**Proceedings of the 9th Annual DARPA/AFGL Seismic
Research Symposium, 15-18 June 1987**

PE 61102F
PR 2309
TA G2
WU 06

6. AUTHOR(S)

Editors: James F. Lewkowicz
    Jeanne M. McPhetres

7. PERFORMING ORGANIZATION NAME(S) AND ADDRESS(ES)

Air Force Geophysics Laboratory, AFSC
AFGL/LWH
Hanscom AFB, MA 01731-5000

8. PERFORMING ORGANIZATION REPORT NUMBER

GL-TR-90-0300
ERP, No. 1069

9. SPONSORING/MONITORING AGENCY NAME(S) AND ADDRESS(ES)

DARPA/NMRO
1400 Wilson Boulevard
Arlington, VA 22209-2308

10. SPONSORING/MONITORING AGENCY REPORT NUMBER

11. SUPPLEMENTARY NOTES

This research was supported by DARPA under PE 61101E and 62714E.

12a. DISTRIBUTION/AVAILABILITY STATEMENT

Approved for Public Release; distribution unlimited

12b. DISTRIBUTION CODE

13. ABSTRACT (Maximum 200 words)

These proceedings contain papers presented at the Ninth Annual Defense Advanced Research Projects Agency/Air Force Geophysics Laboratory (DARPA/AFGL) Seismic Research Symposium held 15-18 June 1987, in Nantucket, Massachusetts. In its capacity as a Technical Agent, the AFGL's Solid Earth Geophysics Branch (LWH) manages the DARPA Nuclear Monitoring Research Office's (NMRO) basic research program in seismology. The scientific objective of this program is to improve the Air Force's capability to seismically detect, locate, identify and estimate the yield of underground nuclear explosions. The purpose of this symposium, which is organized annually by LWH, is to provide the NMRO staff an opportunity to review the research accomplished during the preceding year and outline areas of investigation for the coming year. For the researchers, it provides a forum for the exchange of scientific information, as well as occasions to meet personally with the NMRO and LWH staff to discuss individual projects, ideas and results. In addition, the technical presentations

14. SUBJECT TERMS

underground nuclear explosion, seismic waves, regional
seismology arrays, yield estimation, source coupling

15. NUMBER OF PAGES

255

16. PRICE CODE

17. SECURITY CLASSIFICATION OF REPORT	18. SECURITY CLASSIFICATION OF THIS PAGE	19. SECURITY CLASSIFICATION OF ABSTRACT	20. LIMITATION OF ABSTRACT
UNCLASSIFIED	UNCLASSIFIED	UNCLASSIFIED	UL

serve as a means to inform representatives from other Government agencies about advances in seismic monitoring research, technologies and techniques as part of the important process of technology transition. The papers include studies on regional seismic wave propagation, attenuation and scattering, array processing and seismic techniques of yield estimation.

Accession For	
NTIS GRA&I	☑
DTIC TAB	☐
Unannounced	☐
Justification	

By_____

Distribution/

Availability Codes	
Dist	Avail and/or Special
A	

DTIC
COPY
INSPECTED
1

4

PAPERS PRESENTED
AT THE
9TH ANNUAL AFGL/DARPA SEISMIC RESEARCH SYMPOSIUM
15-18 JUNE 1987
HARBOR HOUSE
NANTUCKET, MA

$P_{\cdot}$ ·t , f

TABLE OF CONTENTS.

SEISMIC SOURCE THEORY AND SCATTERING

SPECIAL SESSION ON DARPA SMALL ARRAY PROGRAM

PAPER AUTHOR:

Vernon F. Cormier M.I.T. Department of Earth and Planetary Sciences

OBJECTIVE:

Observations of teleseismic P waves at large aperture arrays have found amplitude fluctuations across the array as large as those observed over world-wide networks. The amplitude fluctuations and their correlation with travel time variations are consistent with the focusing/defocusing effects of three-dimensional velocity structure beneath the array, rather than the effects of intrinsic attenuation. A reciprocal effect on amplitudes is to be expected for variations in the location of underground nuclear tests within a test site. An objective of this project is to predict these amplitude variations using known 3-D structure within a test site. Fast, asymptotically approximate methods of modeling the body wavefield are used to predict these amplitude variations by forward modeling in structures determined from block 3-D inversions of travel times, as well as more detailed models determined from local geophysical surveys at the Nevada test site. The results of these studies can be used to determine the fundamental scale lengths required to produce a correctable amplitude anomaly of a given size.

RESEARCH ACCOMPLISHED

A technique was developed for patching the dynamic ray tracing equations between regions of an Earth model having 1-D or radially symmetric velocity structure and regions having 3-D velocity structure (Cormier, 1986). Using this technique together with seismograms synthesized by ray theory and superposition of Gaussian beams or Maslov/WKBJ plane waves, the effects of three dimensional structure in the source region on the amplitudes and waveforms of teleseismic body waves were investigated. The effects of three-dimensional models obtained by block inversion of travel times (e.g., Aki et al., 1977) were investigated as well as the effects of a descending slab structure, in which travel time inversions were tied to a thermal model.

CONCLUSIONS AND RECOMMENDATIONS

NTS

A known three-dimensional structure beneath Pahute Mesa, Nevada Test Site (Taylor, 1983) can account for many of the features in the azimuthal amplitude pattern of teleseismic P waves from Pahute underground tests. This model (Figure 1a,b) can be used to correct for focusing and defocusing effects of the structure beneath Pahute Mesa accounting for factors of three in amplitude fluctuation (Figure 2) and for 0.6 sec. in travel time fluctuation (Cormier, 1987a). The reduction in variance of teleseismic magnitude or log amplitude using these corrections is about 25 percent, similar to the reduction of variance in teleseismic travel times. These results are useful in predicting the structural resolution needed for models of other test sites to be useful in making corrections for focusing and defocusing. The NTS results suggest that meaningful corrections can be made if the model resolves 10 to 20 km scale lengths down to 100 km with perturbations of velocity exceeding 4 percent. Velocity inversions that primarily resolve scale lengths larger than these or that smooth over anomalies larger than 2 percent, (e.g., Montfort and Evans, 1982; Minster et al., 1981), are much less useful in formulating amplitude corrections. By analogy to the Taylor inversion for NTS structure, the data required to resolve structure having these scale lengths would consist of origin times and locations of tests widely distributed over linear dimensions on the order of 100 km with siginificant concentrations of tests spaced less than 10 km apart. It is also necessary to obtain an average crustal structure within the test site from seismograms recorded at local and regional range.

The focusing and defocusing effects of 20 to 50 km scale length structure having perturbation in P velocity of several percent is nearly independent in the frequency band of (Figure 3) teleseismic body waves. This conclusion is even stronger in the 0.2 to 10 Hz. band in which measurements are made on the teleseismic P waves of underground nuclear tests. Frequency dependent effects in the coda of teleseismic P waves are probably due to either the effects of heterogeneities having scale lengths smaller than 20 km and/or to frequency dependent effects in the scattering processes occurring near the source and receiver.

Magnitude measurements based on the integrated energy in the coda of teleseismic P waves are likely to be more stable because they can remove some of the focusing/defocusing effects of three-dimensional mantle structure near the source. Coda magnitudes, however, are only partially successful in removing the focusing/defocusing effects of structure beneath the source. They cannot remove these effects from the fraction of the coda that is due to scattering of direct P near the receiver.

EFFECTS OF SLAB STRUCTURE

A P velocity model of the Kuril-Kamchatka lithospheric slab determined from travel time study by Creager and Jordan (1986) has been parameterized in three dimensions to investigate amplitude and waveform effects on body waves. Very broad Gaussian beams were used in a reciprocal sense, shooting from receiver to source, to synthesize broad band S waves. The per cent velocity perturbation on S velocity was assumed to be equal to that in P velocity. Frequency dependent effects in the tail of the S pulse were observed in all azimuths on the side of the slab dipping away from the arc (Cormier, 1987b).

This "slab diffracted" phase rapidly decays away within 10 to 15 degrees of the azimuth parallel to the strike. The character of the slab diffraction agrees with that seen in finite difference calculations by Vidale (1986) for P waves propagating down dip from an hypocenter in the slab.

The results of these studies will be useful in interpreting the waveform studies of P and S attenuation of the type reported by Choy and Cormier (1986), as well as investigating the shadowing and slab multipathing evident in teleseismic P waves from U.S. nuclear tests on Amchitka Island in the Aleutian arc (Davies and Julian, 1972).

REFERENCES

Aki, K., Christoffersen, A., and Husebye, E.S., Determination of three- dimensional seismic structures of the lithopshere, *J Geophys Res*, *82*, 277-296, 1977.

Choy, G.L., and Cormier, V.F., Direct measurement of the mantle attenuation operator from broadband P and S waves, *J. Geophys Res.*, *91*, 7326-7342, 1986.

Cormier, V.F., An application of the propagator matrix of dynamic ray tracing: The focusing and defocusing of body waves by three-dimensional structure in the source region, *Geophys. J. R. Astr Soc.*, *87*, 1159-1180, 1986.

Cormier, V.F., Focusing and defocusing of teleseismic P waves by known 3-D structure beneath Pahute Mesa, Nevada Test Site, *Bull. Seism. Soc. Am.*, in press, 1987a.

Cormier, V.F., Slab diffracted S waves (abstract), ul *EOS Trans. Am. Geophys. Un.*, *68*, 353, 1987b.

Creager, K.C., and Jordan, T.H., Slab penetration into the lower mantle beneath the Mariana and other island arcs of the Northwest Pacific, *J. Geophys. Res.*, *91*, 3573-3589, 1986.

Davies, D., and Julian, B., A study of short-period P-wave signals from Longshot, *Geophys. J. R. Astr. Soc.*, *29*, 185-202, 1972.

Minster, J.B., J.M. Savino, W.L. Rodi, J.F. Masso, and T.H. Jordan, Three-dimensional velocity structure of the crust and upper mantle beneath the Nevada Test Site, Final Technical Report, SSS-R-81- 5138, S-cubed, La Jolla, California, 1981.

Montfort, M.E., and J.R. Evans, Three-dimensional modeling of the Nevada Test Site and vicinity from teleseismic P-wave residuals, Open-File Report 82-409, U.S. Geol. Survey, Menlo Park, California, 1982.

Taylor, S.R., Three-dimensional crust and upper mantle structure at the Nevada Test Site, *J Geophys Res*, *88*, 2220-2232, 1983.

Vidale, J.E., Waveform effects of a high-velocity, subducted slab, *J. Geophys. Res.*, submitted, 1986.
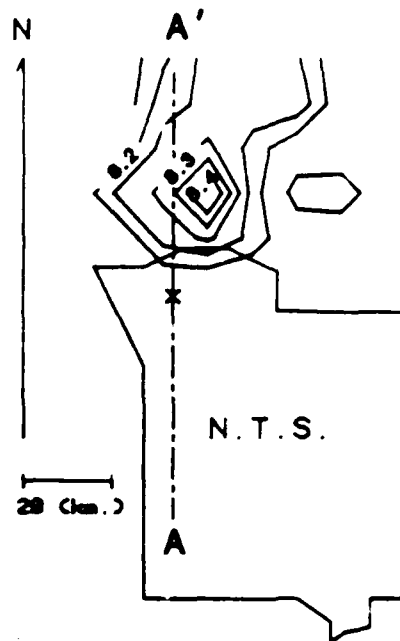
Figure 1a A representative epicenter of an underground nuclear test at Pahute
Mesa is marked by the cross (x). Iso-P velocity contours at 85 km
depth are shown for a high velocity anomaly resolved in the study by
Taylor (1983).
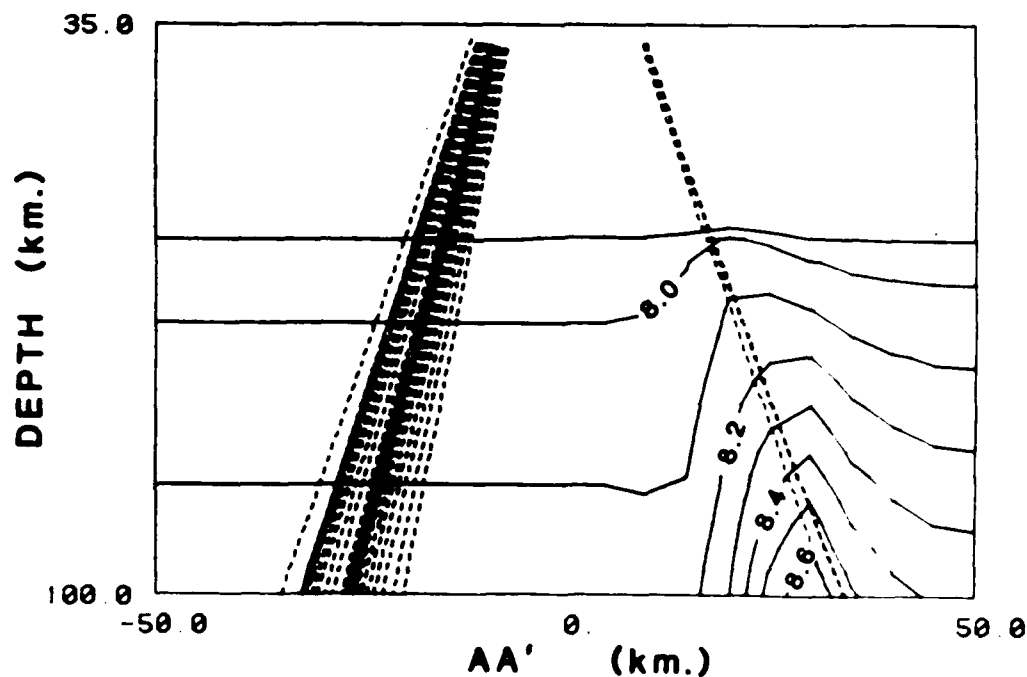
Figure 1bIso-P velocity contours greater than 7.9 km./sec for the Taylor (1983)
model along the AA' cross section shown in Figure 1. Three-
dimensionally traced rays (dashed) are projected on'o the cross sec-
tion if their end points lie within 20 km. of the plane of the cross sec-
tion.

PREDICTED

OBSERVED

Positive

Negative

+ 0.0 < δlogA < 0.1 ◇

+ 0.1 < δlogA < 0.3 ◇

+ 0.3 < δlogA ◇

N E W S
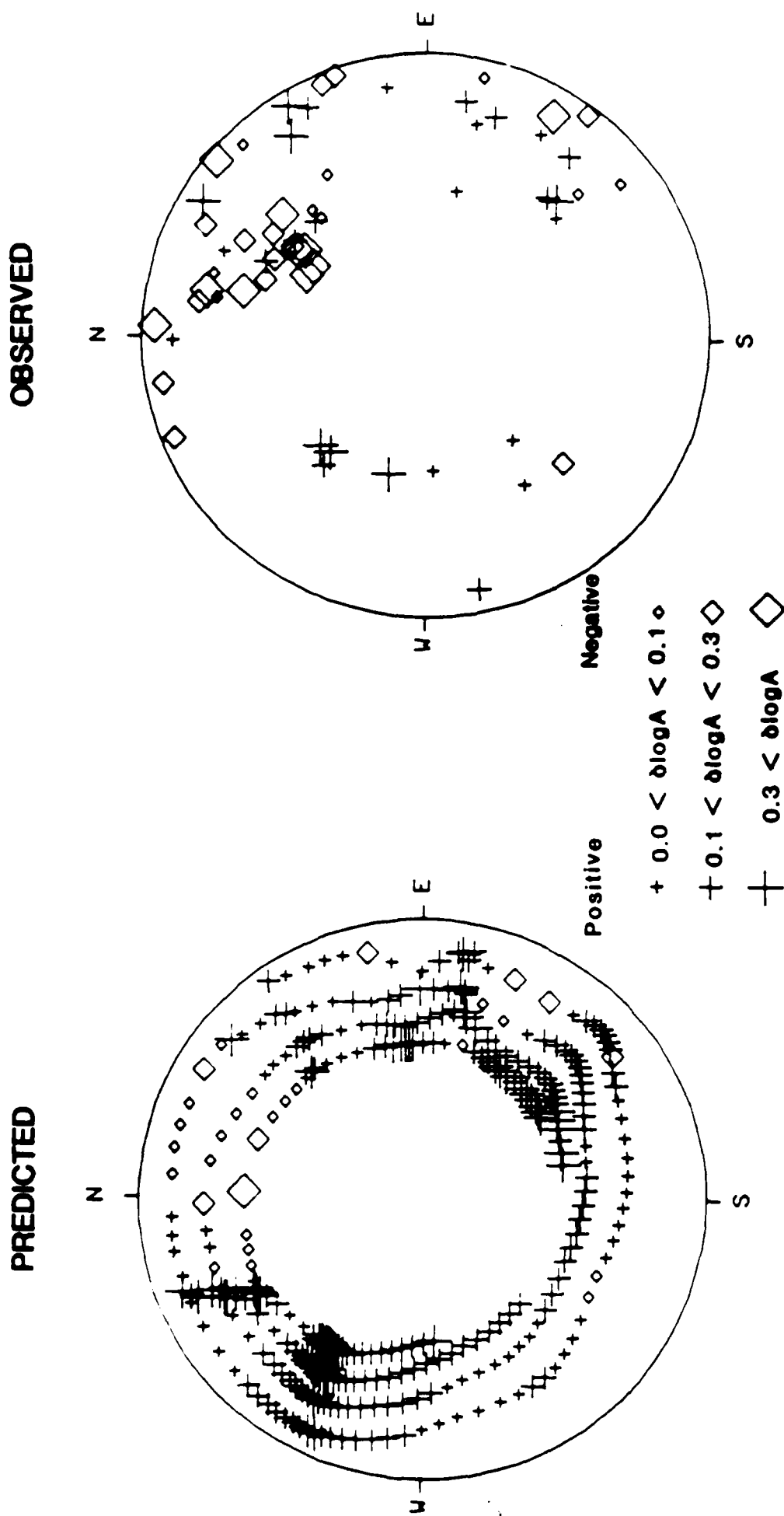
Figure 2 Predicted and observed amplitudes of the Pahute Mesa tests. Symbols are plotted on an equal area, lower hemisphere projection, as a function of vertical and azimuthal angles of the rays leaving the heterogeneous region at 100 km. depth. The radius of the focal sphere is taken to be that for the vertical take-off angle of P waves that propagate to stations at 35° distance in a one-dimensional, radially symmetric earth. δlogA measures the difference in log amplitude from the log amplitude predicted in a 1-D earth.
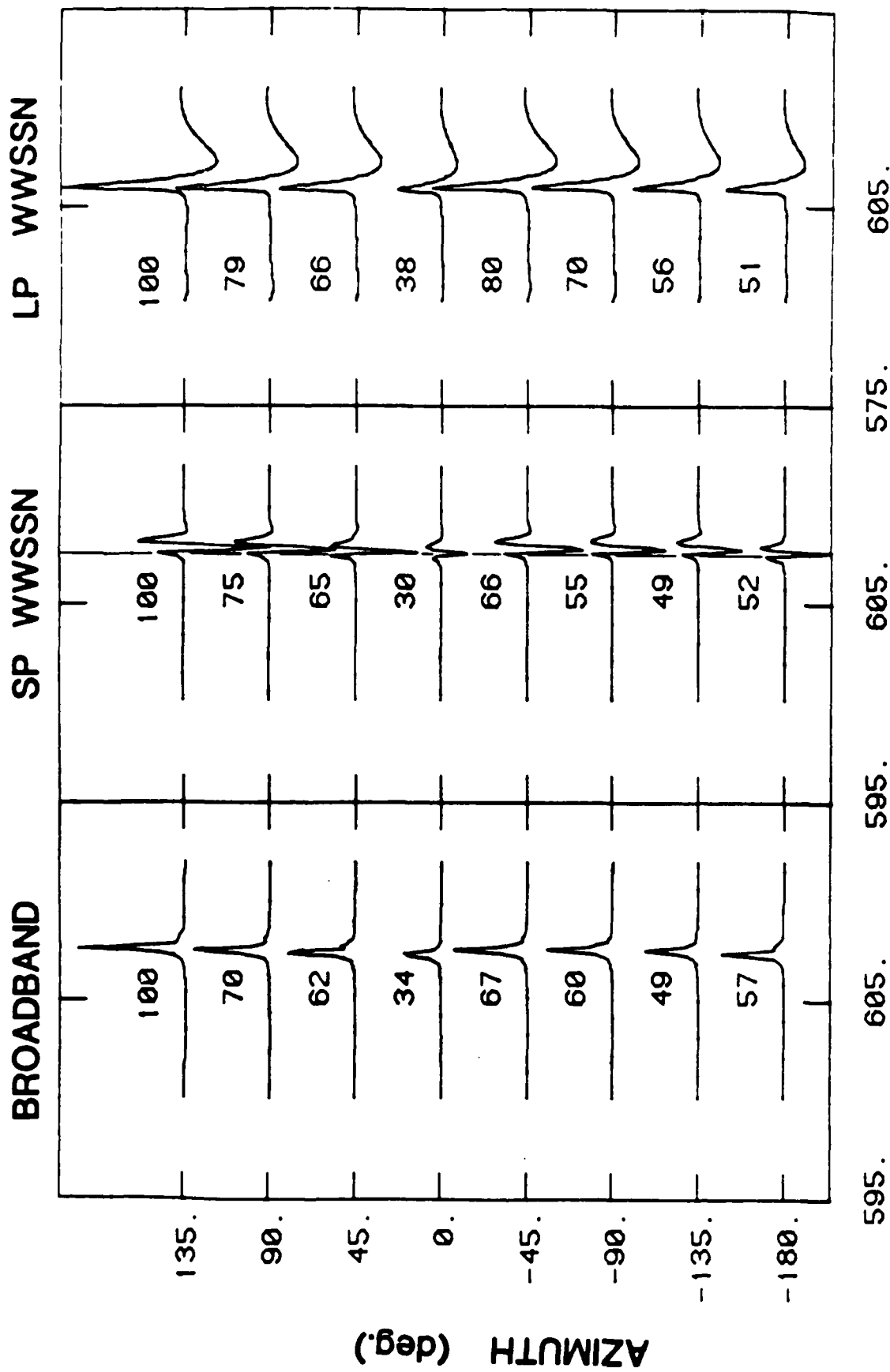
Figure 3. Teleseismic P waves synthesized by superposition of Gaussian beams for stations at 80° distance and variable azimuths for an explosive point source at 1 km depth. The source location is shown in Figure 1. The numbers alongside each seismogram are measurements of peak to peak amplitude. A reference line, from which travel time variations may be measured from the minimum trough, is shown in the short period column.

6

A WIDE-ANGLE SEISMIC PROFILE AT PAHUTE MESA, NV

JOHN F. FERGUSON AND RUSSELL J. HEIDESCH

THE UNIVERSITY OF TEXAS AT DALLAS

OBJECTIVE

The goals of this project have been to obtain a seismic refraction/reflection profile at Pahute Mesa, NV and to produce an integrated interpretation of this data along with Bouguer gravity, borehole geophysics and geology. The resulting model should be useful in the identification of the significant geophysical structure at this test site and in the prediction of the seismic response of nuclear explosions.

RESEARCH ACCOMPLISHED

A new seismic refraction profile has been acquired on the eastern margin of the Silent Canyon caldera. The experiment was designed to obtain detailed coverage of the marginal faults or collapse features and some of the subsequent basin and range structures. A single shot point was located on outcropping Silent Canyon basement outside of the caldera, as it was impractical to site shot points on Pahute Mesa itself. The layout of the survey is shown in Figure 1. The scalloped line indicates the caldera boundary and the Split Ridge, Scrugham Peak, Almendro and Greeley faults are also shown. Individual geophone group locations, 67 m apart, are indicated by the "Y" symbol. The triangles are Dinoseis shot points used to obtain auxilary data on shallow velocites. Nearby boreholes with important geophysical or stratigraphic information are depicted on the map. The seismic data is shown in Figure 2, along with the topography and the travel times observed for the Dinoseis shots.

Velocities appropriate to the caldera fill have also been determined from the borehole geophysical logs. Figure 3 is an attempt to summarize the velocity data at Pahute Mesa. The dashed line is a least squares fit to the tuff interval velocities ("+"). The solid line was determined by inversion of travel times observed locally (i.e. out to 12 km) by Leonard and Johnson (1987). Both functions are gross averages over a laterally variable structure. The two smooth fits are in good agreement over the depth interval covered by well data, but are subject to scatter of $\pm$ 0.5 km/s in the interval velocities. The presence of very subtantial velocity outliers of up to 5 km/s should be noted. These thin high velocity zones occur in both tuff and lava intervals and could result in substantial

amplitude effects, but will have only minor effects on the travel time. Wells with only stratigraphic information are far more numerous than those with velocity or density logs. It is expected that the recognized geologic units can be adequately characterized geophysically and that more detailed, laterally variable models of the upper 1 km will be possible.

A gravity profile coincident with the seismic line was modeled and presented at this same meeting last year (Ferguson, 1986). The model incorporated corrections for shallow high density units, such as the Rainer Mesa tuff and Area 20 lava The gravity could then be accounted for by a hi .. density basement stepping down to the northwest. A very simplistic seismic model based on the linear velocity function and the gravity model is shown in Figure 4. No attempt was made to account for known structural complexity, only the gross features of the travel time curve have been computed by ray tracing. The observed travel times in Figure 2 are well matched by the results in Figure 4, but theyt cannot be relied on for waveform analysis.

CONCLUSIONS AND RECOMMENDATIONS

The preliminary results presented here confirm the existance of the high density, high velocity Silent Canyon basement under Pahute Mesa. The seismic data are of a sufficient quality to permit a waveform modeling approach to the interpretation. At this time an approach is being developed to model this data by a psuedospectral technique in order to match the amplitude and phase of the P-wave signal, as well as the travel time, in an arbitrarily inhomogeneous model. A detailed geologic profile is being constructed, in cooperation with R. G. Warren at Los Alamos National Laboratory, which will be used to predict the geophysical properties in the upper 1 to 2 km of the subsurface. The resulting model will be tested for its ability to predict the seismic character of nuclear tests sited near the profile.

REFERENCES

Ferguson, J., (1986), Geophysical investigations at Pahute Mesa, NV, 8th Annual DARPA/AFGL Seismic Research Symposium, Colorado Springs, CO.

Leonard, M. A. and L. R. Johnson, (1987), Velocity structure of Silent Canyon Caldera, Nevada Test Site, Bull. Seis. Soc. Am., v 77, p 597-613.

Fig. 1

PAHUTE MESA SEISMIC SURVEY 1986
SCALE 1: 126000

Fig. 3

VELOCITY (KM/SEC)

DEPTH (KM)

+ TUFFS

* LAVAS

— · — · — FERGUSON (1986)

————— LEONARD AND JOHNSON (1987)
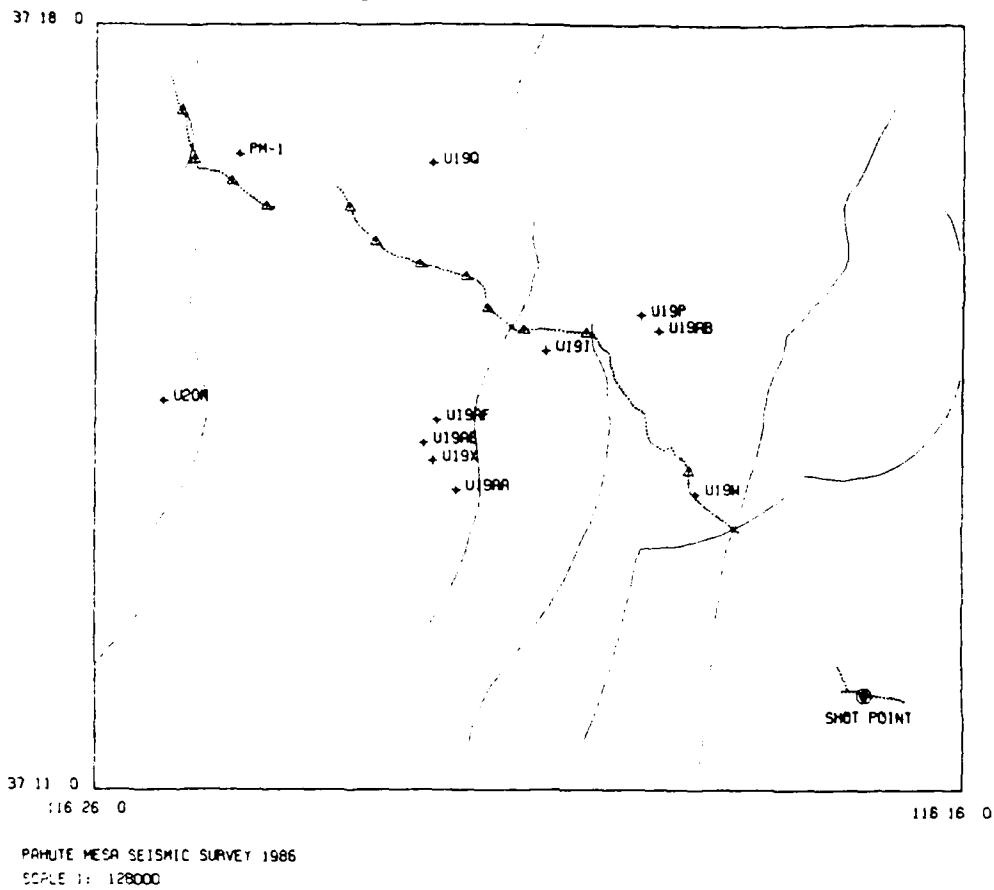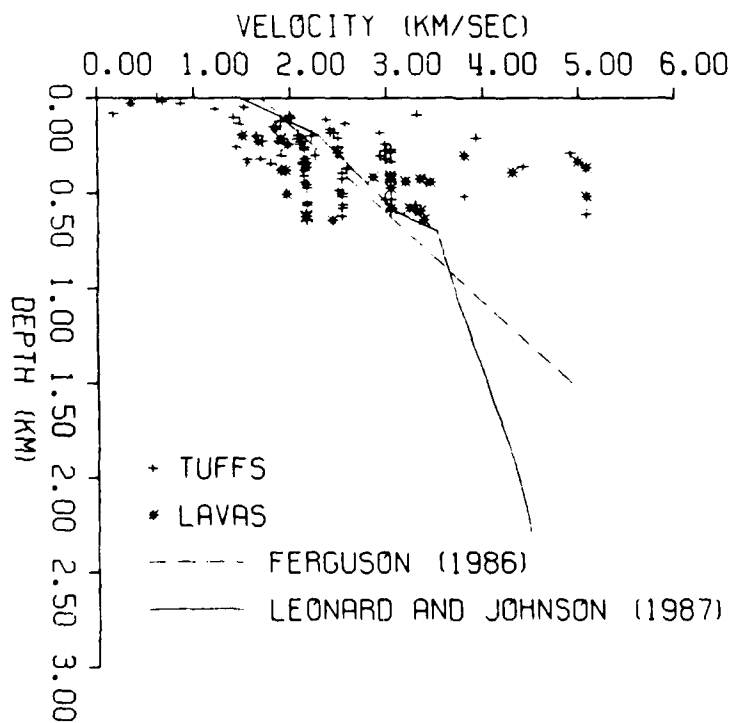
Fig. 2

Pahute Mesa Seismic Line
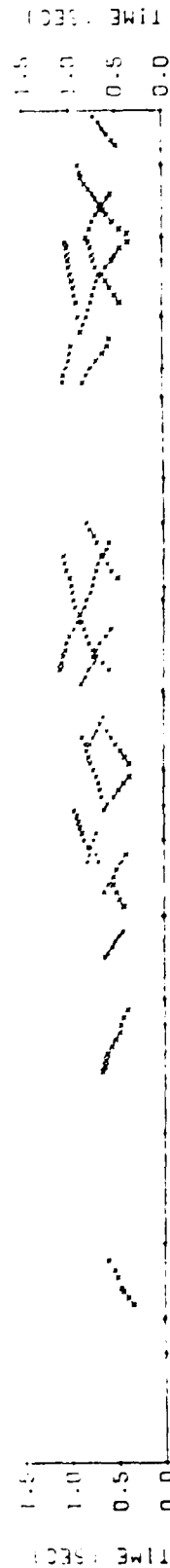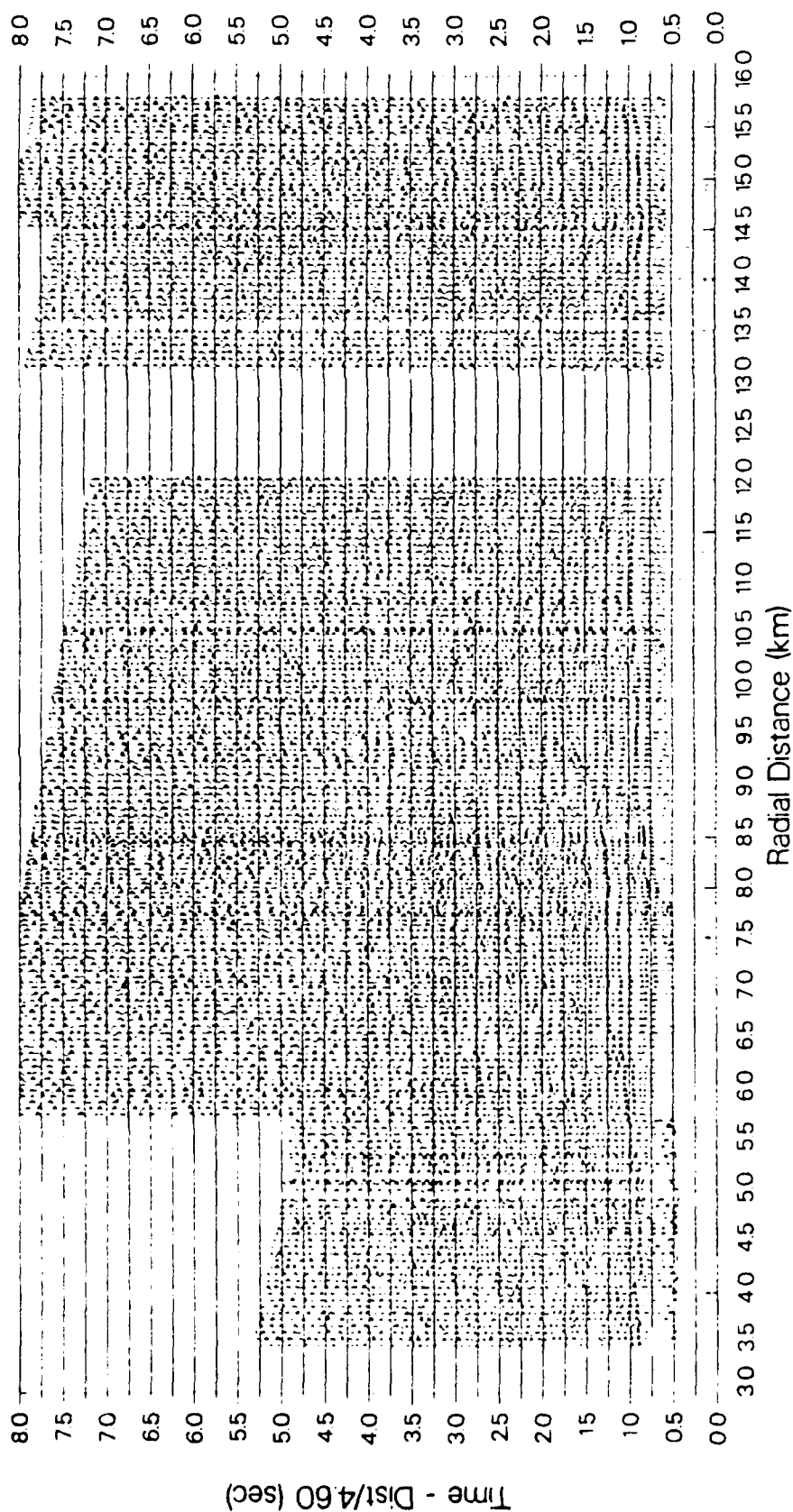
Fig. 4

RAY TRACING IN THE PAHUTE MESA MODEL
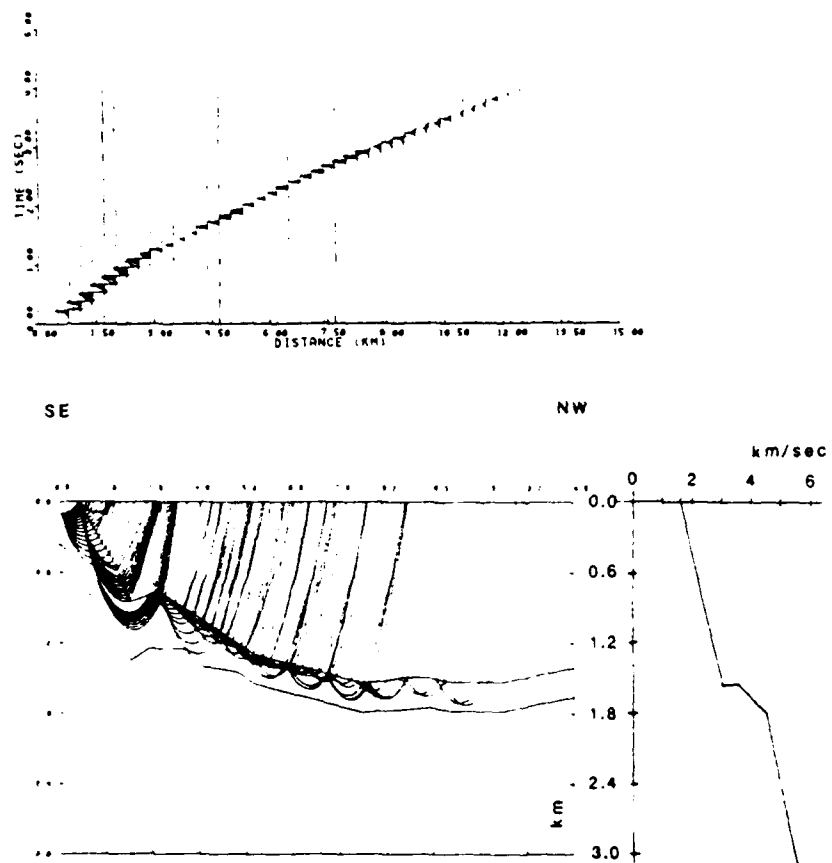
Modeling near source effects on surface wave generation and path corrections

David G. Harkrider

Seismological Laboratory, California Institute of Technology,
Pasadena, California, 91125

RESEARCH ACCOMPLISHMENTS

Given and Mellman (1986) have estimated NTS explosion moments using the surface wave path corrections of Stevens (1986) which are based on a conservation of lateral energy flux simular to the gaussian beam approach. The estimates were obtained using a common source region model and an assumed tectonic release mechanism which corresponds to a vertical strike slip double couple for all of the NTS source areas. For a given m_b, they found that on the average the explosion log moments of events at Yucca Flat were about 0.20 units less than events at Pahute Mesa.

Murphy (1987) was able to remove this difference in log moment by freeing the tectonic release mechanism. In other words, he allowed the dip and the rake of the double couple to vary for each event. The source region structure used in the surface wave corrections is basically a Pahute Mesa strtucture. Since there are known shot point source velocity structure variations at NTS, we evaluated the error in log moment which would occur by assuming the common NTS source structure instead of the actual structure. Using the same approximations, synthetic Rayleigh waves were generated for various shot point structures reported for NTS. These were compared with synthetics using the Stevens (1986) and Given and Mellman (1986) source region to obtain relative moment corrections. The log moment corrections are given in Table below.

Log Moment Corrections For Various NTS Sub-Area Models			
Yucca		Pahute	
South	+0.08	Tuff	+0.03
North	+0.14	Leonard-Johnson	+0.06
Bache	+0.07	Rhyolite	+0.06
Ferguson	+0.15		
Geotech	+0.19		

The source structures used to obtain these corrections are given above Figure 1. The correction values are all positive. Thus, if the event actually occured in this structure, the log moment obtained using Stevens's path correction would be too small by the amount given in the tables. On the average, the corrections for Yucca are about 0.10 units greater than Pahute. This implies that the log explosion moment obtained for these Yucca structures using the NTS source region is 0.10 units less than the Pahute structures. This does not explain the entire difference observed by Given and Mellman but it is in the right direction. It is interesting to note that South Yucca model yields moment values closer to those of the Pahute models than the North Yucca model. If shot point structures can be obtained for each event, they should be used in the determination before freeing the tectonic release component.

One of the most obvious differences between the Rayleigh wave path correction synthetics for different near surface source region structures at NTS and the synthyetic for an explosion in the uniform upper crust propagation model common to all the corrections is the arrival of a burst of high frequency energy at the start of the short period inverse branch of the propagation model Rayleigh wave. This can be seen in Figure 1 The Rayleigh wave at the top of the figure is due to an explosion in the propagation model CIT109. In this model the top crustal layer is 11 km thick. The synthetic below this is for a Bache Yucca Flat source region model coupled to CIT109 using the gaussian beam approximation. The source is at a depth of 0.7 km and the surface receiver is at a range of 3000 km in both models. The presence of the near surface source structure not only enhances the normally present high frequency inverse branch of the CIT109

model's Rayleigh wave, but appears to include a large amplitude short duration pulse at its beginning. The arrival time for this pulse corresponds to the Rayleigh wave velocity of the surface material of CIT109.

One of the interpretations of the dispersed fundamental Raylreigh wave in a layered structure is that it is the costructive interference between the short period free surface Rayleigh wave with the long period interface Stonely wave in the lower part of the structure. Since neither wave is traveling at their natural velocities, both waves will leak primarily SV waves towards each other. The constructive interference of the SV waves between the two waves results in the dispersion of the so called fundamental Rayleigh wave. This view-point leads to a rather simple interpretation of the previous figure.

Before discussing the results of the coupling of a limited source region to the laterally homogeneous propagation model, we show Rayleigh wave synthetics for two laterally homogeneous models, which we will use as propagation models (Figure 2). The first is CIT109 and the second is a homogeneous half-space composed of ths same material as the surface layer of CIT109. Below each synthetic is a cartton showing the source and propagation geometry. The Rayleigh wave for the homogeneous half-space model is an undispersed pulse which arrives at the same time as the beginning of the high frequencies on the well dispersed Rayleigh wave of the CIT109 model shown above it. The seismic moment for all synthetics presented in this report is 10**25 (dyne-cm). The peak-to-peak Rayleigh wave amplitude for the half-space is about 30% greater than the CIT109 wave. For both media the explosion was at a depth of 0.4 Km.

In order to simplify the discussion of the inhomogeneous source region, we have reduced the source region complexity to an 0.8 km layer of tuff overlying the the upper layer material of CIT109. Their combined thicknes is 14 km and the structure below that is CIT109. At the top of Figure 3, we show the Rayleigh wave synthetic for this simple source region coupled to the CIT109 propagation model using the gaussian beam approximation. In the lower half of the figure, we present the Rayleigh wave for this same source layer overlying a half-space of the top material of CIT109 coupled to a half-spavce of the same material for propagation to the surface receiver. Below each synthetic is a cartton showing the source and propagation geometry. In all of our source models, we set the source region radius to zero since we are interested in spectral amplitude which in this approximation is independent of source region radius.

Comparing the half-space propagation results for the low velocity source region with the half space source region (the bottom synthetics of Figures 2 and 3), we see that the presence of the low velocity source layer causes an increase in Rayleigh wave amplitude with very little distortion of the pulse shape. Once this nearfield Rayleigh wave has left the source region, it travels as half-space wave. There is no dispersion since there is no structure at depth to cause a return of the downgoing source energy by either reflection or upward leaking from deeper interface waves. If we had given the source region a horizontal dimension, the resulting phase would have caused some dispersion of the pulse.

Comparing the low velocity source region coupled to CIT109 with the source in CIT109 (the top synthetics of Figures 2 and 3) we see that the increase in amplitude due the coupling with the low velocity source region is not as great as the half-space propagation models. Because of this relative difference in ammplification, the nearfield Rayleigh half-space pulse, which has been amplified by the low velocity source region, is easily seen as a pulse on the dispersed CIT109 Rayleigh wave. With the source in the thick homogeneous upper crust model of CIT109, the free surface Rayleigh wave leaks energy down into the crust-mantle wave guide so that by a range of 3000 km, it only appears as the emergent high frequency start of the inverse branch (top of Figure 2).

It is frequently asserted that the 20 second Rayleigh wave spectra can be modeled by only cosidering the source region velocity structure and the upper crust. This is based on a calculation made in Douglas etal (1971). Conclusions based on models such as theirs where the near surface source structure extends along the whole propagation path may not be appropriate for sources in laterally inhomogeneous media. This may be especially true when the assumed

structure implies that the source and receiver are both in and on the same low velocity material. In Figure 4, we show the amplitude spectra for the low velocity source region coupled to the half-space model and to the more realistic earth model CIT109. Comparing the spectra for two models, we see that the upper crust half-space model does very well out to 25 seconds. At longer periods the halfspace model amplitudes are too large by almost a factor of two. The periods at which this type of halfspace model begins to fail depends on the thickness of the uniform crust. To a depth of 35 km, the shear velocity of the CIT109 model varies from about 3.5 to 3.8 km/sec.

In light of the above discussion, the reduction in spectral amplitude of the more realistic model can be explained as follows. As the free-surface Rayleigh wave travels from the source region it eventually begins to interfere with the deeper long period interface waves generated by the downgoing source radiation. This interference causes the surface Rayleigh wave to leak energy in the form of downgoing SV waves. The resulting constructive interference between the upgoing SV from the lower crust-mantle localized Rayleigh wave and the down going SV energy form the fundamental Rayleigh wave. Modal phase velocities greater than and group velocities less than the local body wave velocity imply constructive interference between upgoing and downgoing body waves in that region of the velocity structure.

Whether the 20 second energy is controlled by the downgoing source energy or the upgoing depends on the thickness of the crust-mantle waveguide. For thick relatively homogeneous crust models such as CIT109 and the 38 km continental crust of Kanamori (1967) used by Douglas etal (1971), the 20 second spectral energy can be modeled by a crustal halfspace model. The suprising part of this is that this 20 second energy is not obvious in the short duration time domain Rayleigh wave pulse. Without further analysis, it is difficult to say whether this halfspace conjecture carries over to the time domain for more realistic models where the 20 second arrival is in the well dispersed part of the wavetrain.

Drawing conclusions based on the spectra amplitudes of this short duration undispersed free-surface Rayleigh wave, which is primarily excited by the upgoing source radiation, presupposes that this wave survives out to the observer or that it has made a major contribution to the 20 second spectral energy seen outside of the near source region. The approximations used to calculate the synthetics guarantees that all the surface wave energy generated in the source region is transmitted to the observer.Helmberger and I have long felt that this wave is much more suseceptible to lateral inhomogenities and surface irregularities and that the observed 20 second energy is more likely to be excited by the downgoing source radiation. The consequences of this can not only reduce observed amplitudes but also cause reversals in phase.

NTS (Stevens)			
Th km	α km/s	β km/s	ρ gm/cm³
0.5	2.00	1.00	1.70
1.0	3.30	2.00	2.10
1.5	4.50	2.70	2.40
1.0	5.90	3.40	2.75
8.0	5.96	3.52	2.78
9.0	6.11	3.61	2.80
10.0	6.37	3.76	2.84
14.0	7.90	4.42	3.30
20.0	8.05	4.50	3.30
15.0	8.10	4.50	3.30
40.0	8.00	4.40	3.30
30.0	7.90	4.30	3.25
30.0	7.90	4.30	3.25
40.0	8.00	4.40	3.30
0.0	8.50	4.70	3.50

Pahute Rhyolite			
Th km	α km/s	β km/s	ρ gm/cm³
0.36	2.30	1.35	1.90
0.20	2.80	1.50	2.00
0.10	3.30	1.50	2.25
0.50	4.00	1.90	2.30
1.00	4.45	1.97	2.37
0.75	4.60	2.00	2.40
0.80	5.30	2.50	2.50
2.25	5.50	2.95	2.70
6.04	6.00	3.50	2.75
9.00	6.11	3.61	2.80

Pahute Tuff			
Th km	α km/s	β km/s	ρ gm/cm³
0.36	2.30	1.35	1.90
0.40	2.80	1.50	2.00
0.70	3.30	1.50	2.25
0.70	4.00	1.90	2.30
0.75	4.60	2.00	2.40
0.80	5.30	2.50	2.50
2.25	5.50	2.95	2.70
6.04	6.00	3.50	2.75
9.00	6.11	3.61	2.80

Pahute (Leonard-Johnson)			
Th km	α km/s	β km/s	ρ gm/cm³
0.05	1.50	0.99	1.90
0.10	1.90	1.25	1.90
0.10	2.30	1.48	1.90
0.10	2.50	1.57	1.90
0.10	2.70	1.66	2.00
0.10	2.91	1.74	2.00
0.10	3.11	1.82	2.25
0.50	3.64	2.01	2.30
0.30	3.90	2.12	2.37
0.30	4.10	2.20	2.37
0.25	4.29	2.27	2.37
0.16	4.37	2.29	2.37
0.75	4.60	2.35	2.40
0.80	5.30	2.50	2.50
2.25	5.50	2.95	2.70
6.04	6.00	3.50	2.75
9.00	6.11	3.61	2.80

Yucca North			
Th km	α km/s	β km/s	ρ gm/cm³
0.20	1.65	0.90	1.60
0.20	2.14	1.14	1.80
1.10	3.70	2.00	2.30
0.50	4.60	2.50	2.70
2.00	5.90	3.40	2.75

Yucca South			
Th km	α km/s	β km/s	ρ gm/cm³
0.40	1.34	0.64	1.50
0.25	2.14	1.14	1.80
0.45	3.00	1.60	2.05
0.90	4.57	2.64	2.50
2.00	5.90	3.40	2.75

Yucca (Ferguson)			
Th km	α km/s	β km/s	ρ gm/cm³
0.25	1.34	0.64	1.00
0.25	2.14	1.14	1.80
0.30	3.00	1.60	1.80
1.20	4.57	2.64	2.50
2.00	5.90	3.40	2.75
8.00	5.96	3.52	2.78

Yucca (Bache)			
Th km	α km/s	β km/s	ρ gm/cm³
0.40	1.65	0.90	1.60
0.60	2.35	1.30	1.86
0.50	4.80	2.60	2.65
0.50	4.80	2.60	2.65
2.00	5.90	3.40	2.75

Yucca (Geotech)			
Th km	α km/s	β km/s	ρ gm/cm³
0.25	1.34	0.603	1.00
0.25	2.14	0.963	1.80
0.30	3.00	1.50	1.80
1.20	4.57	2.285	2.50
2.00	5.90	3.48	2.75
8.00	5.96	3.52	2.78
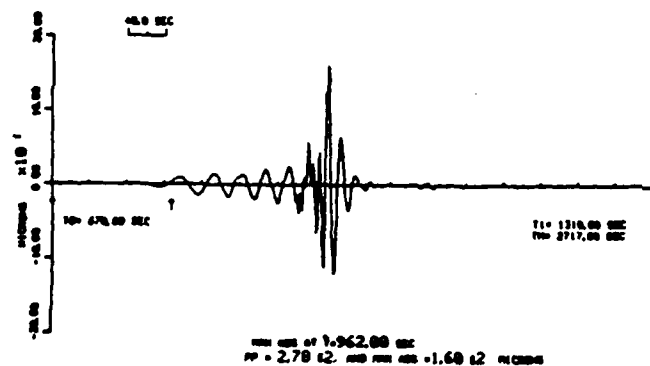
SOURCE DEPTH = .7000
ALPS =6.2000 .BETS =3.5110 .RHOS =2.7360 .MUS =33.7270
TOTAL DISTANCE = 2.000 E3 KM
STEP MOMENT OR RDP EXPLOSION HISTORY
STRESS GLUT =1.000 E0 GIGAPASCALS. SOURCE VOLUME =1.000 E0 KM**3
ZI(INF) = 7.966 E5 M**3.   M0 = 1.000 E25 (DYNE-CM)
INTERPOLATED CRTM CONTINENTAL A
WSN LP T1
PURE CIT109 A0
SURFACE VERTICAL DISPLACEMENT
MICRONS

SOURCE DEPTH = .7000
ALPS =2.3500 .BETS =1.3000 .RHOS =1.8600 .MUS =3.1434
TOTAL DISTANCE = 2.000 E3 KM
GAUSSIAN BEAM APPROXIMATION
SOURCE PATH =0.000. RECEIVER PATH =3000.000
STEP MOMENT OR RDP EXPLOSION HISTORY
STRESS GLUT =1.000 E0 GIGAPASCALS. SOURCE VOLUME =1.000 E0 KM**3
ZI(INF) = 7.747 E6 M**3.   M0 = 1.000 E25 (DYNE-CM)
INTERPOLATED CRTM CONTINENTAL A
WSN LP T1
BACHE YUCCA A0
PURE CIT109 A0
SURFACE VERTICAL DISPLACEMENT
MICRONS

Figure 1

14 km

3000 km

2000 k

Figure 3

3000 km

3000 km

14 km

Figure 2

gb cit109 yucca smol 0 4Km
gb hs yucca smol 0 4Km

DELTA LOG
-.050

17
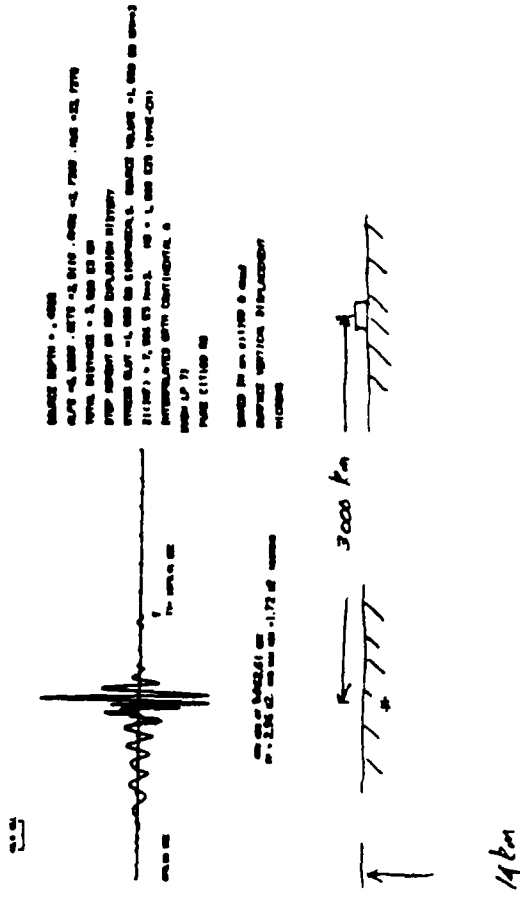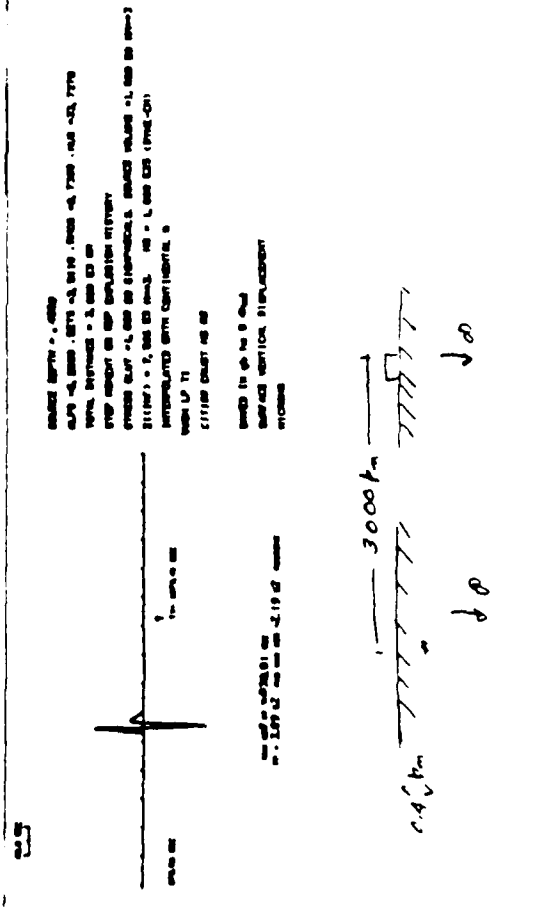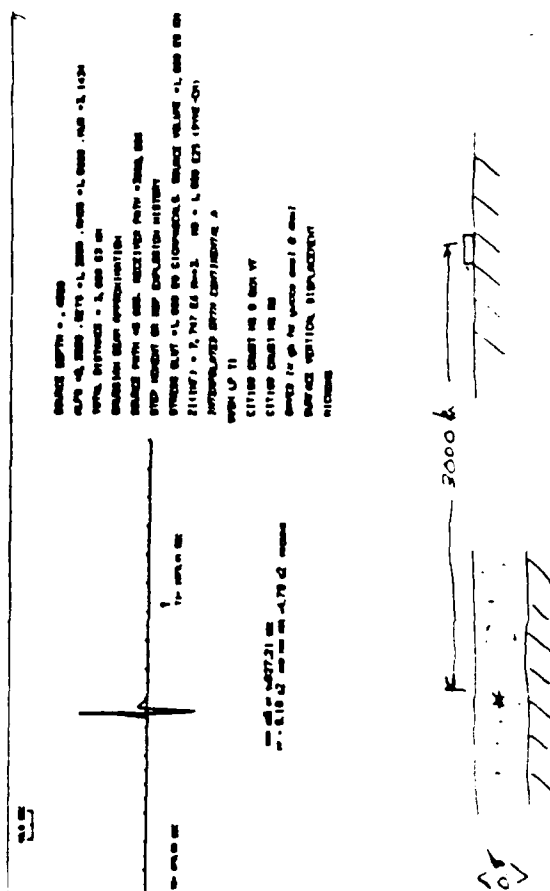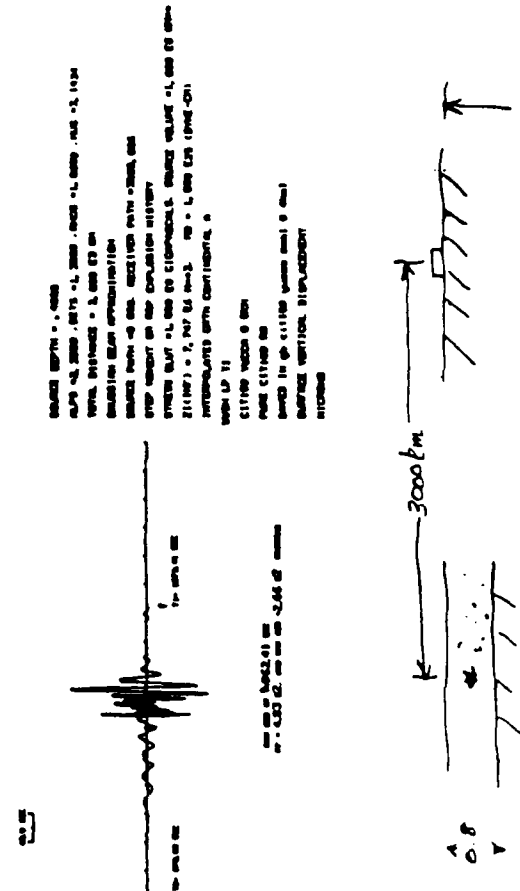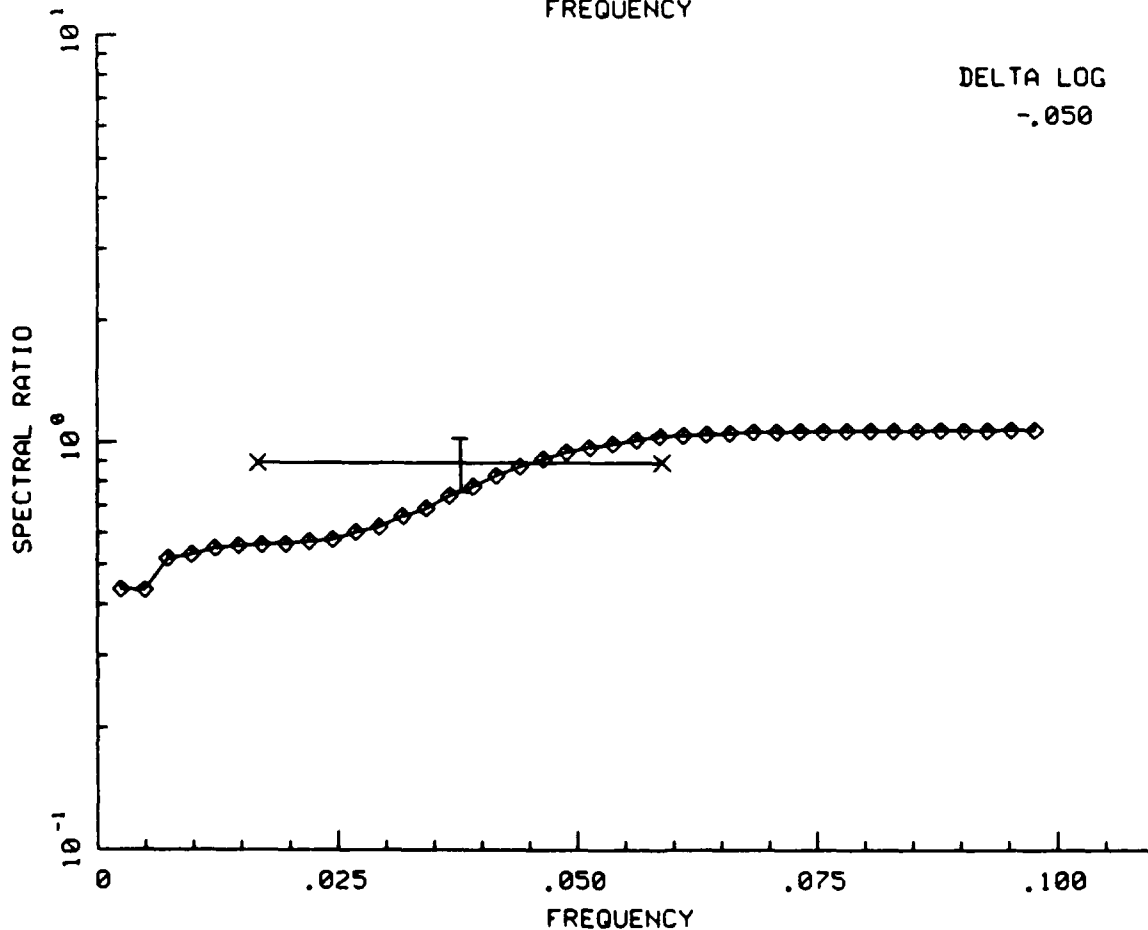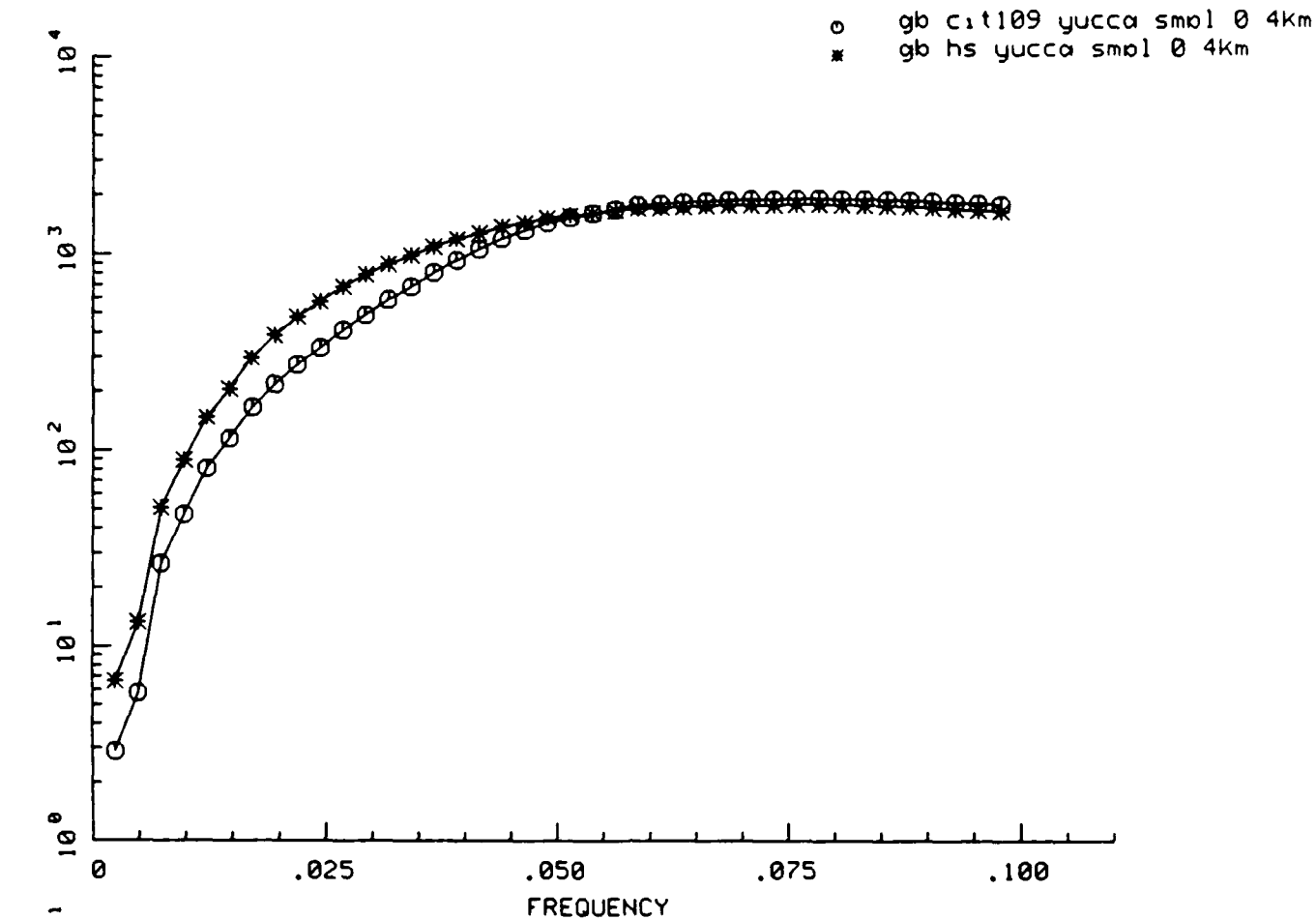
SELECTING SEISMOLOGICAL STATIONS OF A NETWORK

FOR GLOBAL EXPLOSION MONITORING

Hans Israelsson

Center for Seismic Studies
1300 N. 17th Street, Suite 1450
Arlington, VA 22209

1. OBJECTIVE

Assessments of seismic station networks to monitor underground nuclear explosions are usually limited to estimates of *given station networks*. That is to say, the geographical co-ordinates and noise characteristics of the seismological stations are given, and the capability of the network to detect a seismic event is then calculated. One can consider this *network assessment* as a *direct* problem. From the point of view of monitoring, the reverse or indirect problem is also relevant. That is to say, determine the station net ork that satisfies *given desirable performance criteria*. A variant of this problem is to optimize the siting of *a given number* of stations so that some performance criterion is optimized. These *indirect* problems, which are related to *network design*, are seldom addressed, partly because of their complexity and of the fact that widely accepted performance criteria are not available. In this paper we attempt to get some insight into this indirect or network design problem with calculations for various hypothetical networks with regard to event detection, location, and depth estimation.

The scope is limited to a global network of the kind developed by the GSE at the UN conference of Disarmament. Details about desirable performance of this system have only been described in rather general and imprecise terms. It is, however, a system based primarily on *tele seismic* detection. For the purpose of the calculations we assume that a desirable detection threshold is in the range $m_b \approx 4$. We also assume that a *uniform* geographical performance is desirable. It can be discussed to what extent such uniformity should be achieved for the continental as well as the oceanic areas. It also seems reasonable to require that the seismological functions are *balanced*. For example, there should be a minimum gap between the threshold of detection and identification.

2. RESEARCH ACCOMPLISHED

Apart from the general principles of uniformity and symmetry, seismological functions and associated criteria have to be formulated and specified. For example, the functions can be tailored to source type so that the capabilities to detect explosions and to identify earthquakes by the so called $m_b(M_s)$- method or focal depth are maximized. In addition minimizing the unassociated station signal detections is important. This leads us to consider the following monitoring tasks:

Explosions:

The system should be designed to maximize the capability to detect and locate explosions. Moreover, the depth has to be estimated so that the explosions can be identified to have shallow source focus. For simplicity it is assumed that the explosions are carried out in hard rock and are fully decoupled.

Shallow earthquakes:

It is assumed that identification is made primarily on the basis of the $m_b(M_s)$ criterion. Signal detections at individual stations from shallow earthquakes have also to be associated with detected and located events with high probability. In other words the number of unassociated station detections originating from shallow (and deep) earthquakes should be minimized. In principle it is thus not necessary to optimize the capability of detection, location, or depth estimation for shallow earthquakes.

Deep earthquakes:

It is assumed that the occurrence of deep earthquakes is confined to a sub-region of the target area. The most important function is depth estimation, i.e., again it would in principle not be necessary to optimize the capability to detect and locate deep events, but the depth of events that are detected and located have to be determined so that a possible explosion depth can be ruled out. The number of unassociated station detections originating from deep earthquakes (together with those from shallow earthquakes) should also be minimized.

The tasks in relation to source type can be summarized by the following table:

TASK	SOURCE TYPE		
-	Explosion	Shallow Quake	Deep Quake
Event Detection	*		
Signal Association		*	*
Epicenter Location	*		
Depth Estimation	*		*
Source Identification (Surface Waves)		*	

The functions require different kind of information from the seismic recordings. A network designed to optimize only one of the tasks may therefore not necessarily perform in an optimum manner for another. Consider for example the case for which the target area, consists of one site only (one pair of co-ordinates). Then the azimuthal coverage of the stations around the site largely determines the location accuracy, whereas appropriate coverage of certain epicentral distance intervals is important for the depth estimation based on surface reflections *(pP, sP)*.

Siting of the stations to optimize the detection capability is mainly determined by the amplitude attenuation as a function of distance, which may result in a station distribution that is non-uniform in azimuth and distance. If the target area is not just one pair of co-ordinates but for example a continent the situation becomes more complicated. Because of this trade-off between the tasks, a selection of the stations taking several tasks into account has to be some kind of 'compromise' between tasks. One of the tasks above, detection of surface waves, can however be optimized independently of the others provided the long period stations are not necessarily to be co-located with short period stations. On the other hand, it may from a seismological point of view be desirable to maintain such a co-location of different kinds of instrumen ation.

Some parameters that influence the capability of each of these functions have been studied separately with calculated examples for hypothetical networks using the network assessment program, SNAP/D.

The detection capability as a function of number of stations is studied for networks with equal station spacing on a sphere. The problem of finding the coordinates for stations of such networks is however not trivial, for a large number of stations, n. This problem has many analogies in the mathematical literature but so far no general analytical solution has been presented. In the calculations approximately symmetrical networks are used for networks with more than 20 stations. The average detection threshold is reduced somewhat faster than the logarithm of the square root of number of stations ($\log_{10}(\sqrt{n})$, and appears to be asymptotic to $\log_{10}(\sqrt{n})$ for large numbers of stations (Figure 1). About ten stations or more equally spaced on the sphere provides a fairly uniform detection threshold over the sphere, although there are significant variations in areas close to where the stations are located.

Calculated examples suggest that for a given number of sensors, a network consisting of arrays with a small number of sensors seems to give a slightly lower detection threshold than that of a signal station network with the same total number of sensors (Figure 2). This conclusion is valid if the monitored area is limited to a small region and the stations cane be sited at locations with comparable noise an amplitude attenuation. The low detection threshold for array networks is primarily due to the fact that a smaller number of stations are required for event detection than that for a single station network. This relaxed criterion outweighs the number of stations of the network.

Location errors have been calculated for networks with stations that have equal distance to the epicenter and are uniformly distributed around the epicenter. The square root of the area of the joint marginal confidence region for the epicenter is used as measure of location error. The calculated examples suggest that a 90 degree coverage of the source-to-station azimuth gives location errors that are only slightly larger than those for networks with more complete azimuthal coverage.

The computational experiments have also been carried out for hypothetical networks consisting of station only in shield and platform areas. It appears difficult to achieve a global uniform capability with such a network, but sufficient coverage of the territorial areas of the major continents can be obtained.

An iterative algorithm based on detection by optimization has been used to select

sites for stations so that the performance of one or several seismological functions is maximized. For example, the task of selecting a given number of stations with optimum capability of measuring depth phases can be reduced to the problem of chosing the sites so that the variance of the step-out of events in a given region is minimized, and the co-ordinates of the stations can be obtained with this iterative algorithm. The solution is obtained by successive selections, starting with two stations, among a limited set of possible sites. Initially, the coordinates of these two stations are chosen arbitrarily and the coordinates of a third station are chosen so that the variance of the distance distribution is maximized. As a next step of this procedure the coordinates of the first and the second stations are chosen in a similar way for one station at a time again so that the variance of distance distribution is maximized. Finally, the coordinates of the first station are chosen again with the coordinates for the two other stations fixed. When the coordinated for the three stations have been selected, a fourth station is added and the coordinates for all stations are revised in a similar way as the coordinates for the three stations were obtained. When the iteration is completed for four stations, one station is added at a time until all stations have been included.

3. CONCLUSIONS

In this report we summarize studies carried out in order to get some insights into the problem of selecting seismological stations of a global network for monitoring underground nuclear explosions.

Seismological functions are defined and selection criteria are specified on the principles of uniformity and symmetry in performance.

The dependence of various seismological functions of a global network on a number of parameters have been studied.

An algorithm based on detection by optimization have been used to select stations so that the performance of one or more seismological functions are optimized.
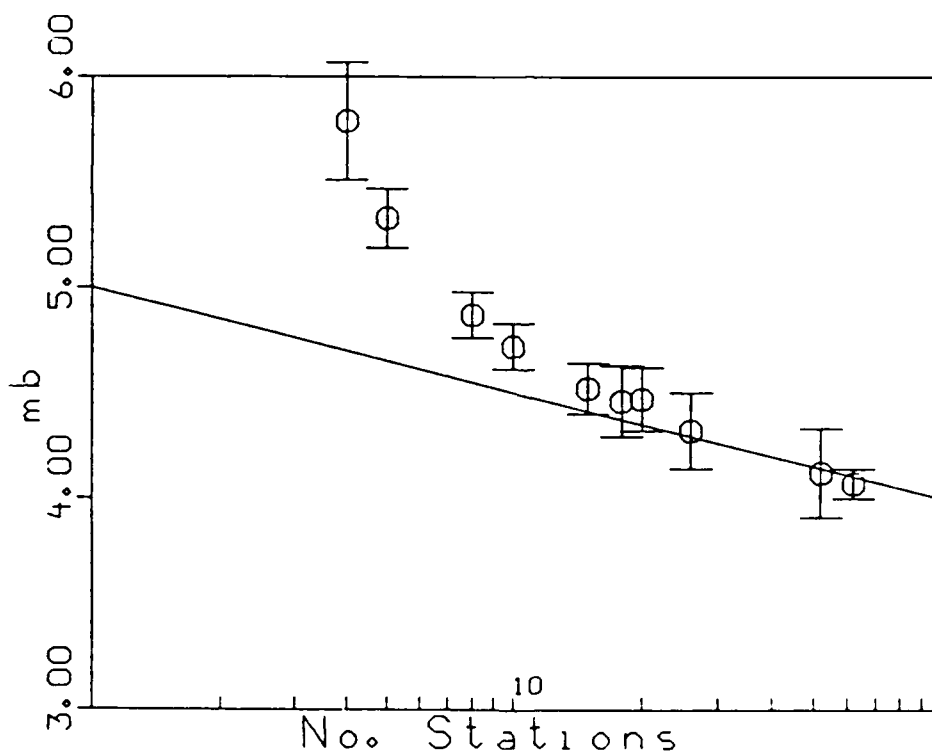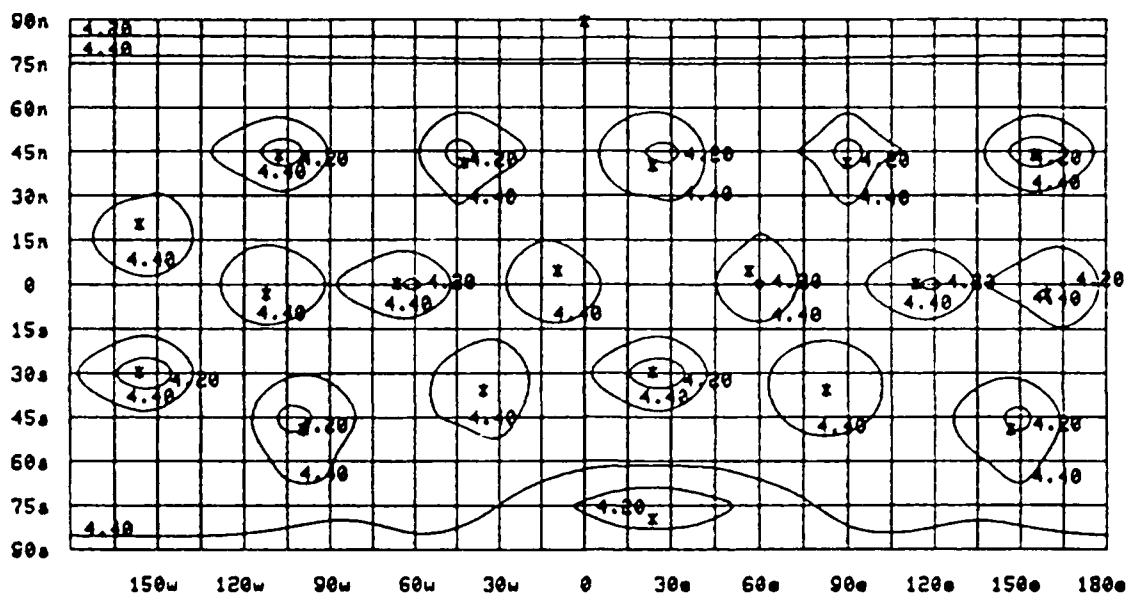
Figure 1 The map (above) shows the contours of the magnitude m_b detection thresholds (90%) for a network of 20 stations equally spaces on a sphere. Station locations are marked with asterisks. The diagram (below) shows the average magnitude threshold as a function of number of stations for networks equally spaced on a sphere. The error bars represent the standard deviation of the threshold for magnitude thresholds calculated every 15 degree latitude and longitude.
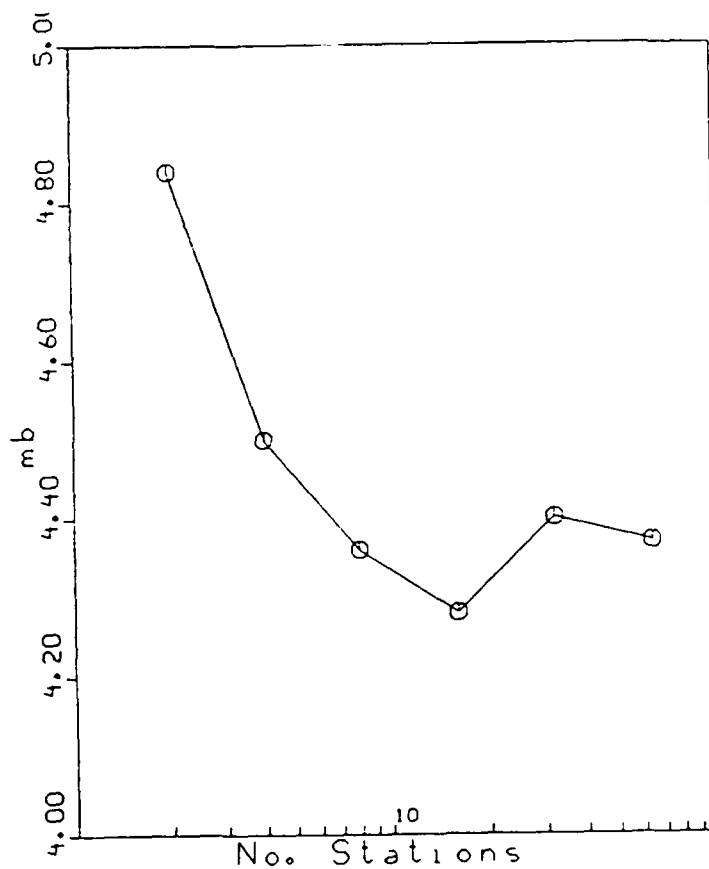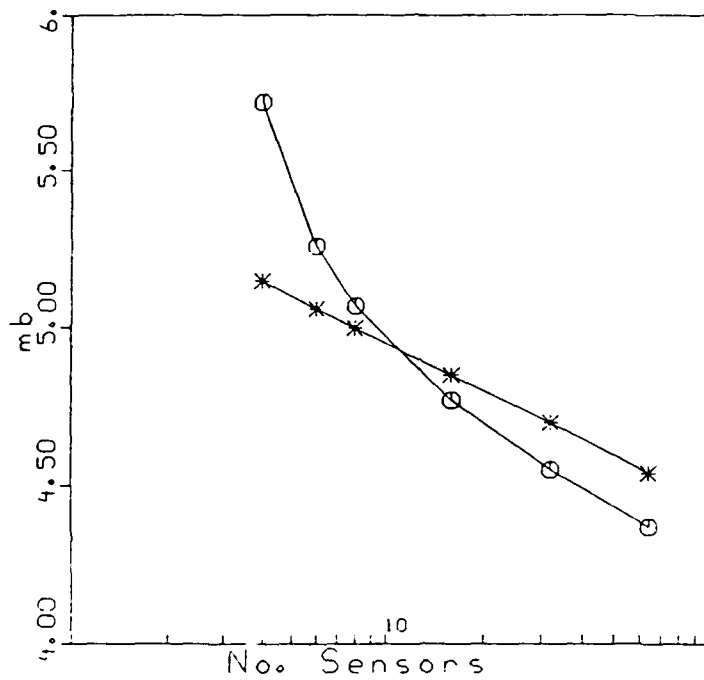
Figure 2 The upper diagram shows the detection threshold as a function of number of sensors for a single stations network (open circles) and for one a array station (asterisks). The curve in the lower diagram represents the detection threshold as a function of number of stations for a given number of (64) of sensors grouped together in arrays of 32, 16, 8, 4, 2, and 1 sensor. The lowest threshold is obtained for 16 stations with 4 sensors each.

REGIONAL STUDIES WITH BROADBAND DATA

L. R. Johnson and T. V. McEvilly
University of California, Berkeley

Objective

The general objective is to study how observational ground motion data can be used to infer properties of seismic sources. The emphasis is on the recording and analysis of broadband three-component data. The goal is to develop methods which are successful when applied to data recorded at distances close to the source and then try to extend these methods to data recorded at regional and teleseismic distances.

Research Accomplished

The problem of estimating the properties of seismic sources has been approached from a number of directions. A common element of these various studies has been the representation of the source in terms of its force-moment tensor. This construct provides a fairly general mathematical representation of the source which allows a convenient separation of the effects of source and propagation. Considerable attention has been given to the examination of the stability and uncertainty of the estimates that emerge from the moment-tensor inversion process.

A critical ingrediant in the moment tensor inversion is the Green functions which are used to remove propagation effects from the seismograms. The accuracy of the final results is directly related to the accuracy of the Green functions, and this depends upon the availability of a good estimate of the velocity and density structure. This general problem was examined for the case of shallow earthquakes in a complicated geologic setting in northern California (O'Connell, 1986; O'Connell and Johnson, 1987). A nine station temporary seismographic network was deployed in the area for one month and good recordings from 39 events were obtained. P and S arrival times were analyzed by the method of progressive inversion to obtain estimates of source locations, average velocity models for both P and S waves, and recording station travel time anomalies. These velocity models were then used to generate the Green functions necessary for the moment tensor inversion of the waveform data. Good results were obtained. Moment tensor estimates of principal stress orientations were comparable with those obtained from P-wave first-motion focal mechanism solutions but were obtained with far fewer stations. In some cases the moment tensor estimates gave definitive results when first-motion solutions using far more stations were completely ambiguous. This study demonstrated that in realistic situations it is possible to separate source and propagation effects and solve the combined inverse problems of velocity structure, source location, and source mechanism.

Another study concentrated on the task of obtaining improved estimates of the velocity structure of Pahute Mesa of the Nevada Test Site. P and S waves generated from 13 different explosions were used to estimate P-wave and S-wave velocity models for the upper 4 km of the Silent Canyon Caldera (Leonard and Johnson, 1987). The structure was modeled using linear velocity gradients, with P velocities increasing from 1.5 km/sec at the surface to 4.5 km/sec at 2.3 km depth and S velocities increasing from 1.0 km/sec at the surface to 2.3 km/sec at 2.0 km depth. This one-dimensional structure must be regarded as a lateral average of actual velocities because there is considerable evidence in the waveform data to indicate that lateral heterogeneity is present.

Broadband seismic data in the distance range of 1 to 10 km were used to estimate moment tensors for two explosions detonated at Pahute Mesa, Harzer and Chancellor. The inversion used the refined velocity model described in the previous paragraph. The results indicate that the sources are dominated by the explosive component but that significant deviatoric components are also present. The explosive component shows a fairly simple time history which is consistent with various models which have been proposed for buried explosives, although the analysis also revealed a trade-off between parameters estimated for the source and the models assumed in making the estimation. The non-explosive component of these sources also shows a simple time history but its physical interpretation is more problematical.

A fundamental concern in the interpretation of moment tensor estimates is the stability and uncertainty of the results. Because it can be posed as a linear inverse problem, standard least-squares techniques can be employed and thus stability can be rigorously analyzed and uncertainities in the data can be mapped into uncertainties in the results. However, such analysis does not take into account uncertainties which may exist in basic assumptions, source locations, and Green functions, and these may be a major concern in some problems. In order to explore some of the effects of these more general sources of uncertainty, the method of solving the inverse problem has been expanded to include L1 norm minimization, positivity constraints, and extremal value estimation. These methods have been tested with synthetic and actual data recorded at near and teleseismic distances from both earthquakes and explosions.

As one might expect, when the sources are simple and large amounts of high-quality data are available, the various methods produce similar results, and the choice of method reduces to the questions of ease of appliction and cost of computation. However, as the quality and quantity of the data are degraded, differences between the methods begin to appear. For the case of a few systematic errors the L1 norm is superior to the L2 norm. But as the number of errors is increased so that a random situation is approached, the L1 and L2 norms begin to show similar sensitivities to the errors. The L1 norm and L2 norm with positivity constraints (quadratic programming) have the advantage that constraints upon the source

are easily incorporated. This device has been used to estimate moment tensors in which the trace has been either maximized or minimized. For explosions recorded at close distances the most compact source time function is obtained when the trace of the moment tensor is maximized and for deep earthquakes recorded at teleseismic distances the most compact source time function is obtained when the trace is minimized. These preliminary studies indicate that a thorough investigation of the source will require that a number of these different inversion methods will have to be applied, particularly when the quantity and quality of the data are low and the question of uniqueness is serious.

Another area of investigation has been the interaction between source depth, source mechanism, and frequency bandwidth. This is a particular concern for shallow explosions recorded at teleseismic distances where bandwidth is limited by attenuation properties of the earth. The situation appears to be rather complicated with a number of different factors interacting in a manner which is not easy to predict. The basic stability of the results is controlled by the eigenvalues of the complete Green function matrix, but the spectral features of individual Green functions are also important and this is affected by the distribution of stations. An inversion which appears to be stable when no noise is present can become unstable for some elements of the moment tensor as the level of noise is increased. A similar effect occurs as the bandwidth of the data is decreased and the effect is now a strong function of the source depth and station distribution.

Conclusions and Recommendations

Some of the practical problems of studying seismic sources by estimating their moment tensors have been examined and the results are quite positive. When reasonable care is given to estimation of velocity models, Green functions can be calculated that lead to reliable and useful estimates of moment tensors in realistic and fairly complicated geologic settings. When working with data of limited quantity or quality or when trying to analyze minor features of the moment tensor, careful attention must be given to analysis of the stability and uncertainty of the results. Using a variety of different inversion methods is helpful in such situations, as is a detailed examination of the eigenvalues of the Green functions.

References

Leonard, M. A., L. R. Johnson, Velocity structure of Silent Canyon Caldera, Nevada Test Site, Bull. Seism. Soc. Am., 77, 597-613, 1987.

O'Connell, D. R., Seismic Velocity Structure and Microearthquake Source Properties at the Geysers, California, Geothermal Area, Ph.D. Thesis, University of California, Berkeley, 1986.

O'Connell, D. R. H., L. R. Johnson, Inversion for the first degree moment tensor of microearthquakes at The Geysers, California, geothermal field, submitted to Bull. Seism. Soc. Am., 1987.

ANALYSIS OF TELESEISMIC P WAVE AMPLITUDE AND CODA
VARIATIONS FOR UNDERGROUND EXPLOSIONS

Thorne Lay
Christopher S. Lynnes

University of Michigan

OBJECTIVE. The principal objective of this contract is to develop and apply techniques for determining near-source contributions to the observed variations in short-period P wave amplitudes, travel times, waveforms and coda for underground explosions. The basic approach involves analysis of large data sets with extensive azimuthal and ray parameter coverage in order to detect systematic event-to-event variations that can reliably be attributed to near-source phenomena.

RESEARCH ACCOMPLISHED. Under our previous contract we established that amplitude and travel time variations for short-period P wave recordings of NTS explosions exhibit a moderate, but significant correlation indicative of focussing and defocussion effects. Systematic slowly varying patterns between the Yucca Flat and Pahute Mesa subsites, which are separated by 30 km, indicate that regional velocity heterogeneity in the crust and upper 200 km of the mantle is responsible for a substantial component of the variations. Figure 1 exhibits the station-averaged magnitude and travel time anomalies for the two subsites. It is apparent that both common features and systematic differences in the patterns for the two subsites are present. The Pahute Mesa patterns at azimuths toward the northeast are accentuated with respect to those for Yucca Flat.

A back-projection technique has been employed to image the upper mantle velocity structure responsible for the intersite differences in Figure 1. The magnitude anomalies have been used to directly image the structure rather than relying on block inversion of the travel times given that existing models obtained from travel times (Minster et al. 1981, Taylor, 1983) predict very different magnitude variations (Lay et al. 1986, Cormier 1987). Our procedure is an adaptation of the thin lens modeling previously applied to NORSAR data by Haddon and Husebye (1978), in which the geometric wavefront curvature equation is used to predict travel time advances on a thin interface that will match the observed amplitude behavior. The observed travel times are compared to the predictions to identify the successful models. Figure 2 presents back-projections of amplitude and travel time anomalies to surfaces at various depths below the NTS source region. The anomalies have been corrected to remove the common average NTS patterns. A projection depth of 160 km was found to yield the strongest correlation between observed and predicted travel time residuals, indicating that the amplitude anomalies have accumulated by the time the rays reach this depth.

A similar thin lens model was constructed for the Pahute Mesa subsite alone, with the subsite station averages being removed from the data. This procedure is sensitive only to very shallow structure because we are isolating spatial systematics in the scatter of the observations at a given station rather than using the station-to-station behavior. A thin lens at 25 km depth proved quite successful for the Pahute Mesa data, indicating that strong crustal heterogeneity affects the amplitude behavior.

Figure 3 shows the preferred thin lens models obtained from the magnitude residuals for the regional NTS data (160 km) and the shallow Pahute Mesa scatter (25 km). The surfaces have been converted to topography on interfaces with increasing velocity contrasts. A regional high undulation of the surface trending northward from NTS results in defocussing and early arrival times to the northeast from Pahute Mesa and toward the north from Yucca Flat. Figure 4 compares observed and predicted differences in mean station amplitude anomalies between the two subsites for the deeper thin lens model. The predicted values were determined using three-dimensional Kirchhoff-Helmholtz theory to construct finite frequency synthetic seismograms. While the range of variations is somewhat underpredicted, the azimuthal pattern is very well reproduced.

The shallow Pahute Mesa structure also exhibits an elevated, defocussing structure located centrally beneath the array. This shallow structure causes systematic location dependent variations in the scatter of magnitude anomalies. Observed and predicted patterns are compared in Figure 5. While the precise range and spatial patterns are not fully matched by this single surface, the general intrasite trends are satisfied by the model, indicating that crustal heterogeneity effects on the magnitude scatter can be deterministically accounted for to a certain degree.

The thin lens models are compared with the results of previous linear travel time inversions in Figure 6. Note the excellent correspondence between fast velocities in the travel time models and elevated topography in the thin lens models. There is undoubtedly some finite extent to the actual velocity heterogeneity, rather than being concentrated at single velocity interfaces, but the success of the thin lens models in predicting subtle features of the amplitude variations indicates linear accumulation of the magnitude anomalies over any actual finite extent of the heterogeneity. We have not yet resolved the spatial extent of the deeper heterogeneity responsible for the common NTS amplitude and travel time patterns, although comparison with regional earthquake anomalies suggest that near-receiver structure is not responsible.

We are also conducting a detailed examination of the near-source contributions to early P wave coda. Figure 7 illustrates systematic magnitude dependence of the event-averaged relative coda excitation. This figure shows that in the 0.4-0.8 Hz frequency band smaller events tend to have stronger coda excitation for both Pahute Mesa and Yucca Flat events. Similar behavior has been established for Novaya Zemlya and Amchitka test site events. Pahute Mesa events also exhibit a magnitude dependence of coda excitation in the 0.8-1.1 Hz band, with larger events having enriched coda levels. This is partially due to pP interference in this band, but the presence of systematic spatial and azimuthal patterns in the behavior indicate that frequency dependent focussing effects are also important.

The event-averaged characteristics of the coda excitation have been related to spatial effects by comparisons like Figure 8, where the Yucca Flat events with enhanced coda amplitudes in the 0.8-1.1 Hz band are found to be located centrally above the valley in the basement structure. Pahute Mesa shows pronounced spatial dependence of the azimuthal patterns in the relative excitation of direct arrivals and early coda for the 0.8-1.1 Hz band. Events in the central part of the Silent Canyon caldera show diminished direct arrivals relative to the coda at azimuths to the north. This behavior corresponds to the enhanced defocussing of downgoing direct P energy by the shallow crustal heterogeneity underlying Pahute Mesa, while the coda appears to average out the effects of the shallow structure.

CONCLUSIONS AND RECOMMENDATIONS. Substantial progress has been made in attaining an understanding of the origins of amplitude and travel time variations produced by mantle heterogeneity beneath NTS, completely on the basis of teleseismic observations. Careful analysis of the scatter in magnitude observations can result in deterministic velocity structures which will provide better intrasite specific magnitude corrections than purely statistical procedures. We are now performing detailed modeling to explain the magnitude dependence observed in early coda excitation in the 0.4-0.8 Hz and 0.8-1.1 Hz passbands. Further attempts to invert for near-source scattering structures that contribute arrivals to the coda are also being undertaken.

Cormier, V. F., 1987. Focusing and defocusing of teleseismic P waves by known 3-D structure beneath Pahute Mesa, Nevada Test Site, Bull. Seism. Soc., in press.

Haddon, R. A. W., and Husebye, E. S., 1978. Joint interpretation of P wave time and amplitude anomalies in terms of lithospheric heterogeneities, Geophys. J. Roy. Astr. Soc., 67, 587-598.

Lay, T., Lynnes, C. S., and Welc, J., 1986. Analysis of teleseismic P wave amplitude and coda variations for underground explosions at U.S. and Soviet test sites, Scientific Report AFGL-TR-86-0038, University of Michigan, Ann Arbor, Michigan.

Minster, J. B., Savino, J. M., Rodi, W. L., Jordan, T. H. and Masso, J. F., 1981. Three dimensional velocity structure of the crust and upper mantle beneath the Nevada test site, Final Technical Report SSS-R-81-5138, Science, Systems and Software, La Jolla, California.

Taylor, S. R., 1983. Three-dimensional crust and upper mantle structure at the Nevada test site, J. Geophys. Res., 88, 2220-2232.

Figure 1. Equal area plots of station mean travel time and magnitude anomalies for the Pahute Mesa and Yucca Flat test sites. The perimeter corresponds to a take-off angle of 22.5° in a source velocity of 3.5 km/s.

Figure 2. Bin-averaged back-projections of magnitude and travel time anomalies with NTS station means removed to surfaces at depths of 35 km, 100 km, and 160 km beneath the test site.

Figure 3. Contour plots (in km) of the velocity discontinuity surfaces obtained from inversion of amplitude anomalies. The deep (160 km) model obtained from intersite differences in magnitude patterns is shown on the left. The shallow (25 km) surface obtained from intrasite differences is shown on the right. Elevated regions correspond to high velocity defocussing structure on the interface.

Figure 4. Comparison of synthetic log amplitude variations with observed variations in m_b. The equal-area plot on the left shows the observed station average m_b values for Yucca Flat differenced from the corresponding station means for Pahute Mesa. The equal-area plot on the right shows synthetic log amplitude variations of Yucca Flat explosions differenced from those of Pahute Mesa. The synthetics were computed using Kirchhoff theory and the 160 km deep surface shown in Figure 3.

Figure 5. Variations of observed and synthetic magnitudes at different azimuths. The synthetic variations are calculated for the indicated stations using the shallow Pahute Mesa thin lens model in Figure 3. The observations are obtained by averaging values from the indicated stations as well as nearby stations.

Figure 6. Comparison of discontinuity models with block inversion models derived from travel times by other authors. The figure on the left is modified from Minster et al. (1981), and is a vertical cross-section through their model, represented by the velocity contours. Symbols indicate the velocity perturbations in the blocks of Taylor's (1983) model that are intersected by the cross section. The thick lines are the profile through the shallow (25 km) and deep (160 km) thin lens velocity discontinuity models. The locations of the cross sections are plotted on contour maps of the surfaces on the right. High velocity region or downward extensions therof in the block travel time models correspond to upwarps of high velocity material in the amplitude-derived discontinuity models.

Figure 7. Correlation of relative event average centroids with magnitude and burial depth in the (0.4-0.8 Hz) and (0.8-1.1 Hz) passbands for Yucca Flat and Pahute Mesa events. Higher positive values indicate relative enrichment of the early P wave coda amplitudes compared to the direct arrival energy.

Figure 8. Map of Yucca Flat showing depth to Tertiary-Paleozoic contact with event average complexity for the 0.8-1.1 Hz passband of Yucca Flat explosions.

Pahute Mesa   Yucca Flat

Δ m_b

◇ ◇ + -|-
-0.4 -0.2 0.2 0.4

Δ t, s

◇ ◇ + -|-
-2 -1 1 2

FIGURE 1.

Magnitudes   Travel Times

35 km

100 km

160 km

Δ m_b   Δ t s
◇ ◇ + -|-   ◇ ◇ + -|-
-04 -02 02 04   -08 -04 04 08

FIGURE 2.

160 km

25 km

FIGURE 3.

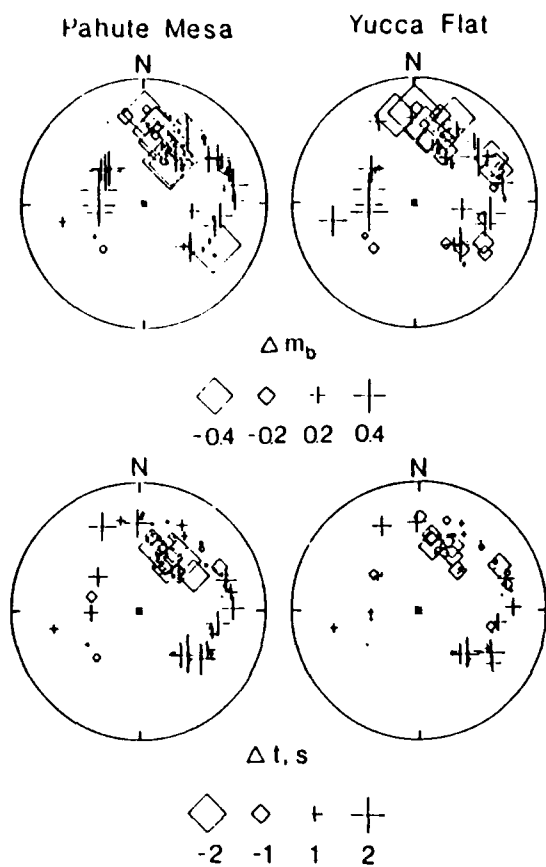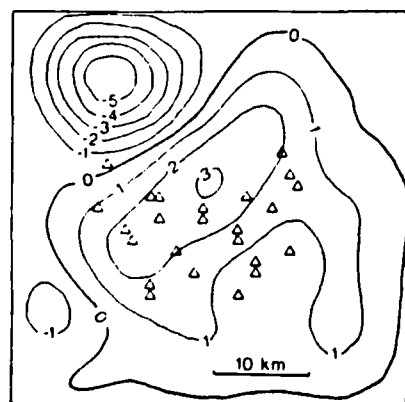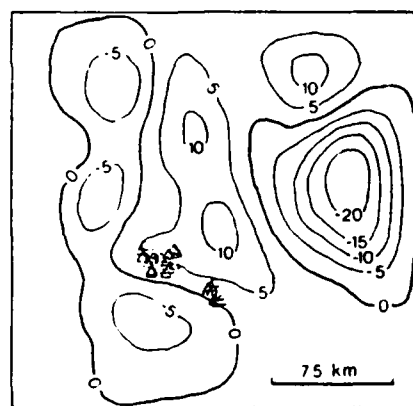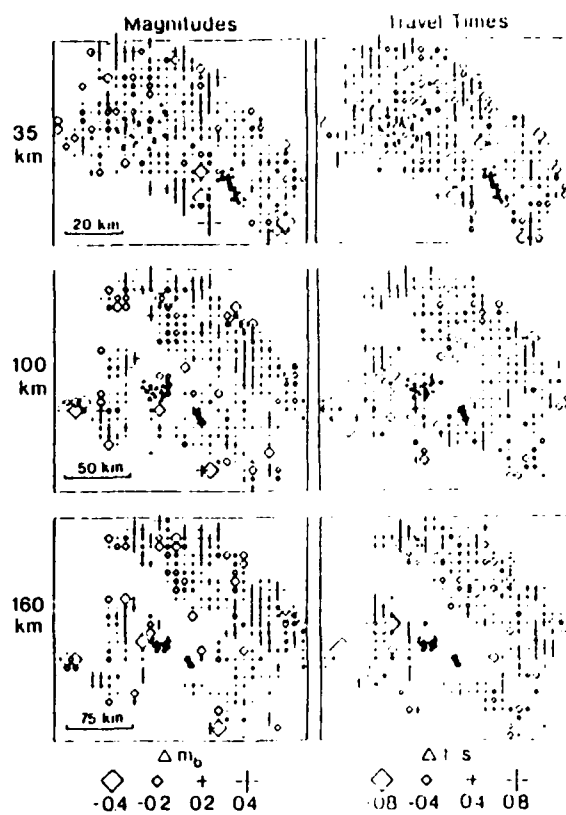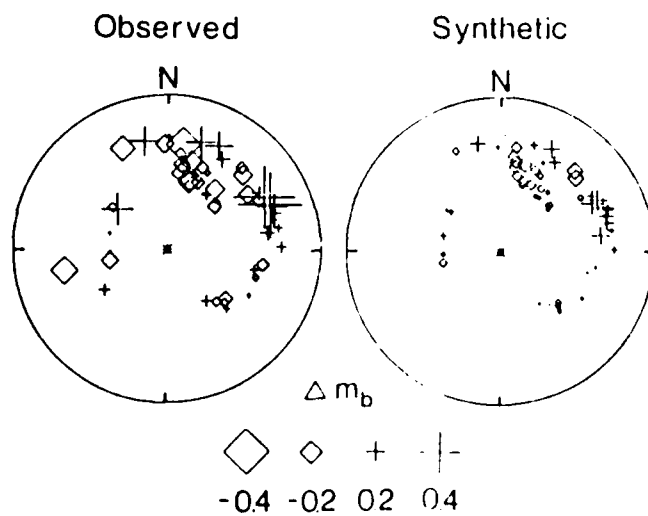Observed   Synthetic

Δ m_b

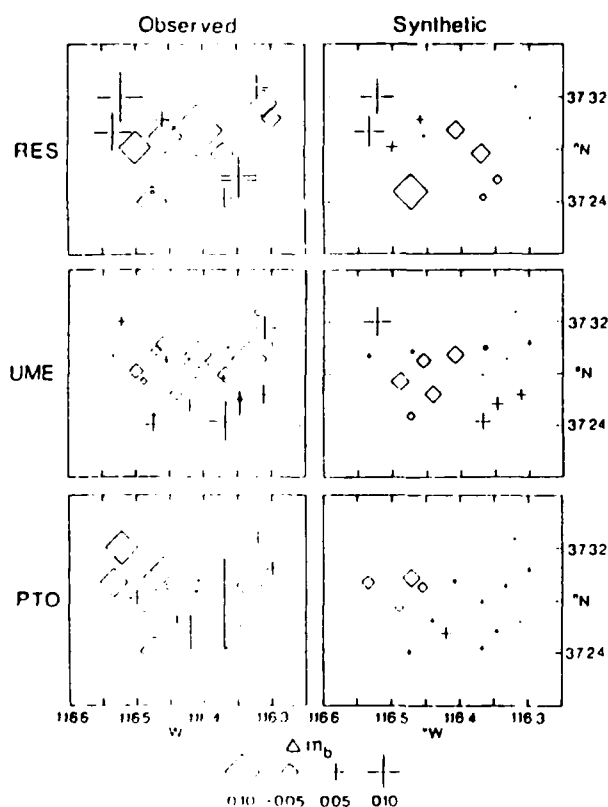◇ ◇ + -|-
-0.4 -0.2 0.2 0.4
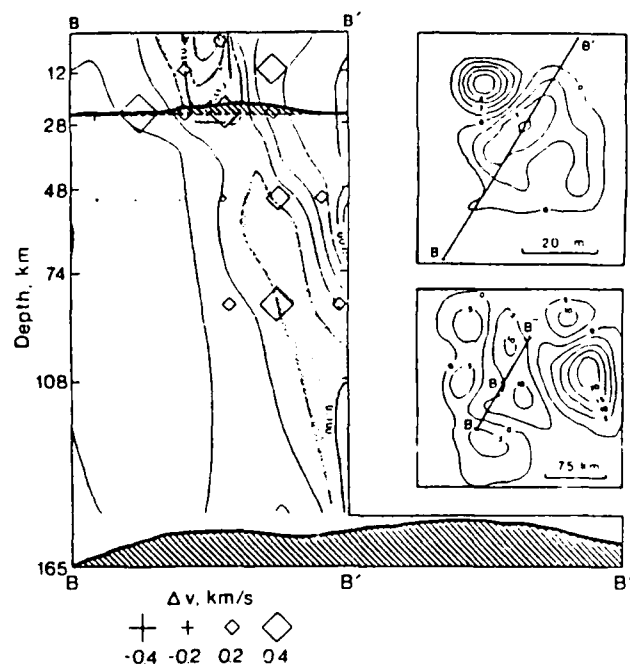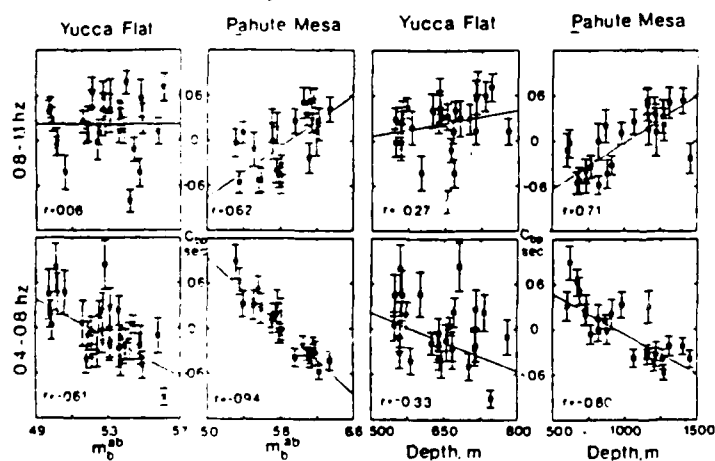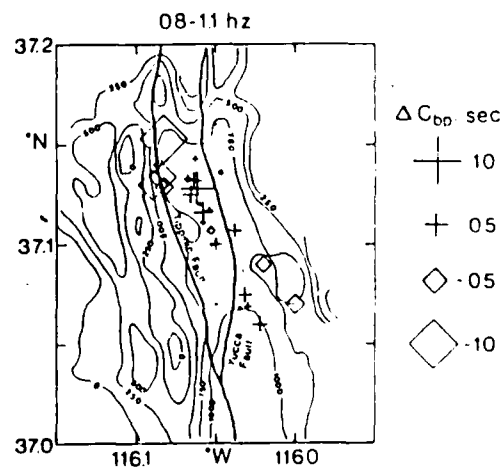
FIGURE 4.

32

FIGURE 5.

FIGURE 6.

FIGURE 7.

FIGURE 8.

34

Tectonics of Eastern Kazakhstan and Implications for Seismic Source Studies in the Shagan River Area

William Leith
U. S. Geological Survey
Reston, VA 22092

Objectives

Eastern Kazakhstan is commonly referred to as a "stable shield". However,the large amount of tectonic release that has accompanied some explosions at the Shagan River test site is somewhat in conflict with that notion. Also, analyses of Asian deformation suggest that the region to the north of Tibet is one dominated by north-south horizontal compression [Molnar and Tapponier, 1975], whereas model solutions for tectonic release at Shagan River imply *northeast* compression. These inconsistencies were examined in light of data on the recent tectonics of eastern Kazakhstan. These data indicate that the region is experiencing compressional tectonics, and shows evidence of contemporary seismicity, Quaternary fault offsets and general crustal uplift. The objective, therefore, is both to provide an understanding of the tectonic environment in which most Soviet underground nuclear tests have occurred, and to apply this toward seismological studies of tectonic release at the Shagan River test site. Because of space limitations here, the reader is referred for background information to a detailed description of the geology and geophysics of the test area presented by Bonham *et al* [1980]. Results indicate that seismological estimates of the mechanism of the component of tectonic release present in many of the explosions at the test site should perhaps be reevaluated with more complex (i.e., oblique-slip) models.

Research Accomplished

We have analyzed the area of eastern Kazakhstan between the Irtysh river and Lake Balkhash, east of Karaganda and west of Lake Zaysan for evidence of recent tectonics (Fig.1). The Semipalatinsk nuclear weapons proving ground is located in the northern portion of this area. Geologically, the test area is located within the Kazakh fold system, a complex of deformed Paleozoic rocks along the eastern edge of the so-called "Kazakh shield" [Babak, 1969]. In general, fold and fault structures to the northeast of the Chingiz fault (including the test site) trend northwest-southeast. These are intruded by numerous granitic massifs, including Degelen Mt., one of the three main test sites [see Rodean, 1979].

Seismicity

While the Kazakh shield is generally considered to be aseismic, in fact, earthquakes in the area are rare, but not unknown. For example, an earthquake near Semipalatinsk in December, 1887, cracked walls in the town, and was followed by numerous aftershocks into the following year [Khovanova, 1961]. Seismicity increase in the Kalba and Altai ranges, to the east, but falls off sharply to the west of about 82°E. Kondorskaya and Shebalin [1977] have cataloged 8 earthquakes with magnitudes greater than about 4 in the region of interest [Fig. 1]. In addition, Khovanova [1961] reported earthquakes near Semipalatinsk in 1911 and 1926 (although the latter may have been a rockburst), and Nersesov *et al* [1982] indicated three smaller earthquakes from 1955-1973, of energy classes 9 and 10 (magnitudes of about 3).

The magnitude threshold for earthquake *location* in this region has been relatively high until recently. The first permanent seismic station in the region was installed in Semipalatinsk in 1934 [Kirnos *et al*, 1961]. However, prior to about 1961, the next closest station was located in Alma-Ata, 800 km to the south. Thus, the distribution of Soviet seismic stations probably did not permit the location of small events on the Kazakh shield before about 1961. Of the ten larger earthquakes noted above (see Fig. 1), most have magnitudes of about 5, and were presumably located with macroseismic data. In about 1961, a seismic station was apparently installed some 90 km from the test site, and has apparently operated since then [Pokrovsky, 1986]. However, this station has not reported local earthquakes in *Earthquakes in the USSR*. Thus, only the three "weak earthquakes" located by Nersesov *et al* [1982] (see Fig. 1) suggest that the magnitude threshold for location has been decreased since the 1950's.

Rodean [1979] provided a preliminary discussion of the 20 March, 1976 earthquake that occurred 100 km west of the Shagan River test site (not plotted on the Nersesov *et al* [1982] maps). More recently, Pooley *et al* [1984] concluded that that "seismic disturbance" was, in fact, an earthquake, and have provided what is the only available focal mechanism for earthquakes in the region (discussed below).

Recent Faulting

The Chingiz Fault. The most prominent structure in the area is the Chingiz fault, which cuts northwest-southeast across the Chingiz anticlinorium. "Rejuvenated by Neogene and Quaternary movements" [Zhuravlev and Uspensky,1971], the Chingiz fault has a particularly clear, linear trace on satellite imagery of the region to the southwest of the test site area [see figure 42a in Rodean, 1979]. Babak [1969], in a useful discussion of the neotectonics of Chingiz fault structures, noted that the fault, like other strike-slip faults, is characterized by zones of compresion and extension related to changes in its strike. As is common along strike-slip faults, compressional fault bends are associated with uplift (up to 500 m) and distinct relief. Babak [op cit] concludes that most faults in the region with northwest strikes are *right-lateral strike-slip faults*, and have developed under sublongitudinal compression. As noted above, this is the direction of maximum compressional stress that would be inferred from the position of this area within the India-Asia collisional orogen.

There are few published observations of Quaternary fault offsets along the Chingiz fault. Kozlovskii [1963] has documented Quaternary offset along this fault, just to the south and east of the test site area. At about 49°N, 79°E (see location T, Fig. 1), he indicates a vertical offset due to reverse fault motion of as much as 30-40 m in Quaternary deposits near the Kudaybergen river.

Other faults. Like the Chingiz fault, many of the other faults exposed in the area of study have clear expression on satellite imagery of the region. This has been cited widely as evidence of recent fault movement, and generally has been borne out by surface observations. One regional fault appears to show evidence of recent offset on SPOT imagery of the region to the northwest of the Shagan River. This fault, the Chinrau [Sukhorukov *et al*, 1970], bounds a Mesozoic coal basin which lies mostly to the northwest of the Shagan river test site, but apparently projects into the test site area. The fault strikes ~125° across the test site (see below).

Uplift

Eastern Kazakhstan is an area of neotectonic uplift. The *Map of Recent Tectonics of the USSR* [1959] indicates a general uplift of a pre-Eocene (25 my) reference surface of from near zero, along the Irtysh river, to more than 1000 m, near Karkaralinsk (adapted in Fig. 1). The greatest uplift occurs southwest of the Chingiz fault in the Chingiz range and the "Central Kazakh Horst", where the Upper Cretaceous/Paleogene reference surface of erosion occurs at more than 1000 m. The general pattern of uplift correlates well with the regions of maximum crustal thickness (cf. Bonham *et al* [1980]). This suggests that the processes are related; i.e., that the uplift is produced by crustal thickening. Because the latter is generally produced by thrusting, this supports the notion that thrust faulting is a major tectonic process in eastern Kazakhstan.

Stress Indicators

Rockbursts in the mining areas of Karaganda, Kounrad and Ziryanovsk (locations shown in Fig. 1) suggest an elevated level of natural tectonic stresses in the region. While there is little data on *in situ* stress measurements in eastern Kazakhstan, there are published stress values for the latter two areas, located in the periphery of the study area. At Kounrad, located just north of Lake Balkhash, measurements at a depth of 200m suggest averaged horizontal stresses of about twice lithostatic [Bulin, 1973]. However, because the data for the horizontal stresses were averaged, no statement can be made as to the direction of the maximum horizontal stress or its magnitude.

At Ziryanovsk, in the southwestern portion of the Altai range ("Rudniy Altai"), a more complete description is available of stress measurements made at at depth of 150 m. Because Ziryanovsk is located in a mountainous, tectonically-active area, these data are presented here because they give an indication of the directions of the principal horizontal stresses. The measurements were made in the crestal portion of an anticline that trends E-W. Median values for stresses were averaged from 8 - 15 points of measurement, spaced along two perpendicular holes, along and across the strike of the anticline. As at Kounrad, large vertical stresses suggest that there are significant vertical stress concentrations in the mine works. The intermediate (horizontal) stress was about zero, and the maximum horizontal stress was compressional, trending about north-south (i.e., along the dip direction of the fold).

Tectonic Release and Local Geologic Structure at Shagan River

Tectonic release is one of the major factors complicating yield determinations based on surface-wave magnitudes for explosions at the Shagan River nuclear test site. The effect of tectonic release on surface wave magnitude (Ms) is somewhat complicated, in that correcting for a pure strike-slip mode of tectonic release will tend to reduce calculated Ms yields somewhat, whereas correcting for thrust faulting will tend to increase Ms yields [see, e.g., Rodean, 1981]. Thrust mechanisms dominate the tectonic release accompanying explosions at Shagan river, although strike-slip mechanisms have been proposed for some events [Helle and Rygg, 1984; Given and Mellman, 1985].

The seismic models of surface wave data used for tectonic release corrections are also very sensitive to the interpreted strike axis of the double-couple source. Modifying the interpreted strike azimuth of the tectonic release from an optimized value, based on pure strike- or dip-slip, has the effect of increasing the earthquake component of the source (Helle and Rygg [1984] p.1897-1898: in their one example, the relative earthquake source strength, F, increases 31% by rotating the strike azimuth 20°). Thus, because of the sensitivity of the method to strike azimuth and the significance of the correction vis-a-vis the yield of an explosion, reconciliation of the interpretation of tectonic release data, the geologic structure and the tectonics of the test site area becomes important. This is expecially true of tectonic release mechanisms are geologically controlled, as they appear to be at the Nevada test site.

Published source mechanisms for the component of tectonic release in Shagan River events imply strike-slip and dip-slip motion along faults striking northwest-southeast [Helle and Rygg, 1984; Given and Mellman, 1985] (Fig. 2). In detail, in the study of seven events by Helle and Rygg [1984], six events fit an interpretation of thrusting on planes striking at about 144° (dip was fixed at 45°), and one event (from 1979) suggests right-lateral strike-slip along a strike of 123° (vertical dip).

In analyzing these mechanisms in regard to the structure and recent tectonics of the test site region, it is first noted that the strike-slip and dip-slip solutions cannot be interpreted as resulting from slip on the planes of maximum shear within a single stress system. That is, if the thrust solutions reflect slip on such planes, the strike-slip event is inconsistent with that system, and vice-versa. Thus, some geologic control on the strike azimuths of the tectonic release seems to be required for at least one of the two tectonic release mechanisms.

Secondly, using the strike of the Chinrau fault (a prominent, apparently active fault intersecting the test site) as an estimate of the structural fabric of the test site, it is clear that the strike-axes for the thrust-type events differ significantly from that strike (i.e., they are more northerly by about 20°; see Fig. 2). On the other hand, the strike-axis of the strike-slip event closely follows that of the Chinrau fault (is identical within the measurement errors).

Thus, we must consider two cases: one in which the strike-slip solution is geologically controlled while the thrust events reflect only the stress system; the other considering that the thrust events are also geologically-controlled, oblique-slip events with strikes closer to that of the strike-slip event.

The first case is perhaps initially satisfying, because the strike slip event was apparently located closest to the Chinrau fault of the evnets studied, and thus some geological control by that fault might be expected. However, if the thrust events are supposed to accurately reflect the stress directions across the test site, then those stresses would not produce right-lateral motion along the Chinrau fault, as is inferred from both the strike-slip event and from general consideration of the tectonics of the test site region. Thus, this scenario is improbable in that it requires strong variations in the stress system across the test site.

The alternative solution is to suppose, because the test site area is small and relatively flat, that it is perhaps reasonable to assume that the principal tectonic stress directions at containment depths do not vary much across the test site. Thus, in order to maintain consistency with the strike slip event, which, as noted above, is itself consistent with the strike of the Chinrau fault, it is necessary to presume that the thrust events were actually more-complicated oblique-slip events along structures parallel to the Chinrau fault, that were modelled as thrusts only as a simplified interpretation. In addition to the simple-stress-system, this hypothesis has two advantages: 1) it fits with the notion of geological control of tectonic release strikes, as is noted for the Nevada test site area; and 2) it fits well with notions of the regional tectonics of the test site region (i.e., mixed right-lateral strike-slip and thrust faulting, and a more northerly-trending principal horizontal compressive stress). It has the "disadvantages" that it requires both the modification of the estimated tectonic release mechanism of most of the events, and the upward revision of the Ms estimates of their explosive yields.

The March, 1976 earthquake provides the only other estimate of the stress field in the test site area. It is considered here for its use in choosing between the hypotheses outlined above. This earthquake was estimated by Pooley et al [1983] to have had an oblique (mixed strike-slip/thrust) mechanism (the nodal plane the most likely corresponds with the fault plane is plotted on Fig. 2). This mechanism would be similar to that proposed in the second hypothesis, above (geologically-controlled thrust orientations). Unfortunately, the geology of the epicentral region [Mt. Murzhik; see Samygin, 1974] does not allow one to choose a more likely candidate from among the nodal planes as estimated by Pooley et al [1983].

Conclusions

If the Shagan river explosions with thrust-type tectonic release solutions actually resulted from motion on faults parallel to the Chinrau fault, then they could represent explosions with especially high double-couple components and, when corrected for this tectonic release, correspondingly higher explosive (Ms) yields. However, in order to rule out

the other possibility --that only the strike-slip events have been geologically controlled-- more data is needed as to the *in-situ* stress directions in the test site area. Seismologically, it becomes important to determine whether or not tectonic release, perhaps through the focusing of energy, exerts an similarly "strike-sensitive" effect on teleseismic or regional body waves. [I gratefully acknowledge the guidance provided in this study by J. Rachlin].

References (Russian titles translated)

Babak, V. I., 1969, The neotectonic structure of the Kazakh shield, Geotectonics 6:411-418.

Bonham, S., J. Rachlin and W. Dempsey, 1980, Geologic Environment of the Semipalatinsk Nuclear Weapons Testing Ground, report to the Air Force Tech. Applications Center, unpublished (official use only), 46 pp, 2 pl.

Bulin, N. K., 1973, Contemporary stresses in rocks according to data from underground workings in the USSR, p. 56-66 in Stress Conditions in the Earths Crust, P. N. Kropotkin, ed., Nauka, Moscow.

Earthquakes in the USSR, published yearly, 1962-1984, Nauka, Moscow.

Given, J. W. and G. R. Mellman, 1985, Source parameters of Shagan River East Kazakh, USSR events using surface wave observations, p. 705-710 in The VELA Program, A. Kerr, ed., D. L. Carlson, Washington, 964 pp.

Gzovskiy, M. V., and many others, 1973, Stresses in the earths crust according to data from underground workings and tectonophysical analysis, p. 32-47 in Stress Conditions in the Earths Crust, P. N. Kropotkin, ed., Nauka, Moscow.

Helle, H. B. and E. Rygg, 1984, Determination of tectonic release from surface waves generated by nuclear explosions in eastern Kazakhstan, Bull. Seis. Soc. Am. 74(5):1883-1898.

Khovanova, R. I., 1961, Earthquakes of the Altai-Sayan zone, p. 349-352 in Earthquakes in the USSR, E. F. Savarenskiy *et al*, eds., Akademiya Nauk, Moscow, 412 pp.

Kirnos, D. P., D. A. Kharin and N. V. Shebalin, 1961, History of instrumental seismic observations in the USSR, p. 9-66 in Earthquakes in the USSR, E. F. Savarenskiy *et al*, eds., Akademiya Nauk, Moscow, 412 pp.

Kozlovskii, G. M., 1963, Fragments of the recent tectonics of the Chingiz range, Izv. AN Kazakh. SSR 54(3),68-73.

Map of Recent Tectonics of the USSR, 1959, N. I. Nikolaev and S. S. Shul'ts, eds., Akademiya Nauk, Moscow (1:5000000, 8 sheets).

Molnar, P. and P. Tapponier, 1975, Cenozoic tectonics of Asia: Effects of a continental Collision, Science 189(4201):419-426.

Nersesov, I. L., A. Nurgambetov and A. Sidikov, 1982, Detailed studies of the seismic regime of Kazakhstan and surrounding regions, Nauka, Alma-Ata, 160 pp.

Pokrovsky, A., 1986, I "see" a nuclear explosion, Pravda, 26 July.

Pooley, C. I., A. Douglas and R. G. Pierce, 1983, The seismic disturbance of 1976 March 20, east Kazakhstan: earthquake or explosion?, Geophys. J. R. Astr. Soc. 74:621-631.

Rodean, H. C., 1979, ISC events from 1964 to 1976 at and near the nuclear testing ground in eastern Kazakhstan, Lawrence Livermore Nat. Lab. No. UCRL-52856, Univ. Calif., Livermore, 57pp.

Rodean, H. C., 1981, Inelastic processes in seismic wave generation by underground explosions, pp. 97-189 in Identification of Seismic Sources - Earthquake or Underground Explosion, E. S. Husebye and S. Mykkelveit, eds., D. Reidel, Dordrecht.

Samygin, S. G., 1974, The Chingiz fault and its Role in the Structure of Central Kazakhstan, Nauka, Moscow, 208 pp.

Sukhorukov, A. A., K. S. Akhmetov and I. V. Orlov, 1973, Jubilee deposit, p. 217-230 in Geology of Coal and Oil Shale Deposits of the USSR, Nedra, Moscow.

Zhuravlev, B. Ya. and E. P. Uspensky, 1979, Large faults of the Chingiz range, Geotectonics 5:305-309.
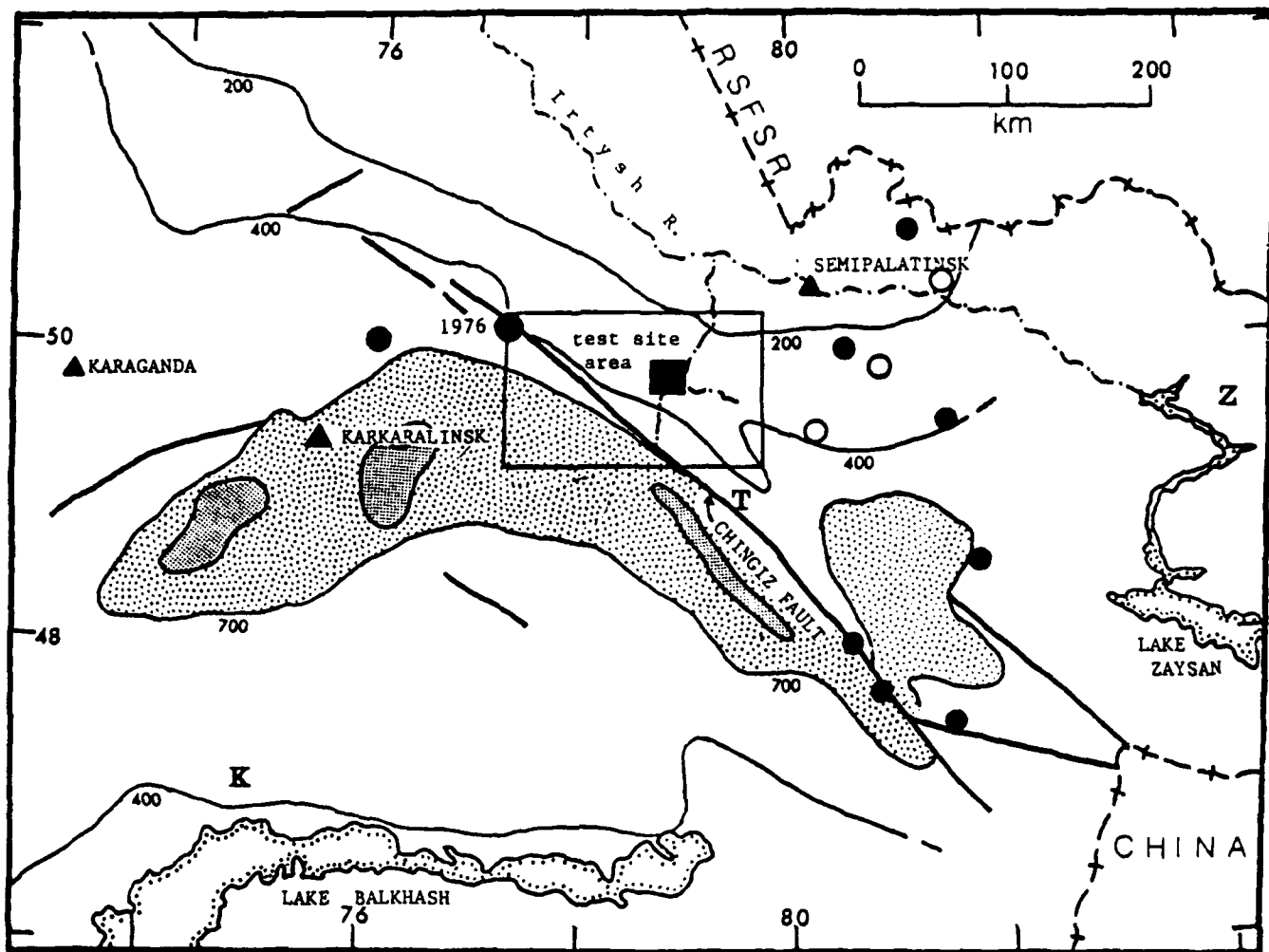
Figure 1. Sketch map of eastern Kazakhstan, showing: the general pattern of Tertiary crustal uplift (contoured, in meters; darker shading for >1000m); major faults (heavy lines); known earthquakes (dots; not plotted east of 82°E or south of 48°N; open dots are from *Nersesov et al,* 1982; others from *Kondorskaya and Shebalin* [1977]; note location of 1976 earthquake); sites of stress measurements (K=Kounrad, Z=Ziryanovsk); T=the fault trenching study of *Kozlovskii* [1982]; and the location of the Shagan River test site (square) within the Semipalatinsk nuclear weapons proving ground.
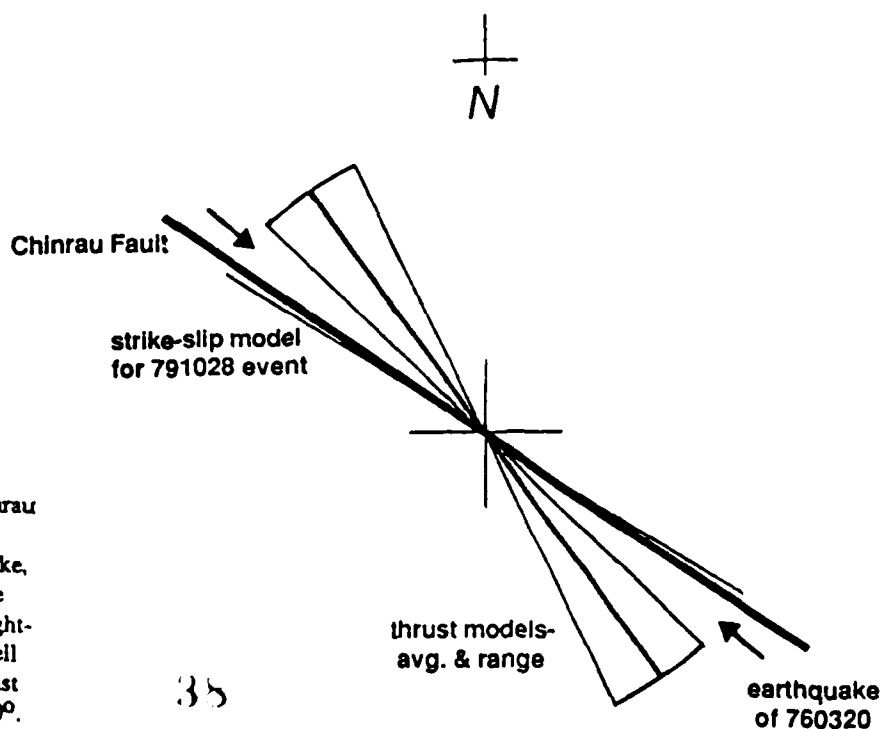
Figure 2. Summary of strike data for the mechanisms of tectonic release at Shagan River, compared with the strike of the Chinrau fault and one of the nodal planes of the mechanism of the March 20, 1976 earthquake, as determined by *Pooley et al* [1982]. Note that, whereas the strike-slip mechanism (right-lateral) for the 1979 explosion conforms well with the strike of the Chinrau fault, the thrust mechanisms are more northerly by about 20°.

35

SPHERICAL WAVE PROPAGATION IN LOW POROSITY BRITTLE ROCKS

By

Geza Nagy and A. L. Florence
SRI International, Meno Park, CA 94025

OBJECTIVE

Computer codes capable of predicting ground motions from nuclear explosions rely on sound theoretical models of dynamic material behavior near the source. Development and validation of these models rely on experimental data obtained in relevant materials. The objective of this research was to support the development and validation of material models (1) by an experimental investigation of the dynamic response of Sierra White granite, a representative low porosity brittle rock, to high amplitude spherical stress waves under well controlled laboratory conditions. The investigation included the effects of porosity, pore water content, confining pressure, and pore pressure (or effective stress).

RESEARCH ACCOMPLISHED

The research accomplished (2-4) had three principal tasks: (1) the development of techniques for enhancing initial porosity conditions in the granite samples, (2) the development of a method for independent control of confining and pore pressures, and (3) the spherical wave experiments. The completion of these tasks resulted in the set of experiments summarized in Table 1.

Table 1. Particle velocity experiments in Sierra White granite

Test No.	Frac.Type.	Porosity (%)	Pore Cond.	Confining Press. (psi)	Pore press. (psi)
308	Thermal	1.2	dry	2000	–
309	Intact	0.8-1.0	saturated	2000	2000
310	Thermal	1.2	saturated	2000	2000
473	Gas	2.5	saturated	1800	1800
474	Gas	2.4	saturated	1600	1600
476	Gas	2.4	dry	2000	–
485	Gas	2.8	dry	2000	–
488	Gas	2.7	dry	1000	–
491	Gas	2.9	saturated	2000	50
492	Gas	2.6	saturated	1000	50
494	Gas	2.9	saturated	2000	1000

Porosity effects were investigated by experiments in intact, 1.2%, and 2.5% porosity rock in dry and saturated states. Pore water effect with different porosities was studied by comparing results in dry and water saturated rock with zero effective stress. The influence of confining pressure and non-zero effective stress in water saturated samples was studied by various combinations of 1000 and 2000 psi confining pressures and 0 and 1000 psi pore pressures. Before presenting the results that show a substantial effect of the parametric variations, we briefly describe the experimental techniques used for generating and measuring spherical stress waves, and producing the initial material and pressure conditions.

Stress Wave Generation and Measurement. The technique for measuring particle velocities generated by a spherical stress wave in rock samples is shown schematically in Figure 1. The test samples are cylinders with approximate diameter and height of 28 cm. The stress waves are generated by a centrally located spherical explosive charge consisting of 3/8 gram of PETN powder packed to a density of 1 g/cm^3 , encased in a 0.24-mm-thick Lucite shell of 1.08 cm outside diameter. The particle velocity gages consist of concentric circular loops of insulated 0.25-mm-diameter copper wire placed along a plane normal to the cylinder axis and containing the source at its center. A constant, uniform magnetic field directed normal to the plane of the gages is generated by a solenoid placed around the sample. Radial expansion of a particle velocity loop generates a voltage (E) proportional to the magnetic field strength (B), the current gage length (l) and the radial velocity of the loop (v) according to Faraday's law: E = Blv. The radially oriented gage leads make no contribution to the signal. The signal at a gage location represents the response of an infinite medium until wave reflections from the sample boundary reach that location. Time integration of the velocity records gives particle displacements.

For installing the source and the particle velocity gages the sample is sectioned at its midheight and the surfaces are ground flat and smooth. Hemispherical cavities are cut into the mating surfaces to accept the source, and an axial access hole is cut into the top half for the mild detonating fuse (MDF) used to initiate the charge. The gage wires, epoxied into 0.3 mm wide, 0.5 mm deep grooves, represent minimum disturbance to the medium. The two halves of the sample are clamped together during the experiment by the applied hydrostatic pressure, or for certain test conditions by an applied axial load (3). The experiments were conducted in a pressure vessel. Water was used to apply the confining pressure and to saturate the pore space. Except for the saturated experiments having the same confining and pore pressures (zero effective stress), the samples were jacketed in rubber Wilson seals.

Porosity Enhancement. A thermal technique consisting of slow heating to 350°C followed by gradual cooling was used to generate an initial porosity of about 1.2% in the samples, a rather small increase that was found to have negligible effects. A substantial increase in porosity was achieved by following this heat cycle by a gas-fracturing method (3) depicted in Figure 2. In this technique the rock sample is placed in a pressure vessel that has a rupture diaphragm incorporated in its top lid. The sample is then pressurized with nitrogen to about 2300 psi which breaks the diaphragm and rapidly decompresses the space around the sample. The high pressure gas temporarily trapped in the pore space generates a large number of microscopic and macroscopic cracks resulting in porosities of 2.4 to 2.9%. Large scale fracturing of the sample during this process is supressed by tightly packed lead shot placed around the sample. The change in porosity and the resulting change in compressibility and other material properties induced by this process was found to be homogeneous and isotropic (5).

Saturation and Pore Pressure Control. Water saturation of the test samples was accomplished by applying vacuum on the pore space then introducing degassed, deionized water under pressure for a sufficient time to achieve complete saturation. For the jacketed, saturated experiments a differential between confining and pore pressures could be maintained by a vent tube and associated valving leading from the space inside the jacket to outside the pressure vessel.
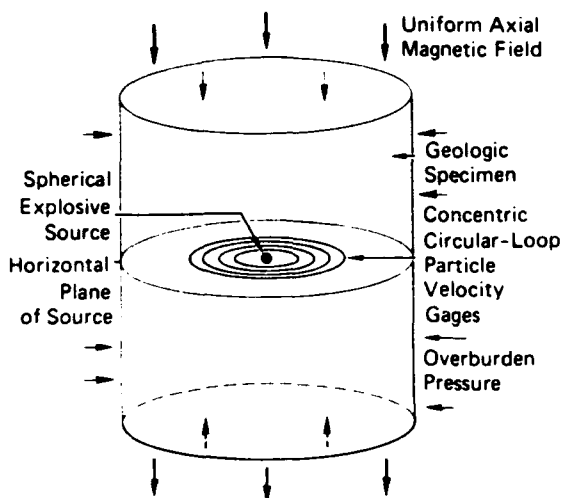
FIGURE 1 Schematic of configuration for particle velocity experiments.
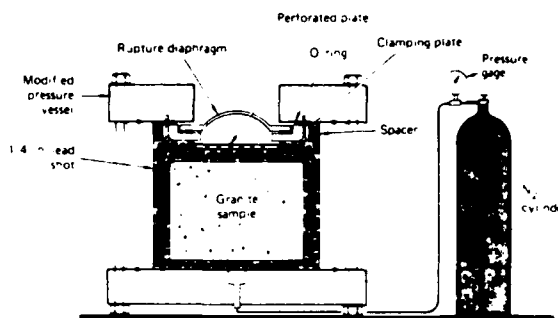
FIGURE 2 Schematic of gas-fracturing arrangement for preparation of velocity samples to achieve desired porosity.

Experimental Results. Particle velocity histories were obtained at 4 to 7 radial locations. The velocity signals are characterized by a sharp rise followed by a gradual decay and a rebound. The parameters varied influenced the rise time, peak amplitude, pulse width and positive pulse duration, as well as the duration and amplitude of the rebound. The results in general show not only an effect of the experimental parameters, but a dependence on radial range as well. Some of the parametric variations show strong effects, others indicate trends. In general, the most significant effects were observed when the porosity was increased to 2.5%. The results in which the parametric variations had a substantial effect are the following:

(1) In dry rock with a porosity of about 2.5%, lowering the confining pressure from 2000 to 1000 psi increases the maximum displacements by about 25% due to wider pulses, as illustrated by the particle velocity records at the 3.0 cm location shown in Figure 3 and the peak displacement attenuation plot shown in Figure 4.

(2) For dry and saturated rock with a porosity of 2.5%, zero pore pressure, and confining pressures of 2000 and 1000 psi, the maximum particle velocities and displacements are substantially higher in the saturated rock at large ranges. This is illustrated by the velocity records at the 6.0 cm location, shown in Figure 5, which have much higher peaks than corresponding records in dry granite, and by the attenuation plots of Figures 6 and 7.

(3) In saturated rock with a porosity of 2.5% and a confining pressure of 2000 psi, increasing the effective stress by lowering the pore pressure to 1000 psi or zero produces substantially smaller maximum displacements because of narrower pulses. This effect is shown clearly by the velocity and displacement records in Figures 8 and 9, and by the peak displacement attenuation plot in Figure 10.

(4) In saturated rock with both confining and pore pressures of 2000 psi

11
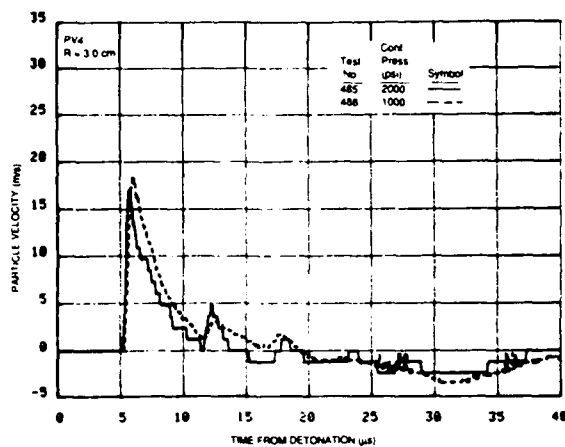
FIGURE 3 Particle velocities 3.0 cm from the center of coupled explosion in dry gas-fractured Sierra White granite.

FIGURE 4 Effect of confining pressure P_c on peak displacements in dry gas-fractured Sierra White granite
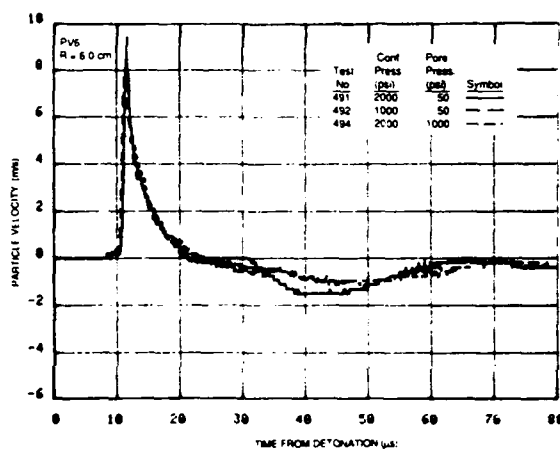
FIGURE 5 Particle velocities 6.0 cm from center of coupled explosion in saturated gas-fractured Sierra White granite.
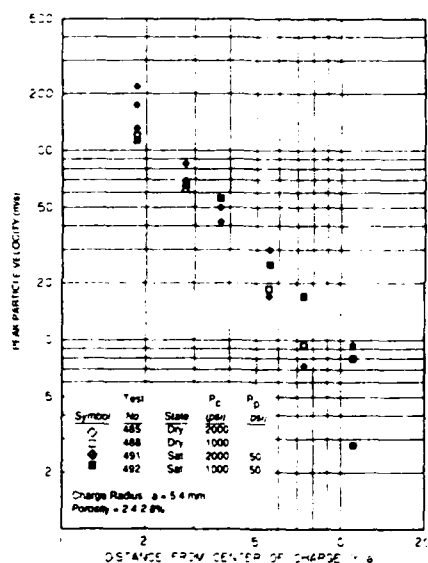
FIGURE 6 Pore water effect on peak velocities in gas-fractured Sierra White granite at two confining pressures and negligible pore pressure.

FIGURE 7 Pore water effect on peak displacements in gas-fractured Sierra White granite at two confining pressures and negligible pore pressure.
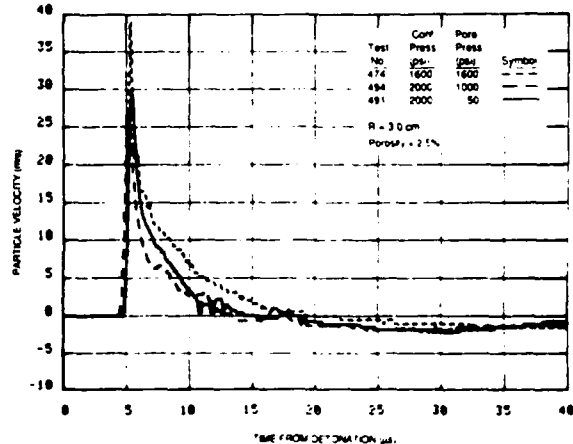
FIGURE 8 Pore pressure effect on particle velocities at 3.0 cm from center of coupled explosion in saturated Sierra White granite.

4
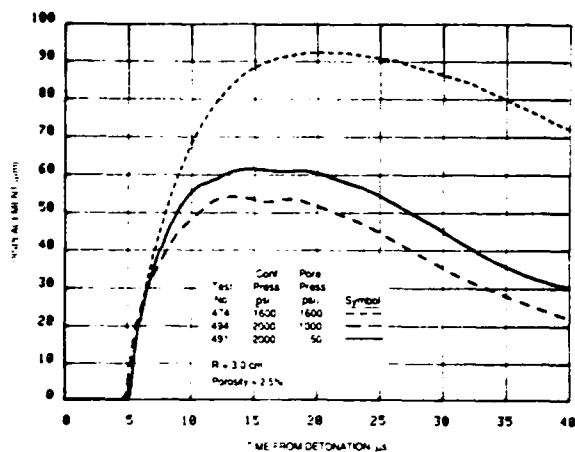
FIGURE 9 Pore pressure effect on particle displacements at 3.0 cm from center of coupled explosion in saturated gas-fractured Sierra White granite.

FIGURE 10 Pore pressure effect on peak displacements in saturated gas-fractured Sierra White granite.

FIGURE 11 Porosity effect at zero effective stress on particle velocities at 3.0 cm from center of coupled explosion in saturated gas-fractured Sierra White granite.
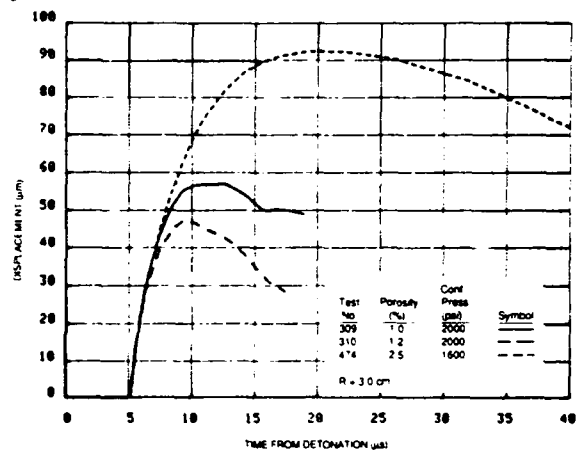
FIGURE 12 Porosity effect at zero effective stress on particle displacements at 3.0 cm from center of coupled explosion in saturated gas-fractured Sierra White granite.

FIGURE 13 Porosity effect at zero effective stress on peak velocities in saturated gas-fractured Sierra White granite.
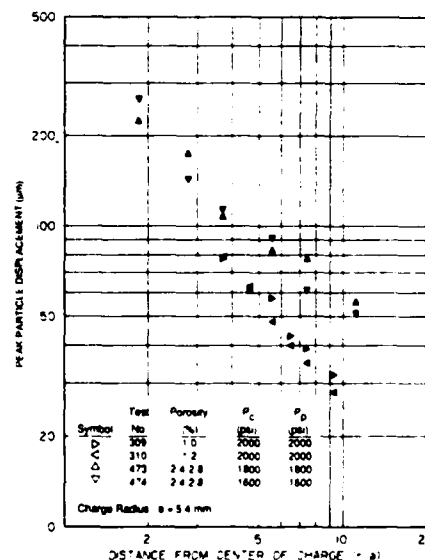
FIGURE 14 Porosity effect at zero effective stress on peak displacement in saturated gas-fractured Sierra White granite.

(zero effective stress), an increase of porosity from the intact value of 1% to 2.5% produces substantially higher maximum velocities and displacements, especially at large ranges. Pulse widths are increased significantly, the increase ranging from a factor of 2 near the source to a factor of 4 far from the source. Figures 11 through 14 illustrate this effect.

CONCLUSIONS AND RECOMMENDATIONS

A comprehensive experimental study of Sierra White granite showed the influences of increased porosity, pore water content, and confining and pore pressures, on the dynamic response to high amplitude spherical waves in the region near the source. The results also indicate that most of the significant effects increase with range, thus with decreasing stress levels. In light of the results and the overall needs of the Nuclear Monitoring program the following recommendations are made:

(1) Because the conclusions reached are based on two, or even a single experiment, we recommend a repeat of the key experiments in Table 1.

(2) Since most of the key effects show a strong dependence on range, a set of experiments should be conducted to study the influence of these parameters on low amplitude waves. This would extend the relevance of these results to regions far from the source in lower stress regimes of interest.

(3) An analysis of the results should be conducted to understand the underlying mechanisms controlling the observed effects.

REFERENCES

1. N. Rimer, J. L. Stevens, and K. H. Lee, "Effects of Pore Pressure and Fractures on Ground Motion in Granite," Draft Final Report, Contract DNA 001-85-C-0249, S-CUBED, La Jolla, CA (June 1986).

2. G. Nagy and A. L. Florence, "Spherical Wave Propagation in Low Porosity Brittle Rocks," Draft Final Report, Prepared for University of California LLNL, Contract No. 9168505, SRI International, Menlo Park, CA (May 1987).

3. G. Nagy and A. L. Florence, "Spherical Wave Propagation in Low Porosity Brittle Rocks," Draft Final Report, Contract No. DNA 001-85-C-0248, SRI International, Menlo Park, CA (May 1986).

4. G. Nagy and A. L. Florence, "Spherical Wave Propagation in Rocks," Technical Report DNA-TR-85-254, Contract DNA 002-83-C-0024, SRI International, Menlo Park, CA (May 1984).

5. R. J. Martin, "Physical Properties of Sierra White Granite," Prepared for University of California Lawrence Livermore National Laboratory, Livermore, CA, Contract 902405, New England Research, Norwich, VT (February 1987).

SEISMIC WAVES FROM SOURCES IN GRABEN-LIKE STRUCTURES STUDIED BY ULTRASONIC PHYSICAL MODELING

M. S. Vassiliou, M. Abdel-Gawad, and B. R. Tittmann
Rockwell International Science Center
1049 Camino Dos Rios, Thousand Oaks, California 91360

1. Introduction

The overall purpose of the Ultrasonic Physical Modeling Program at the Rockwell International Science Center is to model seismic wave propagation in the Earth using ultrasonic wave propagation in scale laboratory models. By using well calibrated sources and receivers our hope is to shed light on the effects of complex structure and geology on the propagation of seismic waves, and thus aid the national research effort in seismic monitoring of nuclear explosions. The intent is to complement numerical modeling, providing insight and guidance in complex situations where such modeling may not yet be feasible, owing to limitations in computer power.

In this report we study wave propagation from a source excited in a scale model of Yucca Flat, Nevada.

2. Previous Work on a Cylindrical "Graben"

In a previous report (Vassiliou et al., 1986) we addressed the propagation of ultrasonic waves when a source was excited in a cylindrical low velocity "graben", or plug, embedded in a high velocity medium. The high velocity medium is a fine grained gabbro with $V_R = 3.3$ km/sec. The plug was filled with lower velocity materials ($V_R = 1 - 1.6$ km/sec). The source and receiver were respectively a breaking pencil lead and an NBS-type conical transducer, the same as in this study (see sections 3 and 4 below). In the earlier study we reached the following conclusions:

(1). The presence of a source region with significantly slower velocities than the surrounding region appears to lead to a more complex signal, with more "ringing" than would be apparent if there were no such source region.

(2). The presence of such a source region appears to result in a relative amplification of the high frequency part of the signal. Periods analogous to 3 or 4 sec, or shorter, in the Earth appear to be amplified relative to lower frequencies.

(3). When the source is set off in the graben in an off-center position, a radiation pattern is established, with amplitude varying by a factor of 2 or more. Material effects appear to be accentuated when the source is excited off-center.

3. The Present Model

We have constructed an accurate scale model of Yucca Flat, based on the generalized map shown in figure 1, which was constructed from the work of Ferguson et al. (1986). The rectangular box outlines an area where many nuclear explosions have been detonated (see, e. g., McLaughlin et al., 1986). The basin was drilled in a fine-grained gabbro "halfspace", and filled with crystal wax. The properties of the gabbro and crystal wax are given in table 1. The source is excited on the surface of the basin, and receivers are placed outside the basin on the "halfspace", as shown in fig. 2.

One mm in the model represents 1 km in the Earth. If the material filling the basin in the Earth

1.

has a Rayleigh wave velocity $V_R{}^e = 1.2$ km/sec, then a 20 sec Rayleigh wave in the Earth has a wavelength of 24 km. Thus the analog of the Earth's 20 sec Rayleigh wave has a wavelength of 24 mm. Given that the basin fill material has a Rayleigh wave velocity of 1.01 km/sec, this corresponds to a frequency of about 40 KHz.

Thus, in this scale model of Yucca Flat, a 40 KHz Rayleigh wave corresponds roughly to a 20 sec Rayleigh wave in the Earth.

4. The Receiver

It is absolutely imperative in a study of this kind to have a receiver with a well known response. We use an NBS-type conical transducer (Proctor 1980, 1982a,b) manufactured by Industrial Quality, Inc. This transducer is a vertical component displacement sensor with a 1mm contact area, and a very flat response. The element is piezoceramic, and it is coupled to a large brass backing which effectively eliminates resonances, as well as minimizing coherent reflections back into the element. Typical displacement response curves for this transducer are reproduced in Vassiliou et al. (1986). The response is flat enough that when we look at a signal from this transducer, we can consider that we are looking essentially at raw vertical component displacement.

4. The Source

Just as important as having a well characterized receiver is having a well characterized source. The source we use is a simple one, but it is quite effective. Basically, we achieve a near-step-function point unloading of the surface by breaking a pencil lead on it. This is a variant of the well known breaking-glass-capillary source used by the NBS, and is discussed in detail by Hsu and Hardy (1978). More information on the source is given in Vassiliou et al. (1986).

5. Lamb's Problem

Fig. 3 shows the result of a measurement made by setting off the source on the gabbro "halfspace", and recording the signal received by the transducer 200 mm away (the standard distance for all the measurements presented in this report). The displacement record is essentially a solution of the classic Lamb's problem (see e.g. Miklowitz, 1978; Mooney, 1974; Breckenridge et al., 1975) for a point force on a surface. Fig. 3 shows, for comparison, the result of Boler et al. (1984) for a similar setup, using a breaking glass capillary source and a true displacement transducer. The results are very similar in appearance to ours. Boler et al. include the theoretical response computed from Lamb's solution. The first arrival P wave is very small in the theoretical solution, and is very small in Boler et al.'s measurements. In our results there is only a hint of it, as a minor inflection before the onset of the large signal. The large signal observed in both our record and in Boler et al.'s is, of course, the S wave followed by the Rayleigh wave.

6. Source Excited Within the Scale Model of Yucca Flat

Figs. 5-8 show the waveforms obtained when the source was excited on the surface of the basin. Fig. 4 shows, for comparison, the waveforms obtained when the source was excited in the gabbro before the basin was excavated. In each case the receiver positions are identical-- 200 mm from the same reference point in the basin (the same point as the source position in fig. 7).

The figures are meant primarily to illustrate waveform character-- they should not be used as an accurate guide to arrival times. Arrival times are not completely reliable because of triggering problems in the apparatus (which have been rectified, but after these measurements were taken).

Examination of figs. 5-8 yields the perhaps rather surprising result that the presence of the basin does not seem to be making much difference in the shape of the waveform. When the source is

anywhere within the rectangular box representing the location of many real explosions (figs. 5,6, and 7), the waveforms appear almost like halfspace responses. There does appear to be some complexity and ringing, but nothing like what is observed in the case of the cylindrical plug graben (Vassiliou et al., 1986). The loss of symmetry in going from a cylindrical plug graben to a more realistic structure seems to have dramatically reduced the focussing effects.

The only case where relatively dramatic effects on the waveshapes is observed is shown in fig. 8, when the source is excited over the deepest portion of the graben. Here, we see some of the same kind of complexity and ringing observed by Vassiliou et al. (1986) in the cylindrical plug graben. This is not difficult to rationalize, because the structure at this position locally approximates a plug or bowl-like structure.

7. Spectral Ratios

Figs. 9 and 10 show some spectral ratios for the data in figs. 6 and 8. At each position, the magnitude spectrum of the waveform obtained with the source excited on the basin surface is divided by the magnitude spectrum of the waveform obtained through the gabbro before the basin was excavated. If the spectral value in the denominator is too small (5% or less of its maximum value), the ratio is set to zero. Thus we obtain some notion of the effect of the structure on the wave propagation.

The spectral ratios indicate that the structure seems to be causing some amplification of high frequencies, above around 400 KHz, relative to the lower frequencies. The spectral ratio for frequencies lower than 400 KHz is generally close to 1 or 2. For frequencies higher than 400 KHz, in the case when the source is within the rectangle in the northern part of the basin, the spectral ratio reaches a maximum of about 5. In the case when the source is located to the south, above the deepest portion of the basin, the spectral ratio in the high frequency portion can be as high as 20. Remembering from Section 1 that a 40 KHz Rayleigh wave in the model is analogous to a 20 sec Rayleigh wave in the Earth, we see that the amplification is occurring for waves analogous to ones with periods of 2 sec and shorter in the Earth.

In both cases, the directions of greatest relative amplification of high frequencies appear to lie to the southeast and the northwest.

8. Conclusions

We have described experiments intended to clarify seismic wave propagation from sources actuated in graben-like structures. We have excavated a scale model (1mm to 1 km) of Yucca Flat, Nevada, into a "halfspace" of fine-grained gabbro, and filled the model basin with low velocity crystal wax.

We have excited ultrasonic waves on the surface of the model basin using a breaking pencil lead as a source; this source represents a step function point unloading of the surface. The waves have been monitored using a true-displacement conical transducer placed on the gabbro halfspace, outside the basin, 200 mm away (this corresponds to receivers 200 km away in the Earth). Rayleigh waves of frequency 40 KHz in the model correspond roughly to Rayleigh waves of period 20 sec in the Earth.

The presence of the basin has some effect on the waveforms obtained. Some ringing and complexity is introduced into the waveform, compared with waveforms obtained on a halfspace without a basin present. However, the effects are less dramatic than those observed when sources are excited on model basins which are perfectly cylindrical in geometry (Vassiliou et al., 1986). The most complex waveforms are obtained when the source is excited over the deepest portion of the graben. Here, we see some of the same kind of complexity and ringing observed by Vassiliou et al. (1986) in the cylindrical plug graben. When the source is anywhere within the rectangular box representing the location of many real explosions (figs. 5,6, and 7), the effects are much less pronounced: the waveforms appear almost like halfspace responses.

The presence of the basin seems to cause some amplification of higher frequencies. Frequencies

higher than about 400 KHz, which correspond roughly to periods of 2 sec or shorter in the Earth, seem to be amplified relative to lower frequencies. This occurs most when the source is in the southern portion of the basin, but occurs also when the source is in the northern portion. The effect seems most pronounced for directions to the northwest or southeast.

9. Acknowledgements

10. References

Boler, F. M., Spetzler, H. A., and Getting, I. C. (1984), Capacitance Transducer with a Point-Like Probe fro Receiving Acoustic Emissions, *Rev. Sci. Instrum.* **55**, 1293-1297.

Breckenridge, F. R., Tschiegg, C. E., and Greenspan, M. (1975), Acoustic Emission: Some Applications of Lamb's Problem, *J. Acoust. Soc. Am.* **57**, 626-631.

Ferguson, J. F., Felch, R. N., Aiken, C. V., Oldow, J. S., and Dockery, H. (1986), Models of the Bouguer Gravity and Geologic Structure at Yucca Flat, Nevada, Submitted to *Geophysics.*

Hsu, N. N., and Hardy, S. C. (1978), Experiments in Acoustic Emission Waveform Analysis for Characterization of AE Sources, Sensors, and Structures, in "Elastic Waves and Nondestructive Testing of Materials", AMD 29, ASME, 85-106.

McLaughlin, K L., Anderson, L. M., and Lees, A. C. (1986), Effects of Local Geologic Structure for Yucca Flats, NTS, Explosion Waveforms: 2-Dimensional Finite Difeference Simulations, AFGL-TR-86-0220, Air Force Geophysics Laboratory, Hanscom AFB, Massachusetts.

Miklowitz, J. (1978), The Theory of Elastic Waves and Waveguides, North Holland, New York, 618pp.

Mooney, H. M. (1974), Some Numerical Solutions for Lamb's Problem, *Bull. Seismol. Soc. Am.* **64**, 473-491.

Proctor, T. J. (1980), Improved Piezoelectric Transducers for Acoustic Emission Reception, *J. Acoust Soc. Am.* **68**, S68.

Proctor, T. J. (1982a), Some Details on the NBS Conical Transducer, *J. Acoustic Emission* **1**, 173-178.

Proctor, T. J. (1982b), An Improved Piezoelectric Acoustic Emission Transducer, *J. Acoust. Soc. Am.* **71**, 1163-1168.

Vassiliou, M. S., Abdel-Gawad, M., and Tittmann, B. R. (1986), Ultrasonic Physical Modeling of Seismic Wave Propagation from a Graben-Like Structure: A Preliminary Report, AFGL-TR-86-0228, Air Force Geophysics Laboratory, Hanscom AFM, Massachusetts.

Table 1.
Properties of Modeling Materials

Material	Longitudunal Velocity Vp, km/s	Shear Velocity Vs, km/s	Rayleigh Velocity VR, km/s	Poisson's Ratio n	Density r, g/cc
Crystal Wax	2.407	1.096	1.01	0.369	1.32
Gabbro	6.200	3.623	3.33	0.240	2.97

Figure Captions

Figure 1.　　Generalized map of Yucca Flat used in constructing the physical model. Map was drawn based on the work of Ferguson et al. (1986). Large rectangle delineates area where many explosions were located.

Figure 2.　　Overall geometry of the model.

Figure 3.　　Signal observed by actuating the source on the gabbro "halfspace". Similar signals obtained by Boler et al. (1984) are shown for comparison.

Figure 4.　　Waveforms obtained on the gabbro halfspace, before the Yucca Flat model was excavated. Vertical scale is 50 millivolts per division. Horizontal scale is 50 microseconds per division.

Figures 5-8.　　Waveforms obtained from sources excited on the surface of the basin. The point "X" in each case is the reference point-- all receivers are 200 mm from this reference point. The dot with the rays coming out of it indicates the position of the source in each case. In each case, the vertical scale is 20 millivolts per division, and the horizontal scale is 20 microseconds per division.

Figure 9.　　Spectral ratios for the data in figure 6. At each position, the magnitude spectrum of the waveform obtained with the source excited on the basin surface is divided by the magnitude spectrum of the waveform obtained through the gabbro before the basin was excavated.

Figure 10.　　Spectral ratios for the data in figure 8. At each position, the magnitude spectrum of the waveform obtained with the source excited on the basin surface is divided by the magnitude spectrum of the waveform obtained through the gabbro before the basin was excavated.

FIG. 2

PLAN VIEW OF MODEL

RECEIVER POSITIONS

34 MM.

45°

200 MM

SOURCES EXCITED ON SURFACE OF BASIN

BASIN FILLED WITH CRYSTAL WAX

FINE-GRAINED GABBRO HALFSPACE

FIG. 1

YUCCA FLAT, NEVADA
Depth Contours in metres
Paleozoic - tuff contact

0
500
1000

116°07'30"

37°07'30"

37°15'

37°00'

KILOMETERS
0   5   10

20
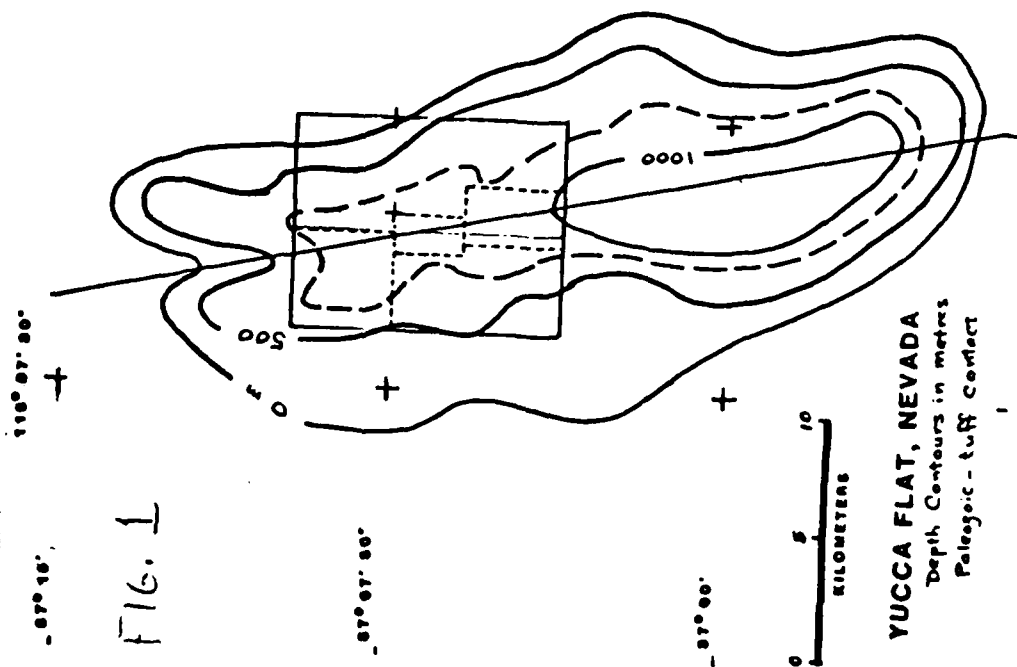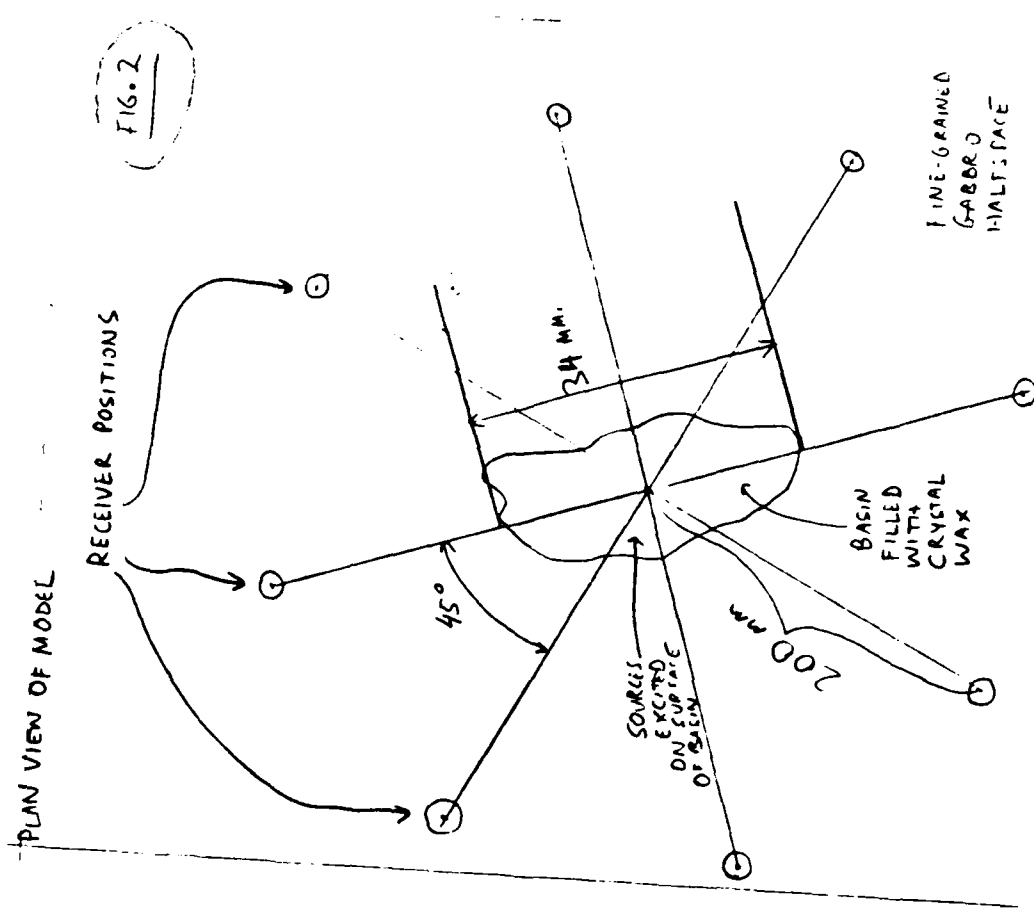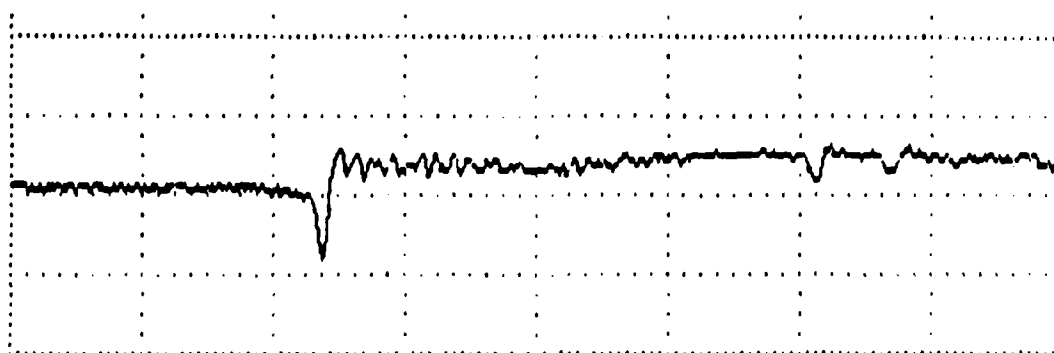
TIME, μSEC

FIG. 3

BOLER et al., 1984 :

FIG. 4

Time, µsec

50

50

millivolts

50

0

52

FIG. 5

20 40
Time, μsec

0

58

FIG. 6

0 20 40
TIME/μsec.

54

FIG. 7

TIME, μsec

0   20   40

5:

FIG. 8

O 20 40
TIME, µSEC

56
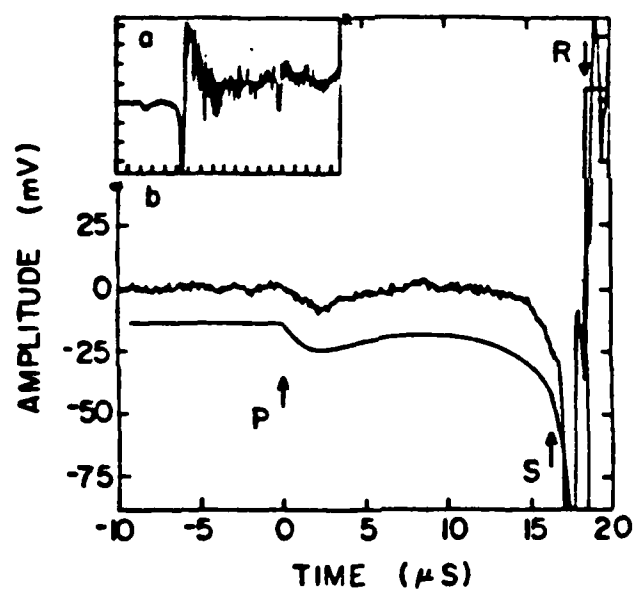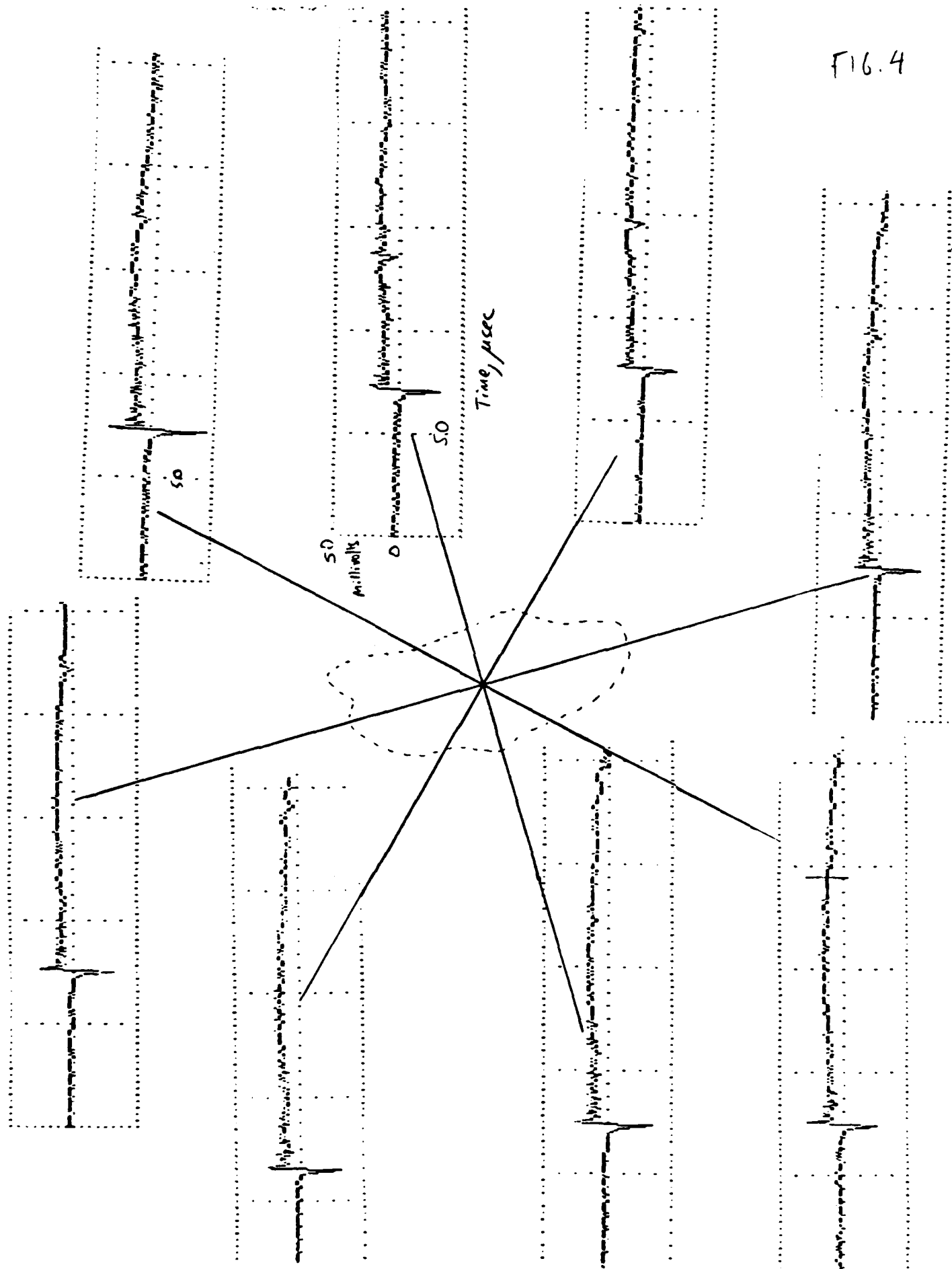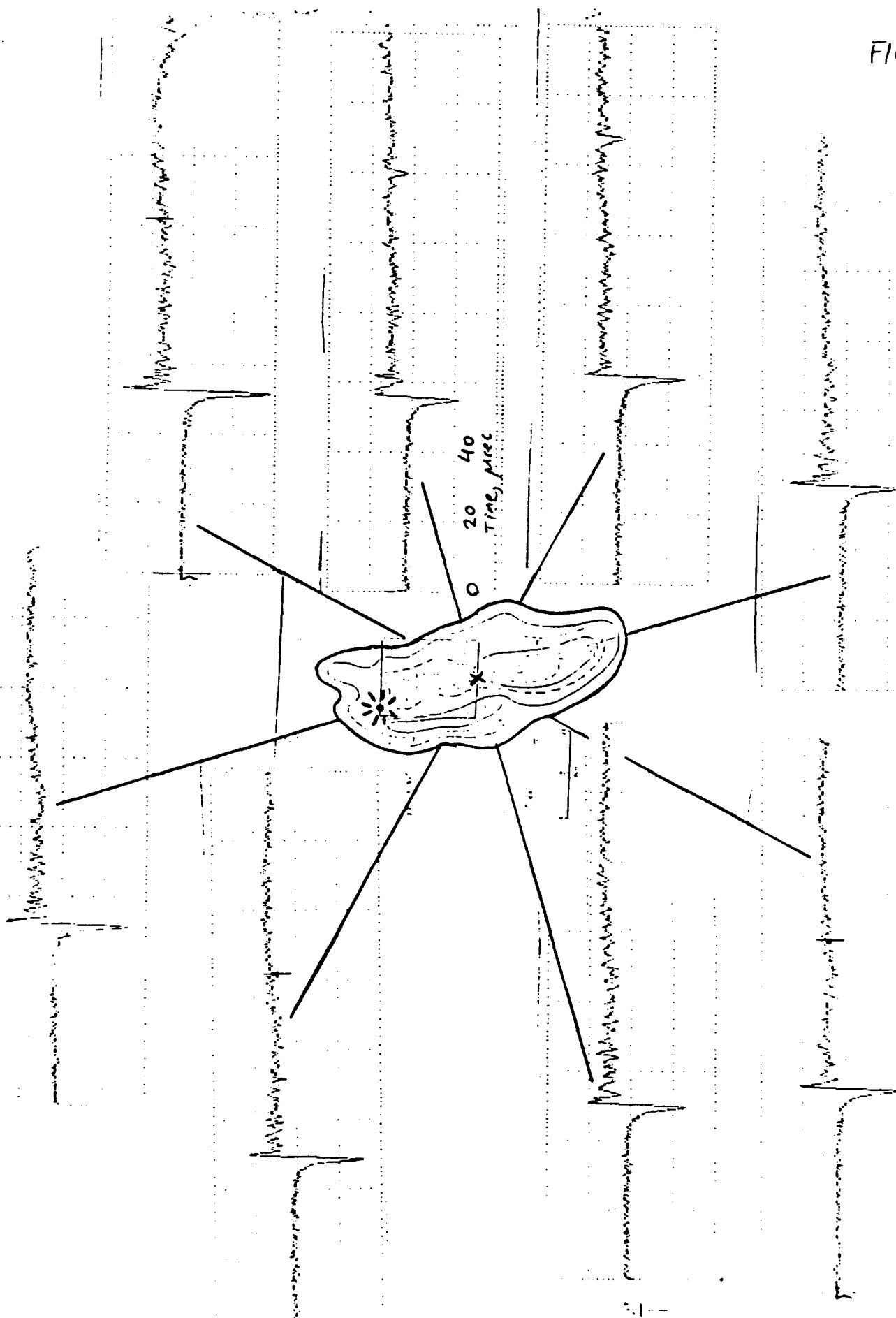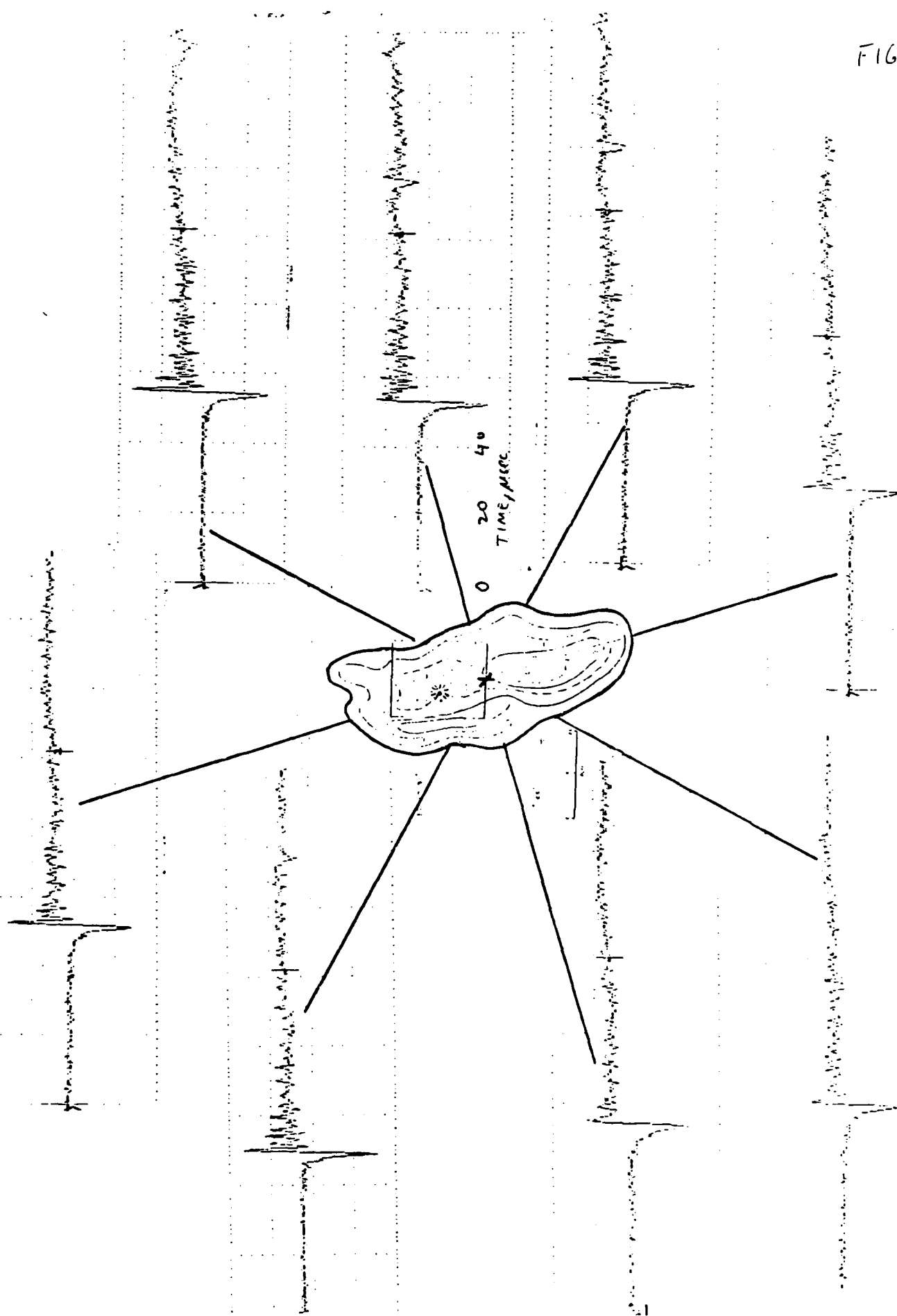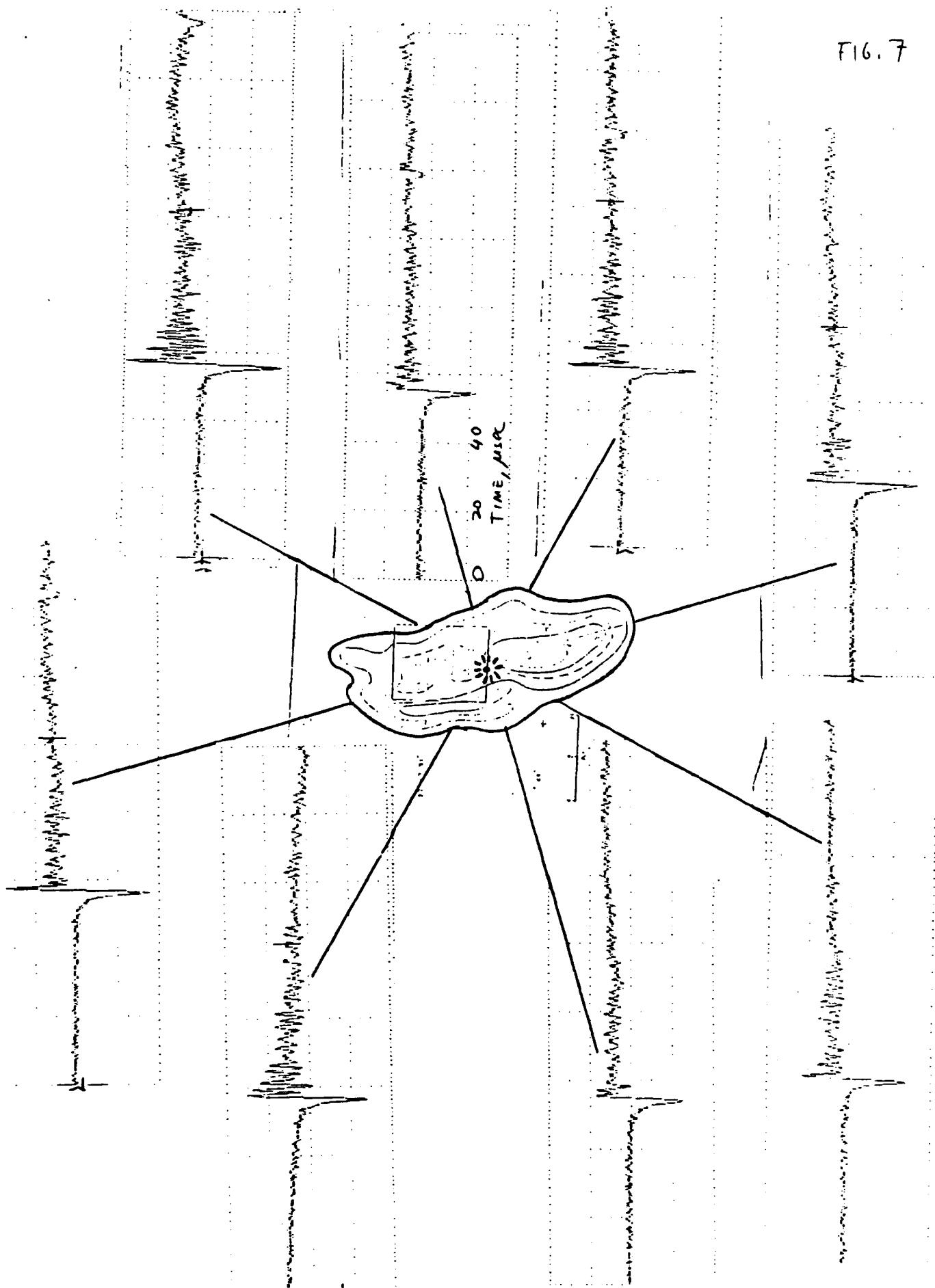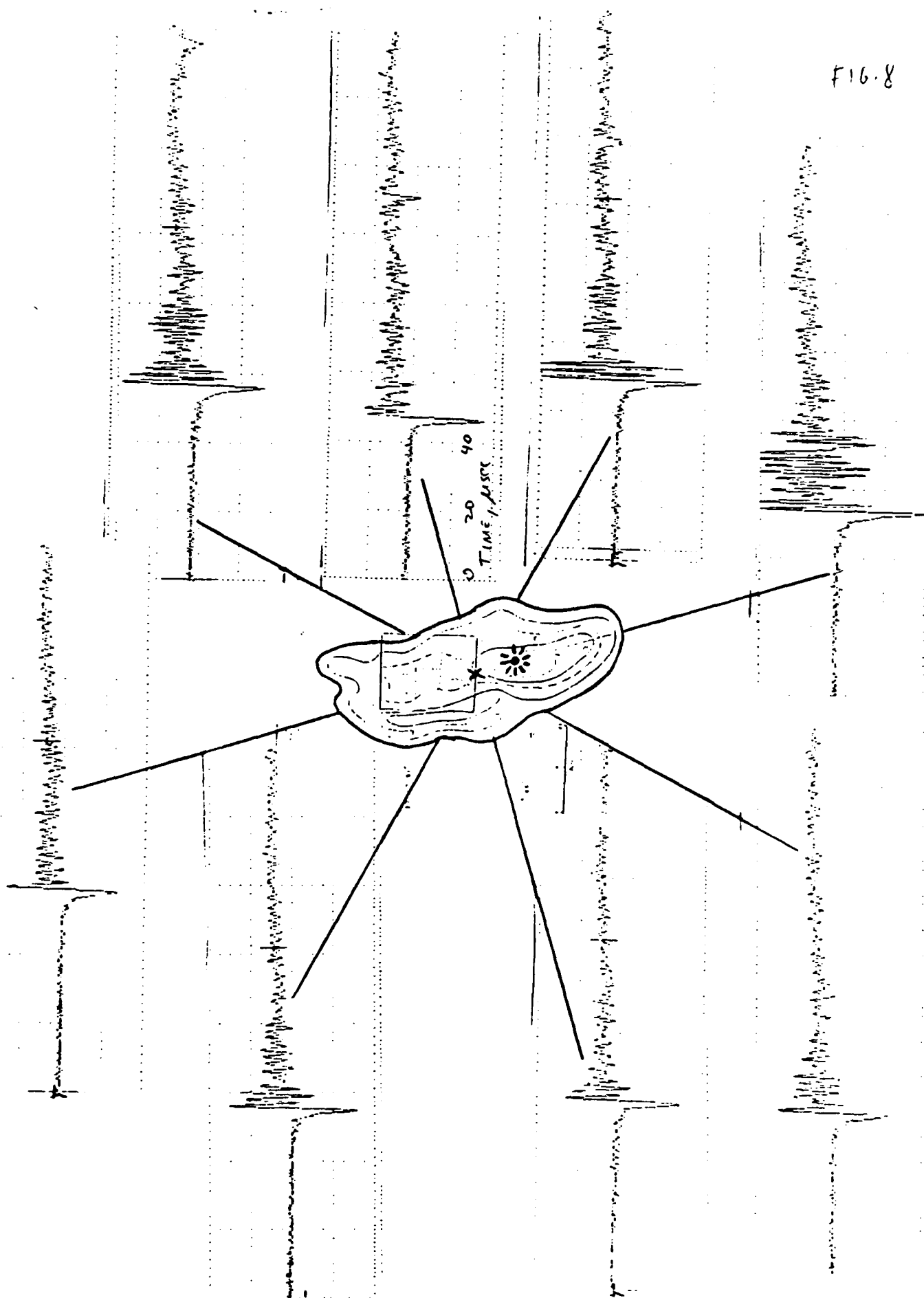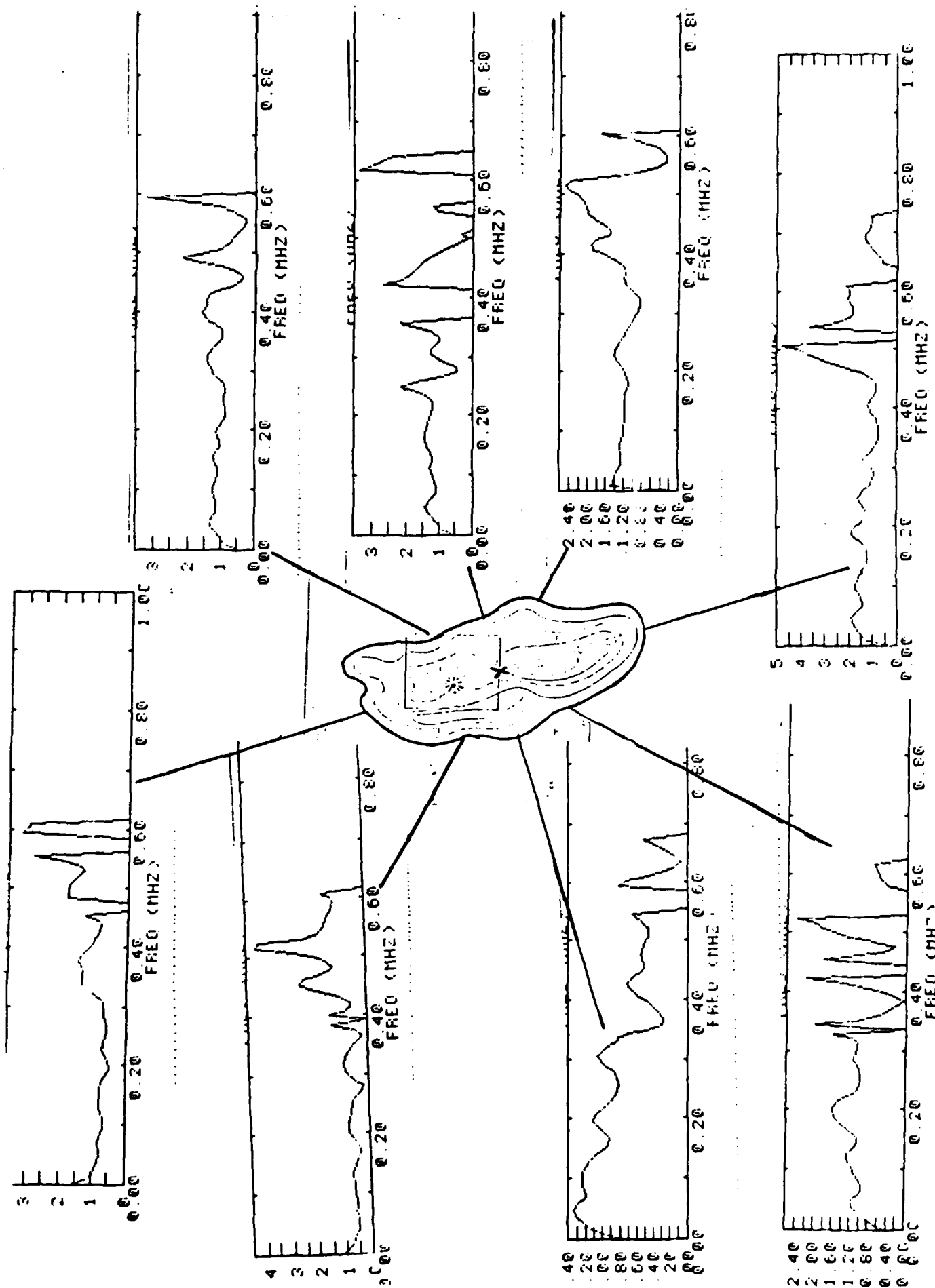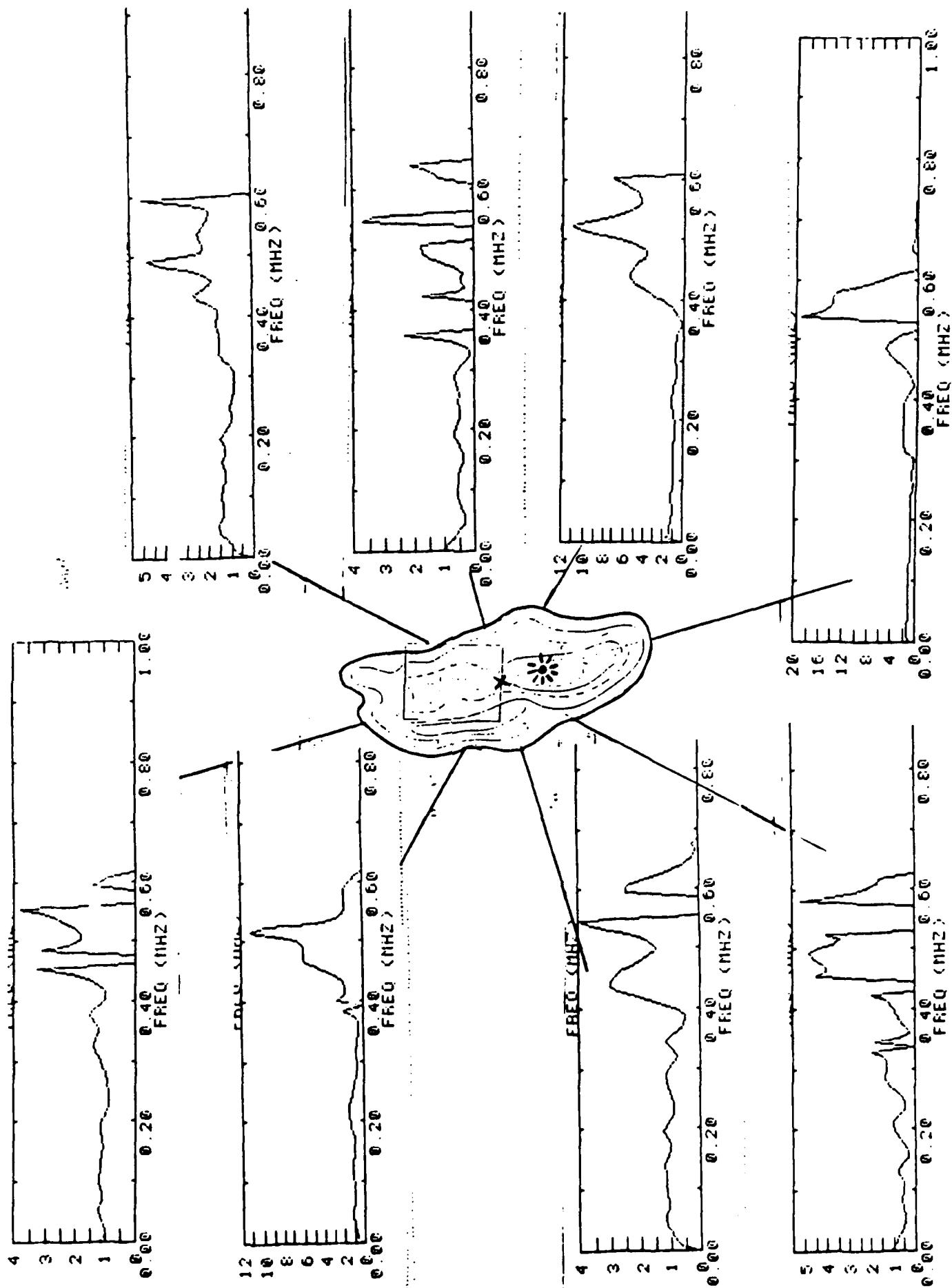
THE USE OF PROPAGATION-CORRECTED Lg SPECTRA TO ESTIMATE YIELDS OF SOVIET EXPLOSIONS AND ISOLATION AND ENHANCEMENT OF REGIONAL PHASES FOR EARTHQUAKES IN THE EASTERN UNITED STATES

ALEXANDER, S. S., L. TANG, A. BORKOWSKI, and D. STOCKAR
Department of Geosciences
The Pennsylvania State University
University Park, PA 16802

OBJECTIVE

The principal objectives of the aspects of the project reported here are: to make use of alternate techniques to coda Q for correcting path effects and estimating yields of Soviet explosions from spectral observations of Lg at regional or teleseismic (but continental) distances; to apply signal enhancement techniques at single three-component stations to isolate separately P, S, and Lg phases at regional distances; and to determine focal depths of earthquakes or explosions by stacking cepstra over a spatially distributed regional array to enhance depth phases and suppress phases that have variable relative delay times over the array.

RESEARCH ACCOMPLISHED

Previous work under this project has shown that the effects of tectonic release on Lg waves is negligible or slight for frequencies above about .3 Hz for both NTS and the Soviet test site at Semipalatinsk and that the transverse component is at least as good as the vertical component for estimating yield. We have concentrated recently on the two spectral techniques that allow one to use single stations to estimate yield; these approaches are fundamentally different from the coda-Q technique. It should be noted that the most desirable situation (which we do not have presently) is a spatially well-distributed array with multiple sources either concentrated or distributed spatially; this permits a three-way decomposition to obtain simultaneously separate least-squares estimates of reduced displacement potential (or moment) for each event, path attenuation, and station site amplification all as a function of frequency.

One of these techniques applicable to the Soviet test site is based on the observation that Nuttli's mbLg formula for eastern US earthquakes appears to be transportable to the Soviet Union (at least for some paths from Semipalatinsk, such as to MAIO). By using the observed difference in excitation of Lg for the earthquake of 20 March 1976 and nearby explosions at Semipalatinsk an empirical correction factor was obtained such that the explosion mbLg calculated using this correction term should agree with Nuttli's coda-Q Lg magnitude and with mb.

Figure 1 shows a plot of mbLg determined in this manner using Grafenberg observations compared to Nuttli's coda-Q mbLg estimates using different stations. The values typically agree within .1 magnitude units. The GRF data were taken from a frequency band centered at .7 Hz, the frequency at which we obtained the least scatter in a regression against mb. Figure 2 shows a plot of

our mbLg vs mb(ISC). These data can be used together with Nuttli's mbLg(coda Q) vs yield calibration curve from NTS or alternative calibration curves to estimate yields of the Soviet explosions.

The second method for correcting for path effects and estimating source strength (yield) consists of using noise-corrected Lg spectra for a suite of explosions at Semipalatinsk recorded at a given station to obtain by least squares regression on the log amplitude spectra the best estimate of the attenuation parameter 1/QU. This average value is then applied to obtain the noise- and attenuation-corrected source spectrum for each event. By comparing this source spectrum with theoretical excitation spectra (e.g. Von Seggern-Blandford) for different yields one can obtain a yield estimate. Alternatively empirical reduced displacement potential curves developed from experience at NTS or elsewhere can be used for the interpretation. Table 1 gives the results of applying this approach to 18 Semipalatinsk events and 2 Azgir explosions recorded by the Grafenberg array. The number in parenthesis indicates the number of stations used in the estimate. The spectral slope was obtained using the .3-1.2 Hz band which we determined to have good signal to noise ratios and negligible contributions from tectonic release. Note that the average Q for this band is comparable to that in eastern North America and close to the value incorporated in Nuttli's mbLg expression for magnitude. Figure 4 shows typical examples of the "observed" reduced displacement potential for several Semipalatinsk explosions compared to the Von Seggern- Blandford theoretical curves for various yields in granite. These spectral fits give least-squares estimates of yield for each event. Figure 3 shows a plot of mb vs yield for 27 Semipalatinsk explosions determined using this method. There is an obvious linear trend with relatively small scatter; these yield estimates agree well with Nuttli's estimates for these same events using coda-Q. Averaging such estimates over as many stations as possible would give even better yield values. Note that this method is fundamentally different from the coda-Q method.

For a low yield TTBT or a comprehensive test ban it is likely that individual three-component stations at regional distances will provide much, if not all, of the seismic information on small events. Therefore, it is important to identify and enhance crustal P, S and Lg arrivals in the typically complicated regional signals. We have found that combined band-pass filtering and (spectral) polarization-filtering effectively enhances desired regional phases. It is especially important for isolating the S-wave arrivals which typically are difficult to extract from the P-coda, higher mode surface waves and noise. We have applied these techniques to small events recorded at regional distances in eastern North America. Figure 5 depicts one example from a recent study by Borkowski (1987); this event is an mbLg 4.2 event observed at a distance of 401 km.

Focal depth determination using regional observations is very difficult unless it happens that the event is located close to one of the observing stations. Because signal bandwidth at regional distances extends to relatively high frequencies (15-20 Hz or higher) cepstral methods, can in principle, be applied to estimate focal depths even for very shallow depths.However, regional recordings typically contain multiple arrivals including near-receiver scattered or mode-converted arrivals that can be confused with true depth phases (pP and sP). We have found that by using cepstra of long P-wave windows and stacking

over a regional array distributed in distance and azimuth, the depth phases are greatly enhanced. In particular, the product of individual cepstra produces the best results for events that we have analyzed for which independent estimates of depth are accurately known. Figure 6 shows the results of cepstral stacking for the regional stations shown tnat recorded the April 22, 1982 mbLg 4.2 Lancaster, Pennsylvania earthquake (Stockar, 1986). From the focal mechanism for this event most of the observing stations would record a strong sP and a very weak pP. The depth obtained from the peak (sP) at 1.95 sec is 4.7 km, which is in good agreement with the 4.4-4.7 km depth estimated for this event's aftershocks using a local source array. Figure 7 shows similar results for a magnitude 3.3 (Mc) aftershock at Ardsley, New York, recorded at the regional stations shown (Borkowski, 1987). The depth estimated from the sP peak at 2.11 sec is 5.63 km compared with an estimate of 5.60 km by Woodward-Clyde Consultants based on a hypocenter location that included nearby stations. In both cases the depth phases are significantly enhanced by the stacking and it appears this approach may be very effective in estimating source depth from regional network observations.

CONCLUSIONS AND RECOMMENDATIONS

Application of an empirical approach to correct observed Lg spectra for propagation effects gives estimates of the source reduced displacement potential vs. frequency fr m which estimates of yield for Soviet explosions can be made. In addition an mbLg calibration technique using the differential excitation of Lg by an earthquake near the Soviet test site compared to nearby explosions gives mbLg values comparable to those obtained by Nuttli using coda-Q. Nuttli's mbLg vs. yield curve can be used with these values to estimate yield.

These approaches should be applied to a larger number of observing stations to determine the variability for different paths and to obtain better yield estimates through averaging of individual station estimates. A broader Lg bandwidth with good S/N would likely give still better estimates of the source RDP.

The signal enhancement techniques discussed help significantly in the identification and isolation of desired crustal phases. Stacking of cepstra over a spatially distributed regional array significantly enhances source depth phases; it appears they can be used to obtain very good depth estimates (better than .5 km in the cases studied).

Additional events whose depths are independently known should be investigated. The technique should also be applied to quarry blasts to determine whether there is evidence of ripple-firing and whether such events can be distinguished from single sources.

REFERENCES

Borkowski, A. H., 1987. Testing and Implementation of a Phase-Difference Polarization Filter and Application o cpstral Analysis to Enhance Regional Seismic Phases, M.S. paper, The Pennsylvania State University, 177 pp.

Stockar, D. V., 1986. Contemporary Tectonics of the Lancaster, Pennsylvania Seismic Zone, M.S. paper, The Pennsylvania State University, 177 pp.

Table 1. Determination of Lg spectral slopes and corresponding average Q for paths to the Grafenberg array.

(EASTERN KAZAKH)

DATE	N	SLOPE
12/07/76	3	-2.141
06/11/78	5	-2.130
09/15/78	6	-1.967
11/04/78	6	-1.716
11/29/78	3	-1.869
02/01/79	4	-1.923
06/23/79	5	-2.059
07/07/79	7	-1.930
08/04/79	10	-1.854
10/28/79	7	-2.191
12/02/79	12	-2.196
12/23/79	9	-2.117
06/12/80	12	-1.930
10/12/80	8	-1.967
12/14/80	9	-1.797
03/29/81	12	-1.912
04/22/81	11	-2.352
09/13/81	8	-2.197
AVERAGE SLOPE		-2.014

AVERAGE Q : 912 ~ 1064

(AZGIR)

DATE	N	SLOPE
07/29/76	3	-1.232
12/18/78	4	-1.317
AVERAGE SLOPE		-1.274

AVERAGE Q : 674 ~ 787

N denotes the number of array stations used for each average slope estimate.

$$m_{bLg} \ (\text{Nuttli}) \ \sim \ m_{bLg}$$

Figure 1

$m_b \, (\text{ISC}) \sim m_{bLg}$

Figure 2

M_b vs Log(Y)
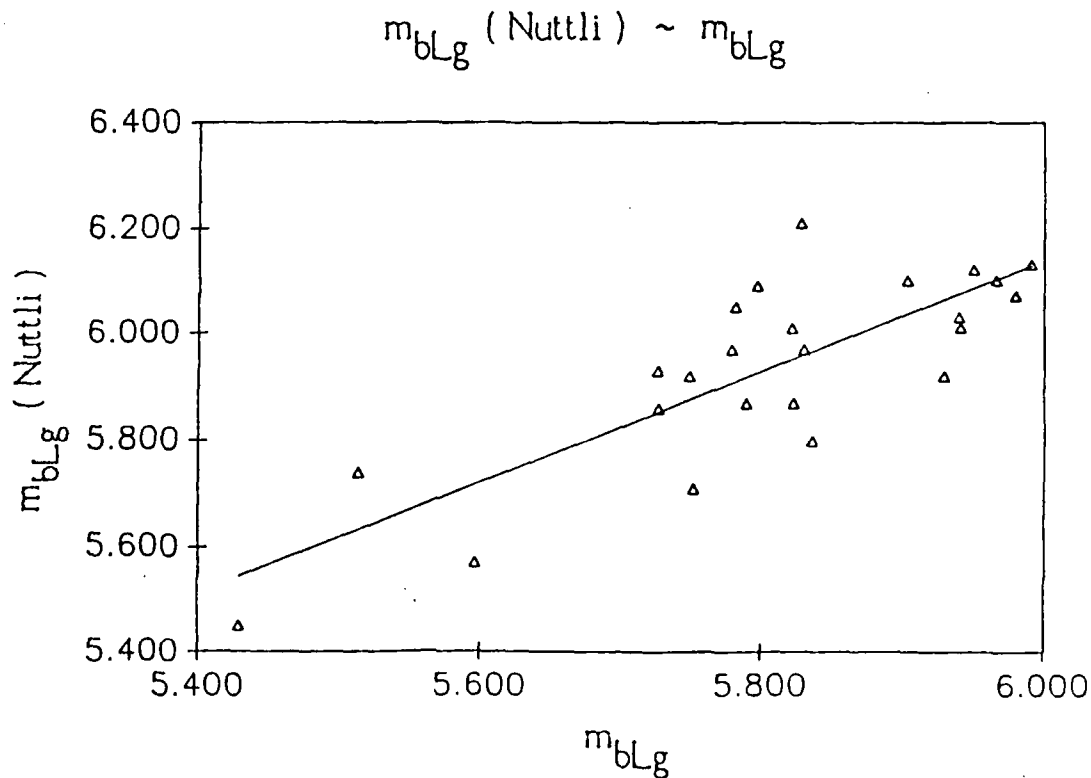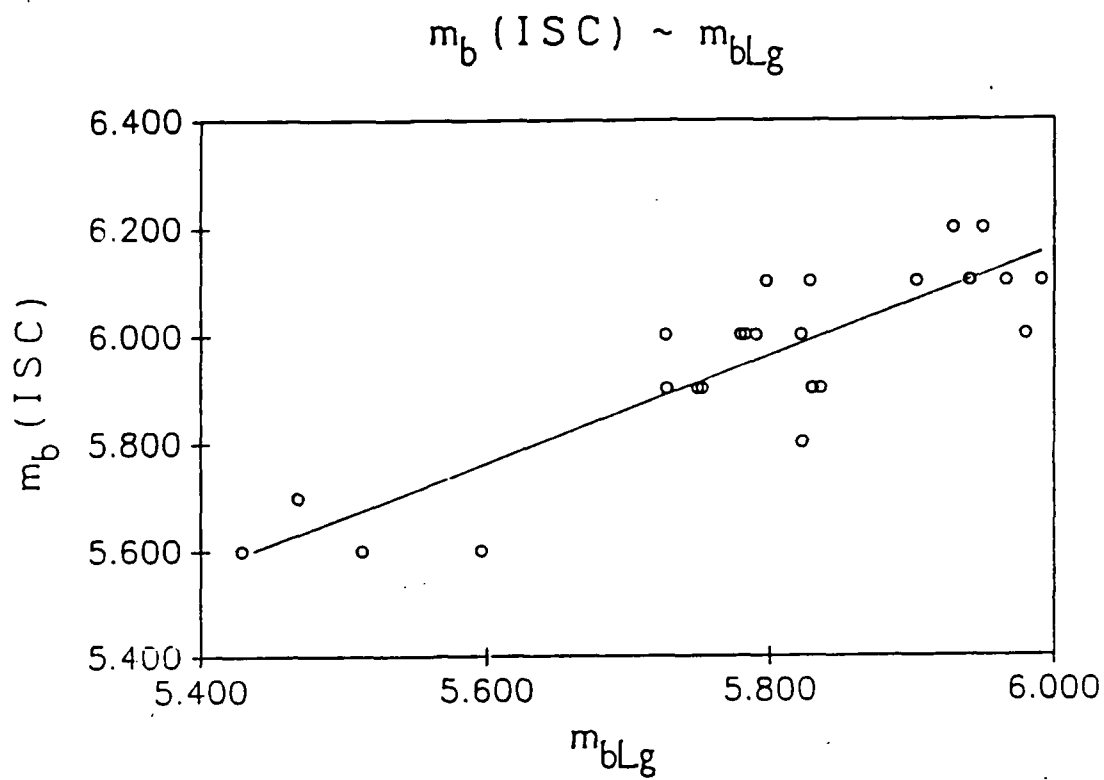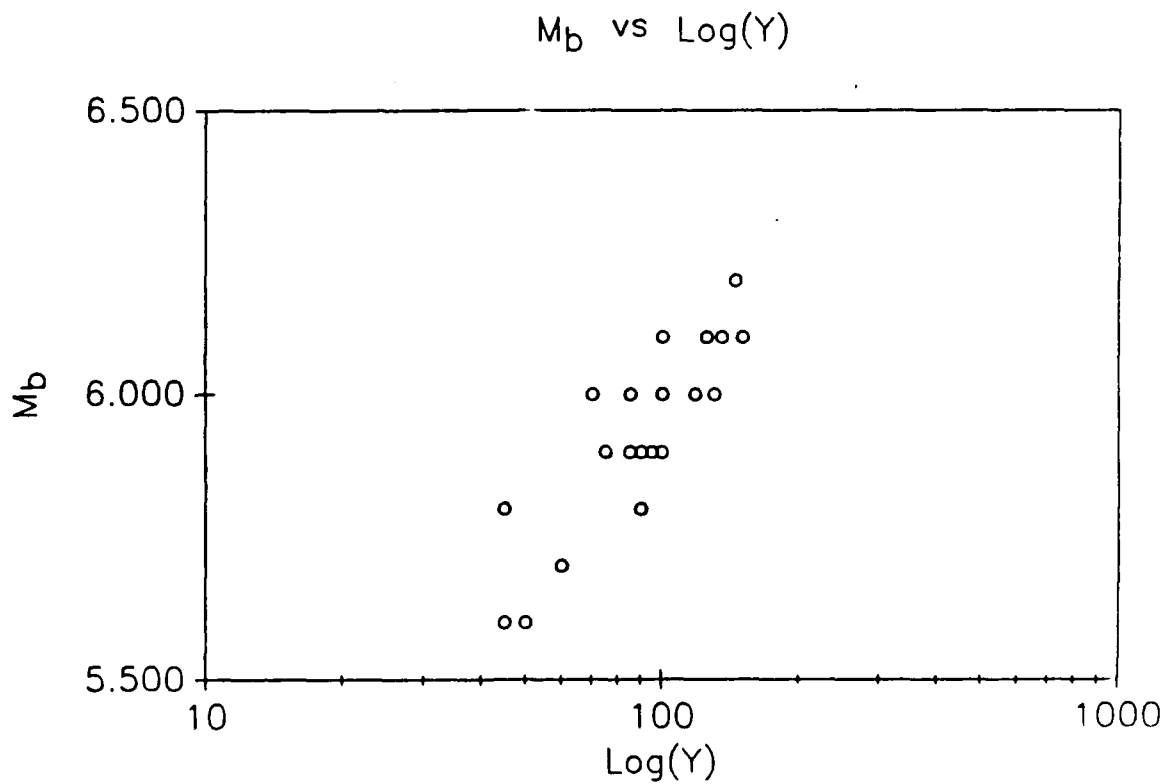
Figure 3

63
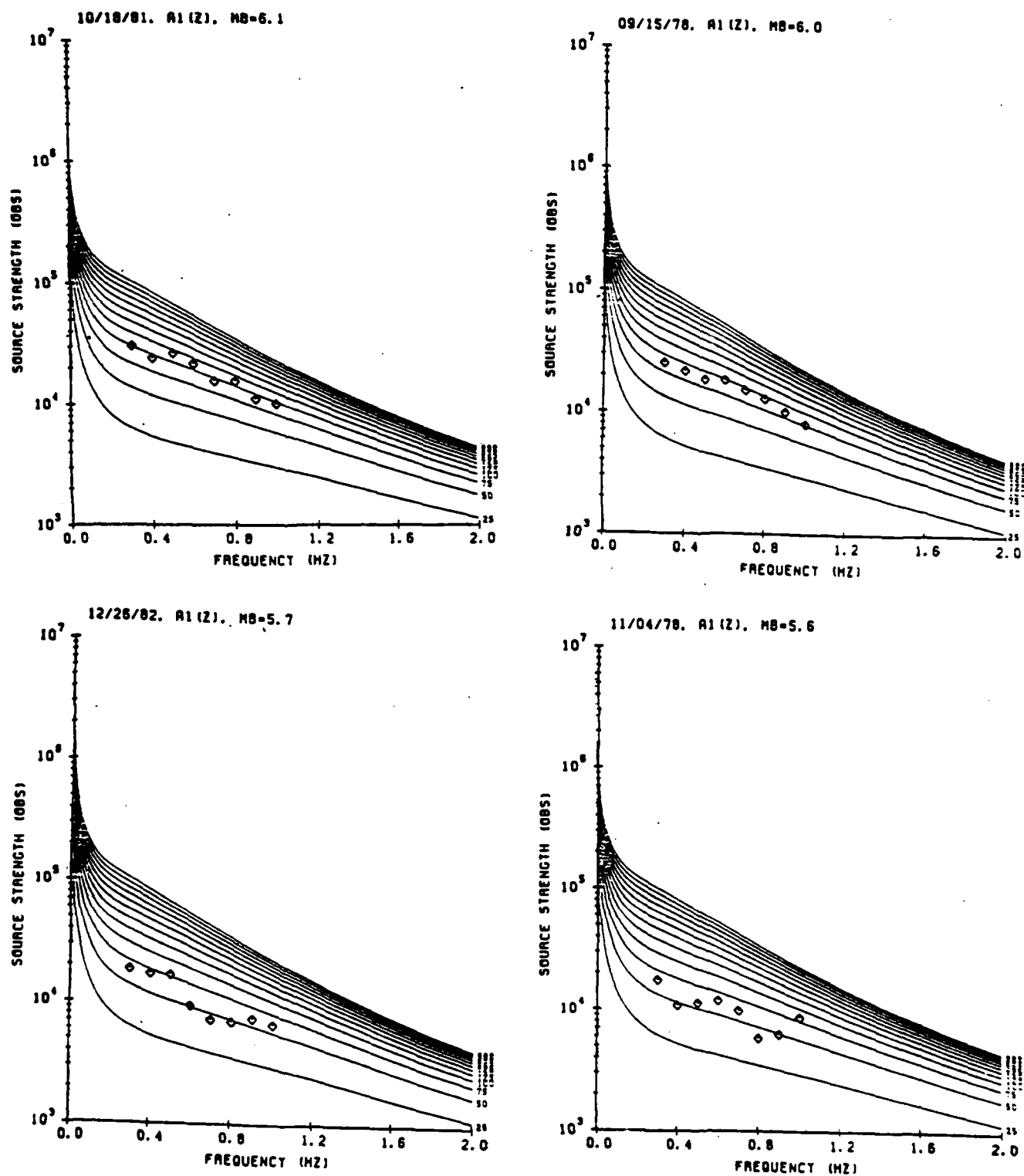
Figure 4. Comparison of observed strength (reduced displacement potential) derived from Grafenberg observations with theoretical curves for different yields in granite. The Von Seggern-Blandford source model was used. The event date and ISC magnitude is given at the top of each plot.
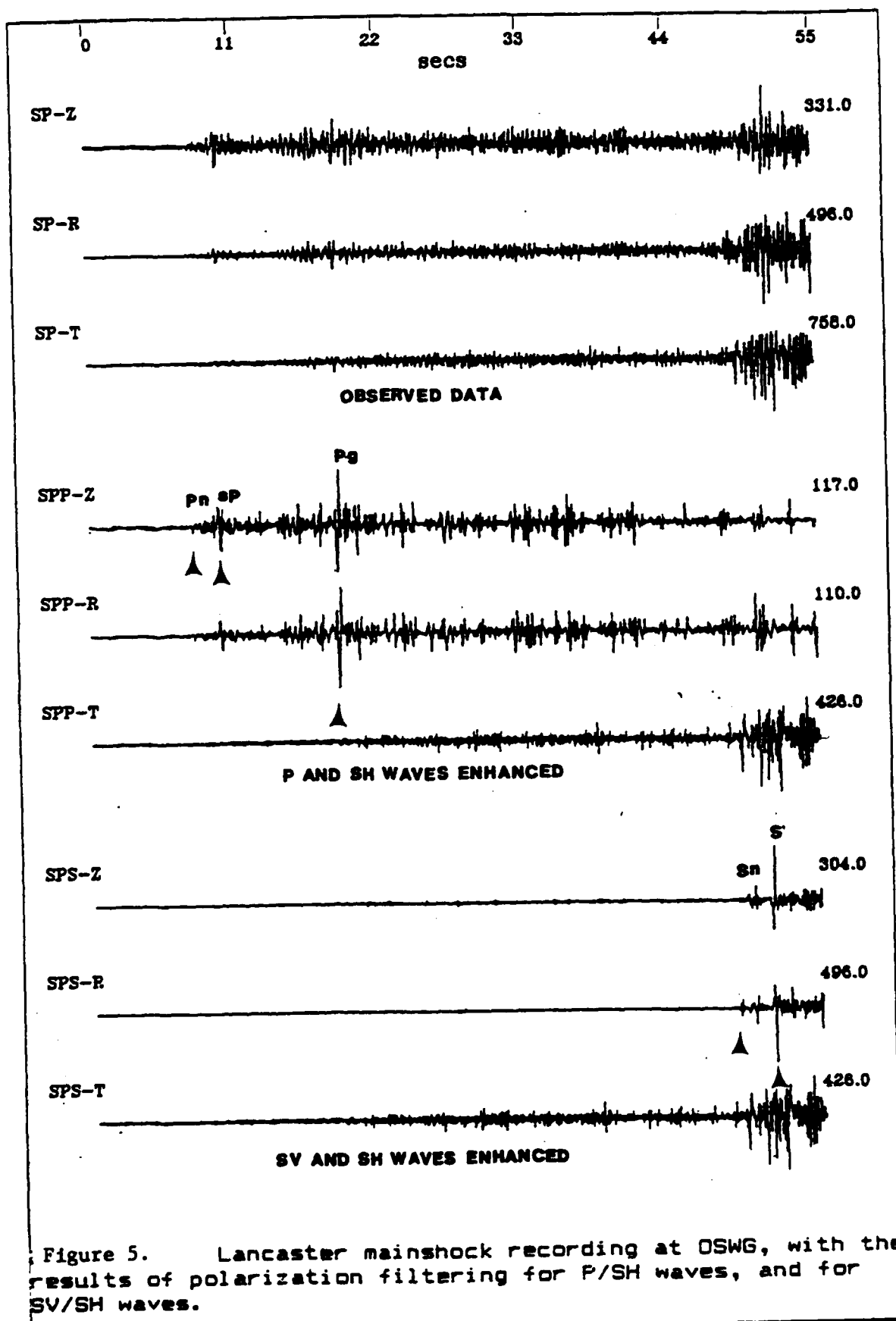
Figure 5. Lancaster mainshock recording at OSWG, with the results of polarization filtering for P/SH waves, and for SV/SH waves.
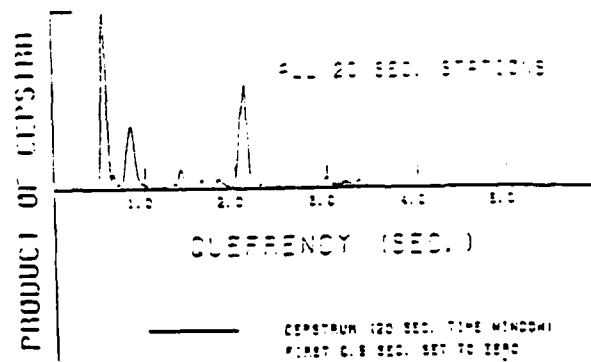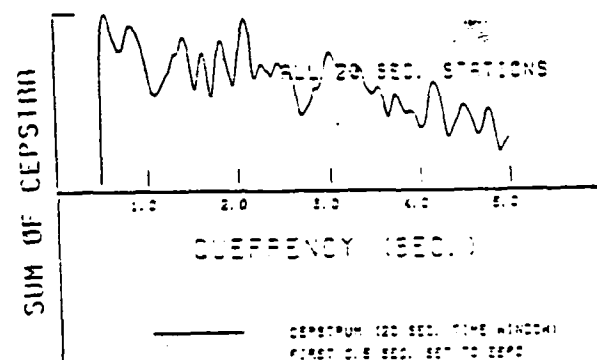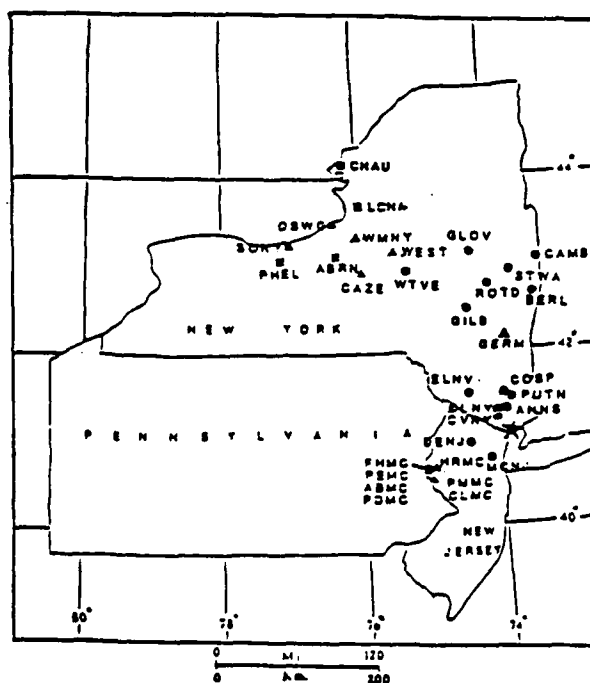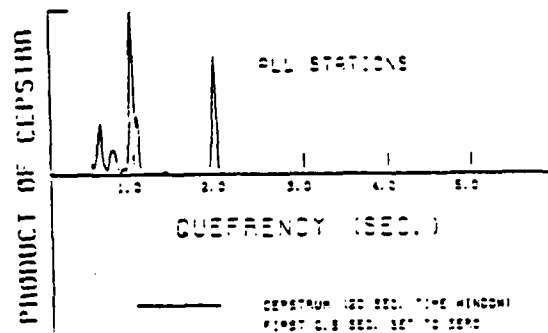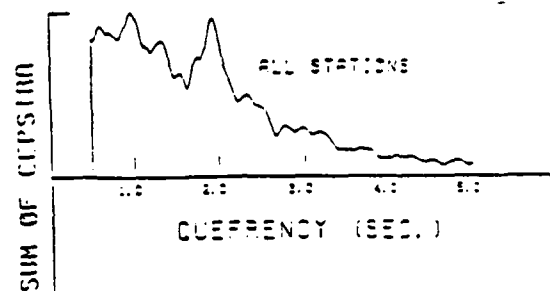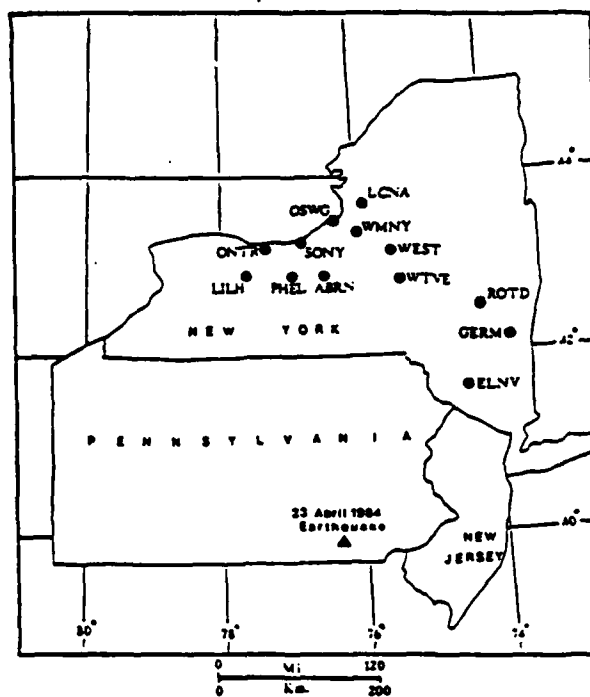
Figure 6 (top) and Figure 7 (bottom) show results of cepstral stacking
for the regional arrays and source locations shown at the left.

Wave Propagation Modeling and Regional Discriminants

J. S. Barker, L. J. Burdick and C. K. Saikia

Woodward-Clyde Consultants

OBJECTIVE

A program of studies is being undertaken to investigate the aspects of regional wave propagation that affect discrimination. It is well known that the characteristics of regional phases vary between tectonic and shield areas. We present examples of detailed wave propagation modeling of regional data from several areas within North America.

RESEARCH ACCOMPLISHED

The October 11, 1983 earthquake near Ottawa (m_{Lg} 4.2) was well recorded on the Eastern Canada Telemetered Network over ranges of 20 - 1000 km. Data from a nearby crustal refraction experiment (Mereu, et al., 1986) provide not only a detailed velocity structure from which to model the earthquake, but also a comparison between earthquake and explosion sources. By plotting the explosion data with an S-wave reduction velocity as shown in Figure 1a, we see the fundamental mode Rayleigh wave dominating the waveforms within 100 km. Strong high-frequency phases identified as S waves post-critically reflected from the Moho are the controlling feature beyond 100 km. A plot of the peak particle velocity with distance (Figure 1b) illustrates that different phases control the peak ground motion at different ranges. Since the relative excitation of these phases is dependent on crustal structure as well as source mechanism and depth, a single attenuation curve fit to the data is inappropriate for predicting ground motions for other situations.

Vertical velocity records observed for the Ottawa earthquake within 200 km of the source are plotted in Figure 2a. The observations are quite sparse, but may be adequately interpolated using generalized ray synthetic seismograms with empirical source functions (Figure 2b). Since the earthquake occurred at a depth of 15.5 km, the Rayleigh wave excitation is greatly reduced, and the peak ground motion is controlled by the S wave and the post-critical Moho reflection. The synthetic modeling indicates that the earthquake body waves are quite sensitive to the interference between upgoing energy and rays that depart downward from the source. The effect is most important for shallow events, such as the March 31 aftershock of the January 9, 1982 Miramichi, New Brunswick earthquake (Figure 2c). This event occurred at 3.5 km depth in the Appalachian crustal structure. By modeling simultaneously the P and S waves from three aftershocks, we have obtained a detailed crustal velocity structure model that includes a mid-crustal discontinuity and a deep Moho. The semi-empirical generalized ray synthetics are shown in Figure 2d, and include high-frequency arrivals due to post-critical reflections from both the mid-crustal and Moho discontinuities. Details of the structure models and synthetic modeling may be found in Barker, et al. (1987).

A modal summation technique is used to investigate the effects of source depth, attenuation and near-surface velocity structure on the relative excitation of fundamental and higher modes observed from quarry blasts in southern New England. Shown in Figure 3a are synthetics computed to 10 Hz for the localized crustal structure model of Saikia, et al. (1987). The relative excitation of the first and second higher modes increases as the depth of the explosion source is increased from 0. to 0.5 km. As shown in Figure 3b, however, the inclusion of a realistic anelastic Q model (Q_β from 100 - 200 in top 2.5 km) effectively eliminates the higher modes and reduces the fundamental mode amplitude. Adding a surface till layer (0.1 km thick in Figure 3c) increases the complexity of the fundamental mode. However, there appears to be a critical value of the layer thickness such that for a very thin layer (0.01 km in Figure 3d) these effects are not observed.

Plane-layered structure models are often inadequate to explain regional observations, particularly for shallow sources. The use of numerical techniques enables the specification of lateral structure variations and improves the modeling. Ho-Liu and Helmberger (1987) used the structure model shown at the top of Figure 4a to model broad-band observations at Pasadena from earthquakes in the Imperial Valley. Finite difference synthetic S and Love waves are shown in Figure 4a for a source at 7.0 km depth in the Imperial Valley at a number of ranges. The basin structure of the Imperial Valley sets up a characteristic dispersion in the waveforms that cannot be modeled with plane-layered structures. This dispersion is strongly dependent upon source depth, and as shown in Figure 4b for a range of 262 km, has a profound effect on the character and amplitude of the synthesized waveforms.

CONCLUSIONS AND RECOMMENDATIONS

We have undertaken studies into the effects of crustal velocity structure, source mechanism and depth that can be deterministically modeled in regional waveforms. These broad-band effects are important in the calibration of a region, particularly for depth discriminants based on body wave/surface wave excitation.

REFERENCES

Barker, J. S., P. G. Somerville and J. P. McLaren (1987). Wave Propagation Modeling of Ground-motion Attenuation in the Northeastern United States and Adjacent Canada, report to the Electric Power Research Institute, Woodward-Clyde Consultants, Pasadena, CA.

Ho-Liu, P and D. V. Helmberger (1987). Source retrieval from regional long period records (abstract), Seismological Research Letters, 58, 7.

Mereu, R. F., D. Wang, O. Kuhn, D. A. Forsyth, A. G. Green, D. Morel, G. G. R. Buchbinder, D. Crossley, E. Schwartz, R. duBerger, C. Brooks and R. Clowes (1986). The 1982 COCRUST seismic experiment across the Ottawa-Bonnechere graben and Grenville Front in Ottawa and Quebec, Geophys. J., 84, 491-514.

Saikia, C. K., A. L. Kafka, S. G. Grewuch and J. W. McTigue (1987). Shallow-crustal velocity models and attenuation structure for localized zones in southern New England from short-period Rayleigh wave dispersion, J. Geophys. Res., in press.
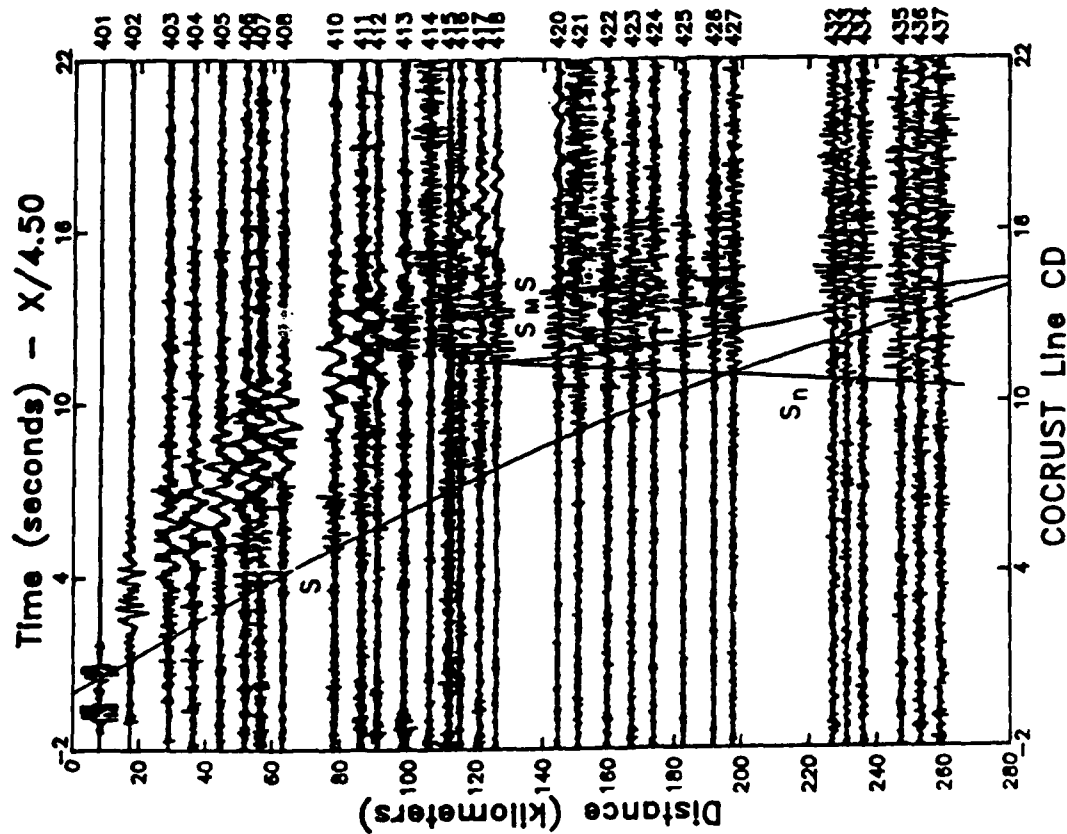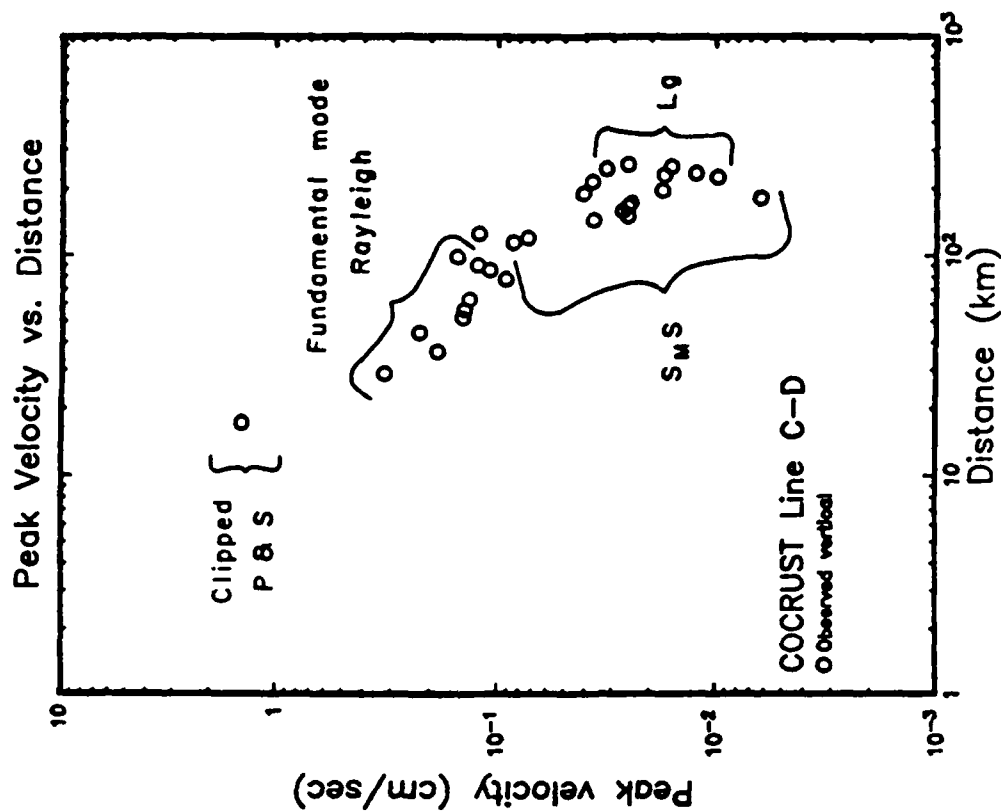
Figure 1. a) Vertical velocity recordings of the COCRUST refraction survey near Ottawa, plotted with an S-wave reduction velocity of 4.5 km/s. Also shown are S-wave travel-time curves for the Grenville crustal velocity structure model determined for these data. b) Attenuation of observed peak vertical velocity for the COCRUST refraction profile. Also indicated are the types of waves that account for the peak velocity.
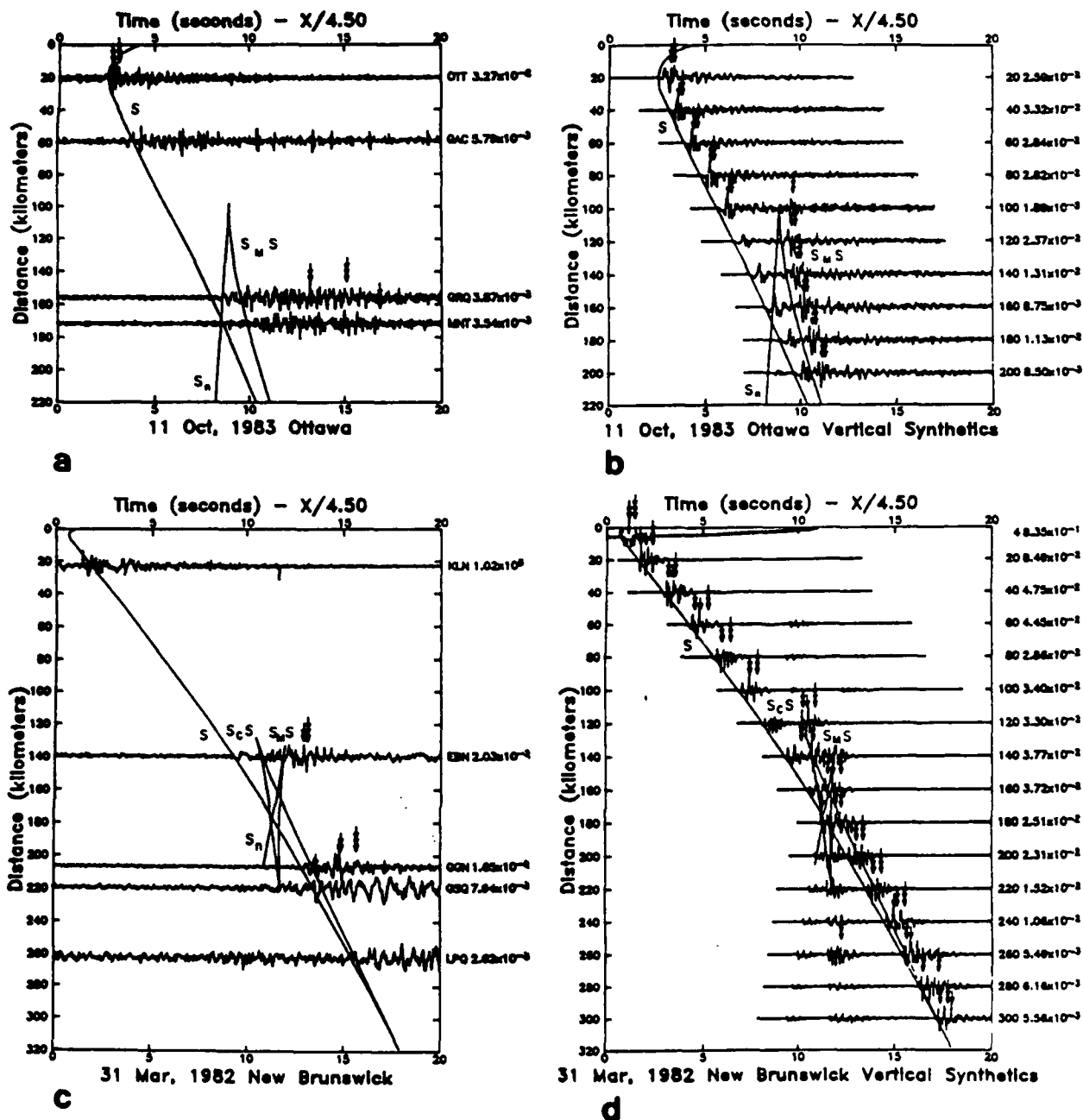
Figure 2. a) Vertical velocity recordings from ECTN stations within 200 km of the 1983 Ottawa earthquake. Superimposed are the S-wave travel-time curves for a source at 15.5 km depth in the Grenville velocity structure model. b) Semi-empirical, synthetic vertical velocity seismograms for a profile running N45°E from the Ottawa earthquake. c) Vertical velocity recordings from ECTN stations within 300 km of the March 31 aftershock. Superimposed are the S-wave travel-time curves for a source at 3.5 km depth in the Appalachian velocity structure model. d) Semi-empirical, synthetic vertical velocity seismograms for a profile running N60°W from the March 31 New Brunswick aftershock.

711

VERTICAL VELOCITY AT   R=100.0 KM

DEPTH   WITHOUT Q   WITH Q

0.0 KM ————————————————————————— .119E+00   ————————————————————— .837E-03

0.2 KM ————————————————————————— .700E-02   ————————————————————— .390E-03

0.5 KM ————————————————————————— .172E-02   ————————————————————— .157E-03

```
23.8    30.1    36.3    42.6    48.8              23.8    30.1    36.3    42.6    48.8
```

TIME IN REDUCED SCALE: (t−X/4.2)   TIME IN REDUCED SCALE: (t−X/4.2)

a   **b**

EFFECT OF TILL LAYER AT R=100.0 KM

DEPTH   TILL: TH=0.1 KM   TILL: TH=0.01 KM

0.0 KM ————————————————————————— .211E-03   ————————————————————— .347E-03

0.3 KM ————————————————————————— .689E-04   ————————————————————— .513E-03

0.6 KM ————————————————————————— .388E-04   ————————————————————— .135E-03

```
22.2    29.7    37.2    44.7    52.2              22.2    29.7    37.2    44.7    52.2
```

TIME IN REDUCED SCALE: (t−X/4.5)   TIME IN REDUCED SCALE: (t−X/4.5)

c   **d**

Figure 3. a) Synthetic vertical velocity seismograms computed by modal summation for an explosion source at 0., 0.2 and 0.5 km depth in southern New England structure. The three pulses at 0.5 km depth correspond to the first, second and fundamental modes, consecutively. b) The same synthetic seismograms when a realistic attenuation model is included. c) Synthetics for an explosion source at 0., 0.3 and 0.6 km depth when a till layer of thickness 0.1 km is added to the top of the structure model. d) The same synthetics with a very thin (0.01 km thick) till layer.

71
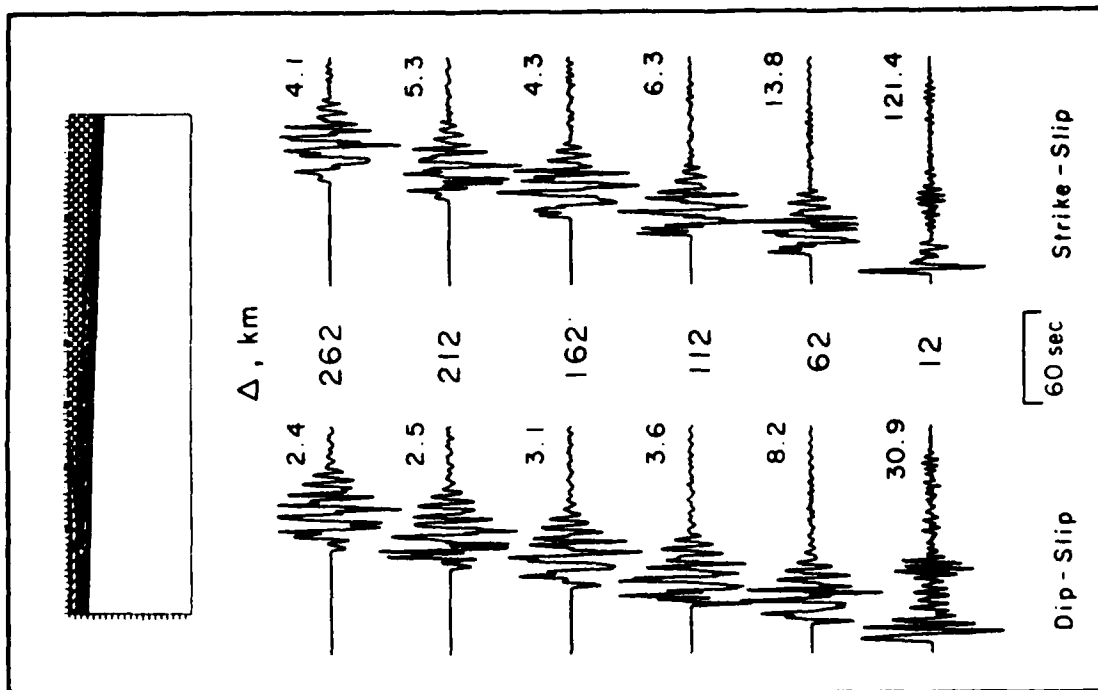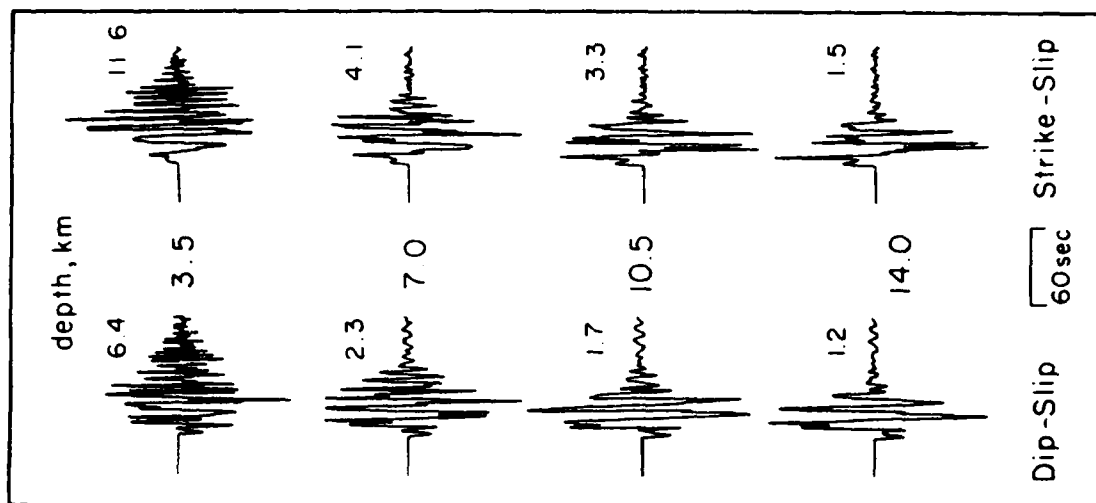
Figure 4. a) SH and Love waves computed for a laterally varying structure model using a finite difference approach. The source is in the Imperial Valley (left) and receivers are located along a line toward Pasadena. b) The effect of source depth on the finite difference synthetics computed at a range of 262 km.

72

Application of the
Theory of Wave Propagation through Random Media
to Phase and Amplitude Fluctuations of Seismic P-Waves

Stanley M. Flatté

Physics and Richter Seismological Laboratory
University of California, Santa Cruz 95064

OBJECTIVE

The long-term objective of this work is to develop a quantitative understanding of the fluctuations in phase and amplitude of seismic wave propagation due to kilometer-scale variations in wave velocity within the earth. The theoretical approach is to describe these variations in a statistical way: in particular to consider the variations as represented by a spectrum that depends on depth, and may depend on geographical location. Data that are relevant to this approach include wave-forms with frequency content above one Hertz received on seismic arrays or on world-wide networks. Relatively high-frequency data is desirable because the ability to discriminate small structure is dependent on the wave having relatively short wavelength. Seismic arrays whose elements are spaced in the kilometers to tens-of-kilometers regime provide analysing power in that regime. Arrays with larger spacing, such as world-wide networks, can still probe small scales if the various available sources have separations in the above range; this can occur for earthquakes in active regions, or for nuclear explosions distributed within test sites.

It is not likely that the seismological community will ever have a complete map of inhomogeneities in the earth down to kilometer scales. Therefore we will not be able to completely predict travel-time and amplitude fluctuations for a source-receiver geometry that is even a few kilometers different from previously measured situations. If we have a realistic statistical picture of the small-scale structure in wave-speed within the earth, then the theory of wave propagation through random media can be used to predict the scale and strength of travel-time and amplitude fluctuations due to earth structure. This information can then be used to calculate the accuracy of yield estimates and detection thresholds based on seismic information from an arbitrary array of seismometers, with *a priori* knowledge of results from nearby explosions or earthquakes. Furthermore, this knowledge can be used to design arrays in an optimal fashion to deal with random earth structure.

RESEARCH ACCOMPLISHMENTS

We set ourselves the task of determining how deep structure must extend to explain the travel-time and amplitude fluctuations observed on the NORSAR array. Our results can be summarized in the following way: first, we have pointed out that the log-amplitude and travel-time fluctuations at large seismograph arrays like NORSAR and LASA have further important statistical information that has not been utilized in previous analyses, especially the coherence function of waves from different sources, and hence different incoming directions; second, we have carried out a statistical analysis of NORSAR data that includes this new information; third, we have presented results from the

modern theory of wave propagation through random media (WPRM) that are some-what simpler than Chernov's, because they are partially in the wavenumber domain, and can accomodate easily any model of the medium spectrum; and fourth, we have presented a model of the inhomogeneities in the lithosphere and asthenosphere under the NORSAR array that is consistent with the available data.

There are three variances involved in travel-time and log-amplitude fluctuations; the variances of travel-time and log-amplitude, and the covariance between the two. Each of these variances leads to a coherence function of any variable being investigated; for example, previous analyses have used the travel-time and log-amplitude transverse coherence functions (TCF's), but we have analyzed for the first time the transverse cross-coherence function between travel-time and log-amplitude, and the set of three angular coherence functions (ACF's). Since the difference in direction between two beams may be as small as 1°, the angular coherence functions at a given receiver probe (in a statistical sense) inhomogeneities that are quite small: on the order of one kilometer at 60-km depth. The transverse coherence functions from a coarse array with ~ 10 km spacing cannot probe for medium structure smaller than 10 km.

The NORSAR data used in our analysis consists of the travel-time anomalies at 22 subarrays for 104 beams; and the log-amplitude fluctuations at 22 subarrays for 185 beams. All the beams have incoming directions within a 35° cone around the zenith. The smallest distance between subarrays is about 10 km, and the largest is about 100 km. The data used were filtered for 1-3 Hz, so the nominal frequency is 2 Hz. It is impor-tant to realize that the data we analyze is insensitive to inhomogeneity wavelengths greater than about 100 km, because of the finite size of the array, and is also insensitive to inhomogeneity wavelengths less than about 5 km, because of two effects: first the data are averages over subarrays that are 7 km in diameter, and second, the wavelengths of the seismic waves are about 4 km.

It does not take a sophisticated theory to draw some dramatic conclusions from the new analysis of NORSAR data. Briefly, the log-amplitude ACF drops rapidly reaching a value of 0.5 at an angle of 2°, followed by a more gradual drop to 0.1 at 10°. In con-trast, the travel-time (phase) ACF drops much more slowly, implying much larger-scale structure. Yet all the TCF's apparently have scales in the range of 10-20 km. We have found that medium spectral models that are homogeneous in depth (that is, the spec-trum does not change with depth) down to a cutoff depth between 0 and 500 km cannot fit all the data. Our models will all involve medium spectra characterized by a power law K^{-p} over the sensitive wavenumber band ($5 < \lambda < 100$ km). Figure 1 shows the best fit to a model involving a single component (with $p = 2.6$) from the surface to a depth $r_1 = 263$ km. The fit has a $\chi^2 = 179$ for 130 degrees of freedom. Figure 2 shows the best fit to a model involving two components with different power-law indices ($p_1 = 1.6$ and $p_2 = 5.5$), both extending from the surface to $r_1 = 268$ km. The fit has a $\chi^2 = 132$ for 128 degrees of freedom. Though the χ^2 value is not bad, there are systematic disagreements between the data and the predictions of all the one-layer models we have tried.

We suggest a two-overlapping-layer model consisting of an upper layer with significant small scale structure ($p = 0$) spanning $0 < z < 140$ km and a lower layer with strength concentrated at large scales ($p = 4.8$) spanning $15 < z < 240$ km. (See Figure 3. This fit has $\chi^2 = 112$ for 128 degrees of freedom.) A specific prediction of the model we suggest is a rapid drop in the log-amplitude TCF for separations of a few kilometers, followed by

a more gradual drop with a scale of tens of kilometers. We have checked this prediction by determining the TCF of log-amplitude from the individual s. tions at NORSAR, using 13 nuclear-explosion events. We find consistency with our pre iction, giving us some confidence in our interpretation.

CONCLUSIONS AND RECOMMENDATIONS

We conclude that small-scale structure in the spatial distribution of wavespeed is required down to about 240 km under the NORSAR array to explain the NORSAR data. Furthermore, we find that considerable constraint on the possible models of medium spectra as a function of depth are provided by the combination of the TCF's and ACF's.

Further work is recommended in a number of directions. First, we should extend our data set for the NORSAR array to include dependence on seismic frequency. Second, we should realize that the raw data contain more information than the ACF's and the TCF's, because these functions do not contain certain aspects of the relation between arrival angle and transverse separation. Third, other data sets should be analysed from the statistical point of view. For example, data from the NORESS array, *in conjunction with the NORSAR data*, would provide finer constraints. Also, data from the New England array, from the old LASA array, and from world-wide networks looking at clusters of events, such as nuclear explosions at NTS, can be used to find medium spectra under New England, Montana, and Nevada.

Another recommended direction of investigation is the use of our derived models of medium spectra to calculate fundamental limits on the accuracy of measurement of yield, and to calculate signal-to-noise and detection thresholds, for future nuclear events that may be set off at different locations, either close to or far from, previously measured events. These calculations can be done for any type of seismic method of estimating yield, not just teleseismic P-wave amplitude or wave-form characteristics. For example, Pn/Sn strengths are dependent on the medium spectrum of the lithosphere, and a theory can be developed to predict that dependence, *given a medium spectrum*.

A final comment to emphasize is that many of the calculations envisaged for the future will be more complicated than the ones carried out up to this point; these future calculations will require some numerical simulations of three-dimensional, forward wave propagation. We now have the capability, through codes we have developed on the CRAY, of doing some of those calculations.

1-COMPONENT   1-LAYER
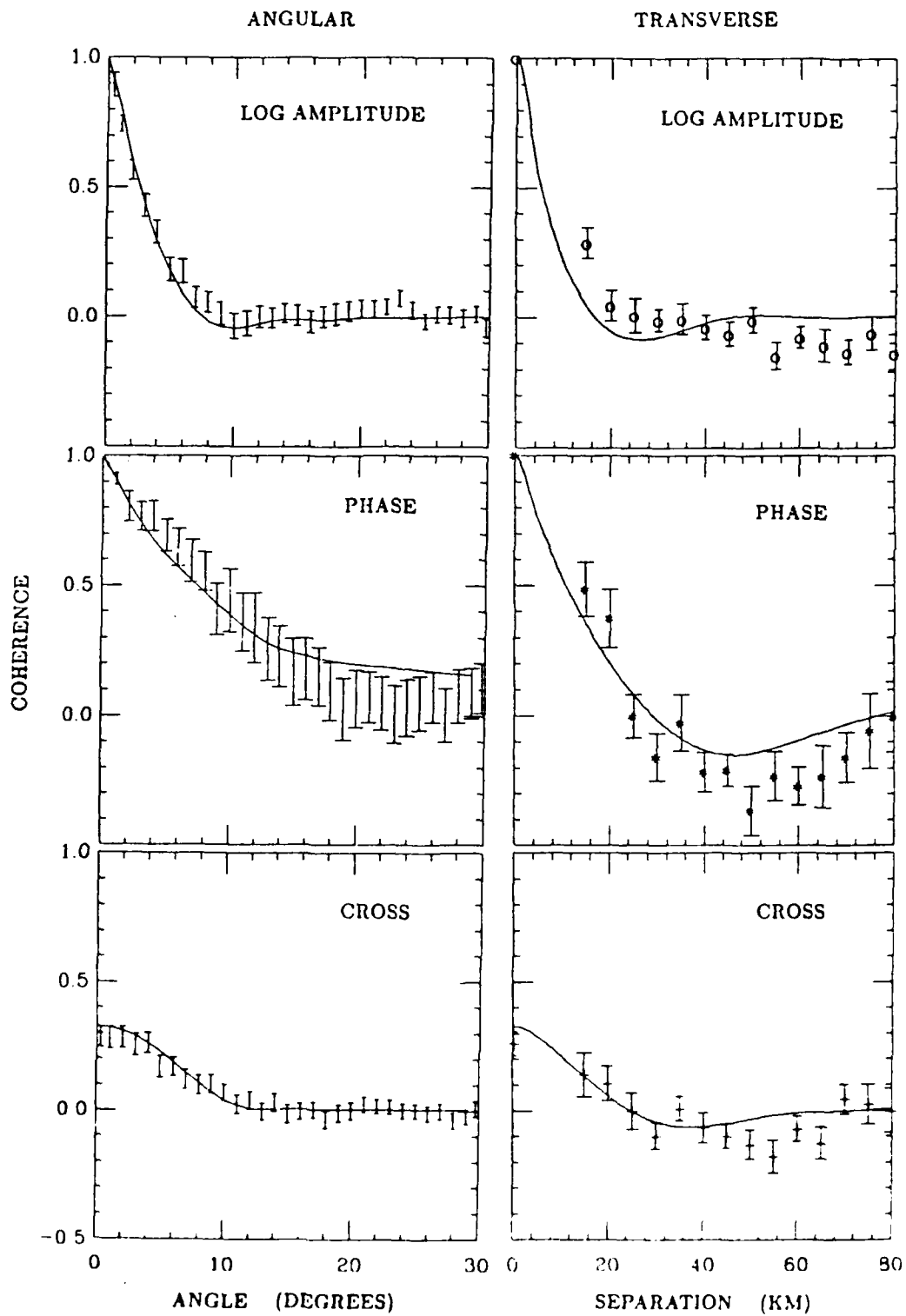
Figure 1

2-COMPONENT 1-LAYER

ANGULAR

TRANSVERSE

LOG AMPLITUDE

LOG AMPLITUDE

PHASE

PHASE

CROSS

CROSS

COHERENCE

ANGLE (DEGREES)

SEPARATION (KM)

Figure 2

77
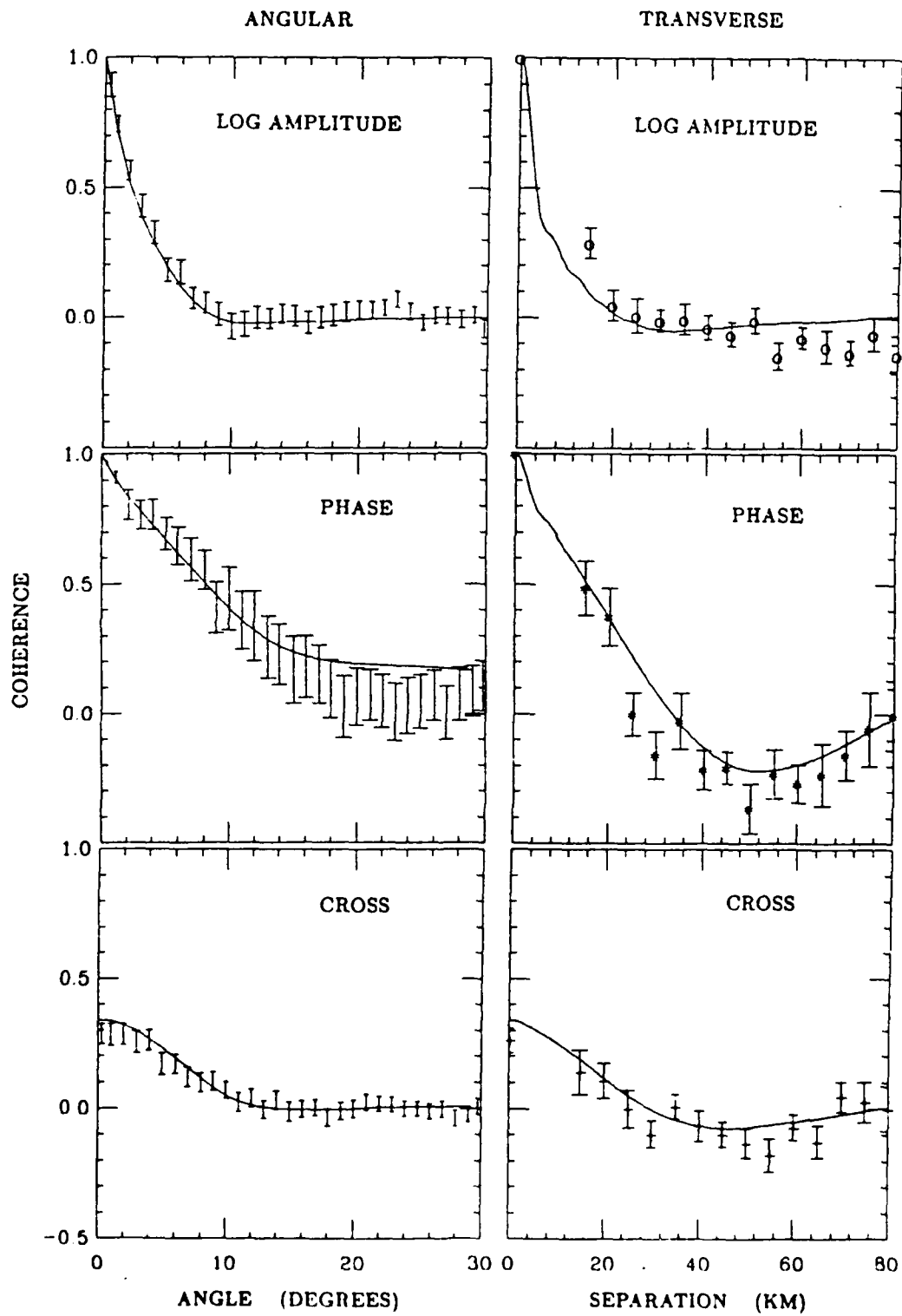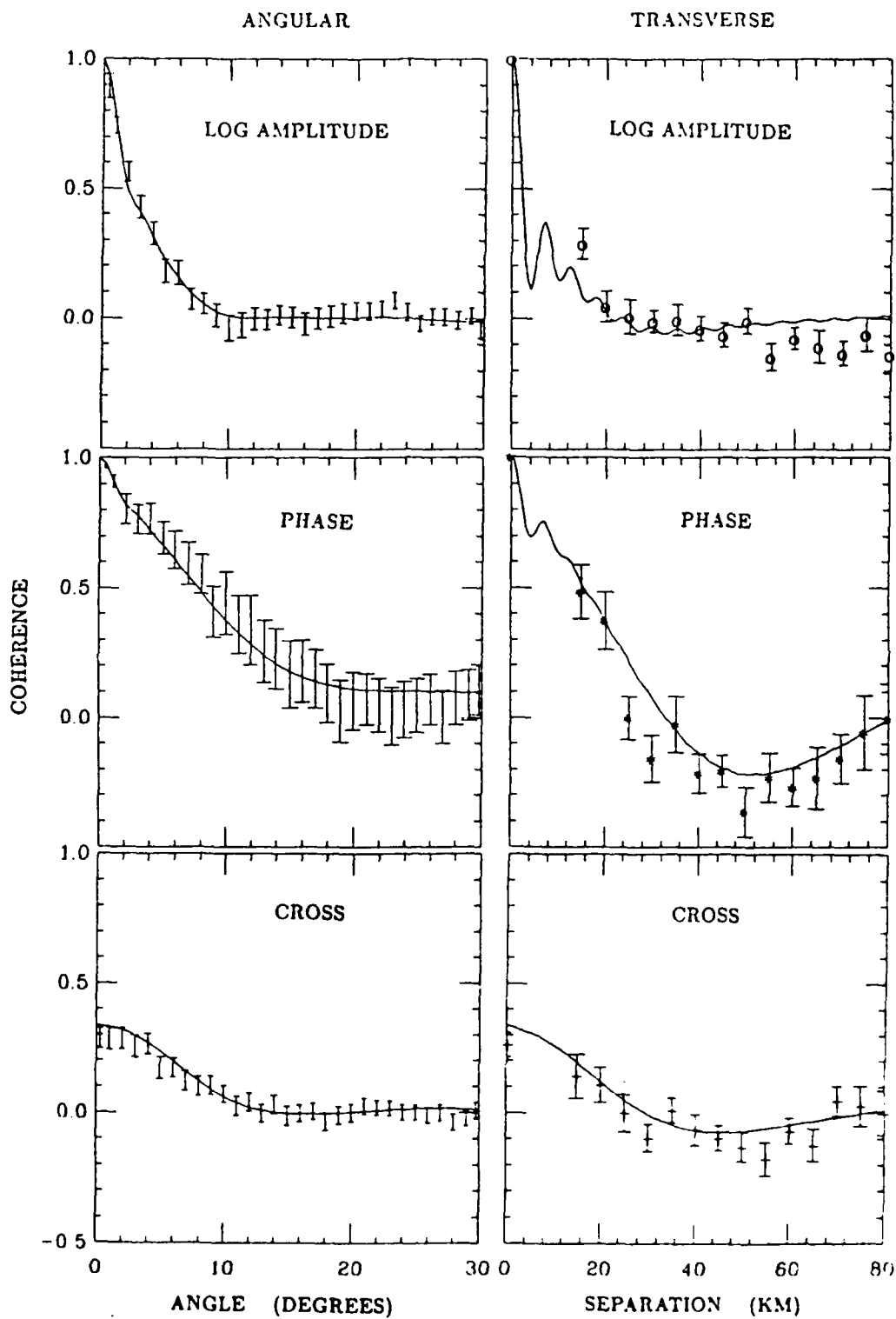
Figure 3

Q as a Function of Depth Beneath a Tectonically Active Area

Stephen Grand and Xiao-Yang Ding, Department of Geology, University of Illinois
Urbana-Champaign, IL, USA 61801

Objective

Determining the Q of the earth as a function of depth as well as how it varies laterally is an important problem for remotely determining the yields of nuclear explosions. This study is an attempt to determine the relationship between Q and shear velocity in the upper mantle. There are several proven techniques for remotely sensing upper mantle shear structure. If Q can be related to mantle shear velocity anomalies, an estimate of the t* bias for just about any test site could be made by doing a relatively easy upper mantle shear structure study.

Research Accomplished

We have begun this study by analyzing S, SS, SSS and SSSS phases which have propagated up the East Pacific Rise and were recorded on WWSSN and CSN long-period stations in western North America. The events and stations used are shown in Fig. 1. Also in Fig. 1 is a map of shear velocity variation beneath the North American plate at a depth of about 185 km (taken from Grand (1987)). The paths of the data used here are all beneath ocean younger than 20 Ma or within the slow western part of North America. Der et al. (1982) studied Q variation beneath stations within the United States. They found the highest Q's beneath stations in the north central part of the country and the lowest beneath the south-western United States. The north-eastern United States and the rest of the western area showed intermediate attenuation. The range in t^*_α bias was on the order of .2 sec. We are encouraged by the correlation of the shear velocity in the low-velocity zone and the measurements of t* bias by Der et al.. Note, in particular, the intermediate shear velocities found beneath the eastern states and the northwest.

The paths of the data studied here sample the slowest mantle shown in Fig. 1. Parts of the propagation paths are south of the structure shown but the travel-times of the shear phases are similar to the times measured for paths further to the north. Thus we assume our data is sampling a shear velocity structure similar to that beneath the Basin and Range and thus a Q structure similar to the lowest Q structure within the United States. The approach we will take to determine the upper mantle Q for this structure is to model the relative amplitude decay of multiple bounce shear phases with similar raypaths through the mantle. Grand and Helmberger (1984) have modeled S and SS phases to determine upper mantle shear velocity structure. We will use their model TNA, appropriate for the western United States and the northern East Pacific Rise, as the velocity structure in this study. This model predicts a large S wave amplitude from 17.5° to 19.5° distance where an arrival from a strong gradient near 300 km depth constructively interferes with an arrival from the 400 km discontinuity. The same rays should cross for SS from 35° to 39°, for SSS from 52.5° to 58.5° and for SSSS from 70° to 78°. Fig. 2 shows a profile of data up the East Pacific Rise illustrating these phases. The S waves are aligned at zero time and are normalized in amplitude. The amplified arrival discussed above can be seen near the end of the seismogram at the appropriate distances. A double arrival is seen in SS from 48° to 52° and in SSS from 70° to 75°. This is the result of the triplication due to the 650 km discontinuity. We will concentrate here on the amplitude decay of the arrivals from above 400 km depth relative to the S waves bottoming in the lower mantle.

The sensitivity to Q in this study results from the very long travel-times in the shallow mantle of the multiple S phases. For instance, the amplified 300-400 km depth SSSS arrival at 74° has a travel-time of about 1900 sec. Small changes in Q in the upper 300 km result in large changes in t* for this arrival. Fig. 3 illustrates this point. Shown there are three Q models above and synthetics for the three models below. The solid line Q model is what we found to be appropriate for the young East Pacific and corresponds to the middle synthetic. Below 500 km, the PREM Q model of Dziewonski and Anderson (1981) was used. The synthetics are

computed using the WKBJ technique (Chapman, 1978). For each ray computed in the synthetic, the t^* for that ray is also computed and the appropriate Futterman operator was then convolved with the response due to that ray. In this figure the S waves are normalized in amplitude and aligned at zero time. Following S are SS, a double SSS arrival from the 650 km discontinuity and the amplified SSSS arrival from 300 km depth. The t^* for the SSSS 300 km arrival varies from 10 sec for the high Q model to 21 sec for the middle model to 38 sec for the low Q model. Note the large change in the SSSS relative amplitude. These kind of amplitude changes in SSSS are easily distinguished in the data. For reference, if we use the relation $t^*_\beta = 4t^*_\alpha$ (Burdick, 1978), we can compute the Δt^*_α bias for one-way teleseismic propagation through the three models. Taking the high Q model as o, the second model predicts a Δt^*_α of .16 sec and the third .26 sec for one-way propagation at 60° distance.

The solid line Q model in Fig. 3 does a good job of fitting the multiple S amplitudes. Fig. 4 shows a comparison of synthetics and data using the TNA velocity model and the middle Q model of Fig. 3. The amplified 300 km depth arrival corresponds to the SS phase in the first two records, the SSS phase in the middle two and the SSSS phase for the last two. The amplitudes shown here are similar to those for many other seismograms from the same area, some of which are shown in Fig. 2. Our model has a Q of 60 from 40 to 150 km depth and reaches 150 below 300 km depth. Over broad tectonically active areas, it is not possible to have Q's below 50 distributed over more than a 100 km depth. If this were the case, the SSSS phases shown here would have far lower amplitudes than observed.

Conclusions

We have derived an upper mantle Q model appropriate for tectonically active areas. Using this model and the relation $t^*_\beta = 4t^*_\alpha$ we can estimate Δt^*_α biases due to the upper mantle variations associated with different tectonic provinces. The high Q model in Fig. 3 may be appropriate for shield regions if Q variations are limited to the seismic lithosphere ie. above 170 km depth. The Δt^*_α bias would then be .16 sec between shield and tectonic areas. A maximum bias estimate can be made by assuming shield Q's are infinite to 375 km depth, the depth to which velocity variations persist. The bias for this extreme model is only .28 sec. We conclude that the tectonic environment Δt^*_α bias between active and stable areas is probably .2 to .25 sec, in good agreement with Der et al. (1982). Larger t^* biases must be due to lower mantle Q heterogeneity or to extremely anomalous shallow low Q structure not generally associated with tectonically active areas.

References

Burdick, L. J., 1976. t^* for S waves with a continental path, Bull. Seism. Soc. Am., 68, pp. 1013-1030.

Chapman, C. H., 1978. A new method for computing synthetic seismograms, Geophys. J. R. astr. Soc., 54, pp. 481-518.

Der, Z. A., T. W. McElfresh and A. O'Donnell, 1982. An investigation of the regional variations and frequency dependence of anelastic attenuation in the mantle under the United States in the 0.5-4 Hz band, Geophys. J. R. astr. Soc., 69, pp. 67-99.

Dziewonski, A. M. and D. L. Anderson, 1981, Preliminary reference earth model, Phys. Earth Planet. Phys., 25, pp. 297-356.

Grand, S. P., 1987. Tomographic inversion for shear velocity beneath the North American plate, submitted to J. Geophys. Res..

Grand, S. P. and D. V. Helmberger, 1984. Upper mantle shear structure of North America, Geophys. J. R. astr. Soc., 76, pp. 399-438.

Depth= 140 to 235 km

-3.0 %   3.0 %
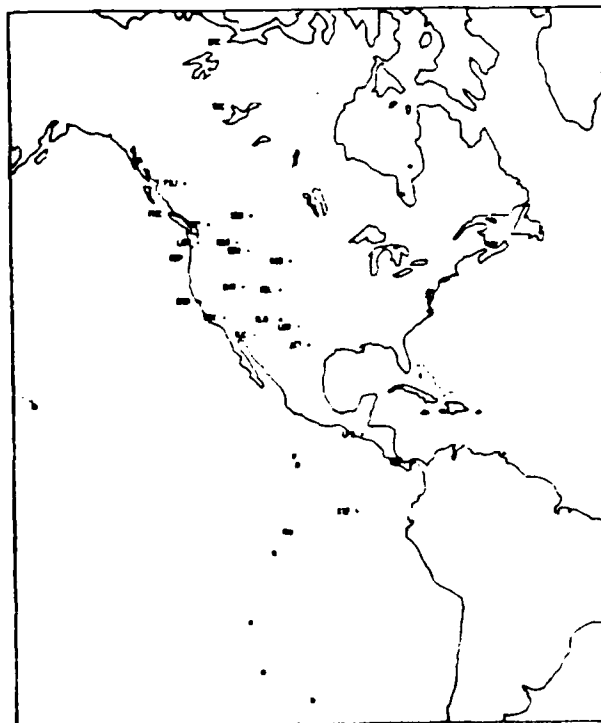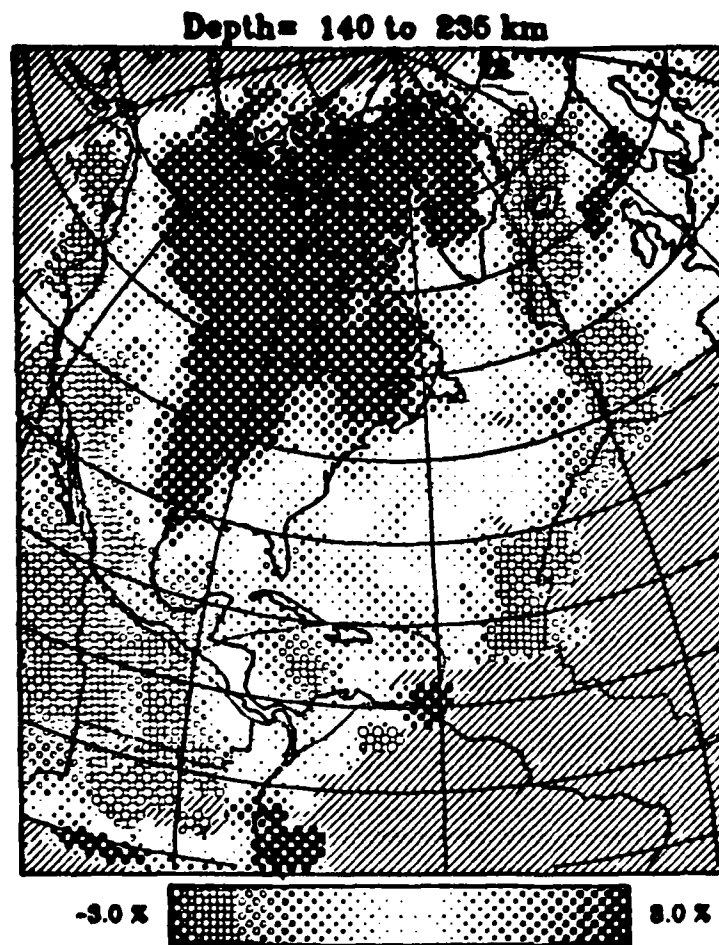
Figure 1. The upper panel shows the variation of shear velocity for a layer from 140 to 235 km depth derived by a tomographic inversion of shear phase travel-times. The scale is shown below in terms of percentage change in velocity and the slanted line areas indicate little or no resolution. The lower map shows the location of earthquakes (stars along the East Pacific Rise) and the stations, which are labeled, used in this study.
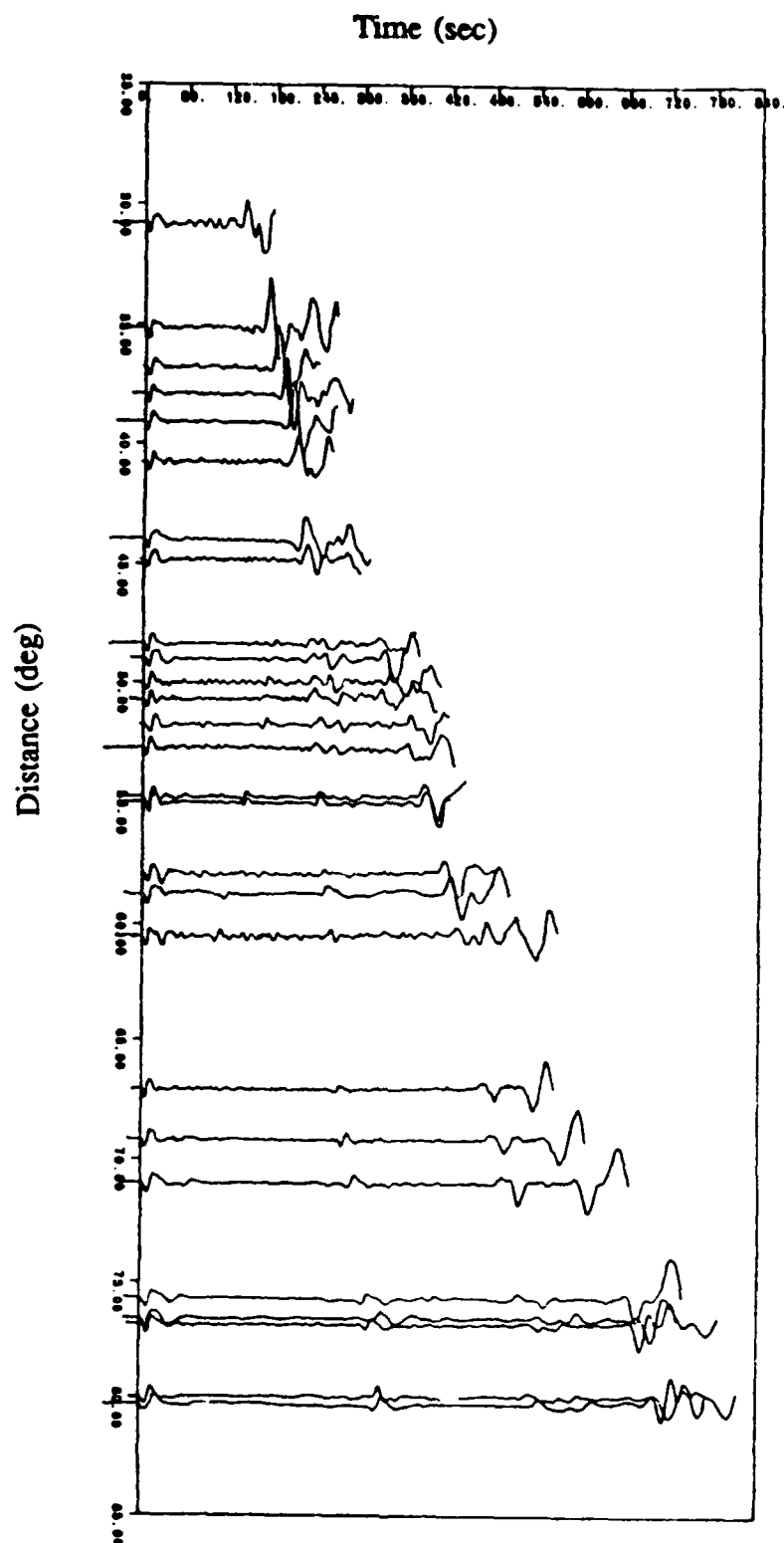
Figure 2. A profile of data which has propagated up the East Pacific Rise is shown. The S waves are aligned at zero time and normalized in amplitude. From 30° to 45° only S, SS and the beginning of the Love wave are apparent. Beyond 48°, the upper mantle SSS wave can be followed reaching a maximum amplitude between 55° and 58°. SSSS is visible beyond 65° as a large downswing following SSS. Note the effect of the $\frac{\pi}{2}$ phase shift for each bounce. SSS and SSSS have a π phase shift relative to S and SS respectively.

Q
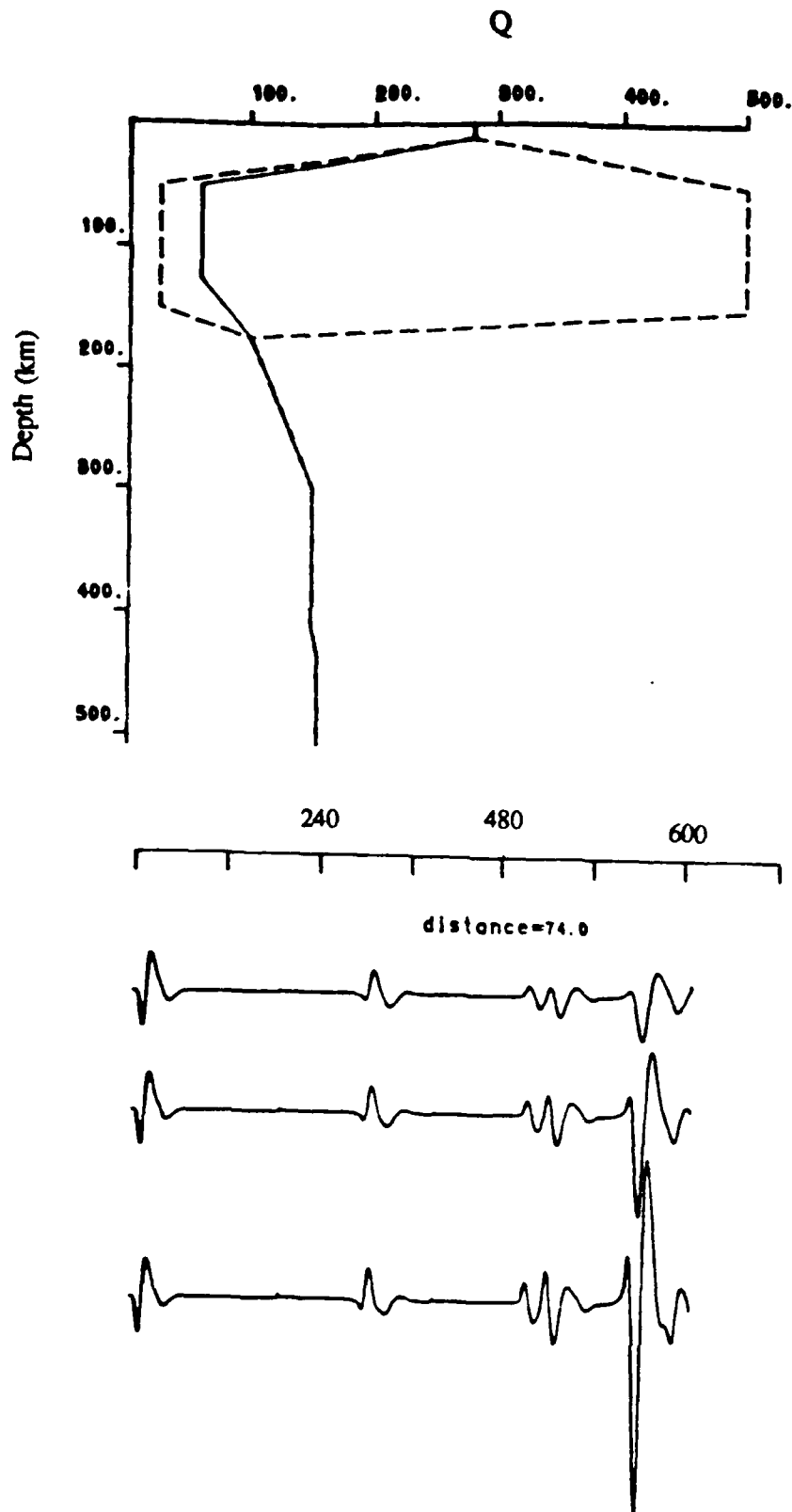
Figure 3. The upper part of the figure shows three Q models. The solid line represents a model which fits the amplitudes of the multiple bounce shear phases shown in Fig. 2. Synthetics for a distance of 74° are shown below computed with identical velocity models but with the three Q models shown above. The upper synthetic corresponds to the low Q model and the lower synthetic to the high Q model. The S waves are normalized in amplitude and are followed sequentially by SS, SSS and SSSS. Relative to S, the SSSS phase changes dramatically in amplitude depending on the shallow Q structure. Note that the SS and SSS waves are not very sensitive to the changes in Q shown above.

83

Time (sec)
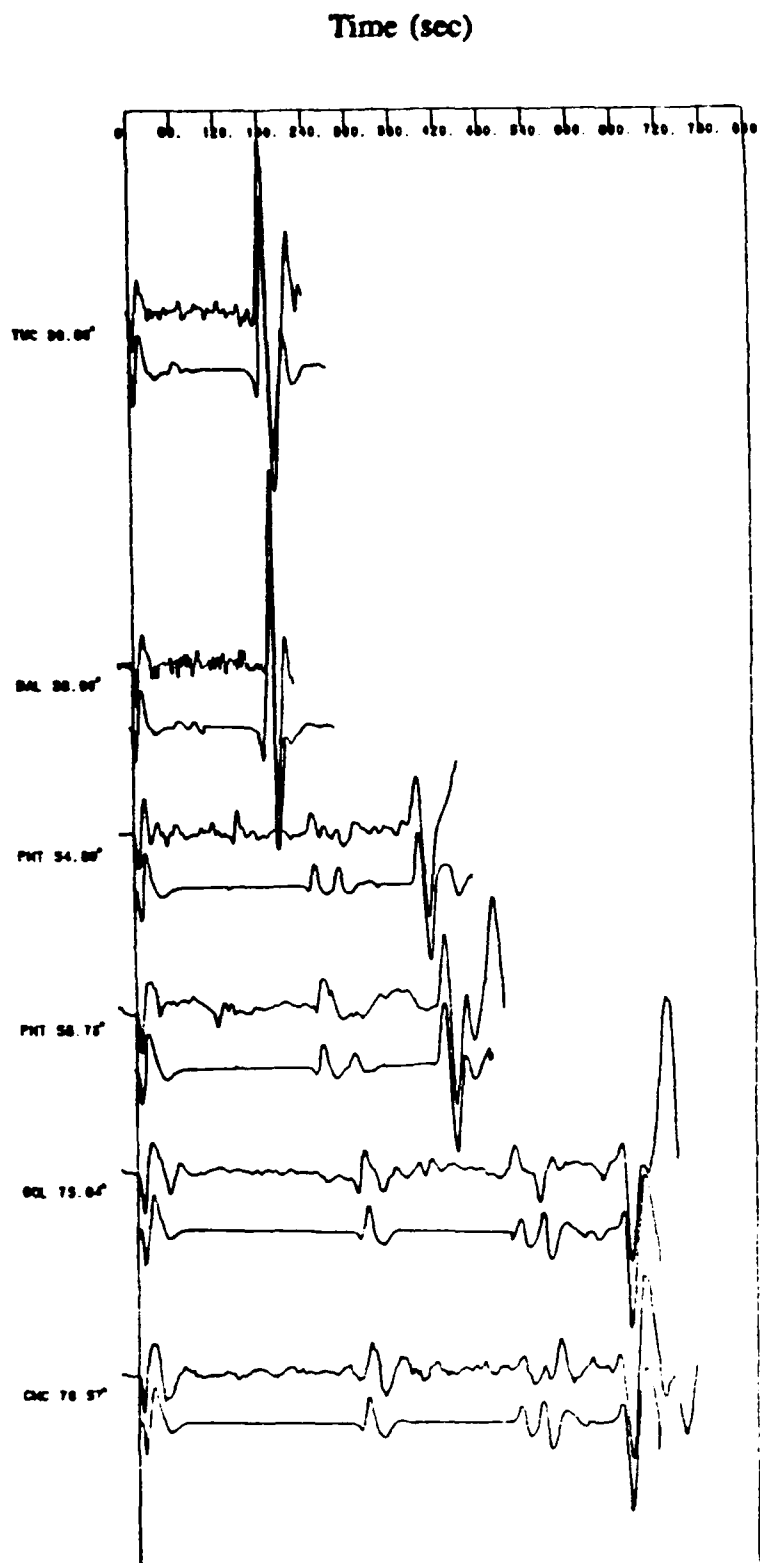
Figure 4. Data and synthetics (beneath the data) are compared using the middle Q model in Fig. 3. The seismograms were chosen to illustrate the amplified 300 km depth arrival which appears as SS in the upper two records, SSS in the middle two and SSSS in the lower two. The distances of the seismograms are indicated at the side with the station which recorded the data. Note the excellent fit of the 300 km arrival from SS through SSSS. The worst agreement is for SSS at 75° and 76°. This may be due to errors in the velocity model near 650 km depth.

81

ON REPRESENTING SURFACE WAVE PROPAGATION IN LATERALLY VARYING MEDIA BY TRUNCATED MODAL EXPANSIONS

B.L.N. Kennett
Research School of Earth Sciences, Australian National University
G.P.O. Box 4, Canberra A.C.T. 2601
Australia

OBJECTIVE

The aim of this work is to develop techniques for handling guided wave propagation in three-dimensionally heterogeneous media, especially for Lg waves, in order to improve the understanding of the nature of regional seismic phases and the way in which the characteristics of the seismic source can be modified by propagation to the receiver.

A good description of the general character of the seismic wavefield at regional distances is obtained by using a horizontally stratified earth model and computing synthetic seismograms for the phases of interest. These construction techniques depend on the independent propagation of plane wave components in media with no horizontal change in properties. As a result, the response of the medium to excitation by an earthquake or explosive source can be constructed in the frequency/wavenumber domain. Theoretical seismograms can then be constructed by numerical integration with the inclusion of appropriate horizontal phase factors.

Once the properties of the earth model vary horizontally as well as with depth, as happens in the real Earth, the simplicity of this construction scheme is lost. Although it is still possible to make a description of the wave propagation process in the frequency/wavenumber domain there is now coupling between different wavenumber components induced by the presence of horizontal heterogeneity (Kennett 1972,1986). A direct numerical scheme based on this procedure is possible but is computationally very intensive, and currently only suitable for small distances away from the source, around 50 km for 1 Hz dominant frequency (Haines 1987).

However, most of the regional phases of interest for nuclear discrimination problems are observed after propagation through considerable distances. These phases are mostly guided through the crust and uppermost mantle, which from a variety of studies are known to be regions with very considerable horizontal variability in properties.

What is therefore needed are schemes which allow the tracking of guided seismic wave propagation through a horizontally heterogeneous crust for distances up to 1000 km or more. Such methods should be able to be used with three-dimensional variations in seismic properties superimposed on the normal increase in seismic wave velocities with depth. A suitable candidate is the coupled mode scheme described by Kennett (1984) which has already been used with some success in understanding the characteristics of Lg wave behaviour (Kennett & Mykkeltveit 1984).

RESEARCH ACCOMPLISHED

Attention has so far been concentrated on testing the limitations of the Kennett (1984) calculation scheme and in assessing suitable approximations to improve computational performance.

The technique depends on representing the seismic displacement and traction fields within a laterally heterogeneous medium, at a single frequency, as a sum of contributions from the modal eigenfunctions of a reference structure, with coefficients which vary with position. The evolution of these modal expansion coefficient terms can be described by a set of coupled partial differential equations in the horizontal coordinates. When the medium is two-dimensional, the calculations can be recast as the solution of non-linear differential

equations for the reflection and transmission matrices connecting the modal expansion coefficients at different positions. The advantage of this rearrangement is that, for each frequency, the boundary conditions on the differential equations are simplified for a generally heterogeneous medium.

If we adopt a reference medium which does not vary with horizontal position, the individual mode contributions propagate independently in that structure. However, once the properties of the true medium differ from the reference, the independence of modal propagation is lost. The effect of the heterogeneity enters into the differential equations for the modal expansion coefficients via a coupling matrix whose dimensions are dictated by the number of modes included in the calculation.

The choice of the number of modes is of considerable importance, all the significant wavenumber components for the seismic phase of interest should be included, as well as an allowance for steeper angles of propagation than would be present in the reference medium, in order to allow for scattering effects. The demands of computation are that the number of modes should be kept as small as possible, since the computation time depends on the square of the number of modes. On the other hand if the truncation is too tight, a poor representation of the displacement field can ensue and the results are of limited use.
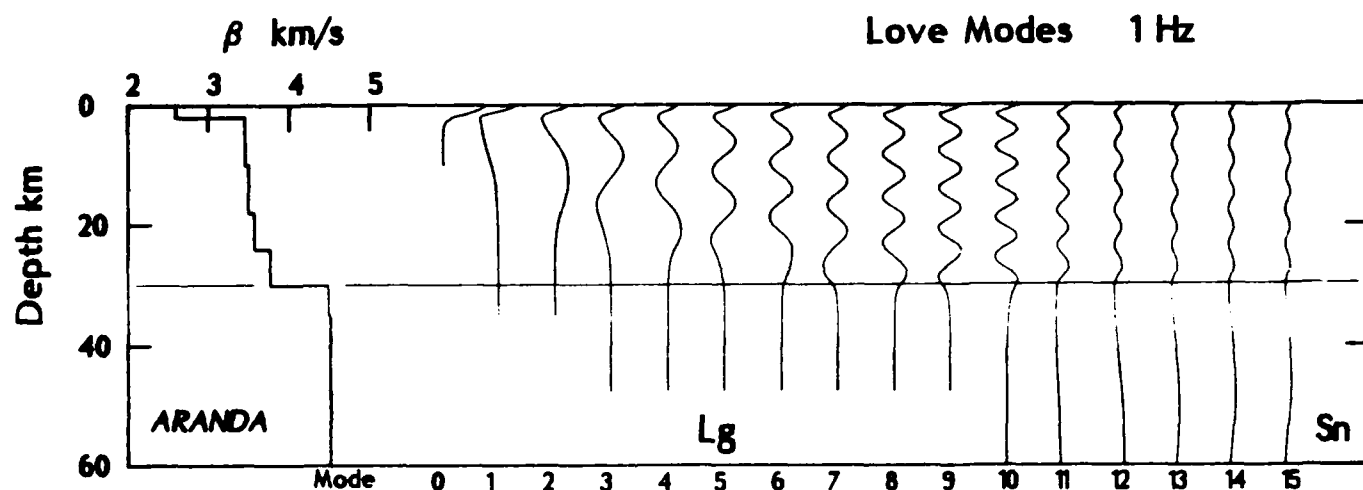
Figure 1: ARANDA reference model and Love mode eigenfunctions with phase velocity less than 4.54 km/s at frequency 1 Hz.

In figure 1 we illustrate the reference model (ARANDA) used for Lg mode calculations, and the modal eigenfunctions for the 15 Love modes included in calculations at 1 Hz. The cut-off criterion was based on the effective depth of penetration of the modes. The fundamental mode and first 9 higher modes are confined to the crust, and are the main contributors to Lg. Mode 10 begins to have significant displacement in the mantle, and the remaining modes carry their main energy in the mantle and represent the Sn phase. The truncation is made at a phase velocity of 4.54 km/s, corresponding in this model to a penetration depth of about 100 km. Features in the wave propagation process corresponding to higher phase velocities than 4.54 km/s cannot be represented by this coupled mode calculation.

As a result, the approach is well suited to heterogeneous models where the behaviour consists of relatively random variations about the properties of the reference model (see e.g. fig 2). In this case, a single incident mode will interact with a limited number of neighbouring modes so that the coupling matrix is diagonal dominated with a limited effective bandwidth (cf fig 3).

Significant perturbations of the major interfaces in the model lead to much more extensive coupling between modes and can induce relatively steep angles of propagation. If such features are required in the models to be considered, then a broad sweep of modes must be taken for the reference model (for the Lg case at 1 Hz, at least 20). With the benefit of hindsight, it would appear that the calculations of Kennett & Mykkeltveit (1984) on the influence of graben structures lie at the limit of acceptable model variations for the modal set adopted.
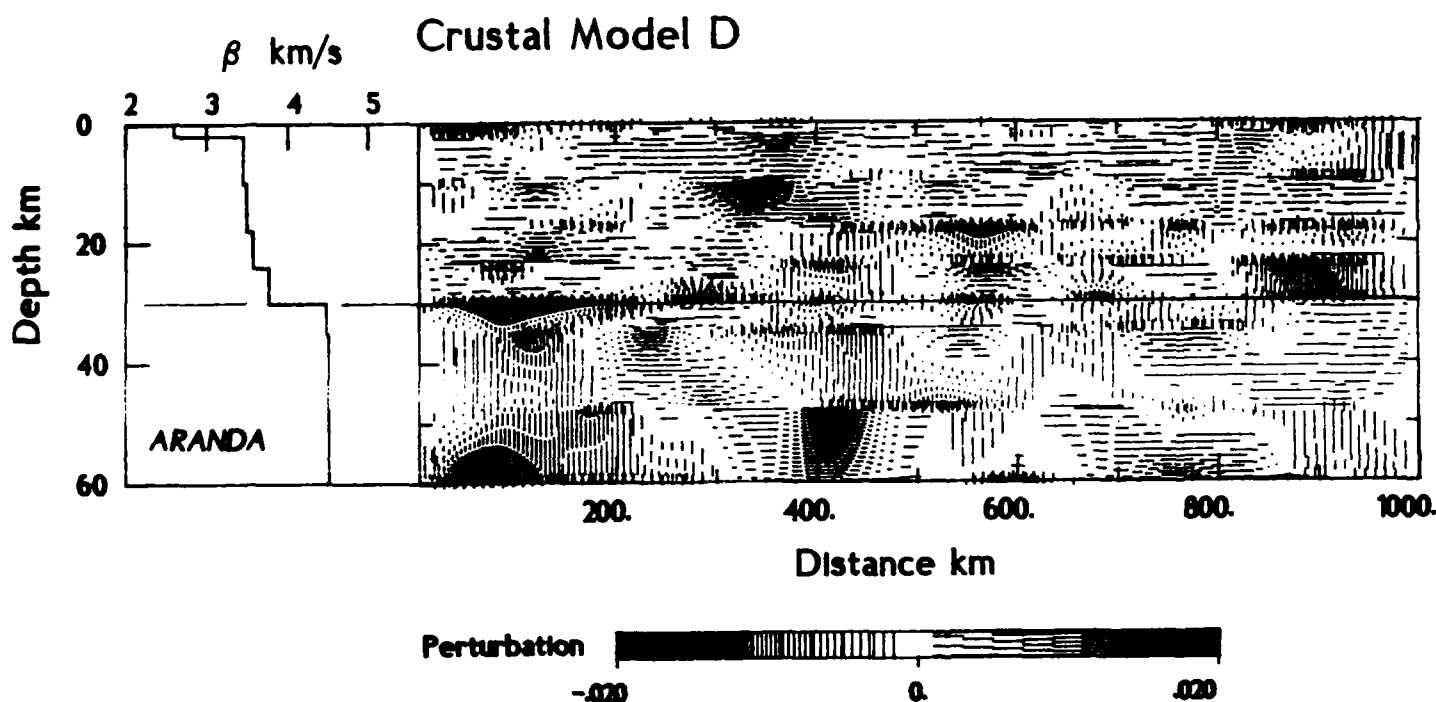
Figure 2: ARANDA reference model and shaded contour plot of perturbations for model D used for Lg wave transmission studies.

In figure 2 we show a two-dimensional test model constructed to examine the frequency dependence of the mode-coupling for Lg waves. This figure shows the ARANDA reference model, and a shaded contour map representation of the perturbations in seismic velocity about the reference. Vertical shading indicates slower velocities and horizontal shading higher velocities, up to a maximum of 2 per cent variation. The horizontal scale of variation is on the order of 100 km so that there is no sharp variation in properties. As a result, reflected waves are relatively unimportant. Tests are underway to establish the conditions under which such reflected waves can be neglected, which would give substantial computational savings.

Crustal Model D   1 Hz

Transmission

Mode No

0 1 2 3 4 5 6 7 8 9 10 11 12 13 14 15

0
1
2
3
4
5
6
7
8
9
10
11
12
13
14
15

0 10 20 30 40 50 60 70 80 90 100
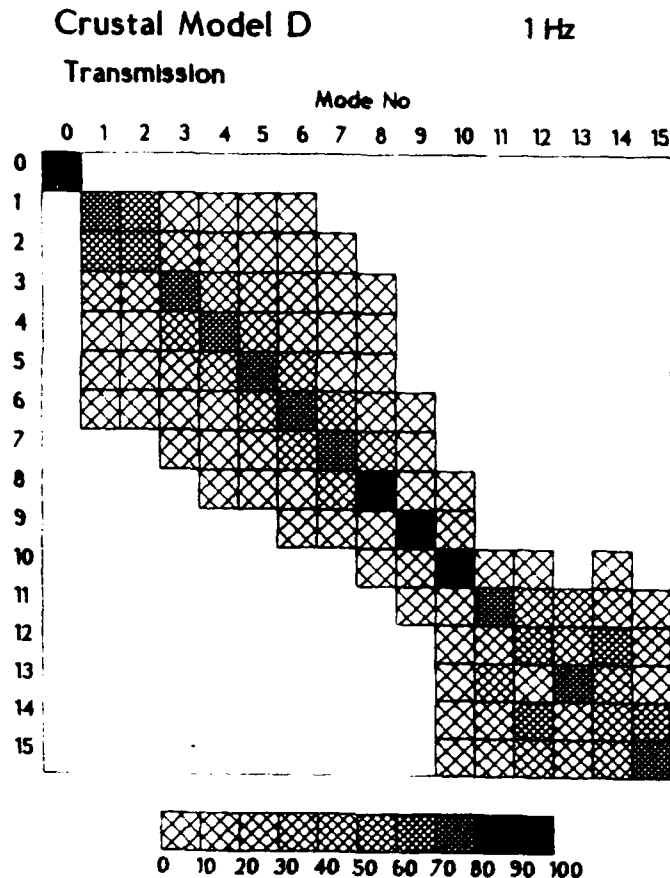
Figure 3: Representation of the transmission matrix for the modes of Fig 1 after passage through 1000 km of model D. Amplitude values less than 1 are left blank.

After passage through 1000 km of such a heterogeneous structure, the energy originally in an incident mode is no longer confined to that particlar mode. In figure 3 we show the transmission matrix for the mode set in fig 1, after passage through the model in fig 2. Each column of the matrix corresponds to the incidence of a single mode of amplitude 100 at 0 km. We see that the behaviour is diagonal dominated, but that significant mode conversions can occur. For the Lg type modes the bandwidth for significant interaction is typically ± 2 modes. The strong interaction of modes 1 and 2 arises because of their similar shape in the top 10 km. For the Sn modes the eigenfunctions are very similar and there is strong interaction due to mantle perturbation extending to 200 km (the lower portion is not shown in fig 2). However the separation from the Lg modes is striking; there is very little interaction except for mode 10 which shares some of the characteristics of each group.

We should note that even for the moderately heterogeneous model D (fig 2) there has been a significant modification of the distribution of energy between modes after passage through 1000 km of structure. Such modifications over a band of frequencies will lead to theoretical seismograms which will differ from the predictions for the horizontally stratified reference model.

As the frequency increases the number of modes need to cover the smae phase velocity range increases, which causes some problems in combining the results from different frequencies. The increased size of the differenti l equation system also means an increase in computation time as the square of the number of modes if all mode interactions have to

be considered. Fortunately, present tests indicate that for the same model the bandwidthnof interaction increases only slowly with frequency. For the Lg waves propagating through models similar to that shown in fig 2, computations can be restructed to a band of 3 modes either side of the target mode without appreciable error. At 1.5 Hz with 21 modes included, this bandwidth restriction has the effect of reducing computation tin.. by nearly a factor of three.

CONCLUSIONS AND RECOMMENDATIONS

The current research effort has been directed towards determining the numerical characteristics of the Kennett (1984) mode-coupling scheme for guided wave propagation over extended distances at frequencies of 1 Hz and above. The existing models are two-dimensional and calculations are carried out for one frequency at a time.

The next phase of work will be directed towards using the experience from the two-dimensional models to design a computational scheme for mode-coupling in three-dimensions for both Love and Rayleigh waves. This schem will take advantage of approximations such as limited bandwidth of interaction to reduce total computatic n time. We will also pursue the problem of generating effective and consistent theoretical seismograms by combing mode-coupling results from a number of frequencies.

This approach to the calculation of guided wave propagation has the potential r¬ enable the character of Lg wave propagation to be determined for classes of model which cai.not easily be treated by other means . This should allow an assessment of structural effects on regional phase propagation which will be complementary to existing techniques using horizontally stratified models.

REFERENCES

Haines A.J. (1987) Synthetic seismogram calculation in laterally varying media using wavenumber coupling (in preparation)

Kennett B.L.N. (1972) Seismic waves in laterally inhomogeneous media, *Geophys J R astr Soc*, **27**, 301-325

Kennett B.L.N. (1984) Guided wave propagation in laterally varying media - I. Theoretical development, *Geophys J R astr Soc* , **79**, 235-255

Kennett B.L.N. (1986) Wavenumber and wavetype coupling in laterally heterogeneous media, *Geophys J R astr Soc* , **87**, 313-331

Kennett B.L..N. & Mykkeltveit S. (1984) Guided wave propagation in laterally varying media - II Lg wave in northwestern Europe, *Geophys J R astr Soc*, **79**, 257-267

SEISMIC ATTENUATION AND YIELD ESTIMATES:
NEW RESULTS USING THE Lg PHASE

by
Brian J. Mitchell, Jia-Kang Xie, and Otto W. Nuttli
Department of Earth and Atmospheric Sciences
Saint Louis University

OBJECTIVE

The objective of this research is to refine a methodology for determining the yields of nuclear events using the Lg phase and to study the factors which influence those yield determinations. One of the more important factors which influence yield determinations from Lg waves is seismic absorption (or Q^{-1}). It is known to vary from region to region and also to vary with frequency; the degree of frequency dependence also varies regionally. We therefore have attempted to study crustal Q to see how it and its frequency dependence vary for various type regions which include both stable shields and areas which have undergone relatively recent tectonic activity.

We also wish to compare various methods of determining Q and its frequency dependence for Lg waves, using 1) the coda-Q method, 2) a spectral-ratio method, and 3) the decrease of amplitude with increasing distance. These methods are applied to data from southern Africa.

Finally, we wish to determine $m_b(Lg)$ values for a set of Novaya Zemlya explosions, ranging in $m_b(P)$ value from 4.2 to 6.9.

RESEARCH ACCOMPLISHED

Seismic surface waves at intermediate periods (5-100 s) have been used to study the anelastic properties of the crust and upper mantle in several regions. Observed attenuation coefficients are inverted to yield shear-wave Q values as a function of depth. Stochastic inversion methods which have commonly been used to obtain the Q^{-1} models usually produce models with very high Q values at large depths. This result occurs because the inversion for Q^{-1} is a linear process in which the starting model for Q^{-1} is assumed to be 0 at all depths. Consequently, in depth intervals where resolving power is low, the Q^{-1} values tend to remain close to the low values of the starting model. This problem has been avoided in recent inversions by using a differential inversion process in which differences in Q^{-1} between adjacent layers are minimized (Russell, 1987). Models resulting from the new inversion process are characterized by higher values of Q^{-1}, or lower Q values, through the lower crust and upper mantle than those which were found earlier. A summary of the new models, from Hwang and Mitchell (1987), appear in Figure 1. As found previously, shear wave Q values are much lower beneath tectonically active areas than beneath stable regions. All regions exhibit Q values which are lower in the crust and upper mantle than in the upper crust. Models for the stable portions of North America and South America achieve minimum shear-wave Q values of about 120 whereas those for the tectonically active portions of the continents, as well as the Himalaya, are about 40. Q values for the Indian shield lie in an intermediate range. The low-Q values in the lower crust and upper mantle can have a significant effect on the attenuation of Lg at 1 Hz,

and thus yield determination, at regional distances. If the low Q values in the Himalaya are neglected, for instance, velocity and Q models for that region produce synthetic Lg wave trains which lead to attenuation coefficient values which are 5% or more lower than those for a model which includes the low-Q values.

The coda-Q method was applied to the analog WWSSN stations in South Africa, namely BUL, GRM, PRE and WIN, using as data source earthquakes in southern Africa. These data by themselves gave ambiguous results, namely different possible combinations of Q_0 and the frequency exponent. However, when a spectral ratio method, using the spectra of equal time intervals but of different lapse time in the coda, was applied to digital data from stations BUL and SLR, stable values of Q_0 were obtained. This allows the frequency exponent to be determined from the coda-Q values. For the earthquakes and stations considered the frequency exponent was found to be 0.4, and the Q_0 values varied from 430 to 740 for various earthquake to station paths. The smallest values were observed for station GRM, on the southern coast of the continent. For all other stations the values of Q_0 were 600 or greater, values typical of shield regions.

Chow *et al.* (1980) determined Q_0 vallues in southern Africa using the fall-off of Lg amplitudes with distance in the range of 0° to 30°, using the data of 575 shallow earthquakes recorded by a Rhodesian seismograph network. They obtained an average Q_0 value of 603 ± 50 for propagation paths that lie along and across the East African rift system.

Values of $m_b(Lg)$ were determined for 29 Novaya Zemlya explosions, from 18 September 1964 to 25 September 1983, and of ISC $m_b(P)$ values ranging from 4.2 to 6.9. The necessary data were obtained from film copies of the WWSSN stations at Copenhagen, Kevo, Kingsbay, Kongsberg, Nurmijarvi, Stuttgart and Umea.

Preliminary estimates of the 1-Hz Q values of Lg waves, and of the frequency dependence of Q, were obtained by measuring the change in wave frequency with increasing time in the Lg coda. The Q_0 values obtained in this way for the paths from Novaya Zemlya to the stations are: COP (628 ± 39), KEV (259 ± 14), KBS (316 ± 23), KON (490 ± 43), NUR (420 ± 22), STU (488 ± 17), UME (437 ± 17). Station corrections were then determined using $m_b(Lg)$ values of events recorded by at least 5 of the 7 stations and on 70-mm microfilm. This resulted in revised Q_0 values of: COP (633), KEV (252), KBS (315), KON (496), NUR (420), STU (531), UME (391). The final Q_0 values for only STU and UME fall outside the original mean ± 1 S.D. values.

Only 4 of the 29 explosions were located in the southern part of Novaya Zemlya. No large difference in Q_0 values for the two test site areas could be observed for the stations used in the study, which varied in epicentral distance between 1000 km (KEV) and 3500 km (STU).

The linear least-squares relation between $m_b(Lg)$ and $m_b(P)$ was found to be

$$m_b(Lg) = (0.586 \pm 0.166) + (0.921 \pm 0.028) \, m_b(P)$$

where ISC values of $m_b(P)$, given only to the nearest tenth of a unit, were used. Explosions for which data of fewer than 4 stations were usable, of explosions of

which the standard deviation of $m_b(Lg)$ exceeded 0.15 units, and of explosions after 1977 for which the copies of the WWSSN seismograms are on microfiche, were given only one-half weight. The $m_b(Lg)$ values estimated from microfiche copies likely are minimum values, as the poor quality of the copy makes it difficult to see the turning points of the maximum amplitude Lg waves.

If a slope of unity is assumed between $m_b(Lg)$ and $m_b(P)$,

$$(m_b(P) - m_b(Lg))_{average} = -0.11 \pm 0.02$$

This suggests an $m_b(P)$ bias of 0.20 units between NTS and Novaya Zemlya, if the Lg-wave coupling is the same in the two areas. The $\pm$ 0.02 is the standard error of the mean.

The largest explosions occurred on 12 September 1973 ($m_b(P)$ = 6.8) and 27 October 1973 ($m_b(P)$ = 6.9). Their $m_b(Lg)$ values were 6.89 $\pm$ 0.18 and 6.97 $\pm$ 0.20, respectively. The large standard deviations may result from the largest Lg amplitudes being off-scale at some of the stations. If that is the case, the $m_b(Lg)$ values for the two events will be larger than given above. Assuming that the NTS-obtained $m_b(Lg)$ versus yield relation applies (Nuttli, 1986), the quadratic form of the relation gives estimated yields of 3600 and 5100 kt for the two events. The linear NTS relation gives estimates of 2400 and 3000 kt, respectively. Dahlman and Israelson (1977) obtained estimates of 2700 kt and 3200 kt, respectively. By waveform correlation Burger et al. (1986) obtained estimated yields of 1402 and 1820 kt, respectively. Using $m_b(P)$, Sykes and Ruggi (1986) obtained 2099 and 4055 kt, respectively. Their M_S values give yields of 1569 and 2841 kt, respectively.

The largest Novaya Zemlya explosion since April 1976 was that of 18 August 1983, which had an estimated yield, using the linear NTS relation of Nuttli (1986), of 158 kt.

CONCLUSIONS AND RECOMMENDATIONS

New shear-wave Q models obtained from the inversion of attenuation coefficients of Rayleigh waves at intermediate periods lead to models which include low values of Q at lower crustal and upper mantle depths. Minimum upper mantle shear-wave Q values range from about 120 in stable regions to about 40 in tectonically active regions. The low Q values in the lower crust and upper mantle have a significant effect on the attenuation of 1-Hz Lg waves.

Three methods give similar results for the average anelastic attenuation of Lg waves across southern Africa. The results are given by $Q(f) = 600 \, f^{0.4}$ for frequencies of about 0.5 to 3 Hz. Future work should include an extension of the area studied to other parts of Africa.

The WWSSN station distribution for Novaya Zemlya explosions is better than that for NTS or East Kazakhstan. Therefore the resulting Q_0 and $m_b(Lg)$ values should be better determined for the former. The principal problems encountered were that the maximum Lg wave amplitudes may have gone off the seismograms for the very large explosions, and that the microfiche copies are of poor quality for reading short-period wave amplitudes. The $m_b(Lg)$ yield estimates of the two largest explosions are similar to those obtained by other

investigators using P-wave or surface-wave data.

REFERENCES

Burger, R.W., L.J. Burdick and T. Lay (1986), Estimating the relative yields of Novaya Zemlya tests by waveform intercorrelation, *Geophysical Journal, R.A.S., 87*, 775-800.

Chow, R.A.C., J.D. Fairhead, N.B. Henderson and P.D. Marshall (1980), Magnitude and Q determinations in southern Africa using Lg wave amplitudes, *Geophysical Journal, R.A.S., 63*, 735-745.

Dahlman, O. and H. Israelson (1977), *Monitoring Underground Nuclear Explosions*, Elsevier, New York.

Hwang, H.J. and B.J. Mitchell (1987), Shear velocities, Q_β, and the frequency dependence of Q_β in stable and tectonically active regions from surface wave observations, *Geophysical Journal, R.A.S.*, in press.

Nuttli, O.W. (1986), Yield estimates of Nevada Test Site explosions obtained from seismic Lg waves, *Journal of Geophysical Research, 91*, 2137-2151.

Russell, D.R. (1987), *Multi-Channel Processing of Dispersed Surface Waves*, Ph.D. Dissertation, Saint Louis University, 180 pp.

Sykes, L.R. and S. Ruggi (1986), Soviet underground testing inferences from seismic observations and historical perspective, *Nuclear Weapons Datebook, Natural Resources Defense Council*, Washington, D.C.
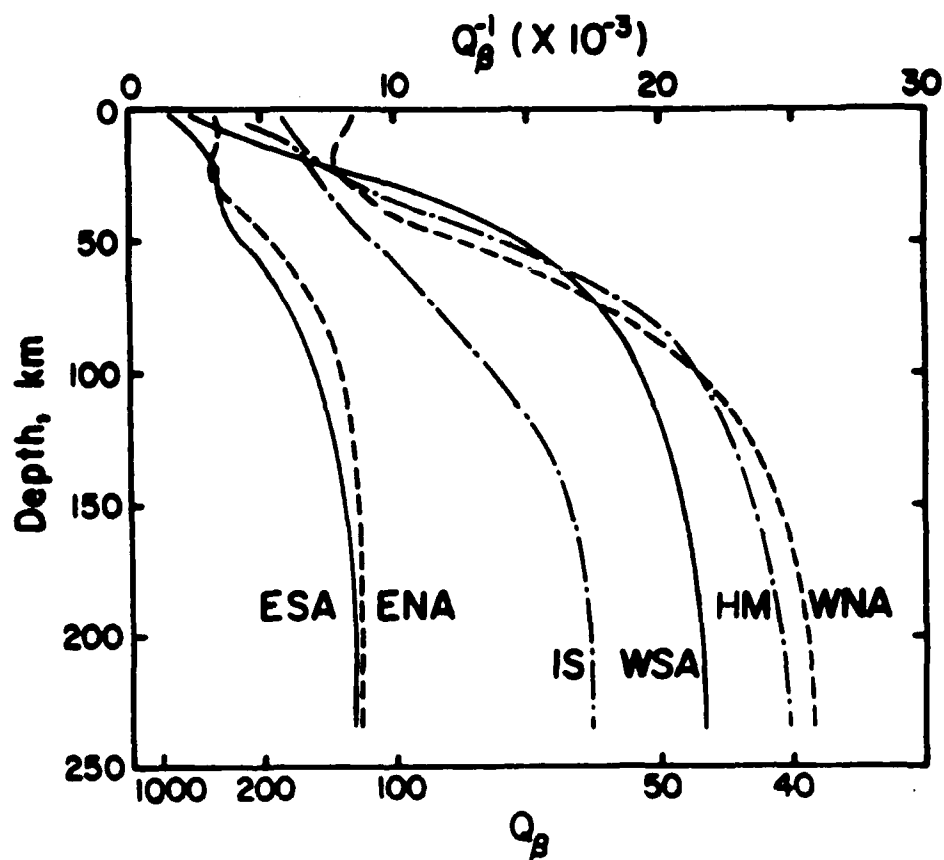
Figure 1. Shear-wave Q_β models obtained from the inversions of
surface-wave attenuation-coefficient values in eastern North
America (ENA), eastern South America (ESA), the Indian Shield
(IS), western North America (WNA), western South America (WSA),
and the Himalaya (HM).

Apparent Q of Pg and Lg in the Great Basin

David E. Chavez and Keith F. Priestley
Seismological Laboratory, University of Nevada, Reno, Nevada 89557

Objectives

Our current research is directed toward understanding in detail the generation and propagation of crustal phases in the Great Basin, in particular the phase L_g. L_g consists of a superposition of higher mode surface waves and because of its averaging properties in excitation and transmission, Nuttli (1986) has suggested that it can be used to accurately estimate the yield of nuclear explosions. However, as Nuttli has demonstrated, it is necessary to know the L_g attenuation to within 30% along the propagation path in order to estimate the yield to within 10%.

We are also examining the effects of structure on L_g propagation. L_g propagates in the continental crust but is disrupted at major structural boundaries and eliminated across even short oceanic paths. However it is not understood how secondary structures influence L_g propagation. We are examining L_g propagation along two Great Basin profiles, one across the structural grain, and one parallel to the structural grain (Fig. 1). The first consists of broad band digital recordings of three nuclear explosions along a 350 km long profile to the northwest of NTS. The second consists of broad band digital recordings of 20 Chalfant, California earthquakes from July, 1986. In addition, we are examining L_g propagation characteristics from an earthquake data set distributed around the Great Basin. The first profile provides a data set from a relatively uniform source (nuclear explosions) but with relatively large structural variations. The second profile provides data along a relatively homogeneous path. Because the earthquake sources are particularly well located, and because they span both a large depth (1-13 km) amd magnitude (M_L 3.0-5.5) range, we can examine the effects of the source on L_g excitation. The second earthquake data set allows us to evaluate how well regional phase propagation characteristics for a particular path can be estimated from a set of widely distributed earthquake recordings.

Research Accomplished

Figure 1 is a map showing the paths and source regions which we are currently studying. The profile striking NW (herein termed the NW path) is 300 km long and was instrumented to record the Nevada Test Site explosions Kinibito, Bodie, and Hardin. We have reported on preliminary attenuation results for the vertical component L_g phase using the Kinibito data (Chavez and Priestley, 1986). The NE striking profile is part of the northern Nevada PASSCAL experiment. Aftershocks of the July 1986 Chalfant, California earthquake were recorded along this path. In this paper we will address only those data recorded along the NW path.

In our 1986 analysis of the Kinibito data, we modeled the observed log-log L_g spectra as

$$\log_{10} A(f,R) + \log_{10} R^{0.5} = \log_{10} S(f) - \left| \frac{1.364 f}{Q(f)} \right| t \tag{1}$$

where $A(f,R)$ is the spectral amplitude observed at a distance R, f is frequency, t is the travel time, $S(f)$ is the source term, and Q is the quality factor. After correcting the spectral amplitudes for an assumed geometrical spreading term of 0.5, we fit least squares lines to the amplitude distance data for each frequency and solved for Q. We concluded that Q of vertical component L_g along the NW path could be represented by $Q(f) = 206 f^{0.68}$ for the frequency band $0.1 \leq f \leq 10.0$ Hz.

One drawback in using the above method to measure Q is that it is difficult to estimate the error in Q at each frequency. In order to do so, we have reprocessed our data using a moving window spectral analysis technique described by Butler *et al.* (1987). The data are windowed for many different group speeds using overlapping Gaussian functions whose widths are scaled by the epicentral distance in such a manner that the windows are identical with respect to group speed at each distance. The amplitude spectra for each window are then themselves Gaussian windowed at intervals of 0.25 Hz, and the windowed spectrum is integrated to yield amplitude as a function of group speed and frequency. Figure 2 is an example of results of this procedure. Representing seismic data in this manner provides a quantitative description of the frequency content of the signal as a function of time. The phases P_g and L_g are clearly visible as ridges in frequency-group speed space. The loss of high frequency energy in the coda is also apparent.

Once these data are corrected for geometrical spreading we can solve for Q as described above, only this time we obtain apparent attenuation *as a function of group speed as well as frequency*. The attenuation for a particular phase is determined by taking the average over the group speed window for that phase. The standard deviations obtained at each frequency are then a measure of the error in attenuation for that phase.

Before doing this type of analysis, it is neccesary to first address the question of the nature of geometrical spreading when using this technique. L_g is composed of higher mode surface waves which decay in the frequency domain as $R^{-0.5}$. However, the moving window spectral analysis method employs narrow time windows which individually do not contain the entire phase. If any energy at a particular frequency remains outside a given window, then the amplitude at that frequency and group speed will have an *apparent* geometrical spreading term greater than 0.5.

We have investigated the effect of moving window spectral analysis on geometrical spreading with an experiment using synthetic seismograms. L_g was synthesized at distances and azimuths corresponding to the stations along the NW path by summing the fundamental and first 25 Rayleigh wave modes for an attenuation-free Great Basin model (Priestley and Brune, 1978). The seismograms were then processed in the manner described above, and the amplitude versus distance data were used to determine apparent geometrical spreading as function of frequency and group speed. The results are plotted in Figure 3 which shows that geometrical spreading is fairly constant for those frequencies and group speeds for which there is signal. Figure 3 also shows the average apparent geometrical spreading at each frequency in the group speed window 3.7 to 3.0 km/sec., corresponding to L_g. It can be seen that the decay term is, for the most part, greater than 0.5, although there is some scatter.

The above experiment indicates that a geometrical spreading term of 0.6 is more appropriate than 0.5 at most frequencies, although at other frequencies terms in the range 0.4 to 0.8 are obtained. In order to determine how significant the scatter is, we processed the data recorded along the NW path assuming geometrical spreading terms of 0.0 to 1.2 in steps of 0.1 and solved for Q. Average Q at each frequency was obtained for L_g windows of 3.7 to 3.0 km/sec and P_g windows of 6.0 to 4.5 km/sec. The log-log Q versus f data were fit by least squares to give, for each spreading term, the function $Q(f) = Q_o f^a$ where Q_o is the Q at 1 Hz. Figure 4 summarizes the results. The frequency dependence terms obtained for vertical and transverse L_g vary little with assumed geometrical spreading, and the Q_o term becomes stable for spreading terms above 0.6. This suggests that (a) the apparent Q of both vertical and transverse L_g is frequency dependent, and (b) the scatter in spreading term about 0.6 evident in Figure 3 should not introduce any serious error.

Figure 4 also shows that P_g behaves differently than L_g with respect to assumed geometrical spreading. The frequency dependence term for this phase consistently decreases with increasing spreading while the Q_o term increases. However, if we assume that the actual Q of P_g behaves as $Q_o f^a$, then the linear correlation coefficients shown in Figure 4c indicate that an apparent geometrical spreading of less than 0.7 is required. We will eventually model the apparent spreading of P_g as we have done for L_g, however for the moment we shall assume that it is the same as found for L_g, namely 0.6.

Assuming an apparent geometrical spreading term of 0.6, we obtained Q along the NW path. Figure 5 shows the results for each frequency and group speed and averaged over windows corresponding to L_g and P_g. Vertical L_g has Q similar to both vertical P_g and transverse L_g for frequencies below about 1.5 Hz. Above that, vertical L_g Q is consistently greater than the others, except above 10 Hz, where both vertical and transverse L_g again have similar Q. There is a pronounced bump in all the plots at 2 to 3 Hz. Since this feature appears for all the phases considered, we suspect that it might be an artifact due

to recording site conditions. Finally, vertical L_g and vertical P_g both have Q independent of frequency for the range 4 to 9 Hz.

Conclusions and Recommendations

The moving window spectral analysis technique has been used to estimate apparent Q and appears to give useful results providing uncertainties in geometrical spreading can be resolved. We intend to model P_g geometrical spreading in a manner similar to what we have done for L_g, and also to apply time domain geometrical spreading corrections. The Q function which we obtained for the NW path using our earlier technique differs from that which we obtain here. This discrepancy must be investigated further.

References Cited

Butler, R., C.S. McCreery, L.N. Frazer, and D.A. Walker, 1987. High-frequency seismic attenuation of oceanic P and S waves in the western Pacific, *J. Geophys. Res.*, 92, 1383-1396.

Chavez, D.E. and K.F. Priestley, 1986. Measurment of frequency dependent L_g attenuation in the Great Basin, *Geophy. Res. Lett.*, 13, 551-554.

Nuttli, O.W., 1986. Yield estimates of Nevada Test Site explosions obtained from seismic L_g waves, *J. Geophys. Res.*, 91, 2137-2151.

Priestley, K.F and J.N. Brune, 1978. Surface waves and structure of the Great Basin of Nevada and western Utah, *J. Geophys. Res.*, 83, 2265-2272.
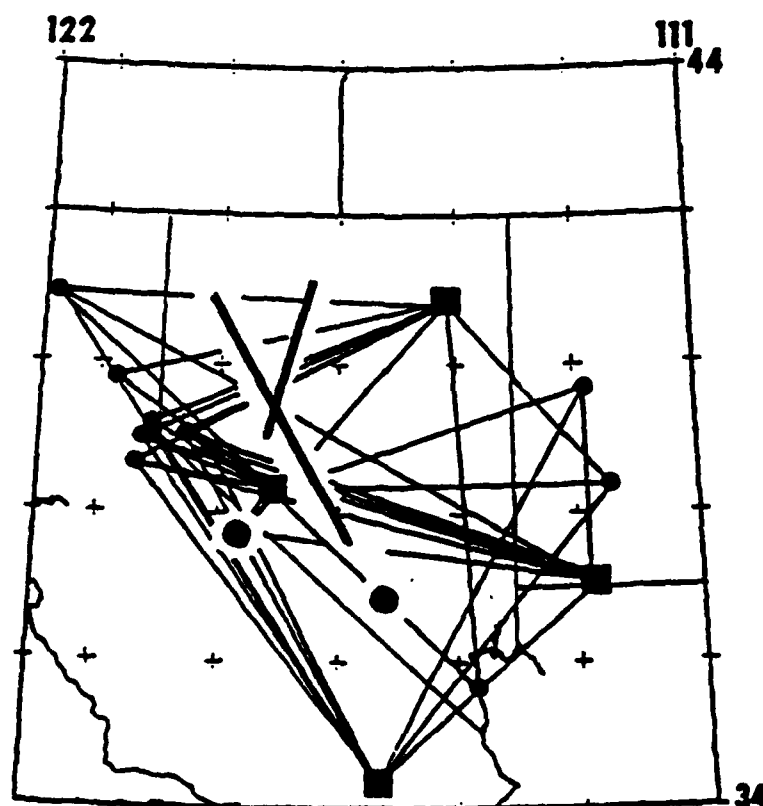
Figure 1. - Location Map showing data base
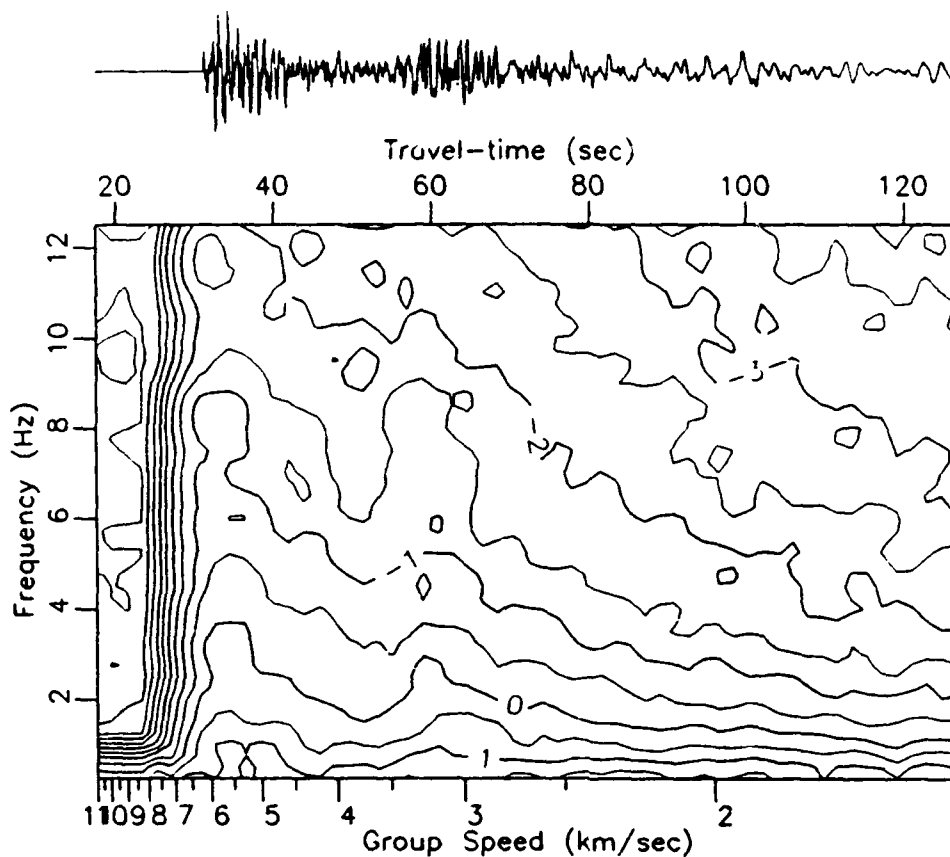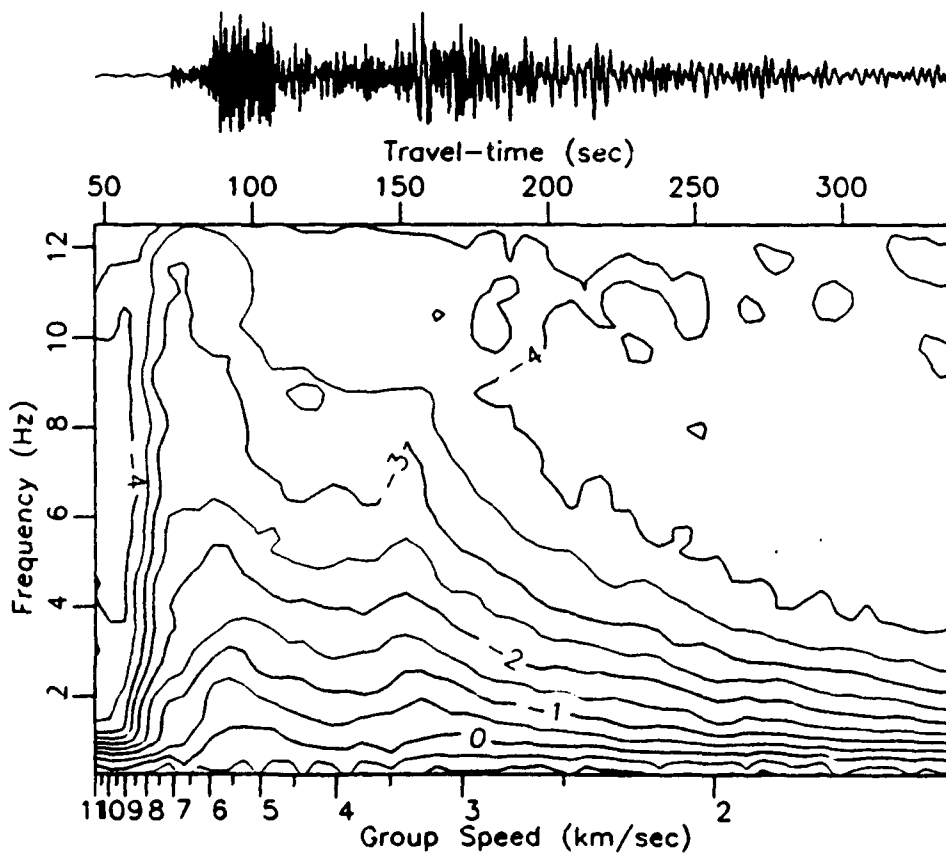
Figure 2   Examples of moving window spectra for the closest (top) and furthest (bottom) stations along the NW path in Figure 1. Contours are log ground amplitude in microns.

Figure 4 Effect of geometrical spreading on determination of Q(f) by applying the moving window spectra technique to the data recorded along the NW path. Arrows in (a) and (b) indicate the term solved for by fitting average log Q and log frequency values for group speed windows appropriate for the phases Lg and Pg. (c) is the linear correlation coefficient obtained from the least-squares fits.

Figure 3 Apparent geometrical spreading along the NW path determined by inverting synthetic data. Bottom figure is average apparent geometrical spreading for the indicated group speed window. The dashed line is at 0.5, the solid line at 0.61 is the average.
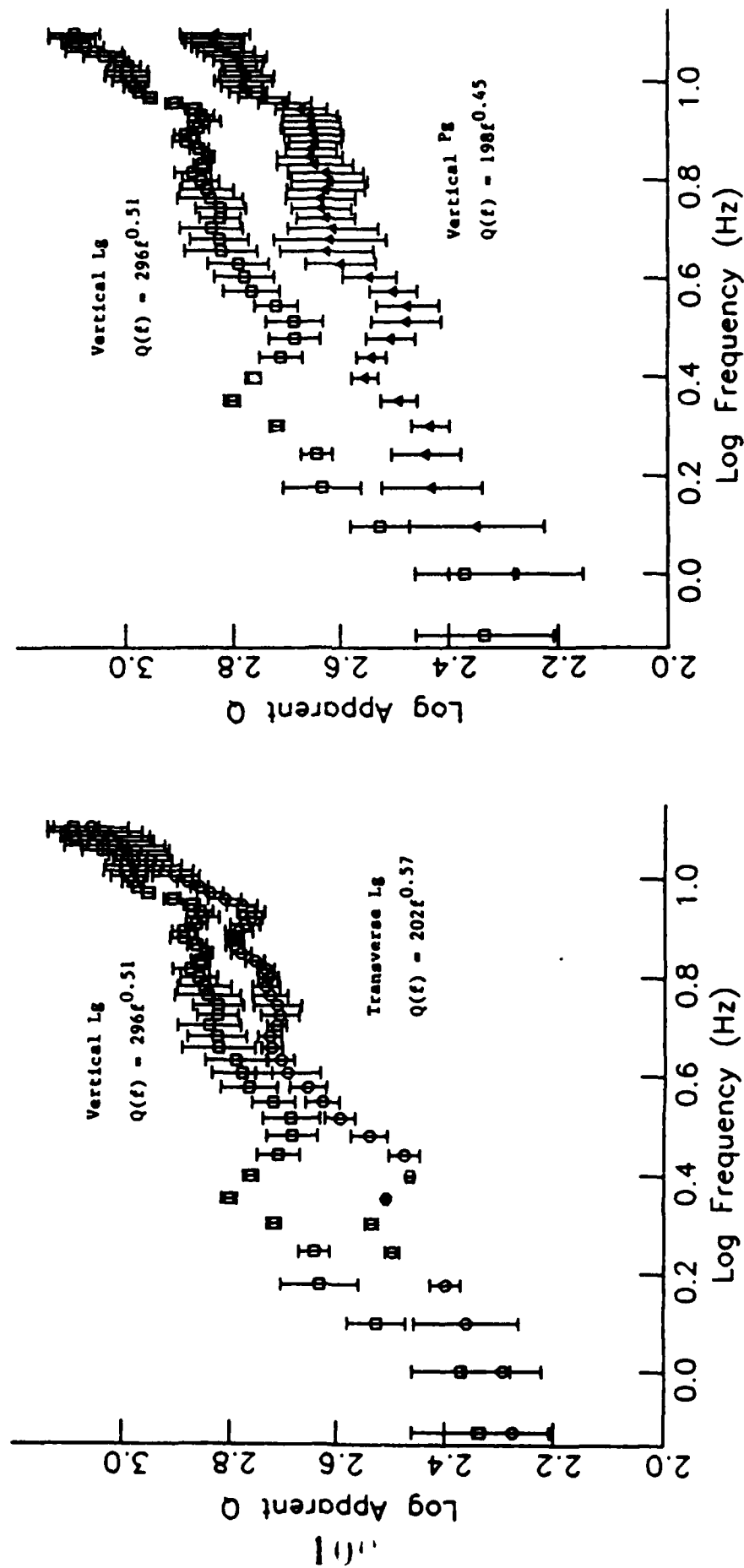
Figure 5   Apparent Q functions for vertical and transverse Lg and vertical Pg, obtained by the moving window spectral analysis technique assuming a geometrical spreading term of 0.6.   Error bars represent the standard deviation in apparent Q at each frequency for averages over 3.7 to 3.0 km/sec for Lg and 6.0 to 4.5 km/sec for Pg.   Least-squares fits to the data yield the relationships shown next to each curve.

10["

DEPENDENCE OF RAYLEIGH WAVE AMPLITUDE ON LATERAL HETEROGENEITY

Ta-liang Teng, Keiiti Aki, and Yao-Hua Zhen
Department of Geological Sciences
University of Southern California
Los Angeles, CA 90089-0741

OBJECTIVE

Recent findings on the lateral heterogeneity of the earth's crust and upper mantle suggest that a significant correction factor is needed on the Ms determination. The actual decrease of Rayleigh wave amplitude with distance can depart significantly from the simple geometrical spreading law commonly assumed for a laterally homogeneous earth. Stronger lateral heterogeneity in the upper lithosphere translates to a more complex amplitude variation of surface waves with respect to both distance and azimuth, particularly for the 20s Rayleigh waves whose amplitudes form the basis of the Ms determination. This research project applies the method of dynamic ray tracing and Gaussian beam calculation to an analysis that leads to an improvement on the Ms determination based on a refined structure of the lateral heterogeneity. The software to implement the methodology is being developed. Computational results are compared against two data sets: the first being a nuclear blast data set from Novaya Zemlya recorded by the WWSSN statons in the U.S., the second being a set of Ms station correction data derived from statistical analysis of 20s Rayleigh waves data from a large number of NTS explosions.

Through a correlation analysis, a refined model of crustal and upper mantle lateral heterogeneity will result that will allow an improvement on the accuracy of Ms determination and yield estimate.

RESEARCH ACCOMPLISHMENTS

A. Amplitude Distribution of Surface Waves:

Based on the present knowledge on the crustal and upper mantle structure of the Arctic region, we have computed synthetic surface waveforms of Rayleigh waves originated from Novaya Zemlya and recorded at stations in the U.S. Due to the lateral heterogeneity primarily in the Arctic region, Rayleigh wave ray paths show pronounced focusing and defocusing that result in a remarkable amplitude variations in the U.S. Figure 1a shows a sample result of the ray map for 20s Rayleigh waves. The ray map is generated by the applications of dynamic ray tracing to a global phase and group velocity models compiled by Rosa of MIT. A phase velocity contour map for 20's Rayleigh waves is given in Figure 1b that shares the same geographic coordinates of Figure 1a. Notice the velocity distributions in the Arctic region primarily dominate the ray distributions, therefore the amplitude distributions, in the U.S. For a Gabor waelet, the Gaussian beam synthetic Rayleigh waveforms of 20s period are given in Figure 1c for all WWSSN stations in the U.S. Amplitude variations of corresponding synthetic 20s Rayleigh waves across the U.S. along the 40 degree north latitude is given by the solid line in Figure 1d. As expected, the amplitude variatoins are strongest for short-period waves, and become weaker for longer-period waves. A sample calculation is also given by the dashed line in Figure 1d for 40s Rayleigh

waves. Curves in Figure 1d will become a straight line either in the long-period limit or for the case of a laterally homogeneous crust and upper mantle.

B. Observed Amplitude Variations for Sources in U.S.S.R.

For a nuclear explosion at Novaya Zemlya (73.30 N; 55.16 E) that took place on 09/12/1973 (06:59:54), all WWSSN seismograms are collected and Rayleigh waveforms digitized. Digital waveforms are bandpassed to simulate the results of the synthetic Gaussian beam waveforms for a source time function of the form of a Gabor wavelet. This allows a direct comparison of the observed with the calculated amplitude values for various periods. Figure 2 gives the result of this comparison for 20s Rayleigh waves for the 16 WWSSN recording stations in the U.S. The amplitude distribution of the synthetic waveforms is very similar to the solid curve in Figure 1d, the minor difference is, of course due to the slight variations in epicentral distances for stations in Figure 2. Observations fit the synthetics surprisingly well considering that a very rough velocity models of the Arctic region is used in the calculation and that waves have travelled over very long paths. We note however that relatively large discrepancies are seen for stations COL, JCT, DUG, TUC, and OGD. Because of the small difference in the back azimuth angles, the discrepencies cannot easily be explained as a result of possible tectonic release that might have imparted a radiation pattern on the source function. Rather, the departure of fit is more likely be the result of an inadequate crustal and upper mantle structure used, mainly in the Arctic region, for that region contains the majority portion of the ray paths. Therefore, the departeure of observations from synthetics gives importante constraints for a refined model of the Arctic crustal and upper mantle structure. And a refined model of the Arctic region will help improve the Ms determinations in the U.S. for sources in the U.S.S.R. To commplish this we are presently conducting a surface-wave tomographic mcpping primarily aiming at the Arctic region.

C. Observed Amplitude Variations for NTS Sources

A statistical analysis of vertical component Rayleigh wave data recorded from a large number of NTS explosions has been carried out by investigators in S-Cubed. The intention of this analysis is to obtain the statin corrections for Ms (20s) determinatins. These station corrections form a very useful data set in that it may provide observational insight into the amplitude variations of Rayleigh waves as they propagate across the U.S. These station corrections are obtained by a process described as follows:

1. Bandpass filtered the Rayleigh waves through a narrowband filter centered at 20s period, the maximum amplitudes of the filtered output are determined.

2. The amplitude data are corrected for geometrical spreading for a laterally homogeneous medium and for the anelastic attenuation (by an operator $\exp[-\gamma x]$, $\gamma = 1.3 \times 10^{-5}$ km^{-1}, and x in km). Here, $\gamma = \pi f/(Qv)$, giving $Q = 3450$.

3. Contribution of tectonic release for an assumed vertical strike-slip faulting is assumed and the effect removed.

4. The logarithm of these corrected amplitudes are input into a least-squares estimation program which simultaneously estimates network-averaged magnitude values and station corrections under the constraint that the station corrections have a zero sum.

This data set thus gives the statistical average of the Rayleigh wave amplitude data for which the tectonic release effect is minimized. We have completed computations based on available phase velocity data of the U.S. Narrow bandpassed (with 20s center period) Gaussian beam synthetic Rayleigh waveforms are computed to give the amplitude values, which, upon taking the logarithm, yield the computed station corrections. The computed station corrections are compared to the obsered data from the S-Cubed. Figure 3 gives the comparison results. The correlation of these two sets of data is very satisfactory. This implies that the observed NTS Ms station corrections can be largely explained by the path effect due to Rayleigh waves propagating over a laterally heterogeneous medium. If the structure of lateral heterogeneity is well-known, a significant improvement on Ms determination can be realized. Even based on the presently known phase and group velocity of the U.S., the contributions of path effect accounts for more that 50% of the observed Ms stations correction values. This can be seen by the deviations of the corresponding values of the observation correction and the synthetics corrections in Figure 3. We find this result very encouraging, and a refinement of the path structure is the logical next step to accomplish more accurate Ms determinations.

CONCLUSIONS AND RECOMMENDATIONS

Lateral heterogeneity of the crust and upper mantle has a dominant effect on the propagation of surface waves. With the present knowledge of global phase velocity distribution, pronounced focusing and defocusing of ray paths can take place even for mild lateral variations of regional phase velocity. This causes amplitude variations large enough to produce a ±0.3 changes in Ms values. While the present global phase velocity data are used in our method to provide a first order correction to the Ms determination, a refinement on this correction requires a better phase velocity database. For events originating in the U.S.S.R. and recorded in the U.S., the phase velocity data in the Artic region is particularly relevant in the application of the method of dynamic ray tracing and Gaussian beam synthesis. An intensive effort is currently being made in seeking a refined phase velocity model for the Artic region through a surface wave tomographic mapping.

Novaya Zemlya T = 2C Seconds
$\phi = 13.6^0 \lambda = -9.4^0$

Longitude

Fig.1a
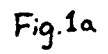
VELOCITY CONTOUR PLOT (20)

LATITUDE

104

LONGITUDE

Fig.1b

Novaya Zemlya ($\phi = 55.0^0$ $\lambda = 73.0^0$)

(T = 20 Seconds. L_0 = 1 0. S_0 = 1 .\.δ, =2^0.Q =500)

(Peak Amplitude = 0.92E -02)

Station Number

Fig. 1c

AMPLITUDE PROFILE ACROSS US (LAT.=40^0)

$1 0 3$ LONGITUDE (DEGREE)

Fig. 1d

AMPLITUDE PROFILE (T=20 SEC)

1.COL   9.OXF
2.BKS   10.SHA
3.DUG   11.AAM   ⊙—OBSERVATION
4.TUC   12.BLA
5.ALQ   13.SCP
6.GOL   14.GEO   ⊕—SYNTHETICS
7.JCT   15.OGD
8.DAL   16.WES

Fig. 2

NTS Ms(20) STATION CORRERCTION

⊙ --OBSERVATION CORRECTION
⊕ --SYNTHETICS CORRECTION

1.COL   8.JCT   15.AAM
2.COR   9.DAL   16.BLA
3.LON   10.BLC   17.SCP
4.MSO   11.FLO   18.GEO
5.BOZ   12.OXF   19.OGD
6.GOL   13.SHA   20.WES
7.LUB   14.ATL   21.ALE

Fig. 3

106

Inversion of ISC Travel Times for Earth Structure

Kenneth M. Toy and John A. Orcutt
Scripps Institution of Oceanography

Objectives

Global travel-time inversion seeks to analyze earthquake ray travel times in order to study the velocity structure of the Earth. Utilizing seismic tomographic techniques, the deviations of these travel times from a reference Earth are mapped to points along the ray path, minimizing some measure of the total misfit of all path residuals. We have used over 2.4 million P and S-wave, teleseismic, source-to-receiver ray paths, from over 24,000 events taken from the International Seismological Centre's global earthquake catalogue, to produce radially symmetric, lower mantle P and S-wave velocity models. These data represent teleseismic P and S ray paths in the 35°-105° epicentral distance range (bottoming depths from 1000 kilometers to the core-mantle boundary). We find that we are able to reduce the variance in the travel-time residuals considerably with respect to the PREM model of Dziewonski and Anderson (1981). We have also constructed 1484 P and 305 S-wave station corrections. The P station corrections that we have derived are much improved from those of Dziewonski and Anderson (1983) and the S corrections are possibly the first usable set of corrections, for S, that have ever been derived. We see a very highly coherent pattern of residuals for the North American stations, as a function of longitude, with the western stations having a tightly bunched set of positive corrections trending to the negative eastern station corrections. This correlates very well with the accepted slow-west / fast-east tectonic structure of N.A. There is a coherent "elevation correction" component in our station corrections that can be modeled quite well using a simple model of isostatic compensation and realistic crustal and lithospheric densities and velocities. We find that the proposed correlation of station correction and station gain (Grand, Kanamori, 1986, personal communication) does not exist. The S corrections scale on a 3:1 ratio to the P which implies a $dln(v_s)/dln(v_p)$ of 1.7.

Research Accomplished

The Earth's mantle velocity structure has been the subject of extensive study for several decades. The first complete global study, by Jeffreys and Bullen (1940), involved the construction of travel time curves modelling the Earth's spherically averaged structure. This was followed by numerous other studies, notably the one by Cleary and Hales (1966) in which the "time-term" analysis common to refraction seismology was applied to the spherically averaged mantle travel time problem. We have applied a time-term type analysis to develop radially-symmetric P and S-wave lower-mantle velocity models and station correction sets.
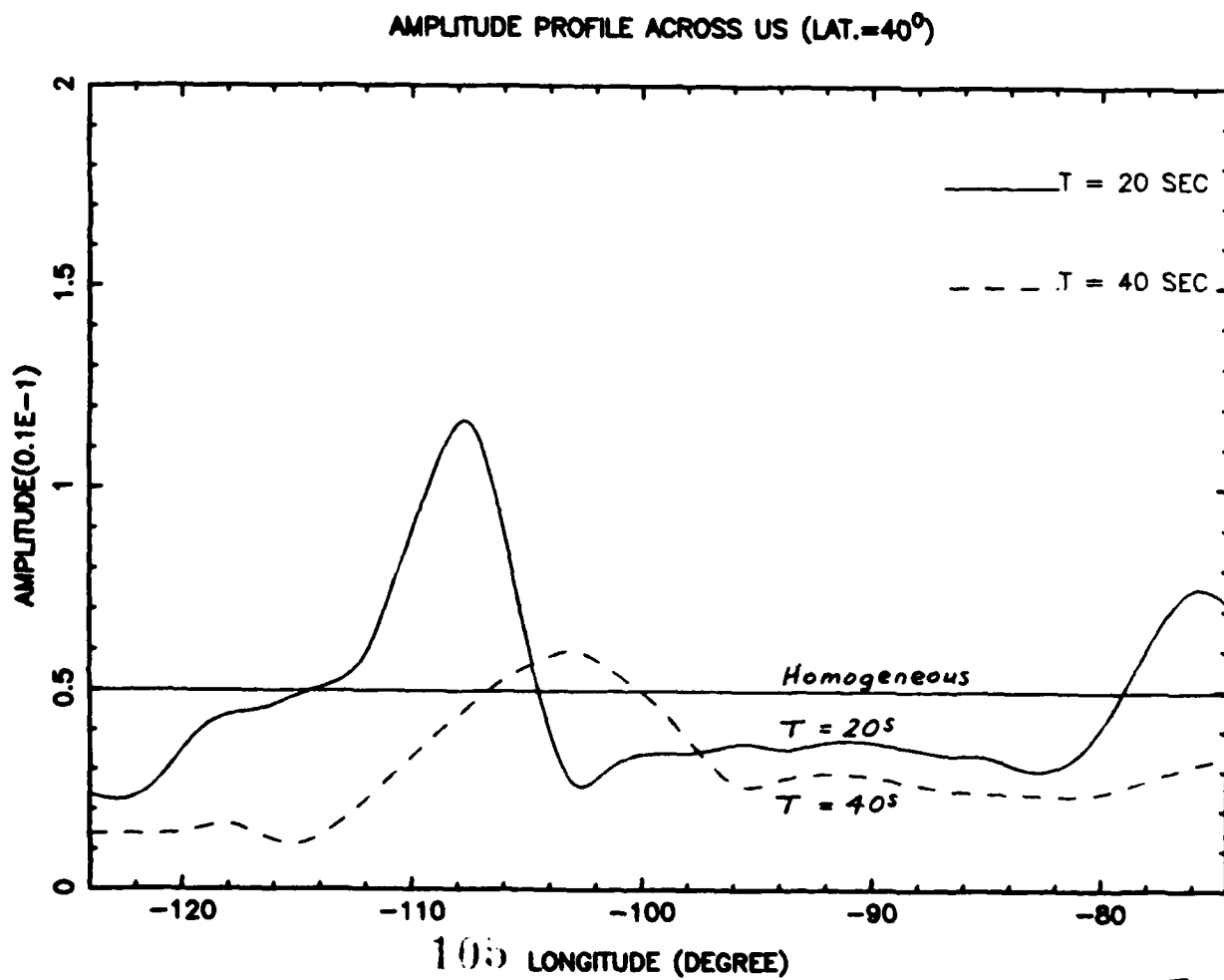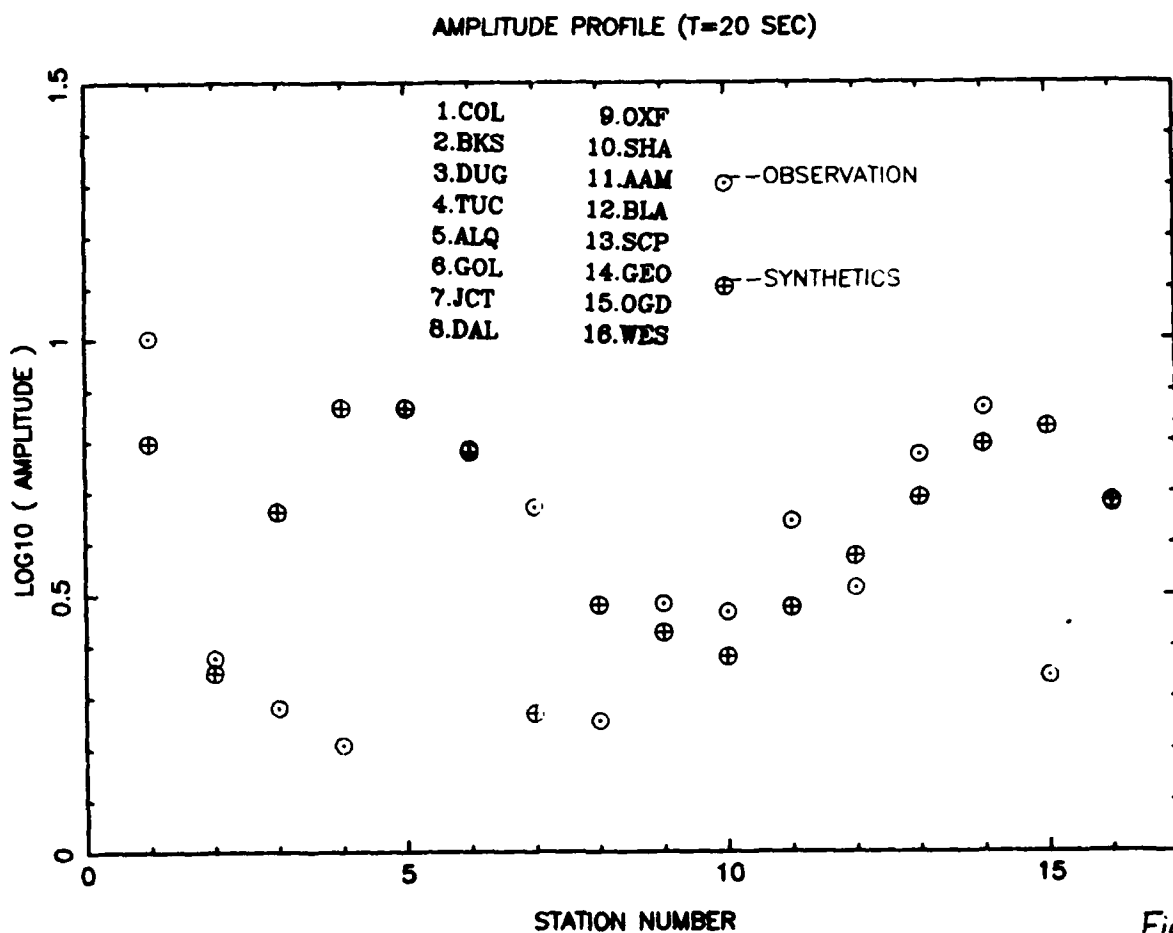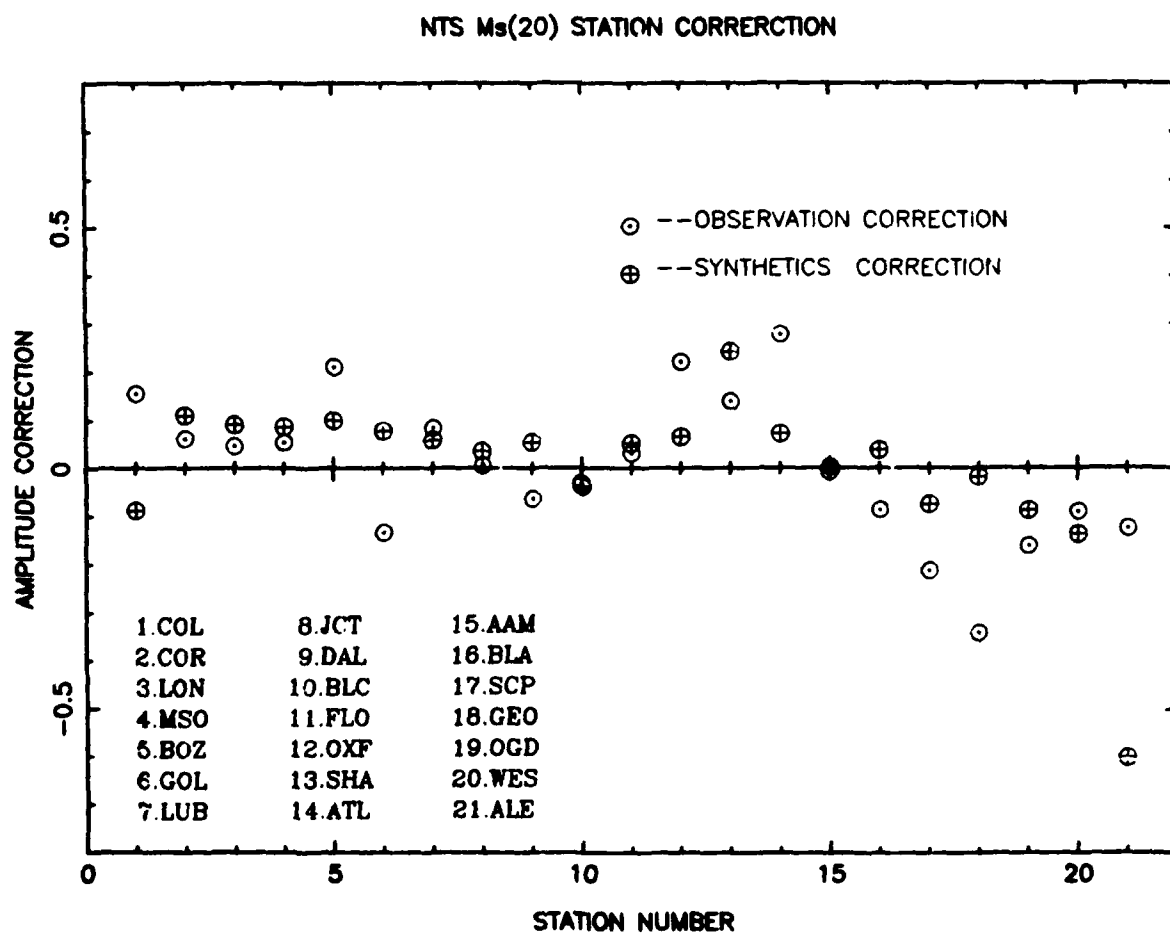
After a scheme proposed by Backus and Gilbert (1969), we solve for perturbations, dv, to a starting velocity model given input travel time residuals, dt, as data. The mantle is parameterized by 190 velocity values that represent 10 kilometer depth spaced knots from 1000 kilometers depth to the core-mantle boundary (2890 km). We invert for station corrections simultaneously with the mantle parameters, which allows for the two sets of parameters to trade-off with one another. In order to minimize the non-physical, high-frequency, least squares artifacts, we impose a second difference smoothness constraint on the total model perturbation. The forward and inverse problems are iterated until the travel time residuals have been reduced to a zero mean for all epicentral distance ranges. We are using a row-action, large matrix inversion technique with a Chebyshev acceleration criterea (Olson, 1986) to solve the large system of equations involved. (The forward and inverse problems are discussed in more detail in Toy, et al. - 1987a,b,c.)

The top curve, in Figure 1, shows the P-wave travel time residuals, as a function of bottoming depth, that were derived from the Preliminary Reference Earth Model (PREM) of Dziewonski and Anderson (1981). The PREM model misfits the travel time data by nearly a second at the core-mantle boundary with decreasing but sizeable amounts of misfit at shallower depths. The bottom curve shows the travel time residuals from our lower-mantle model and, as can be seen, the residuals have been reduced to zero mean through most of the lower mantle. There has been a substantial reduction in the RMS misfit for this phase. The bottom plot in Figure 2 shows the final model perturbation, from PREM, that produced the zero meaned residuals. There has not been an extremely large perturbation, amounting to -.025 km/s at the core-mantle boundary. The top figure plots the starting PREM model (solid line) and the final, perturbed model that was derived (dashed line).

Dziewonski and Anderson (1983) determined P-wave station corrections for 994 globally distributed stations

(henceforth known as DA83). We have derived 1484 P corrections as a result of our analysis. Figure 3 shows the correlation between the 994 DA83 corrections and our corresponding corrections. There is a correlation between the two results with our results having, on average, smaller values. This can be seen in the slope of the cloud of points being less than the 45° line plotted.

Figure 4 contains plots, for both sets of corrections, of station correction versus the number of rays that contributed to the determination of each value. (In this and all subsequent comparison plots only the 994 stations in our correction set that correspond to those in DA83 are shown.) Our results were generated with 9/5 more data, with the scaling nearly linear between the individual stations, so the horizontal axes of both plots have been scaled accordingly to allow for a more direct comparison of the results. Assuming that station corrections are Gaussianly distributed about a mean value, one would expect an larger amount of scatter, from the central value, for vertical slices with larger number of stations. There is a concentration of stations at the low count end and a smaller number of stations at the high count end with a band of approximately constant number of stations in the center. This should lead to a horizontally banded behavior in the central area of the plot with a tapering towards the high ray count end and a slight expansion at the low count end. This pattern is in fact evidenced in both ours and the DA83 results. One would also expect a slight increase in the scatter of the data, at the low count end, due to the smaller number of data and their consequent inability to reduce the variance in the station corrections. The DA83 results, however, show a much higher degree of scatter with the low ray count stations having a much higher degree of scatter than for our results. We take this to be indicative of both:

        a) a generally larger amount of scatter in the DA83 results as well as
        b) the low count DA83 stations (< 700) being poorly determined.

Figure 5 shows both station correction sets, for the 208 U.S. seismic stations, plotted as a function of longitude. The two studies agree qualitatively but the DA83 results, again, have a much higher degree of scatter. The decrease in station correction trending positive to negative, west to east agrees well with the tectonics of the U.S., with the hotter, and hence slower, western U.S. having positive residuals and the colder and faster eastern U.S. having negative ones. Figure 6 is a map view of our U.S. station correction data with positive station corrections shown as pluses and negative ones as octagons. We see very strong regional coherence with a smooth transition west to east. This result correlates very well with that from a study by Butler (1983). His short period teleseismic P-wave amplitude result, derived from totally independent data, shows the same pattern. Butler analyzed both nuclear explosion as well as earthquake data, looking at the pattern of relative trace amplitude for the U.S. We see his results in Figure 7 and the pattern is the same as in Figure 6.

Station corrections are derived with respect to an elliptical earth, with no compensation made for the elevation of the seismic station. Hence, this constant offset term (elevation correction) should be discernable in the station correction data. Figure 8 shows a plot of station correction versus elevation and a very strong correlation can be seen in our results. A trend can also be seen in the DA83 results with a much higher degree of scatter, however, still present. For teleseismic energy, the ray is nearly vertical at the station, so a theoretical value for the elevation correction can be calculated. Figure 9 shows the two end member models of either complete isostatic compensation or no compensation. Assuming the values of density and seismic velocities shown and calculating the additional time required for a ray to arrive at the station given the added elevation it has to travel, one arrives at the values of .29 and .17 sec/km of elevation, respectively. Varying the values of densities and velocities, one obtains ranges of .2-.3 sec/km for the isostatically compensated case and .14-.17 sec/km for the non-compensated model. Figure 10 plots elevation correction values for both the 208 U.S. stations as well as for all 994 worldwide data, as have been derived from both studies. The elevation corrections shown have been calculated as the best fitting, least-squares straight line through the data points. On the premise that low count stations are in some way less well constrained than the higher count stations and taking this as a measure of the accuracy of the corrections, the elevation correction values have been calculated for subsets of decreasing numbers of data, with stations with the smallest number of ray arrivals being discarded first. For example, our elevation correction value for the U.S., for a minimum ray count of 1000, is approximately .22 and was calculated by fitting a straight line through only those stations with at least 1000 phase arrivals. Our results converge on the elevation correction values of .19 sec/km of elevation for the U.S. and .22 sec/km of elevation for the world, while the DA83 results do not show a coherent correlation of station correction with elevation until most of the low count stations have been discarded. These calculated values fall between the two theoretical model extremes which is suggestive of incomplete isostatic compensation, with the U.S. showing a smaller than the world-wide average amount of compensation.

There has been reported (Grand, Kanamori, 1986, personal communications) a potential correlation between station gain and station correction. It has been postulated that low gain stations, because of the late emergence of the seismic signal from the noise, might have higher than average, positive station corrections. Figure 11, which shows station correction versus log station gain for the 115 WWSSN worldwide stations for which gain information is available, is an equivalent plot to the plot from which the proposed correlation was first postulated. We do see a possible "trianglar" correlation in the DA83 results, with a grouping of low gain/high positive correction stations in the upper left-most

portion of the plot. The linear correlation coefficient, however, is quite low with a value of 0.32. The plot for our corrections does not show this "triangular" behavior and, in fact, shows the expected pattern, seen in the correction versus ray count plot, of a higher scatter about a mean for the central, vertical gain bins with more stations, with the width of the plotted points narrowing at either end where there are fewer stations. We, thus, expect both the bulbous shape as well as a near zero linear correlation coefficient. Figure 12 is illustrative of the mechanism that we propose for the apparent correlation in the DA83 results. It is a plot of the number of rays that contributed to each station correction determination as a function of log station gain. It can readily be seen that there is an inverse correlation between the number of rays and the station correction. It was seen, in Figure 4, that the DA83 low ray count stations have a high amount of scatter. Hence, the low gain/high correction correlation seen in the DA83 WWSSN plot is due, not to any apparent late arrival of the signal, but rather to the DA83 correlation of low ray count with high station correction and hence with low gain. We have been able to find station gain information for 356 worldwide stations and these are plotted, against station correction, in Figure 13. We again see a small grouping of low gain/high correction stations in the DA83 results, with a triangular shape which is not nearly as coherent as for the WWSSN data. However, the correlation coeffient is now quite low. We again see the expected "bulbous" shape in our results, with a near zero correlation coefficient. Our results indicate that there is not any demonstrable correlation of low station instrument gain with high, positive station correction that is indicative of any real, physical mechanism.

Although the S results are still preliminary, we will briefly discuss our results to date here. The S corrections show similar patterns as the P corrections, in terms of N.A. patterns, ellipticity corections, etc. Figure 14 is a comparison of the S and P station corrections that we have derived. The correlation is quite high, given the scatter that still exists in the S results (which have not yet been zero meaned). This correlation between P and S station corrections is better than any results (e.g. Dziewonski, personal communication) that have been reported to date. A line with slope 3 is plotted on Figure 14, and is the best fitting, least squares straight line through the data. This implies that the S station correction residuals scale with a factor of 3 with respect to the P. Other work (summarized in Souriau and Woodhouse, 1985) have found the value of the scaling of the S to P station corrections to range from 1.8 to nearly 5, with the more recent values lying in the upper range. If one assumes that a station correction value is indicative of the heterogeneity in the uppermost 700 kilometers of the earth, then our 3 to 1 scaling predicts a $dln(v_s)/dln(v_p)$ scaling of approximately 1.7. Other researchers have recently reported values for $dln(v_s)/dln(v_p)$ to lie in the range 2.0-2.5 (Anderson, 1986; Dziewonski, et al, 1986) while Masters et al. (1982) reported a value of 1.25. Our values lie in the middle of the ranges of the previously reported values but lower than the most recent numbers.

References

Anderson, D.L. (1986). II. Shear properties and thermodynamics of the lower mantle, *Phys. Earth Plan. Int.*, (in press).

Backus, G. and F. Gilbert (1969). Constructing P-velocity models to fit restricted sets of travel-time data, *BSSA*, 59, 1407-1414.

Butler, R. (1984). Azimuth, energy, Q and temperature: variations on P wave amplitudes in the United States, *Rev. Geophys Sp. Phys.*, 22, 1-36.

Cleary, J. and A.L. Hales (1966). An analysis of the travel times of P waves to North American stations, in the distance range 32 to 100 degrees, *Bull. Seism. Soc. Am.*, 56, 467-489.

Dziewonski, A.M. and F. Gilbert (1976). The effect of small, aspherical perturbations on travel times and a re-examination of the corrections for ellipticity, *Geophys. J. R. Astr. Soc.*, 44, 7-17.

Dziewonski, A.M. and D.L. Anderson (1981). Preliminary reference Earth model, *Phys. Earth Plan. Int.*, 25, 297-356.

Dziewonski, A.M. and D.L. Anderson (1983). Travel times and station corrections for P waves at teleseismic distances, *J. Geophys. Res.*, 88, 3295-3314.

Dziewonski, A.M., J.H. Woodhouse, D. Giardini, X. Li and A. Morelli (1986). Global images of the Earth interior, *EOS* (abstract), 1100.

Jeffreys, H. and K.E. Bullen (1940). Seismological Tables, Brit. Assn. Gray-Milne Trust.

Masters, G, T.H. Jordan, P.G. Silver and F. Gilbert (1982). Aspherical Earth structure from fundamental spheroidal-mode data, *Nature*, 298, 609-613.

Olson, A.H. (1986). A Chebyshev condition for accelerating convergence of iterative tomographic methods - solving large least squares problems, *Phys. Earth & Plan. Int.*, (in press).

Souriau, A. and J.H. Woodhouse (1985). A worldwide comparison of predicted S-wave delays from a three-dimensional upper mantle model with P-wave station corrections, *Phys. Earth & Plan. Int*, 39, 75-88.

Toy, K.M., A.H. Olson, J.A. Orcutt and J.F. Gilbert (1987a). Seismic tomographic inversion of travel times, *Proc. of Geophys. Soc. of Tulsa Symp.*, (in press).

Toy, K.M., J.A. Orcutt, A.H. Olson and J.F. Gilbert (1987b). Refined P and S-wave lower mantle velocity models from ISC travel time data, (manuscript in preparation).

Toy, K.M., A.H. Olson, J.A. Orcutt and J.F. Gilbert (1987c). New P and S-wave station corrections sets: a joint inversion of ISC travel time data, (manuscript in preparation).
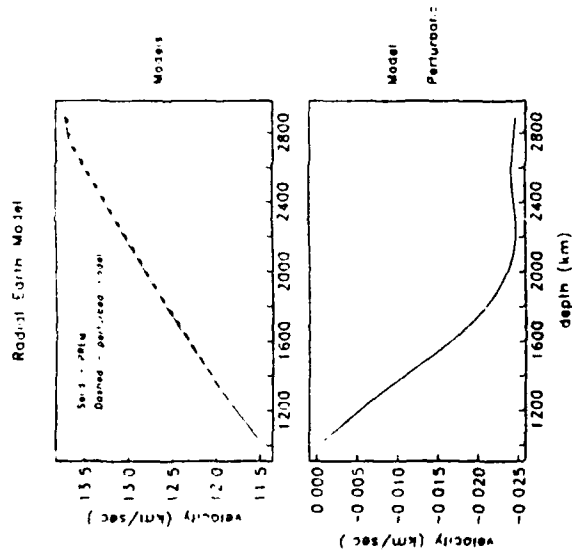
Figure 1. Travel time residuals from PREM and our radially-symmetric, lower-mantle, P-wave velocity model. The residuals have been reduced to a zero mean for our model.
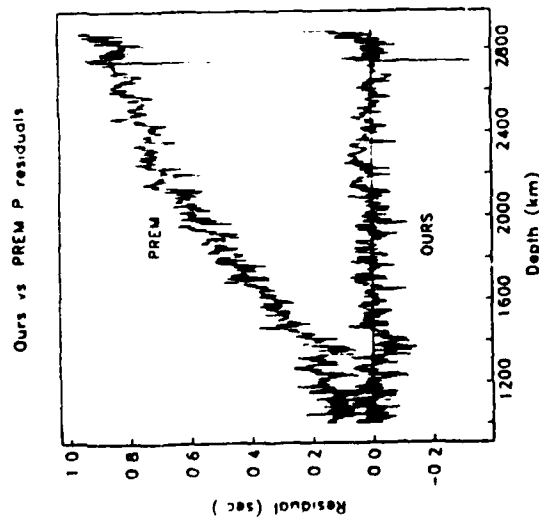
Figure 2. Model perturbation and our final lower mantle P-wave model.
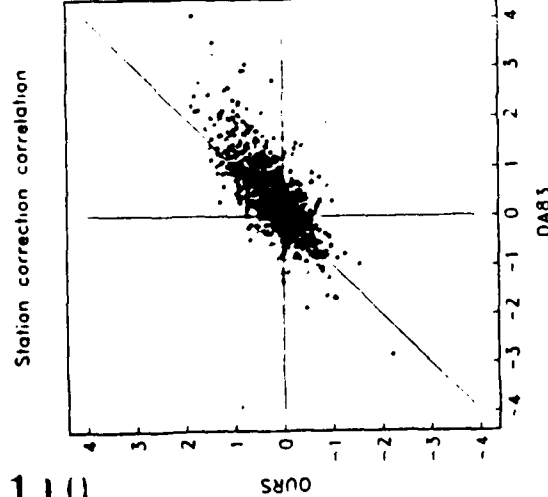
Figure 3. Correlation between the 904 Dziewonski and Anderson station correction values and the ones derived in this study. They correlate well, with ours having on average smaller values.
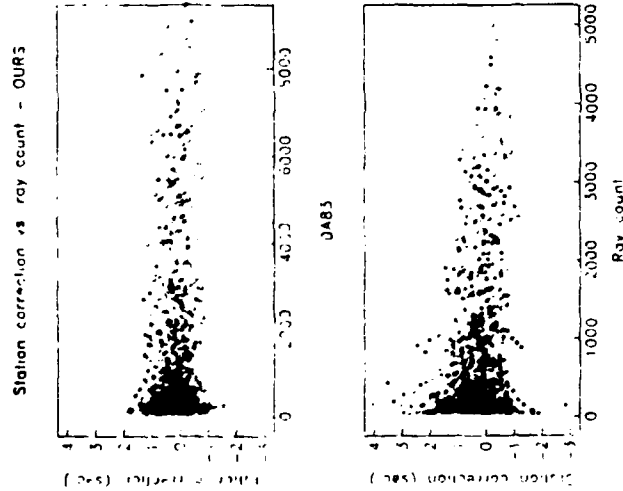
Figure 4. Station corrections plotted as a function of the number of rays used to calculate them. Note the higher scatter in the DA83 results.
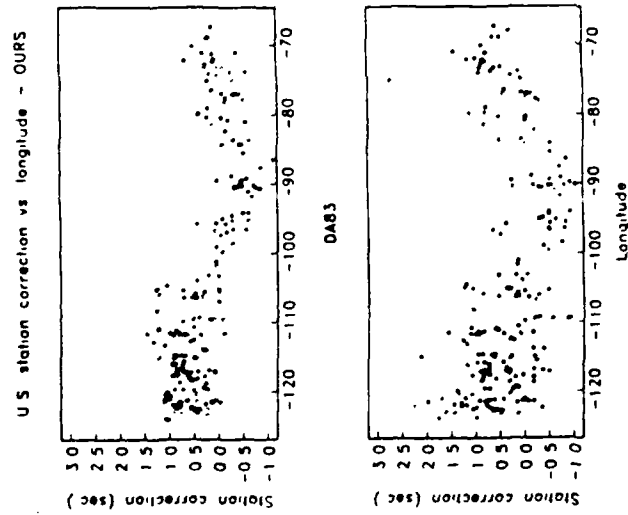
Figure 5. Both sets of station corrections, as a function of longitude, for the 208 U.S. stations. As in the other figures there is a much higher amount of scatter in the DA83 corrections.
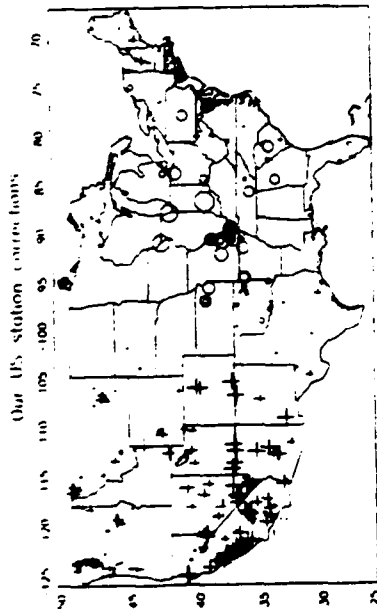
Figure 6. Our 208 U.S. station corrections in map view. There is a highly coherent, positive trending negative west to east pattern.
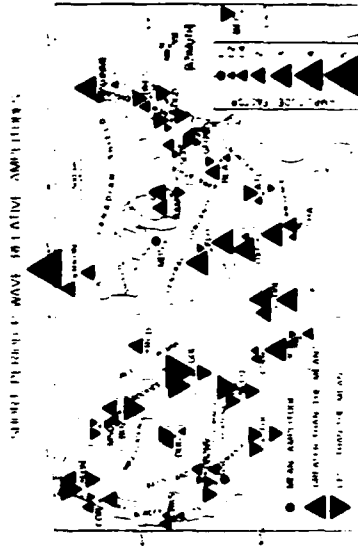
Figure 7. P-wave relative amplitudes from Butler (1983). His derived pattern agrees quite well with the one from our 208 U.S. corrections (figure 6).

Elevation correction vs min ray count – U.S.

WORLD

Figure 10. Elevation correction values calculated for subsets of stations with decreasing minimum ray counts. Our U.S. values approach .19 while our worldwide values approach .22. This is suggestive of incomplete compensation with the U.S. being less compensated.

Isostatic compensation

No compensation

Figure 9. Isostatic compensation, assuming vertically travelling rays, predicts a .29 second delay per kilometer of station elevation while no compensation predicts .17 sec/km.

Station correction vs. elevation – OURS

DA83

Figure 8. Station correction vs. station elevation. Note the definite trend of higher stations having more positive station corrections with again more scatter in the DA83 results.

111

DA83

DA83

Log station gain (115 stations)

Log station gain

Figure 11. 115 WWSSN station correction values vs. station gain. The DA83 results suggest a weak correlation of low station gain with positive station correction.
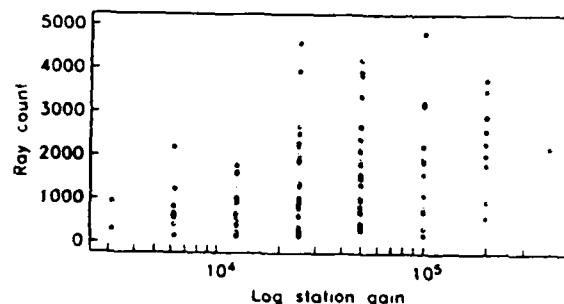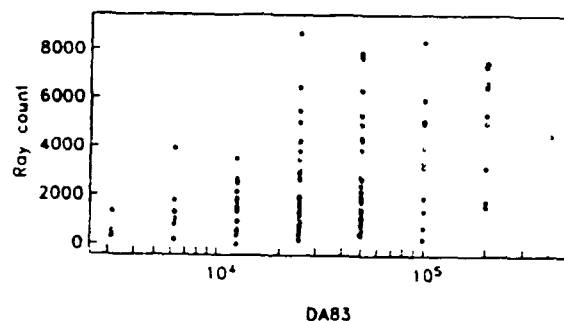
Figure 12. Ray count vs. log station gain for the 115 WWSSN stations. There is an inverse correlation which, along with the higher scatter seen in the low count DA83 stations (figure 4), can explain the low gain/positive correction correlation in the DA83 results.

Worldwide station correction/gain correlation - OURS

Station correction correlation

DA83

Log station gain (356 stations)

P
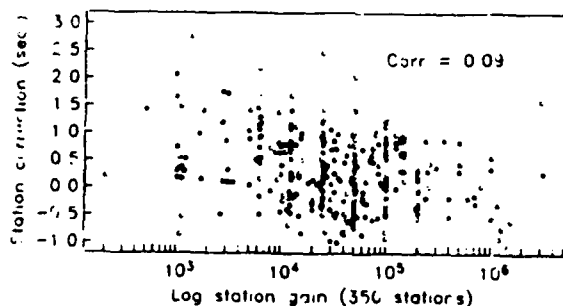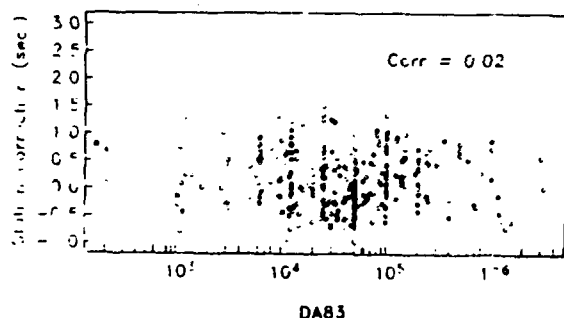
Figure 13. Station corrections, for the 356 worldwide stations for which gain information is available, plotted as a function of log station gain. No correlation can be seen.
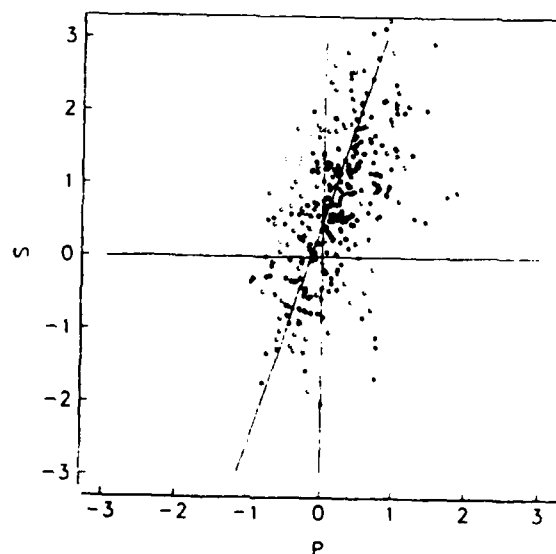
Figure 14. Correlation of the S and P station correction values derived in this study. The 3:1 scaling predicts a $dln(v_s)/dln(v_p)$ of 1.7.

119

STRAINS NEAR EXPLOSIONS AND EARTHQUAKES

L. J. Burdick and J. S. Barker
Woodward Clyde Consultants

OBJECTIVES

A mounting body of evidence from laboratory studies has shown that when typical geological materials are subjected to levels of shear strain in excess of 10^{-6} they begin to behave in a nonlinear fashion (Mavko, 1979; Stewart et al. 1983). This nonlinearity manifests itself as a lowering of effective Q in a manner which is frequency, amplitude and pressure dependent. Figure 1 is redrafted from Mavko (1979) and illustrates his basic result. The value of Q is observed to begin to decrease at about 10^{-6} strain with the effect becoming very significant by 10^{-5} strain. The magnitude of the effect also depends strongly on the geologic material involved. It is generally believed that the decrease in Q is caused by frictional sliding on cracks and thus depends also on the density of cracks in the material. As overburden pressure closes these cracks, it becomes increasingly difficult for sliding to occur, so the nonlinear reduction in Q probably does not extend to great depth in the earth. Day and Minster (1986) have discussed the potential significance of this phenomenon to interpretation of ground motion data from a series of small explosions in salt, but the events were so small that it is difficult to relate their results to observations from nuclear explosions or earthquakes. Also, the recording geometry of their experiment was so simple that they could use whole space wave propagation results. Near-field wave propagation is usually much more complex near to general seismic sources (Burdick et al. 1984; Heaton and Helmberger, 1978). It is important to establish the levels of dynamic strain that occur near typical sources in media where wave propagation is more complex in order to determine how important nonlinear reduction of Q is to interpretation of seismic data.

Large data bases of near-field velocity records have been collected and analyzed in the past, whereas high frequency dynamic strain measurements have seldom if ever been made. The objectives of this study have been to establish and apply methods for utilizing the data base of velocity records, to infer the levels of strain that typically occur near to explosions and earthquakes and to look for evidence of whether nonlinear reduction in Q does occur to a significant degree. We began by developing the theory necessary for computing stresses and strains (rather than seismic motions) using the generalized ray methodology. We demonstrated that in a layered half space the far field strain wave is very similar to the far field velocity wave. We developed transfer operators which, when convolved with observed velocity records, produce estimates of strain records. We applied these operators to a suite of velocity records from a nuclear explosion and from a small earthquake to determine the levels of shear strain they produced and how it decayed with distance. We compared the decay rates to the predictions of elastic theory to find whether there was evidence of a significant reduction in Q.

RESEARCH ACCOMPLISHED

Strains in a Layered Halfspace The nonzero components of the stress (and thus strain) tensor are computed automatically in standard wavenumber integration calculations. Unfortunately, the technique used most often in modeling studies of near-field data is summation of generalized rays because it provides high frequency synthetics in much less time. Some slight modifications of the approach are required to generate synthetic strain-time histories rather than motion-time histories. Following Helmberger (1974), we can express a single generalized ray at high frequency in the far field as

$$ray(t) = \sqrt{\frac{2}{\pi r}} \, \frac{d}{dt}\left[\frac{1}{\sqrt{t}} \, * \, \Im m\left(\frac{p^{1/2}\, dp}{\eta \; dt} \right) \prod A \, R \right]$$

evaluated along the Cagniard contour in the complex p plane. The factor Π is the product of the reflection/transmission coefficients along the raypath, A is the source radiation pattern term and R is called the receiver function. The only difference between a strain generalized ray and a seismic motion generalized ray is a change in the expression for the receiver functions. These functions for either motion or strain are given in table 1. The variables p and η are horizontal and vertical slowness, α and β are the P and S velocities and the factor ϵ' is ± 1 depending on whether the ray is up or downgoing at the receiver. The functions on the left are for receiver points in the medium and those on the right for points on the free surface.

<u>Strains Near Nuclear Explosions</u> In a whole space, the strain pulse due to a point source is just the velocity pulse divided by the P velocity of the medium. In a layered half space, the velocity and strain time histories differ to some degree because of the differences in the receiver functions. A general approach to transforming velocity to strain is to utilize theoretical frequency dependent velocity to strain transfer operators. These are generated by computing theoretical velocity and strain pulses for a given observation and deconvolving the former from the latter. Estimates of strain records are generated from observed velocity records by convolving them with the transfer operators. In most cases, the transfer operators are very delta-like functions with amplitudes controlled by the velocity at the receiver site.

The first data base processed using the transfer operators was a suite of near-field velocity records from 5 Pahute Mesa nuclear explosions. They were SCOTCH, INLET, MAST, ALMENDRO and BOXCAR. The recording sites were at horizontal ranges between 3.3 and 22.5 km. The recording instruments were L7 velocity meters which have a flat response to velocity throughout the seismic band, so the signals recorded on them are essentially velocity versus time. In order to compute the transfer functions, it is necessary to select a layered crustal model for Pahute Mesa. The one used is given in Barker et al. (1985) who developed it specifically to give accurate near field synthetics. It is in basic agreement with the models of Helmberger and Hadley (1981), Hamilton and Healy (1969) and Carroll (1966), differing only in the fine details of the gradients.

An example of the computation of a tranfer operator for a 1000 kt event located at 1 km depth in the Pahute Mesa structure is shown in figure 2. The synthetic vertical and radial velocity pulses are shown on the left, the four nonzero partial derivatives of displacement with respect to spatial coordinates in the center and the transfer functions on the right. The top strain is E_{zz}, the bottom is E_{RR} and the average of the center two is E_{RZ}. Note that the two center traces sum exactly to zero so that the free surface condition is maintained. The transfer functions are computed by transforming the velocity pulse and corresponding partial derivative pulse into the frequency domain using a fast fourier transform algorithm. The latter is divided by the former and the inverse transform taken. The resulting transfer operators strongly resemble delta functions with a signal to noise ratio of about 5 to 1. To suppress the noise, a gaussian filter with a cutoff of 5 hz was applied before convolving the filter with the data. In principle, both the radial and vertical records could be used along with the appropriate transfer operators to estimate strain. In practi·e, it is difficult to do so because the synthetics are never really exact and generally the vertical component of motion is predicted better than the radial. It is difficult to achieve the delicate cancellations required to maintain the free surface condition. Therefore, the vertical component was used to generate one of the two components of strain which are nonzero for an explosive source, and the free surface condition was used to generate the other from it.

The decay rate of peak shear strain with range is shown in figure 3. Theoretical curves are shown for the largest event, BOXCAR, and the smallest, SCOTCH. The curves are computed assuming that elastic theory is appropriate and using the same velocity structure as in the calculation of the transfer functions. It is important to emphasize that this structure is consistent with those determined using a variety of low strain types of measurements.

The observed values from the processed records are shown as data points. The range of strains over which Q values appeared to vary in the laboratory (figure 1) was 1 to 70 μstrain. This level is only half way up the logarithmic scale in figure 3. The theoretical curve for the smallest event does not drop below 1 μstrain by 25 km. Thus the entire data set is within the strain regime in which the nonlinear processes observed in the laboratory are believed to be significant. It is interesting that the observations show the same rate of decay as the theoretical curve which was computed assuming linear elasticity holds. The nonlinear effects, if they are important, should have influenced the shape of the decay curve. However, it is important to remember that the effects are probably only strong at shallow depths. All of the generalized rays important to the P pulse dive downward into the crust and only enter the region where they might be attenuated as they emerge under the receiver. In other words, all of the signals from a given event might be attenuated by more or less the same amount. The reduction in amplitude by the nonlinearity would then be reflected in an underestimate of the absolute size of the event.

Strains Near Earthquakes The next records to which we applied our velocity to strain transfer operators were from an aftershock of the 15 October 1979 Imperial Valley earthquake. The aftershock was studied in some detail by Liu and Helmberger (1985) wo provided a mechanism, moment and time function for it. They reported the event depth as 9.5 km. The largest arrival at all stations was a strong, unusually simple S wave, so in this case we computed S rather than P transfer operators. The polarity information in the data set was very clear, and it allowed Liu and Helmberger (1985) to constrain the mechanism to be almost pure vertical strike slip. They reported a moment of 1.0×10^{24} dyne-cm and a triangular time function with a rise of .1 s and a fall of .1 s. From our modeling studies, however, we conclude that a moment value of 0.6×10^{24} dyne-cm is and a source with a rise of .3 and a fall of .1 s. is more accurate.

The nonzero strains generated by incident SV are E_{ZZ} and E_{RR}. As before, we wished to insure that the free surface condition would be satisfied, so we used only the radial component of motion and generated both strain time histories from it. The observed transverse components of motion were used to generate the third nonzero, off-diagonal component of strain. Another important difference between the Pahute Mesa and Imperial Valley data sets is that in the latter, Liu and Helmberger (1985) found evidence for very low crustal Q in the form of a strong frequency shift between P and S. The values they used for shear Q in the top 1/2 km of there model were on the order of 10. This results in a relatively distance independent t* of .132 s. In the calculations that follow, we used this value along with the layered crustal model they presented. Values of shear Q as low as 10 are surely atypical and could easily be interpreted as an indication that nonlinear processes like those suggested by the laboratory data might be taking place.

An example of the velocity to strain operators for the earthquake case is given in figure 4. As before, the relevant theoretical velocity traces are shown on the left, the spatial derivatives in the center and the transfer operators on the right. In this instance, the velocity traces are Q (radial) and V (tangential). The transfer operators are shown with the gaussian (cutoff 5 hz) convolved through. Again, the operators are very delta-like functions. The epicentral range for the calculations shown in figure 4 is 10 km just as for the explosion operators in figure 2. The strains for the earthquake are slightly larger than for the megaton explosion which is somewhat suprising. This is not true at all ranges because, as we shall show in the following, the earthquake strains decay at a much slower rate. The transfer operators for the earthquake source-station geometry were generally simpler than for the explosion case meaning that we are probably obtaining more reliable estimates of the strain time history for the earthquake.

The observed peak strain values for 16 observing stations of the Imperial Valley aftershock ranged from 5 to 65 μstrain. Because of the azimthal radiation pattern of the double couple source, they did not show a clear pattern of decay with range. To attempt to view the decay of strain independently of the azimuthal pattern, a calculated radiation term was divided out of all of the radial and tangential S wave records. This corrects the former to the SV radiation max where SH should be zero and the latter to the SH max where SV should be zero. Peak strains were then computed from each record making the assumption in each case that the other components of S wave motion were zero. The results are shown in figure 5. The observed values scatter about the curve predicted by elastic theory. There is no general downward shift of the data points as might be expected if strong nonlinear losses are occuring.

CONCLUSIONS AND RECOMMENDATIONS

The close relationship between velocity and strain pulses in a whole space appears to be maintained for a layered half space. The large data base of near field velocity records can be transformed into a data base of near field dynamic strain records. Near field strains for large explosions which have been successfully modeled using linear elastic theory are as high as 10^{-3} at the surface. Those near to a small earthquake appear to be about 10^{-5}. These strains are large enough so that one might expect a nonlinear response in near surface materials. No direct evidence for such a response can be found in the observed decay of peak strain with distance. It appears to follow the predictions of linear elastic theory. For the time being, it seems best to presume that the results of the linear elastic modeling studies are valid. More work is needed to predict just what the effects of a nonlinear reduction in Q on near field waveforms should be.

REFERENCES

Barker, J. S., S. H. Hartzell, L.J. Burdick and D. V. Helmberger, Determination of effective source functions at Pahute Mesa, WCCP-R-85-02, Woodward Clyde Consultants, Pasadena, CA., 1985.

Burdick, L. J., T. Wallace and T. Lay, Modeling the near field and teleseismic observations from the Amchitka test site, *J. Geophys. Res.*, **89**, 4373-4388, 1984.

Day, S. M. and J. B. Minster, Decay of wave fields near to an explosive source due to high strain nonlinear attenuation, *J. Geophys. Res.*, **91**, 2113-2122, 1986.

Carroll, R. D., Preliminary interpretation of geophysical logs, UE2OF, Pahute Mesa, Nevada Test Site, technical letter: special studies-I-37, supplement 1, *U. S. Geol Survey Open File Report*, 1966.

Hamilton, R. M. and J. H. Healy, Aftershocks of the BENHAM nuclear explosion, *Bull. Seism. Soc. Am.*. **59**, 2271-2281, 1969.

Heaton, T. H. and D. V. Helmberger, Predictability of strong ground motion in the Imperial Valley: modeling the M4.9, November 4, 1976 Brawley Earthquake, *Bull. Seism. Soc. Am.*, **68**, 31-48, 1978.

Helmberger, D. V., Generalized ray theory for shear dislocations, *Bull. Seism. Soc. Am.*, **64**, 45-64, 1974.

Helmberger, D. V. and D. M. Hadley, Seismic source functions and teleseismic observations of the NTS events Jorum and Handley, *Bull. Seism. Soc. Am.*, **71**, 51-67, 1981.

Liu, H. and D. V. Helmberger, The 23:19 aftershock of the 15 October 1979 Imperial Valley earthquake: more evidence for an asperity, *Bull. Seism. Soc. Am.*, **75**, 689-708, 1985.

Mavko, G. M., Frictional attenuation:and inherent amplitude dependence, *J. Geophys. Res.*, **84**, 4765-4775, 1979.

Figure 1 Linear plot of attenuation versus strain amplitude for six different dry rocks (redrawn from Mavko (1979)).

TABLE 1

Receiver Functions

Seismic Motions

At the Free Surface

$$R_{PZ} = 2\eta_\alpha(\eta_\beta^2 - p^2)/\beta^2 R(p)$$
with $R(p) = (\eta_\beta^2 - p^2)^2 + 4p^2\eta_\alpha\eta_\beta$

$$R_{PR} = -4\eta_\alpha\eta_\beta/\beta^2 R(p)$$

$$R_{SZ} = 4p\eta_\alpha\eta_\beta/\beta^2 R(p)$$

$$R_{SR} = 2\eta_\beta(\eta_\beta^2 - p^2)/\beta^2 R(p)$$

$$R_{S\theta} = 2p$$

In the Medium

$$R_{PZ} = -\epsilon'\eta_\alpha$$

$$R_{PR} = -p$$

$$R_{SZ} = p$$

$$R_{SR} = -\epsilon'\eta_\beta$$

$$R_{S\theta} = p$$

Strains

$$R_{PZZ} = -cpR_{SZ}$$
with $c = (\alpha^2 - 2\beta^2)/\alpha^2$

$$R_{PZR} = -pR_{PZ}$$

$$R_{PRZ} = pR_{PZ}$$

$$R_{PRR} = -pR_{PR}$$

$$R_{SZZ} = cpR_{SR}$$

$$R_{SZR} = -pR_{SZ}$$

$$R_{SRZ} = pR_{SZ}$$

$$R_{SRR} = -pR_{SR}$$

$$R_{S\theta Z} = 0$$

$$R_{S\theta R} = -pR_{S\theta}$$

$$R_{PZZ} = -\epsilon'\eta_\alpha R_{PZ}$$

$$R_{PZR} = -pR_{PZ}$$

$$R_{PRZ} = -\epsilon'\eta_\alpha R_{PR}$$

$$R_{PRR} = -pR_{PR}$$

$$R_{SZZ} = -\epsilon'\eta_\beta R_{SZ}$$

$$R_{SZR} = -pR_{SZ}$$

$$R_{SRZ} = -\epsilon'\eta_\beta R_{SR}$$

$$R_{SRR} = -pR_{SR}$$

$$R_{S\theta Z} = -\epsilon'\eta_\beta R_{S\theta}$$

$$R_{S\theta R} = -pR_{S\theta}$$

117

VELOCITY TO STRAIN TRANSFER

(1000 Kt, Pahute Mesa Structure, Range = 10 km)

Figure 2. An example of the computation of the velocity to strain transfer functions for the Pahute Mesa structure. The velocity traces on the left are deconvolved from the strain traces in the center to produce the transfer operators on the right.

PEAK SHEAR STRAIN DECAY NEAR NUCLEAR EXPLOSIONS
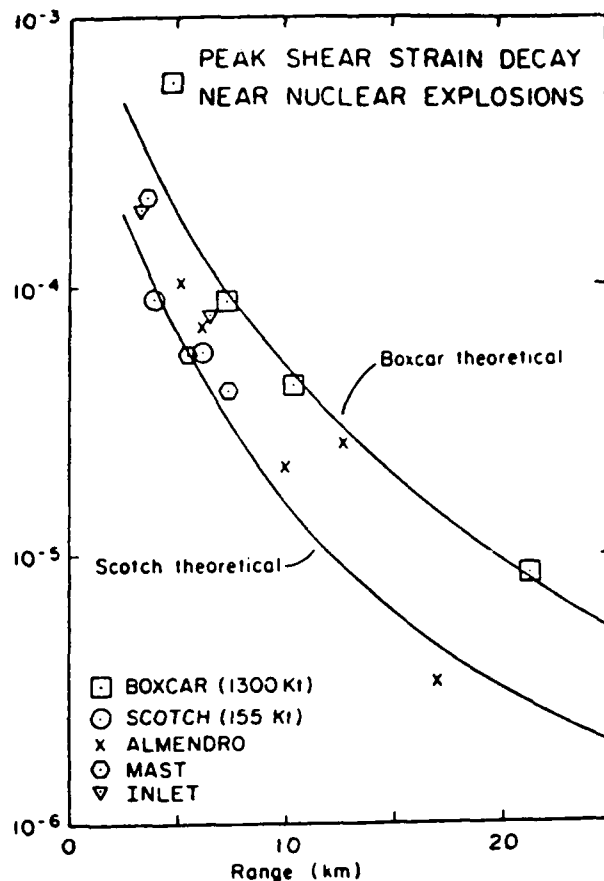
Figure 3. The decay of peak shear strain near to nuclear explosions. Theoretical curves are shown for the largest and smallest events.

VELOCITY TO STRAIN TRANSFER

Imperial Valley Aftershock, Range = 10 km
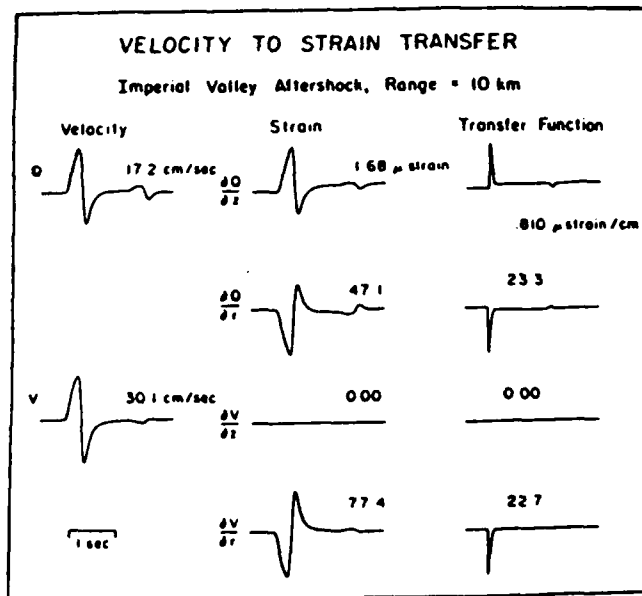
Figure 4. An example of the computation of the velocity to strain transfer functions for the Imperial Valley structure. The velocity traces on the left are deconvolved from the strain traces in the center to produce the transfer operators on the right.

Imperial Valley Aftershock Radiation Corrected Peak Shear Strain Decay
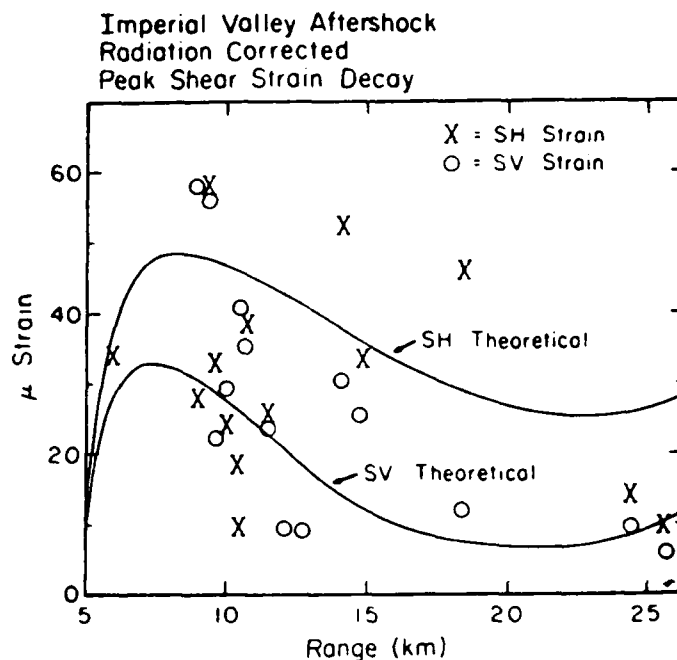
Figure 5. The decay of peak shear strain near to the Imperial Valley aftershock.

SPECTRAL ESTIMATES FROM P-WAVE CODA

Eugene Herrin and Christopher Hayward
Geophysics Laboratory
Southern Methodist University

The most reliable power spectral estimate of seismic background noise assumes a nearly stationary process so that overlapping blocks of data can be windowed, transformed using FFT algorithms, and then averaged to obtain the estimates. Spectral estimates of P-wave signals are usually based on the Fourier transform of a single window of data containing only a few cycles of the waveform. One may argue that this procedure is correct for the spectral analysis of short transients, but the P-wave arrival always includes a coda and tends to approach the level of the ambient noise at higher frequencies. For shallow sources such as explosions, the first few cycles may include interfering surface reflections. All of these characteristics contribute to uncertainties in spectral estimates for the P-wave.

We have observed that teleseismic P-wave codas from large underground explosions persist well above ambient background for as long as 500 seconds. Furthermore, we have found that although the total power in the coda decreases with time, the shape of the power spectrum is nearly constant until the power in the coda falls to ambient noise levels. The process thus has a nearly stationary auto-correlation function although the autocovariance changes with time. We have designed a spectral estimation procedure, shown in Figure 1, which makes use of this near-stationary property to produce normalized spectral estimates using a modification of the well known block-averaging procedure. These estimates are particularly useful in determining spectral decay for studies of source properties and frequency dependent attenuation.

Figure 2 shows about 600 seconds of vertical component, short-period data from station RSNT which includes the teleseismic P-wave arrival from a large event near Semipalatinsk. Figure 3 shows normalized, block-averaged spectral estimates for all three short-period components for this event. The first set of spectra are for 40 seconds of noise just prior to the P arrival. Subsequent spectra are for adjacent 40 sec windows from the first arrival into the coda. Several features are apparent on the figure. The normalized spectra are fairly smooth and are similar for all three components. The spectral shape changes with increasing time only when the coda power drops to that of the ambient seismic noise. We assumed a simple source spectrum for this event with a decay of f^{-2} above a 1.6 Hz corner frequency and found $t^* = 0.26$ in the range 2 to 5 Hz. Although one can use other source models, our approach should allow us to compare t^* for other stations recording the same event. Figure 4 shows similar spectral estimates for the same event recorded at RSON. The spectra are more complicated and suggest that the

that the spectral slope changes with frequency. We found a
t* between 0.3 and 0.45 depending on the frequency band.
Figure 5 shows spectra for the same event recorded at RSSD.
The calculated t* for this station was 0.40 in the range 2 to
4 Hz. In the frequency band important for determining Mb, Q is
lower beneath RSON and RSSD than beneath RSNT.

Figure 6 shows the normalized spectra for NORESS, Z component,
C-2, for a large event at Semipalatinsk. The first group of spec-
tra represents ambient noise before the P-arrival, the second set
(next 40 second window) is for mixed noise and signal and the
third set is for P-coda. Assuming the same source model as pre-
viously used, the calculated t* is for 0.11 for the 2 to 7 Hz band.
This value is less than half of the t* found at RSNT for a Semi-
palatinsk source. Care must be taken, however, in making com-
parisons between stations with such a great difference in epi-
central distance, because these low values of t* are probably
distance dependent.

Figure 7 shows spectra from the same component at NORESS for
a large event at Novaya Zemlya. The calculated t* for these spec-
tra was 0.11 in the range 2 to 7 Hz, the same as that observed
for the Semipalatinsk event. Since the distances from NORESS to
the two Soviet test sites are similar, we infer from these data
that the crust and upper mantle attenuation beneath the two sites
is nearly the same.

Figure 8 shows the conventional spectral estimate of the
P-arrival from a magnitude 3.5 earthquake west of Amarillo, Texas,
as observed at the GFRL (Z component) station 52 km. from the
epicenter in the Stone and Webster Engineering Company network
centered at Amarillo. The data window was about 5 seconds long
starting with the first arrival. This spectrum shows a clear
corner and a spectral-rolloff above the corner a little steeper
than f^{-3}, but there is considerable uncertainty in determining
that slope. Figure 9 shows the normalized spectral estimates for
16 seconds of noise and 16 seconds of P and P-coda for the same
event. From this spectrum the spectral decay from 8 to 30 Hz
was determined to be 54dB, implying a slope which fits well within
the uncertainty of the spectral estimate shown in Figure 8.

We believe that the normalized, block-averaged method for
spectral estimation can be used to determine the spectra of P-coda
with good precision where the signal-to-noise ratio is adequate,
and that the P-coda spectra are representative of the combined
effect of the source spectrum and frequency dependent attenuation
of P-waves from both explosions and earthquakes.

FIGURE 1

Procedure for calculating normalized,
block averaged signal spectra

1. THE SEISMIC SIGNAL IS REPRESENTED BY THE TIME SERIES, $f_i(t)$
    THE SAMPLING RATE WAS 40 SPS or 100 SPS.

2. N SAMPLES ARE SELECTED FOR THE jth WINDOW. FOR THESE RESULTS
    N=256.

3. A HAMMING WINDOW, $W_{ij}(t)$ IS APPLIED TO THE DATA.

4. THE VARIANCE, $\chi_j = \frac{1}{N} \sum_i^N [W_{ij}(t) f_i(t)]^2$ IS CALCULATED FOR THE jth
    WINDOW, AFTER THE MEAN HAS BEEN REMOVED.

5. THE WINDOWED DATA IS PADDED WITH ZEROS TO 512 POINTS.

6. THE FAST FOURIER TRANSFORM, $F_j(f)$, IS PERFORMED ON THE PADDED,
    WINDOWED DATA.

7. THE NORMALIZED TRANSFORM IS CALCULATED: $\phi_j(f) = F_j(f) / \chi_j$

8. THE $j+1^{th}$ WINDOW IS FORMED BY SHIFTING THE jth WINDOW BY
    M SAMPLES. FOR THESE RESULTS M = 100 SAMPLES, PRODUCING AN
    OVERLAP OF 60%, AND STEPS 3 THROUGH 6 ARE PERFORMED.

9. THIS PROCESS IS REPEATED P TIMES. P = 16.

10. THE RESULTING SPECTRAL ESTIMATE IS $f(f) = \frac{1}{P} \sum_1^P \phi_j(f)$
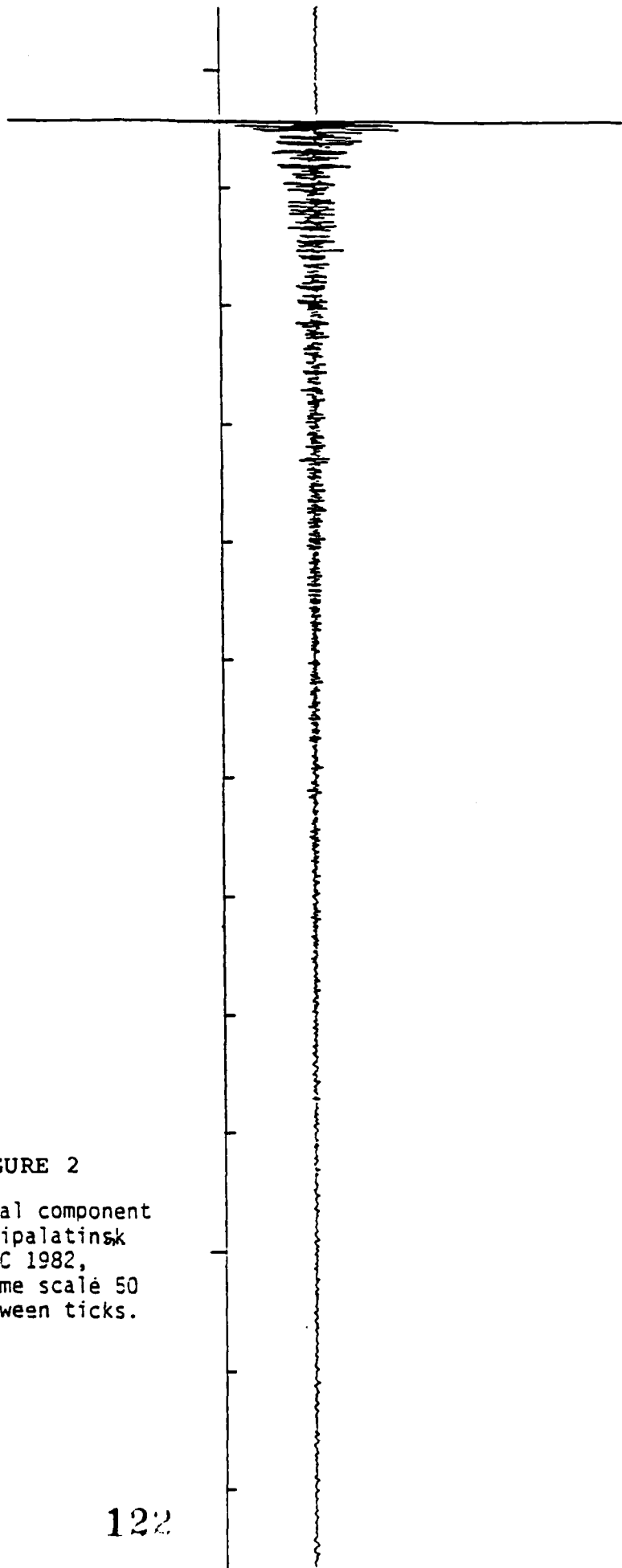
FIGURE 2

RSNT vertical component
record, Semipalatinsk
event, 5 DEC 1982,
Mb 6.1. Time scale 50
seconds between ticks.

122
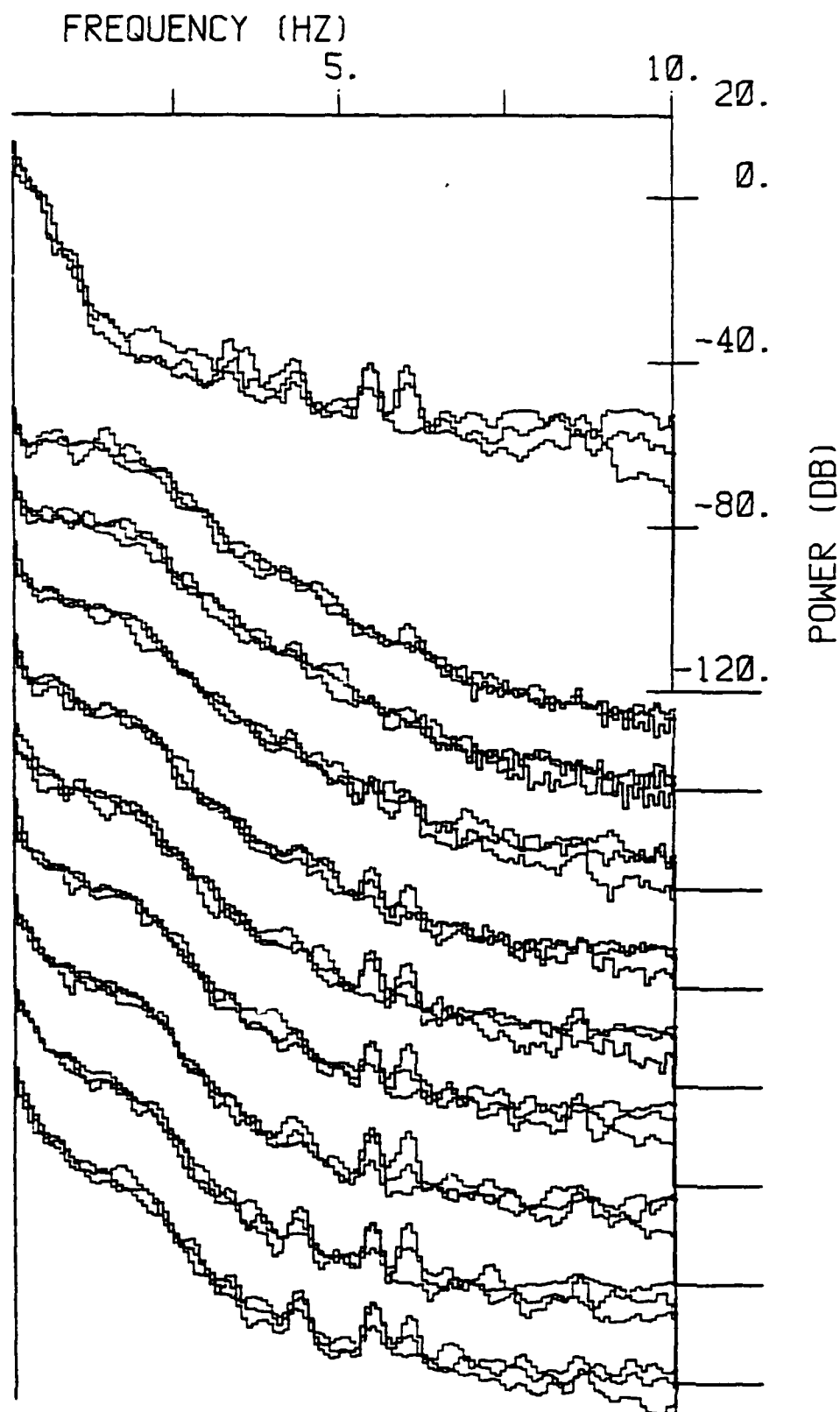
FIGURE 3

Normalized, block averaged displacement spectra,
RSNT, Semipalatinsk event, 5 Dec. 1982, Mb 6.1

FIGURE 4
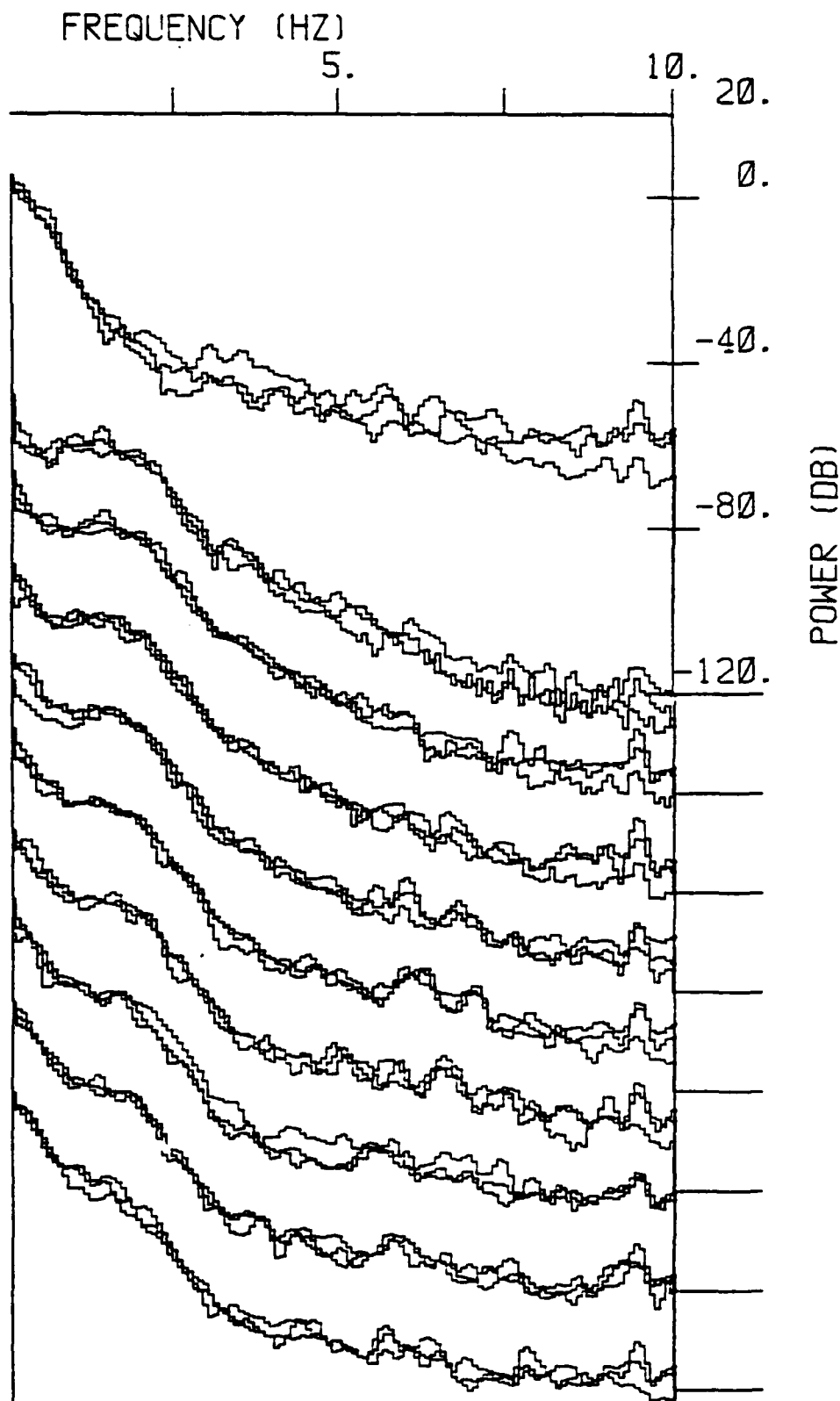
Normalized, block averaged displacement
spectra, RSON, Semipalatinsk event,
5 Dec. 1982, Mb 6.1 1 ? :
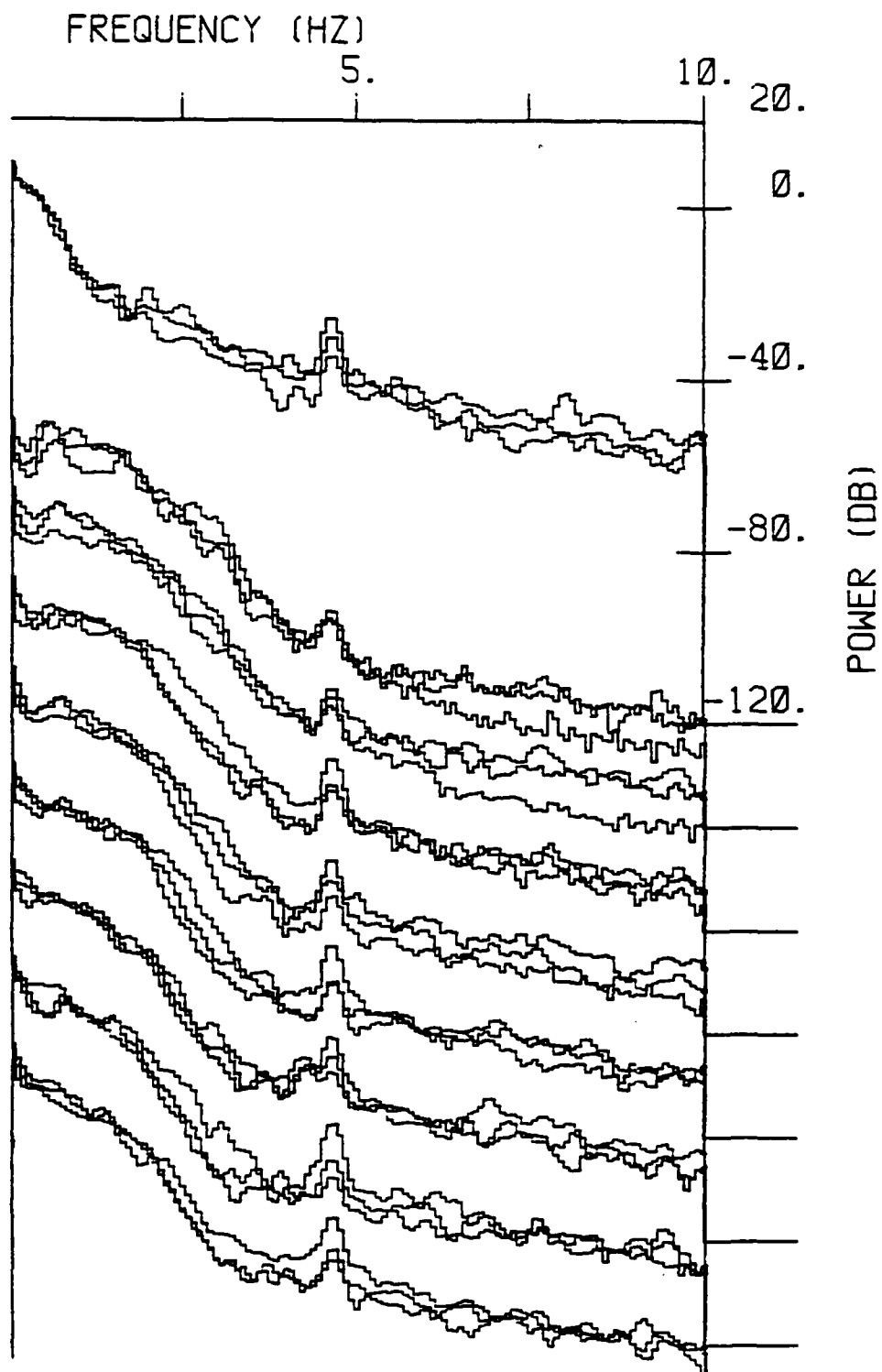
FIGURE 5

Normalized, block averaged displacement spectra,
RSSD, Semipalatinsk event, 5 Dec. 1982, Mb 6.1

FIGURE 6

FREQUENCY (HZ)
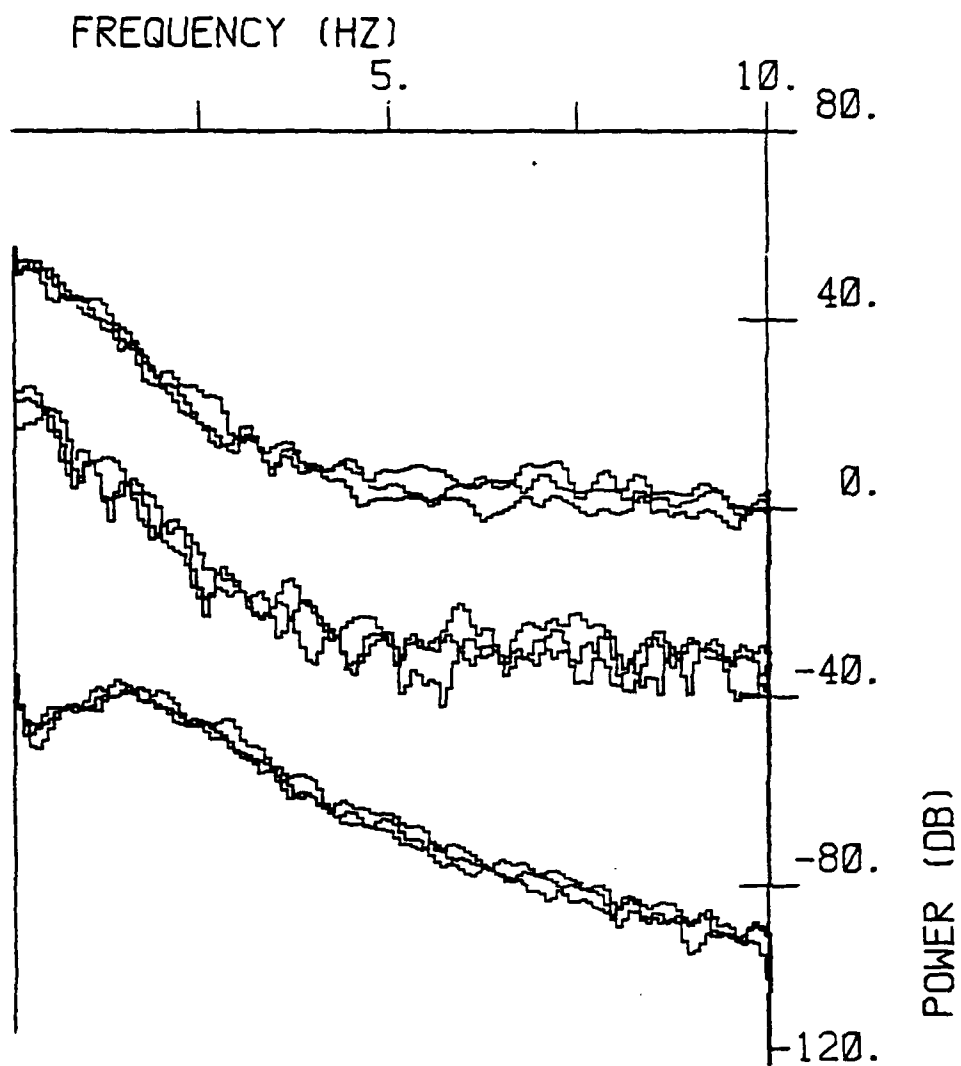
Normalized, block averaged displacement spectra,
NORESS, Semipalatinsk event, Day 351, 1984, Mb 6.1

FIGURE 7
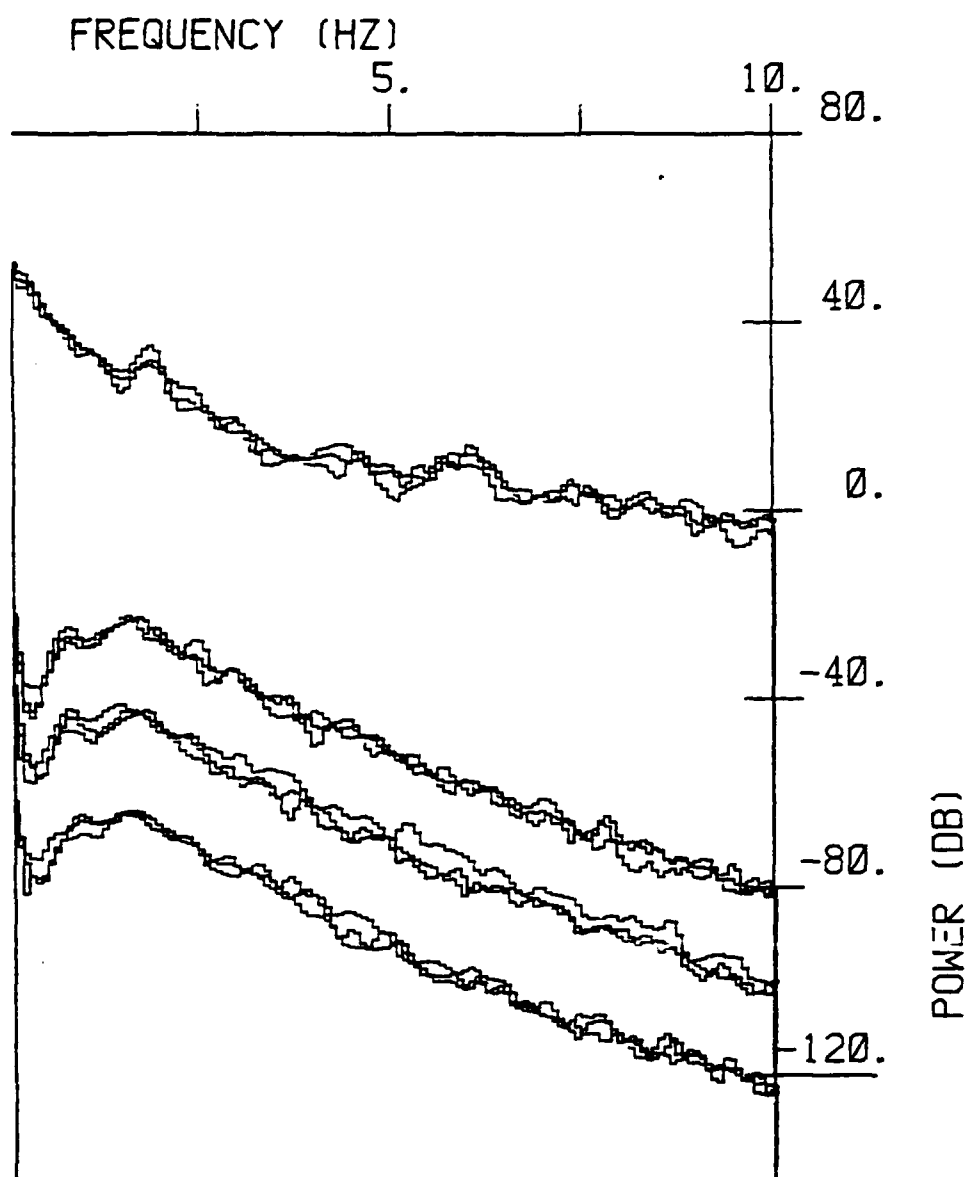
Normalized, block averaged displacement spectra,
NORESS, Novaya Zemlya event, Day 299, 1984, Mb 5.9

FIGURE 8
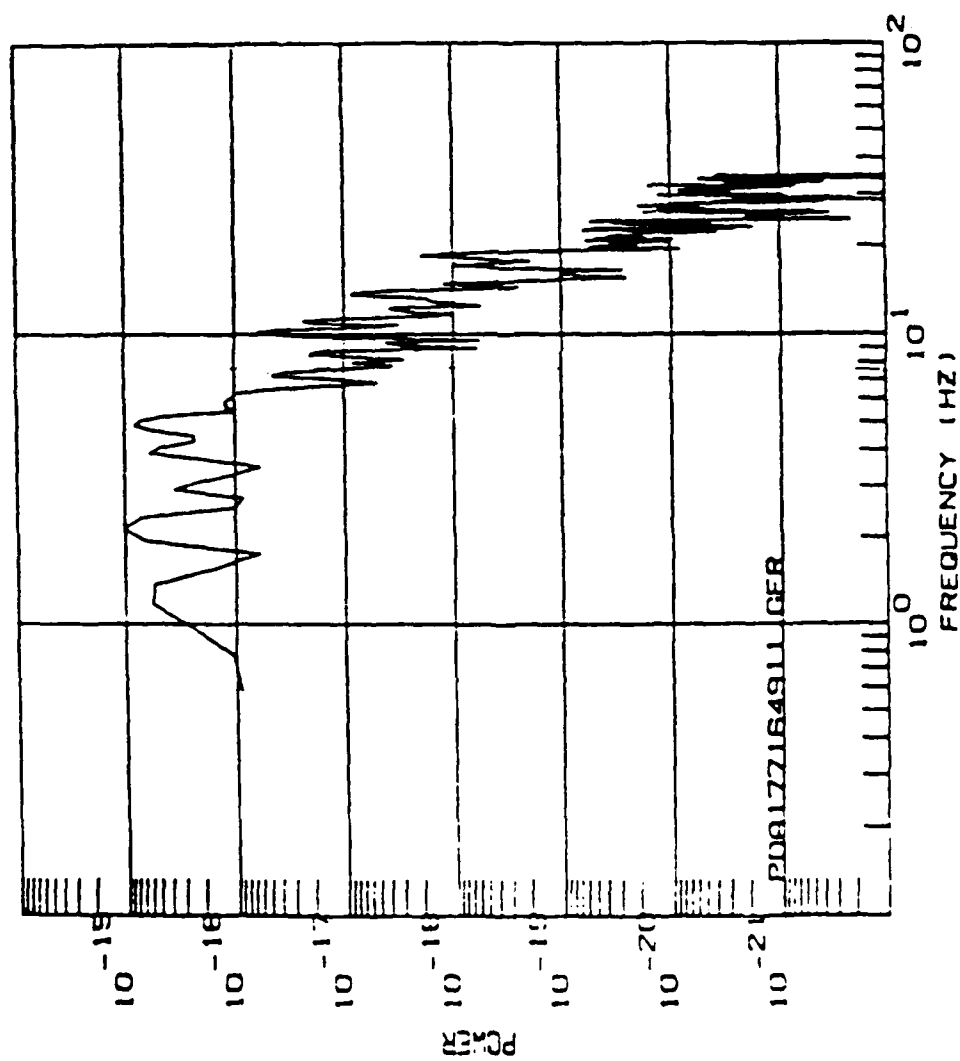
TUCUMCARI EVENT GFRL STA, CORRECTED FOR DISPLACEMENT

1 BLOCK OF 512 SAMPLES, SAMPLING RATE = 100

FIGURE 9
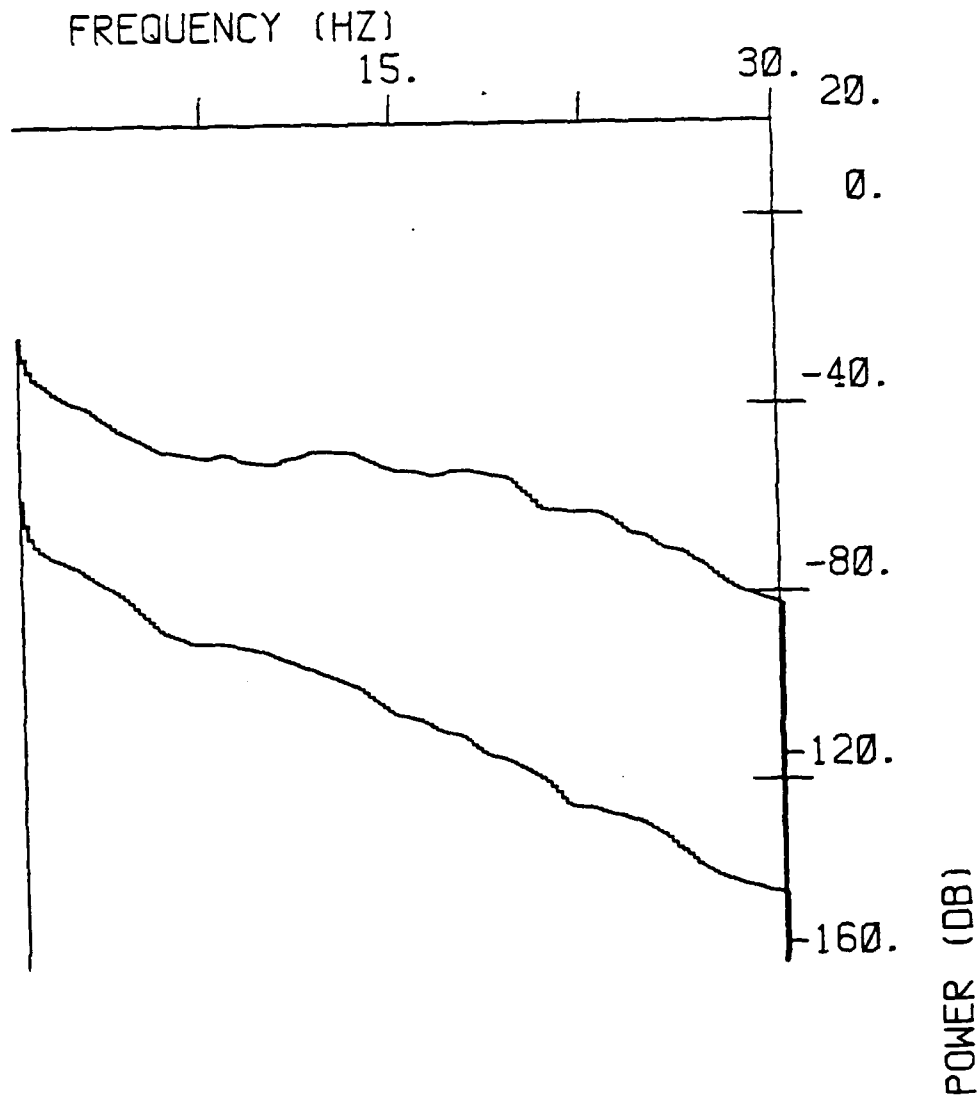
Normalized, block averaged spectra, for
GFRL, Amarillo earthquake, Day 177, 1985,
Mb 3.5.

Finite Difference Simulations of Rayleigh Wave Scattering
by 2-D Rough Topography and Shallow Heterogeneity

K. L. McLaughlin, R. S. Jih, Z. A. Der, and T. W. McElfresh
Teledyne Geotech, 314 Montgomery Street, Alexandria, VA 22314

SUMMARY

We have performed second order 2-D numerical Rayleigh-wave scattering experiments on models containing ramps, (simple ramps, trenches, ridges), rough topography, and imbedded heterogeneities in order to investigate many situations encountered in seismic testing. Some general conclusions can be drawn from these experiments with regards to the generation of seismic P coda waves at test sites.

NUMERICAL EXPERIMENTS: SIMPLE INCLINED SURFACES

Experiments were first conducted to justify that, in the case of a homogeneous half-space, the grid dispersion only modulates the spectra of the propagating Rayleigh wave. No significant attenuation of the Rayleigh wave could be measured for the half-space. Following this check, we introduced the simple ramp. We measured the transmission and reflection of Rayleigh waves incident upon simple uphill or downhill slopes with variable height. The reflection and transmission coefficients are dependent on the ratio of the ramp height to the wavelength as well as the direction of the ramp. For the same height, the downgoing slope always causes more reflection and less transmission as compared to the upgoing slope. Reflection coefficients are always less than transmission coefficients. Examples are shown in Figure 1. The diffraction pattern generally becomes much more complicated when the height of the ramp is larger. In all cases the corners act as point sources radiating converted bodywaves (mainly S). When the incident Rayleigh wave encounters a rising hill, made up of two ramps, some energy is converted to P wave energy and propagates in essentially the same direction as the incident Rayleigh wave, while in the case of going down hill, the converted P wave scatters in all possible directions (Figure 2). Converted P waves are predominately forward scattered for $\lambda < h$, and are more isotropic at low frequencies. Converted S waves are roughly the same amplitude in the forward and backward directions for both high and low frequencies for Rayleigh waves incident on a downhill slope, and for uphill slopes are dominated by forward-scattered waves at high frequencies and by back-scattered waves at low frequencies.

These experiments with simple topographic profiles are instructive since they show us that Rayleigh-to-bodywave conversion occurs near corners (changes in slope), is frequency dependent, directionally dependent, and in general depends on the sign in the change of slope. These phenomena are more difficult to observe in more complicated topographic profiles.

NUMERICAL EXPERIMENTS: ROUGH TOPOGRAPHIC PROFILES

In order to generate random topography, a random number generator was used to produce Markov sequences of values 0, 1, or -1 with a chosen transition probability matrix. The associated random walk (integrated sequence) is then derived. Fifteen rough topographic profiles were inserted into a grid with flat ground on both sides to simulate the propagation of Rayleigh waves across a section of terrain with rough topography. The initial incident waveform, and the reflected and transmitted waveforms were then measured at near surface "sensors" away from the rough topography. Transmission coefficients and the attenuation factor $Q(f)$ were then computed in the frequency domain. Table 1 gives the statistics of several topographic profiles used and the corresponding attenuation factor Q at the dominant frequency. Here we computed the attenuation factor Q via $Q^{-1}(f) = -ln(T(f))(V_R / 2\pi f X)$. The roughness coefficient Ω_1 (or normalized total variation) is defined by $\Omega_1 = \sum |H_i - H_{i-1}| / X$ where H_i is the elevation at ith column of the nontrivial portion of the topography, X the traveling distance. This statistic reflects the idea that in a smooth sequence of points the differences between successive values are all small, and hence the numerator will be small. The denominator is simply a scaling factor. Further investigation on whether such Ω_1, as a measure of roughness, can characterize all general rough topographic features is necessary.

In these numerical tests, smoother topographic profiles have larger Q as expected. For the specific profiles listed in Table 1, the ordering is preserved if Ω_1 were replaced by the normalized l^2 norm of the elevation change, Ω_2, which is defined by $\sqrt{\sum(H_i-H_{i-1})^2} / X$. Q estimates are much the same whether shear or dilatational strain energy were used to measure attenuation. Several calculations were run at grid sizes differing by factors of 2 and 1.428. The resultant Q's were nearly identical. The attenuation of Rayleigh waves as they propagate over rough topography is dominated by the conversion to body waves and not by refelction for all models examined.

TABLE 1. Rough Topographic Profiles			
topography	span(km)	Ω_1	Q(.8Hz)*
3	8.7	.18	629
15	11.4	.39	184
5	11.9	.40	37
4	12.1	.46	33
10	11.5	.49	28
6	12.2	.52	25
11	11.2	.54	21
8	12.0	.58	15

* (V_R =2.71 km/s, λ =3.2km)

NUMERICAL EXPERIMENTS: SHALLOW HETEROGENEITIES

Shallow heterogeneous layers are created by convolving a 2-D white noise field with 2-D Gaussian filters with specified sizes of the dominant scatterers (*i.e.* grain size, *a*) which turns out to be proportional to the mean spatial correlation distance. These smoothly varying heterogeneous media were then embedded into a homogeneous half-space.

Finite-difference simulations were performed for 18 combinations of shallow heterogeneities with 3 rms velocity fluctuations (5%, 7%, and 10%), 2 mean scatterer sizes (1km and 2km), and 3 different depths of the heterogeneous layer (1km, 2km, and 3.2km). Figure 3 shows some snapshots of the displacement fields due to a Rayleigh wave propagating in a model with a shallow heterogeneous section. The attenuation of Rayleigh waves incident upon such media are dependent on the factors: v , a, h, the rms value of heterogeneity, gain size, and depth of heterogeneity. Results show that attenuation is well predicted by first order (Born approximation) scattering theory for velocity variations up to 20% rms. The production of converted body waves is again predominately forward scattering for high frequencies and back scattered or nearly isotropic for low frequencies. Conversion to P-SV body waves dominates the attenuation of the Rayleigh wave as it propagates through shallow heterogeneity in the range where $\lambda \approx a$.

FINITE DIFFERENCE EQUIVALENTS OF RAYLEIGH WAVES

In simulating the scattering of Rayleigh waves on lateral heterogeneities and topography it is important to have a way of initiating the propagation of a Rayleigh pulse without also generating some distracting body waves in the finite-difference (FD) grid. We have experienced some difficulties, however, when we attempted to use the analytical solutions in the manner of Levander (1985) for layered structures which had strong vertical velocity contrasts, such as would be the case for Yucca Flats, Nevada Test Site. Apparently we need exact solutions to the FD approximate equations of elasticity rather than the analytical solutions for layered structures.

We therefore need the exact FD solutions to start the Rayleigh wave pulses in models of structures. The part of the grid where we initiate the solutions must be a flat layered structure such that we can finish the input of a transient Rayleigh wave before any reflections from lateral heterogeneities arrive. In general it makes no sense to talk of Rayleigh waves otherwise, since the mere concept of

Rayleigh waves itself has no meaning in laterally changing structures. Therefore we seek surface wave solutions for 2D laterally homogeneous grids for initializing the motion in laterally heterogeneous grids.

We have obtained solutions for the FD formulations of Kelly et al (1976) the algorithm we use in our FD work. Analogous to the analytical case the evanescent solutions in the underlying half spaces in the model are selected by selecting the two decoupled solutions arising from the eigenvalue-eigenvector decompositions of the FD propagator matrices. These are subsequently continued upwards in the manner described in Aki and Richards (1980), and pairs of ω and k are found by iteration that corresponding to fundamental Rayleigh waves. The solutions obtained are to be used as forcing functions on one side of the grid to initialize Rayleigh waves in layered structures with strong vertical heterogeneities. This will enable us to model Rayleigh-to-P scattering at Yucca Flats and Pahute Mesa.

REFERENCES

Aki, K. and P. Richards (1980). Quantitative Seismology: Theory and Methods, Freeman, San Francisco, CA.

Clayton, R. and B. Engquist (1977), Absorbing boundary conditions for acoustic and elastic wave equations. *Bull. Seism. Soc. Am.*, *67*, 1529-1540.

Kelly, K., Ward, R. W., Treitel, S. and M. Alford (1976), Synthetic seismograms, a finite-difference approach. *Geophysics*, *41*, 2-27.

Levander, A. (1985), Finite difference calculations of disperse Rayleigh wave propagation. *Tectonophysics*, *113*, 1-30.
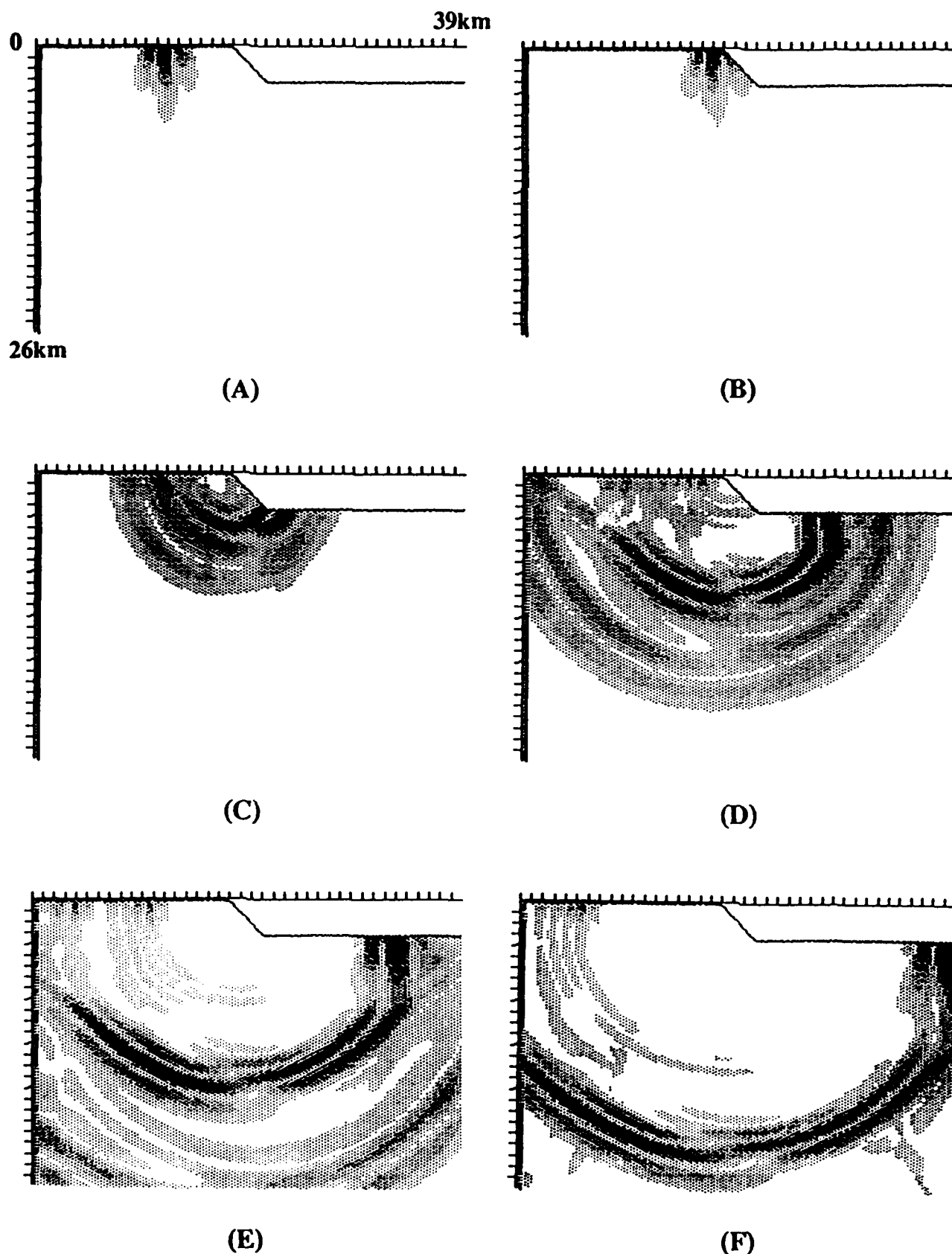
Figure 1 Snapshots of the displacement field due to a Rayleigh wave incident upon 45° ramp. Successive frames are separated by 2 sec intervals. Displacements are proportional to the darkness of the plot and are normalized to the maximum in each frame. The diffraction pattern generally becomes much more complicated when the the height of the ramp is larger. The corners act as point sources radiating converted bodywaves (mainly S wave).
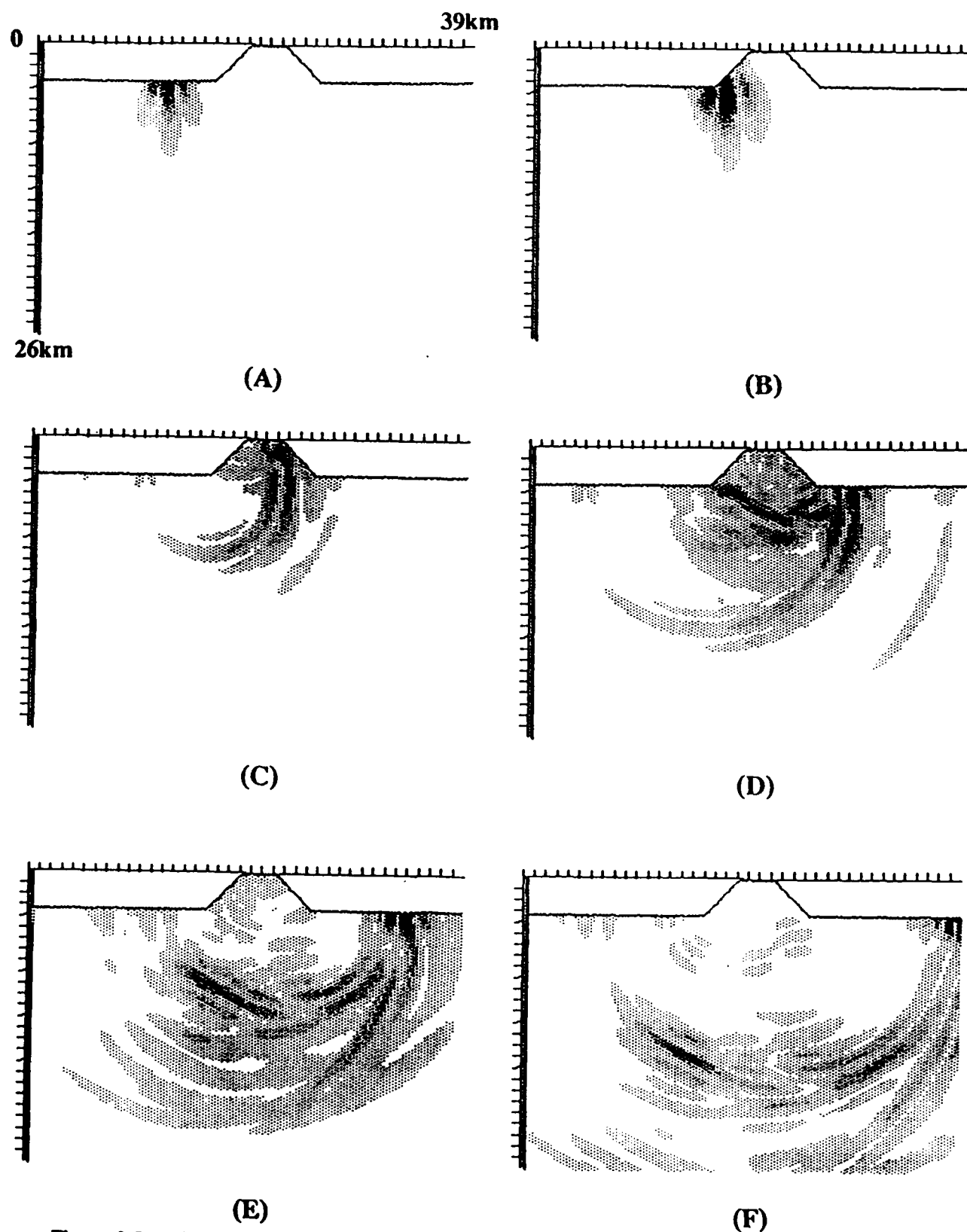
Figure 2 Rayleigh wave incident upon a trapezoidal mesa of height 1 λ. The high-frequency fraction of the Rayleigh wave propagates along the mesa surface while the low-frequency fraction tunnels through the mesa.
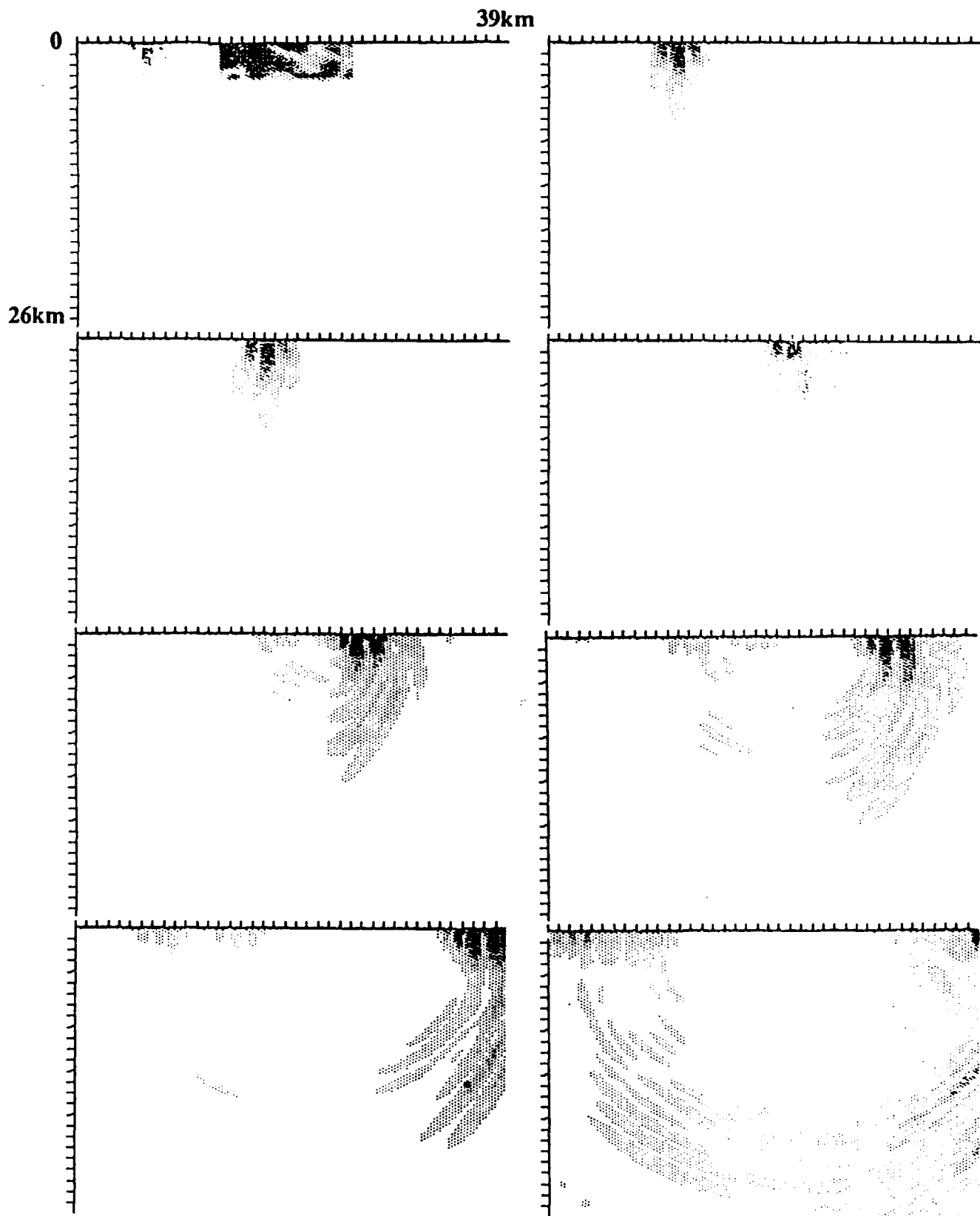
Figure 3 Snapshots of the displacement field due to Rayleigh wave propagating in a medium of size 39km by 26km with shallow heterogeneity of $\sigma = 7\%$, $a = 2km$, $h = 3.2km$, $L = 12km$ embedded in the central portion.

135

HIGH FREQUENCY SEISMIC SOURCE FUNCTIONS FOR CAVITY
DECOUPLED UNDERGROUND NUCLEAR EXPLOSIONS

J. R. Murphy

S-CUBED

OBJECTIVE

The objective of this program is to conduct a more rigorous theoretical investigation of the high frequency characteristics of decoupled seismic sources and to assess the implications of these investigations with regard to the detection and discrimination of small decoupled explosions. This is being accomplished through a combination of detailed deterministic simulations and analyses of new empirical data recorded from partially decoupled explosions at the Nevada Test Site.

RESEARCH ACCOMPLISHED*

The seismic source approximation for decoupled explosions which has been used in most previous studies of detection and identification (e.g., Evernden et al., 1986) corresponds to the linear, elastic solution for a simple step in pressure acting in a spherical cavity. In fact, however, it has long been recognized that this is a very crude approximation to the actual pressure induced in a cavity by a nuclear explosion, particularly at high frequencies. For example, Figure 1 shows a comparison of the cavity pressure history for a fully decoupled 5 kt explosion computed by Patterson (1964) using a nonlinear finite difference code with the corresponding step pressure approximation. It can be seen that the more precise finite difference solution predicts a large (more than 1.5 kilobar) initial pressure spike on the cavity wall, followed by a rapid decay and subsequent oscillation about the steady-state value characteristic of the step function approximation. The nature of this initial pressure spike can be most easily understood by considering the pressures induced by an atmospheric nuclear explosion. Brode (1968) has

---

* Since this project was only recently initiated (April 1, 1987) this discussion will be limited to an overview of our research objective plan.

shown that for peak incident shock pressures (P_S) of more than a few hundred bars, the peak value can be expressed as a function of yield (W) and range (r) by the approximate relation

$$P_S \approx \frac{3.08 \times 10^6 \ W}{r^3} \qquad (1)$$

where r is in meters, W in kt. Now, to a first order of approximation, the reflection of the shock from the cavity wall can be analyzed by assuming the wall is rigid. In this case, Brode (1968) has shown that the shock reflection factor, F_S, can be approximated by the relation

$$F_S = \frac{2 + 1.067 \ P_S}{1 + 0.082 \ P_S} \qquad (2)$$

Thus, for the Patterson calculation shown in Figure 1, which corresponds to a 5 kt explosion in a cavity with a radius of about 50 m, the peak incident shock pressure from (1) is about 125 bars and the corresponding shock reflection factor from (2) is about 12, leading to an initial pressure spike estimate of 1.5 kilobars, in good agreement with that shown in Figure 1. The subsequent oscillations in Figure 1 represent the reverberations of this shock in the cavity, which eventually damp out to the late-time equilibrium pressure value of 75 bars.

It is not clear at the present time how this complex pressure history might affect the corresponding decoupled seismic source function, but Figure 2 shows a frequency domain comparison of the reduced velocity potentials computed from the two pressure histories of Figure 1, assuming linear, elastic response of the cavity wall. It can be seen that while these two source estimates are comparable at low frequency, they diverge significantly for frequencies above 10 Hz. Thus, for example, the peak at about 65 Hz in Patterson's (1964) finite difference source corresponds to the inverse of the shock reverberation time in the cavity, which has no counterpart in the step approximation. A more fundamental concern is that the large initial pressure spike may well induce nonlinear response in the surrounding medium which could significantly modify the solution at both high and low frequencies.

In an attempt to address these issues, we plan to carry out a series of detailed, nonlinear finite difference simulations in which the seismic response to more realistic explosive pressures will be computed for a range of spherical cavity configurations. In these simulations, the full nonlinear response of the cavity wall to the simulated pressure loading will be computed using a finite difference zoning adequate for the accurate representation of frequency

components up to 40 Hz and all problems will be run to a range at which the medium response is completely linear. Representative calculations will be performed for salt, granite and tuff media and the results of these calculations will be compared with those predicted using the simple step pressure analytical model employed by Evernden et al. (1986) in order to establish uncertainty bounds on the seismic characteristics of decoupled explosions at high frequencies.

In addition, data recorded from recent NTS explosions in hemispherical cavities (i.e., MILLYARD) are being investigated in order to provide further empirical constraints on decoupled seismic source models. Specifically, we plan to analyze the ground motion data recorded on the surface directly above the cavity with the objective of defining the high frequency source characteristics of such tests. In principle, the high frequency components of these ground motions should be dominated by the initial shock on the cavity wall and thus should provide valuable insight concerning the high frequency seismic radiation to be expected from corresponding spherical cavities.

CONCLUSIONS AND RECOMMENDATIONS

Since this project has just begun, it is not possible to state any definitive conclusions at this time. However, it does seem clear that the simple step function approximation to the cavity pressure induced by a decoupled explosion can only be considered to be applicable in the low frequency limit. At higher frequencies, complex phenomena associated with pressure spikes on the cavity wall will have to be evaluated to determine their influence on estimates of regional detection and identification capability.

REFERENCES

Brode, H. L. (1968), "Review of Nuclear Weapons Effects," Annual Review of Nuclear Science, 18, 153.

Evernden, J. F., C. B. Archambeau and E. Cranswick (1986), "An Evaluation of Seismic Decoupling and Underground Nuclear Test Monitoring Using High Frequency Seismic Data," Reviews of Geophysics.

Patterson, D. W. (1964), "Theory of Nuclear Explosion in a Cavity Including the Effects of Shock and Nonelastic Effects on the Wall and Comparison with Tamped Explosions - Project Dribble," UCRL-7916.
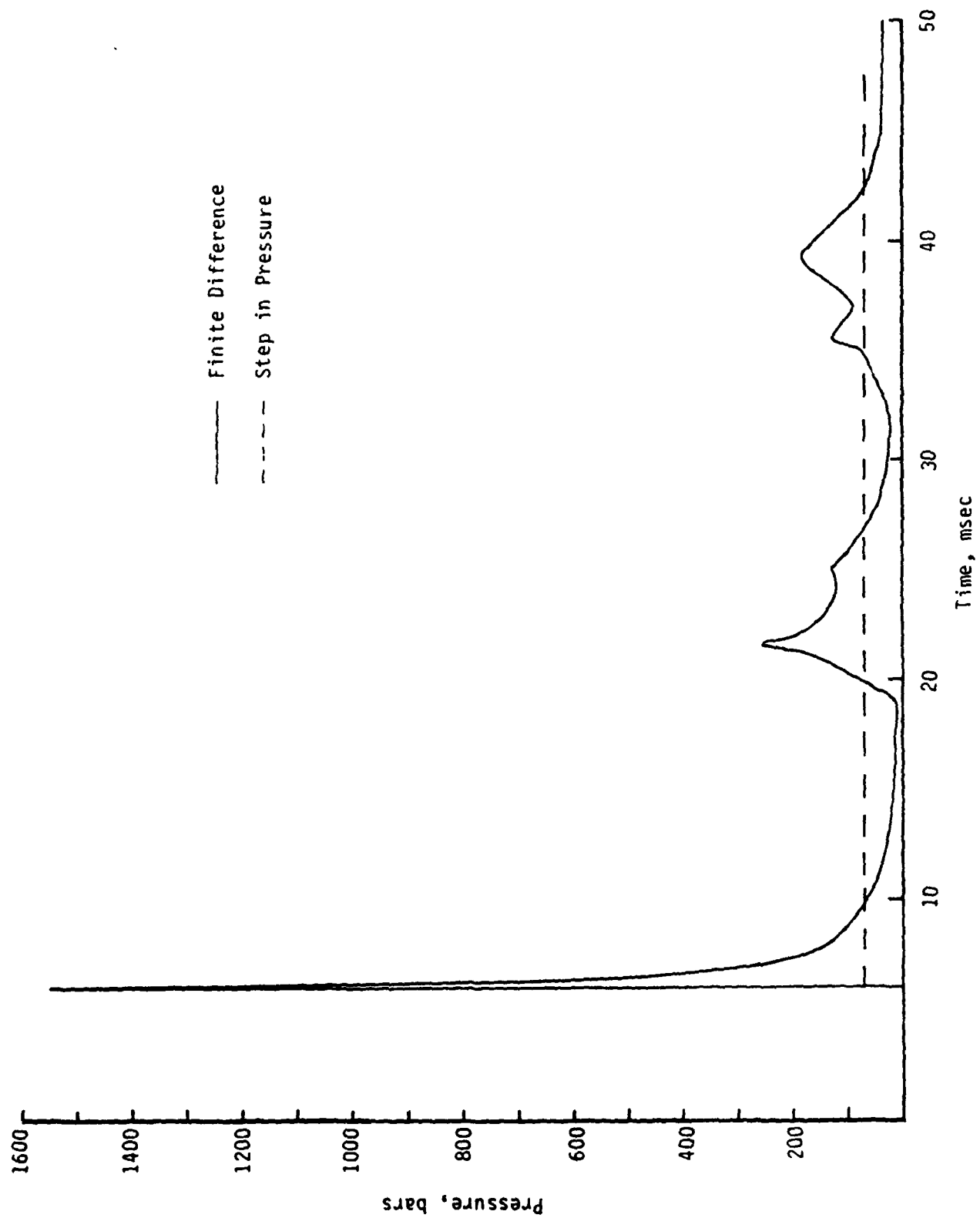
Figure 1. Pressure on cavity wall associated with a fully decoupled 5 KT explosion.

Legend:
- Finite Difference
- Step in Pressure
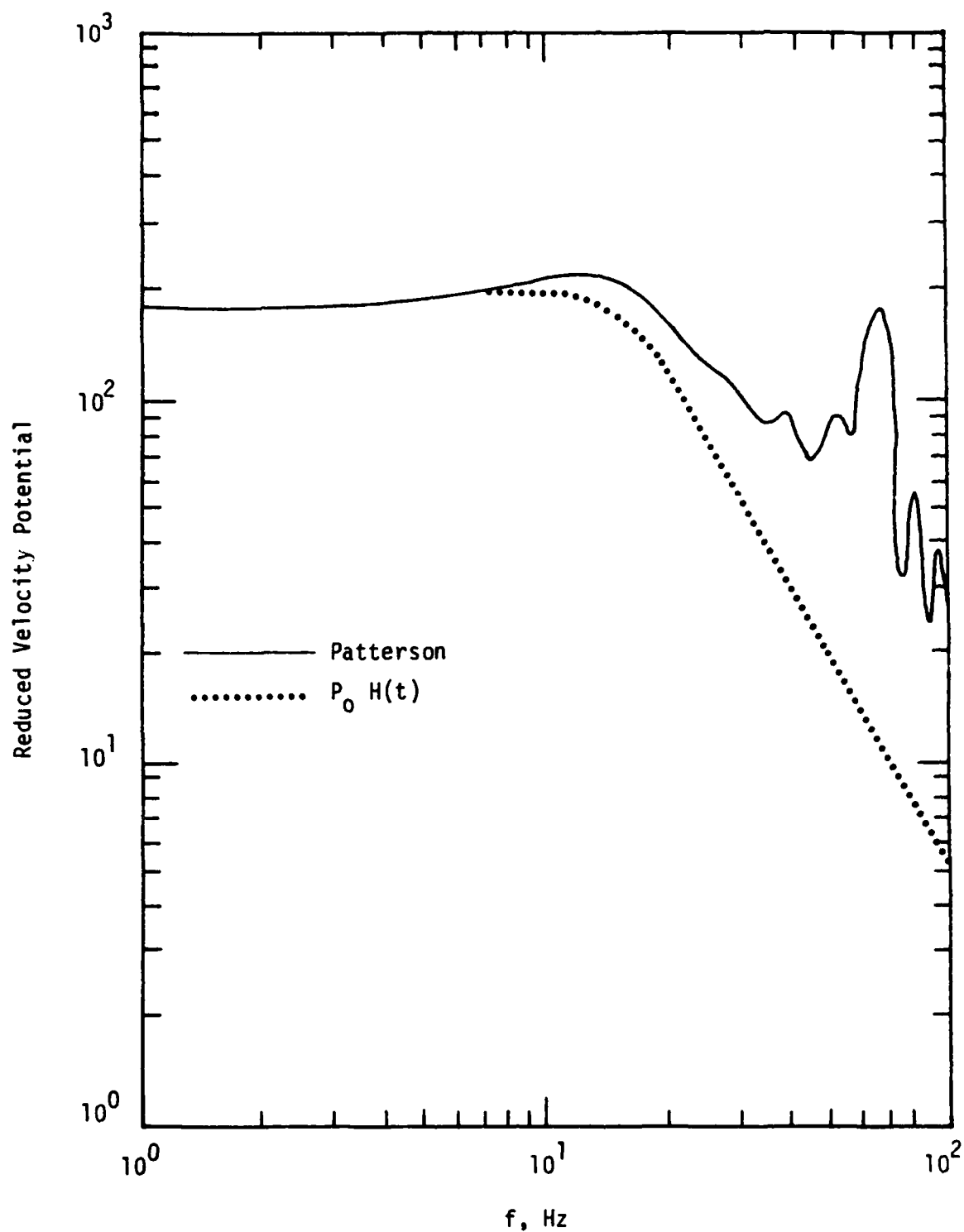
Figure 2. Comparison of decoupled seismic source functions, W = 5 KT, salt.

Charles G. Sammis and Xiao Fei Chen
Department of Geological Sciences
University of Southern California, Los Angeles, CA 90089-0741

Steven M. Day
S-Cubed
P.O. Box 1620
La Jolla, California 92038-1620

OBJECTIVE

The primary objective of this research is to develop a constitutive relation for rock which incorporates the physics of crack nucleation, growth, and interaction under stress conditions generated by an underground nuclear explosion. This approach is motivated by 1) the desire to include variables such as porosity, water saturation, and the density and orientation of preexisting cracks and joints into the modeling, 2) discrepancies between the calculated and observed near-field velocity pulse for explosions in low-porosity crystalline rock, and 3) discrepancies between the velocity pulse observed in small-scale laboratory simulations and that observed in the field

Toward this goal, we are formulating a "damage mechanics" for compressive loading. For a given distribution of initial flaws (cracks or pores in the rock), we calculate the nucleation and growth of microfractures as a function of stress using linear elastic fracture mechanics. The state of crack extension at any time is represented by a damage vector. As damage accumulates, the elastic stiffness decreases and the stress-strain relation becomes non-linear. At large values of damage, the fractures interact, and damage accumulation is accelerated A peak stress is achieved after which the strength decreases with additional strain. The current theoretical challenge is to develop the correct model for fracture interaction, since the peak (failure) stress and subsequent stain weakening are sensitive to the interaction. Although there have been several preliminary formulations (Costin, 1985; Sammis and Ashby, 1986a,b) the interaction has not been adequately treated

In parallel to the formulation and testing of the damage mechanics model, we are implementing it in a numerical source simulation in order to

test our working hypothesis that the strain-weakening associated with the fracture interactions is responsible for the pulse shapes observed in the near field of U.S underground nuclear tests in granite

RESEARCH ACCOMPLISHED

For the three U.S underground tests in granite, the particle velocity was measured in the free field as a function of distance from the shot-point In each case, numerical simulations using continuum mechanics with strength values measured in the laboratory have failed to predict the velocity pulse width to within a factor of about 5 (Rimer *et al* , 1987). Models which have predicted the correct pulse-width all have required a large reduction in post-shock strength to values well below those measured in the laboratory, even for prefractured samples

The physical mechanism responsible for the post shock weakening has been less clear Cherry an Rimer (1982) have invoked an "effective stress" mechanism in which the free crack and pore space is eliminated during the initial compression. Fluids in the remaining saturated cracks are compressed to high pressures which support part of the confining stress thus lowering the failure surface However, Scholz (1982) has argued that dilatancy hardening is expected to override any weakening produced by the effective stress effect

Russian scientists (Zamyshlyayev *et al* , 1980) have also shown that post-shock weakening can produce the pulse broadening observed in the Hard Hat explosion, but their proposed mechanism is quite different They attribute weakening to the time dependent growth of cracks behind the shock front. They also assert that shear deformation behind the shock front produces a rotation of the blocks of rock between fractures, and results in dilatancy. Based on their modeling, they conclude that post-shock weakening and dilatancy contribute equally to the observed pulse shape The proposed weakening is shown in Fig 1 (from their paper;
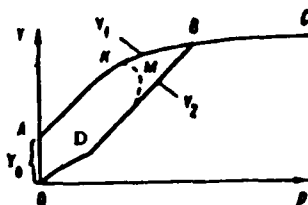
Figure 1 Post-shock weakening path from Zamyshiyayev *et al* (1980) Y_1 is the strength of the undamaged rock. Y_2 is the strength of the damaged rock The dashed path represents the strength reduction which accompanies crack growth

Our explanation of weakening is, in principle, the same as that proposed by Zamyshlyayev _et al_ (1980) except that our model is based on the micromechanics of crack growth and interaction (see eg Sammis and Ashby, 1986a,b, Ashby and Hallam, 1986) As illustrated in Fig 2, we model the activation of preexisting cracks and joints (of initial length a) by the explosive pulse
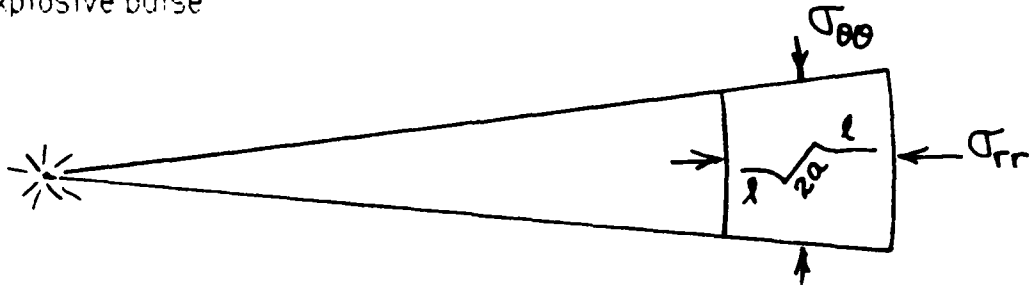
Figure 2. Out-of-plane extension of preexisting fractures in an explosion generated stress field

We have developed analytic expressions for the out-of-plane extension, l, of such flaws in terms of the applied stress

$$\sigma_{rr}\sqrt{\pi a}/K_{1c} = F_1 + F_2 \qquad (1)$$

where F_1 describes the initiation and growth of an isolated fracture and F_2 describes the additional crack growth due to the interaction which we model as arising from the bending of beams of solid rock between fractures. This interaction is broadly analogous to the block rotation proposed by the Russian investigators as discussed above. Analytic expressions for these two contributions are:

$$F_1 = -(1+L)^{3/2}/[[1-\lambda-\mu(1+\lambda)-4.3\lambda L][0.23L+1/(\sqrt{3}(1+L)^{1/2})]] \qquad (2)$$

$$1/F_2 = -(\sqrt{2}/\pi)D_0^{1/2}(L+\alpha)^{1/2}[[1-(8/\pi)D_0\lambda(L+\alpha)^3][1-(2/\pi)D_0\lambda(L+\alpha)^3]]^{1/2} \qquad (3)$$

In these expressions, $\lambda=\sigma_{\theta\theta}/\sigma_{rr}$ is the ratio of hoop stress to radial stress, μ is coefficient of friction on the starter crack, $L = l/a$, and $D_0 = \pi a^2 N_A$ (N_A is the number of fracture per unit area) measures the initial fracture density. The geometrical factor $\alpha=1/\sqrt{2}$

If we define damage as $D = l^2 N_A = L^2 f_A/\pi$ where f_A is the fraction of the total area which contains starter cracks, then Equation (1) can be

used to calculate the stress as a function of damage. As shown in Fig 3, this analysis predicts a peak strength which we identify as the compressive strength. As damage increases beyond this point the strength falls. Strain-weakening thus appears as a natural consequence of the fracture interaction at large values of damage.
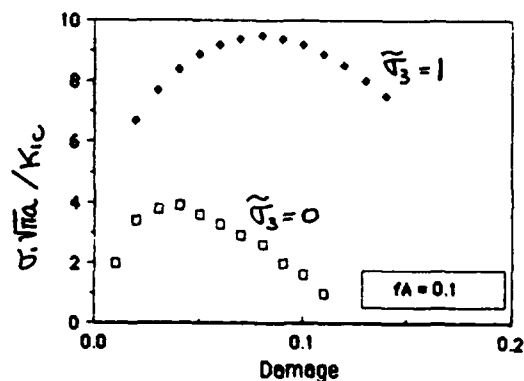
Figure 3 Stress as a function of damage calculated using Eqn (1)

It is sometimes assumed (see eg. Scholz, 1982) that the lower limit to the strength of a shattered rock is given by the friction law. However, this may not be the case if weakening is due to runaway interaction and growth of fractures, since friction is not involved in this process. Rather, dilatancy and crack growth are driven by the rotation of blocks between fractures.

The damage mechanics approach may also help interpret the results of a recent set of laboratory simulations in granite which were designed to investigate the pulse-broadening observed in the field (Nagy and Florence, 1986). The results of these experiments are summarized in the table below.

SAMPLE DESCRIPTION	PULSE SHAPE
As received (dry)	Narrow
(wet)	Narrow
Thermally fractured (dry)	Narrow
(wet)	Narrow
Gas fractured (dry)	Narrow
(wet)	Slightly wider (2-3x)

The gas fractured samples were the most extensively fractured, and probably had the largest fractures since they were barely cohesive. Only these samples which contained water (at a pressure equal to the confining pressure) showed any pulse broadening. All other cases produced a narrow pulse in agreement with numerical predictions based on strength parameters measured in the laboratory.

We interpret the lack of pulse broadening in these simulations to be the consequence of scaling effect inherent in the physics of crack growth. The stress necessary to nucleate and extend out-of-plane crack growth scales as the inverse square root of the initial flaw size a (see Eqn (1).) Since the maximum fracture length in the simulation is limited by the sample size, the experimental results can be explained if these flaws are too short to be activated at the stress levels produced by the scaled explosion. Quantitative verification of this explanation will require a full numerical simulation (which itself depends on the rheology), however, the following example illustrates the scaling effect.
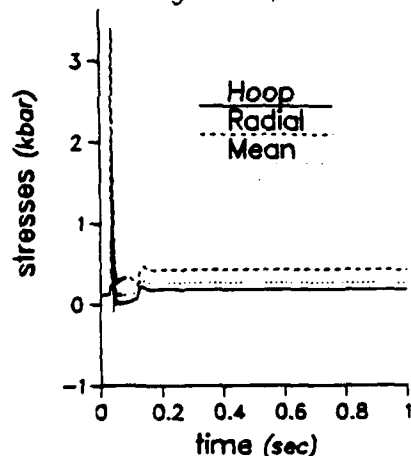
Figure 4 Stress pulse at a distance of 204 m from the Piledriver explosion (from Rimer *et al*., 1987)

Consider the stress pulse at a distance of 204 m from the Piledriver explosion shown in Figure 4. This stress pulse was calculated using laboratory strength data for granite. At the stress peak, σ_{rr} = 334 MPa and $\sigma_{\theta\theta}$ = 135 MPa. Equations (1) and (2) were used to calculate the crack growth under these conditions, and the results are shown in Fig 5a. The case $\mu=0.6$ is expected in the dry case. It is assumed that water saturation in the cracks will reduce the coefficient of friction to $\mu=0$. For either value of μ, the hoop stress is large enough that significant crack growth does not occur. This minimal crack growth justifies our neglect of the interaction terms given by Equation (3).
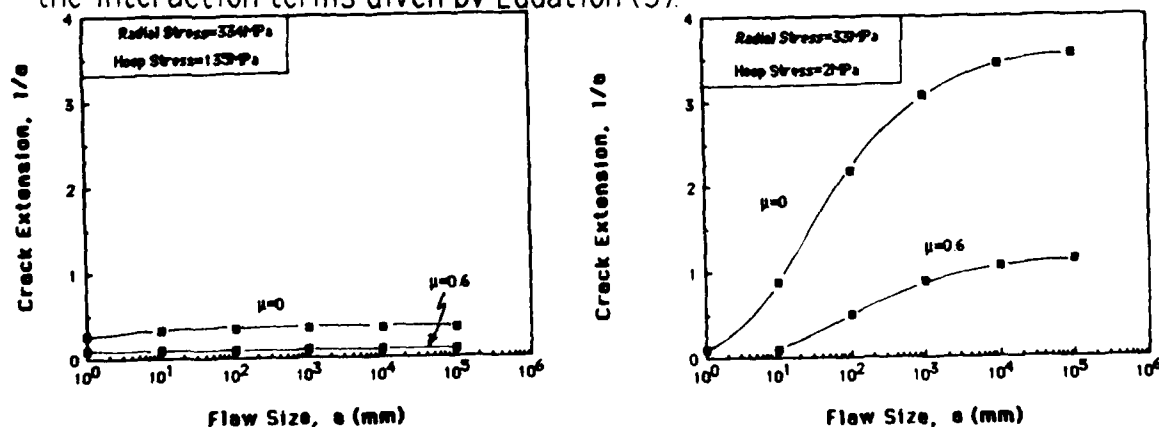
Figure 5. Crack extension as a function of initial crack size. Case a is at peak stress, case b is post-peak.

After the peak, the stresses fall to values of σ_{rr} = 33 MPa and $\sigma_{\theta\theta}$ = 2 MPa. Crack growth under these conditions are shown in Figure 5b. Note that in the dry case, cracks larger than about one meter show significant growth. Hence a model experiment using a sample with dimensions approximately equal to or smaller than one meter would not show weakening. For the wet case, cracks larger that one centimeter show significant growth. Hence a meter size sample might be expected to snow some weakening effects if it were saturated.

CONCLUSIONS AND RECOMMENDATIONS

Based on the above analysis we draw the following conclusions:

1) Strain weakening is a good candidate for the post-shock strength reduction required to fit the pulse shapes observed for U.S. underground explosions in granite.

2) Strain weakening may potentially reduce the shear-strength below frictional values.

3) Lack of pulse broadening in laboratory simulations may be the result of $1/\sqrt{a}$ scaling in out-of-plane fracture propagation. The effect of fluid saturation in such experiments may be to reduce sliding friction on existing fractures thereby allowing the extension of smaller starter cracks.

Further progress will require the incorporation of damage mechanics into the numerical simulations.

REFERENCES

Ashby, M.F. and S.D. Hallam. 1986. The failure of brittle solids containing small cracks under compressive stress states, Acta metall., 34, 497-510

Cherry, J.T., and N. Rimer, 1982 Verification of the effective stress and air void porosity constitutive model, S-Cubed Report VSC-TR-83-1

Costin, L.S., 1985. Damage mechanics in the post-failure regime, Mechanics of Materials, 4, 149-160

Nagy, G. and A. Florence, 1986. Spherical wave propagation in low porosity brittle rocks, SRI Report DNA-TR-86-000.

Rimer,N., J.L. Stevens, and S.M. Day, 1987. Effect of pore-pressure, fractures, and dilatancy on ground motion in granite, S-Cubed Report SSS-R-87-8670

Sammis, C.G. and M.F. Ashby, 1986a. The failure of brittle porous solids under compressive stress states, Acta metall, 34, 511-526

Sammis, C.G. and M.F. Ashby, 1986b. The damage mechanics of brittle solids in compression, Proceeding of the 8th annual DARPA/AFGL seismic research symposium, 66-85.

Scholz, C.H., 1982. Rock strength under confined shock conditions, S-Cubed Report SSS-R-83-5906.

Zamyshlyayev, B.V., L.S. Yevterev, and S.G. Krivosheyev, 1980. Equations of rock state under explosion-induced loads, Doklady Akademii Nauk SSSR, 251, 322-326

FINITE EXPLOSIVE SOURCES IN SPACE AND TIME

Brian Stump, Sharon Reamer
Southern Methodist University
Dallas, Texas 75275

OBJECTIVE

This work is designed to constrain the physical and mathematical models of near surface explosive arrays. These source arrays range from two dimensional surface sources which are detonated simultaneously for military purposes to three dimensional arrays of explosives which are ripple fired for mining purposes.

Our goal is to understand long period coupling, corner frequency variation and high frequency role-off for these explosive arrays. This source quantification will allow comparisons to be made with fully contained explosions and earthquakes.

The thrust of this work is the acquisition and analysis of near source data from these types of sources. The near-field data will be used to constrain source variations. Regional data from the same explosive events will be utilized in a study of source and propagation path trade-offs.

RESEARCH ACCOMPLISHED

In the two months since contract initiation work has focused on the acquisition of data in two areas. The first is a set of near-field acceleration measurements from a series of 2 dimensional planar explosive shots conducted by the Air Force Weapons Laboratory. These rectangular sources had equivalent TNT yields of 150,000 lb. (SS), 300,000 lb. (SSR), 2,000,000 lb (LS) and 3,300,000 lb (LS-IR). Two component data were recorded in the 260 to 5500 ft. range. The tests were conducted near Yuma, Arizona in desert alluvium.

Representative waveforms from SSR, SS, and LS are given in Figure 1. The effect of source sizes is reflected in both the amplitude and pulse widths of the waveforms. Propagation complications become evident at the 5500' range. Particle motion diagrams of the data indicate initial rectilinear motion of the body waves, followed by a prograde higher mode surface wave, and concluding with the retrograde fundamental mode.

Spectral estimates in Figure 2 give a qualitative feel for the possible variations in source characterization over the yield range of 150,000 to 2,000,000 lbs. The largest event has a source corner between 1 and 1.5 Hz while the smallest event has a source corner between 3 and 3.5 Hz. Spectral ratios, Figure 3, of the largest to smallest event also support this interpretation. At the very high frequencies (5 hz) the spectra overlie one another.

The second set of data which will be utilized in this study is from a series of quarry explosions in New England. A field

program to acquire this data is being jointly implemented by AFGL, AFWL, MIT, BC, and SMU. The experiments are scheduled to take place over the 13-24 July 1987 time period. Preliminary plans call for a 40 station instrument array. Approximately 10 of theses instruments will be used to complete the near source characterization while the remaining instruments will be utilized in the quantification of the regional motion field. The different geological environment along with ripple fire characteristics of the surface nmining shots will be contrasted with the Yuma, Arizona sources.

CONCLUSIONS AND RECOMMENDATIONS

Data from a series of military chemical explosions spanning the range of yeilds 150,000 to 3,300,000 has been gathered. Preliminary analysis indicates significant variations from source to source. Work is continuing on quantifying these variations. The next step will be a data modeling exercise and the testing of scaling relations.

A summer field series designed to acquire near source and regional data from a set of quarry explosions in New England is planned.

RELATIVE VERTICAL VELOCITY

FIGURE 1a

149
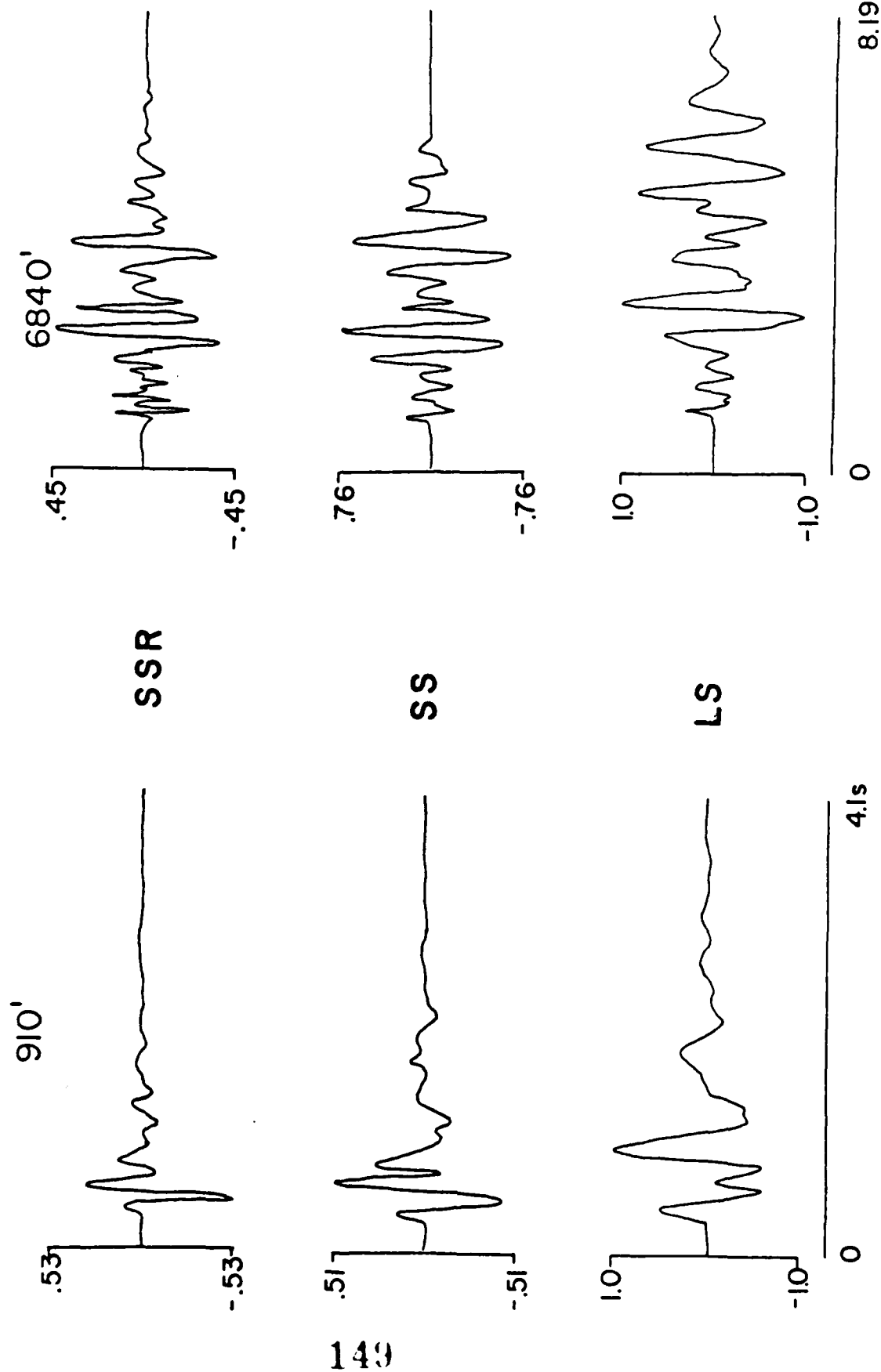
RELATIVE RADIAL VELOCITY
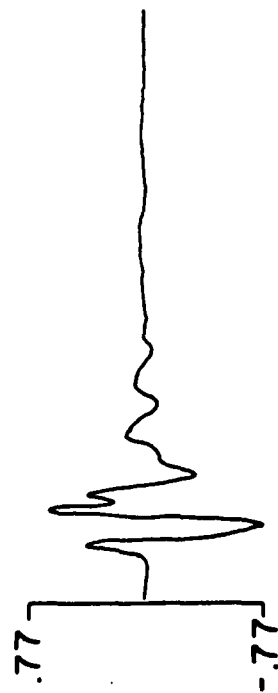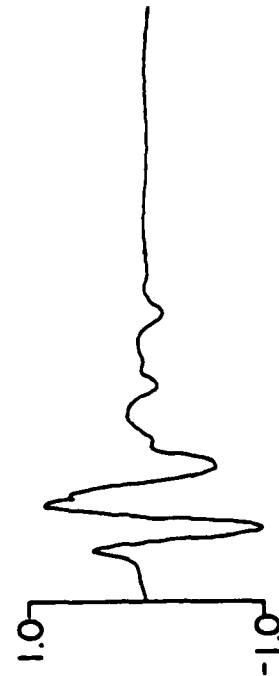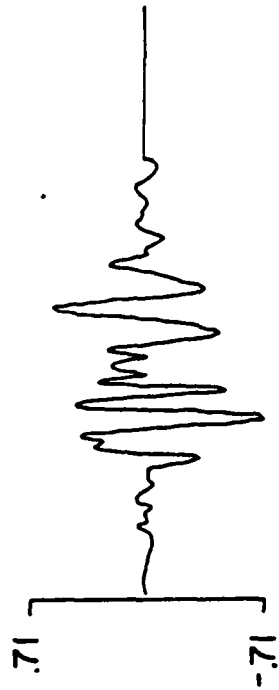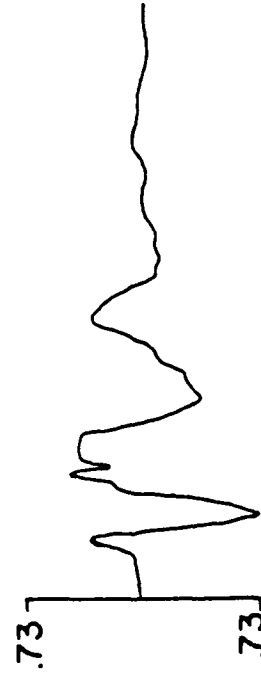
FIGURE 1b

RELATIVE DISPLACEMENT SPECTRA

RADIAL 6840'

VERTICAL 6840'

RADIAL 910'

VERTICAL 910'

—— LS 2×10^6 lb

--- SS 3×10^5

········ SSR 1.5×10^5

FIGURE 2

151

SPECTRAL RATIOS
LS/SSR

RADIAL 6840'

VERTICAL 6840'

RADIAL 1919'

VERTICAL 910'
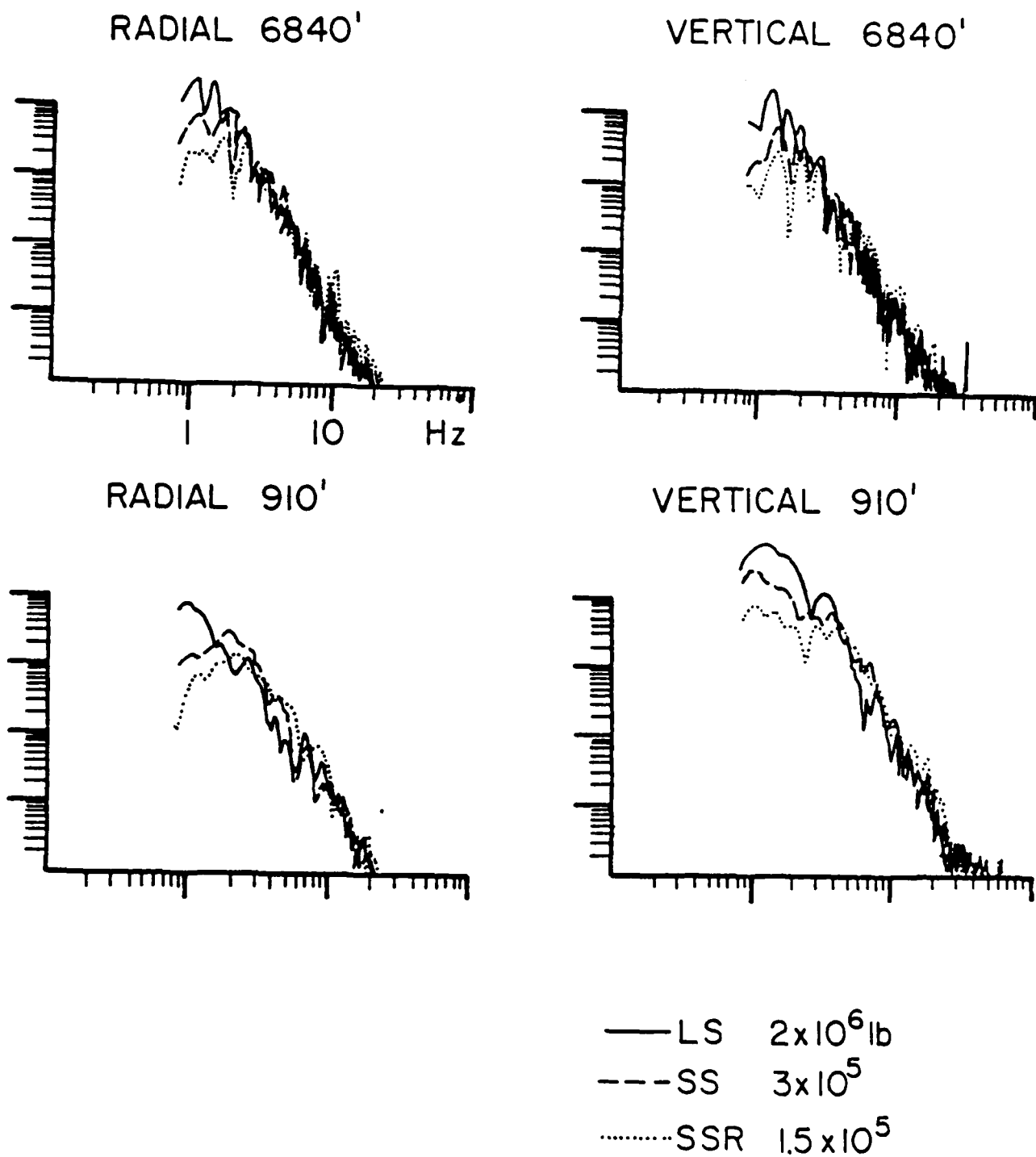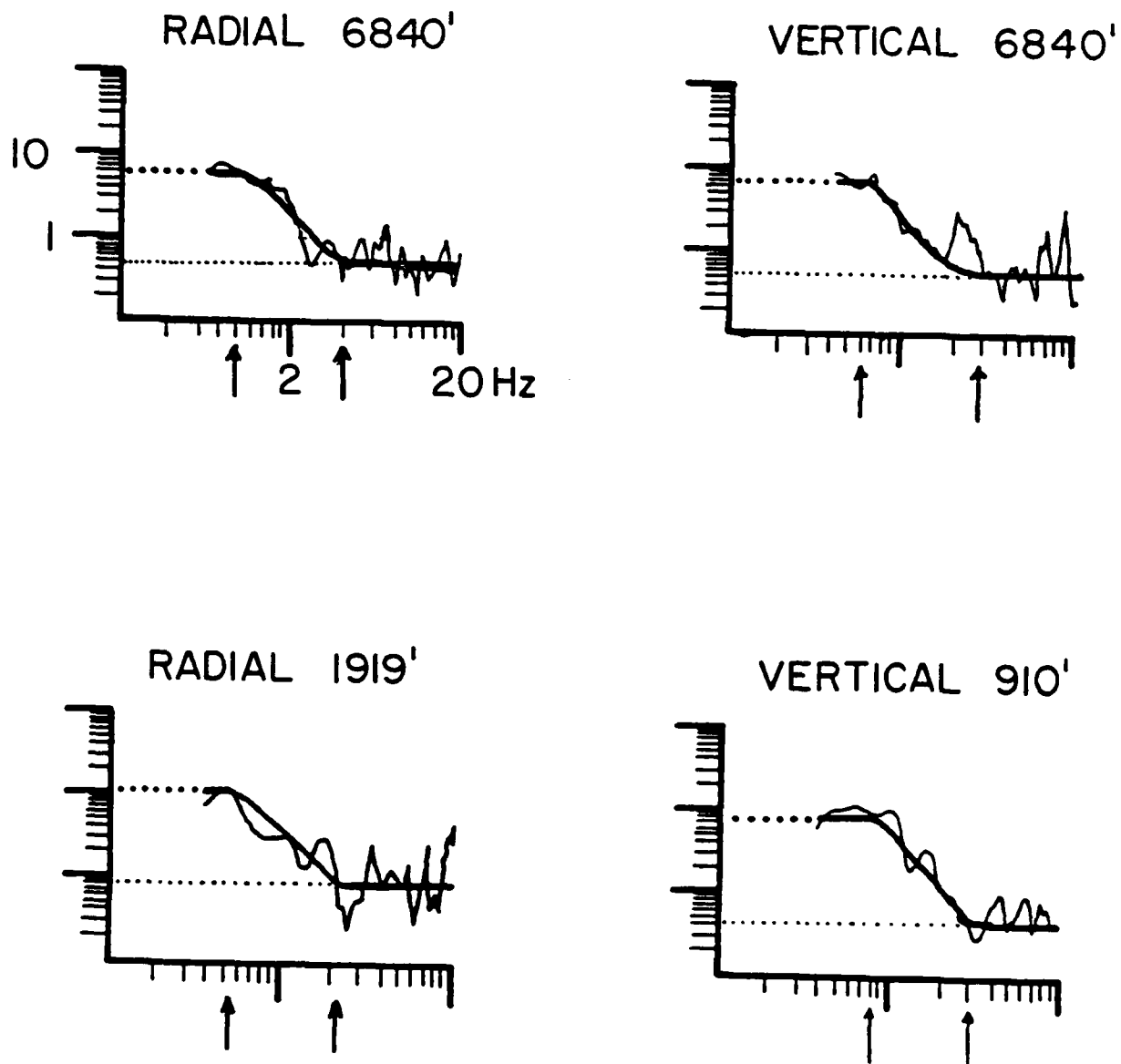
FIGURE 3

SCATTERING AND ATTENUATION IN NEW ENGLAND

M. NAFI TOKSÖZ, ANTON M. DAINTY, EDMUND REITER AND VERNON CORMIER

EARTH RESOURCES LABORATORY
DEPT. EARTH, ATMOSPHERIC, AND PLANETARY SCIENCES
MASSACHUSETTS INSTITUTE OF TECHNOLOGY

OBJECTIVE

The dependence of ground motion U of frequency ω with distance r from the source may be described by the equation

$$U(r,\omega) = S(\omega) \cdot F(r) \cdot \exp[-r\omega/(Qv)] \qquad (1)$$

In (1) S represents the source and v is the seismic wave velocity. The factor $F(r)$ is the geometrical spreading factor due to the propagation of motion in a perfectly elastic medium without random scattering. In a homogeneous medium $F(r) = 1/r$ for body waves and $= 1/\sqrt{r}$ for surface waves (not including the effect of dispersion), and this form is often used at ranges of less than 100 km. The exponential term parameterized by Q describes the effect of attenuation due to imperfect elasticity (anelastic attenuation) and random scattering. Our objective is to examine the relative contribution of scattering and random attenuation in New England.

While physical definitions of Q are given in the literature in practice Q is usually measured by methods based on equation (1) or the corresponding time equation. A difficulty that arises with this "operational" definition of Q is that different results may be obtained based on different methods of measurement even in simple cases (Aki and Richards, 1980, p. 168). A particularly important case is the influence of scattering. If a short pulse travels through a medium in which both scattering and anelasticity occur, then the total Q, Q_t, is (Dainty, 1981)

$$1/Q_t = 1/Q_i + 1/Q_s \qquad (2)$$

In (2) Q_i is the anelastic Q. The loss of energy from the pulse due to scattering is described by $Q_s = \omega/(2gv)$, where g is the scattering cross section per unit volume, or turbidity. Equation (2) indicates that for the case of a short pulse the influence of anelastic attenuation and scattering cannot be separated unless some model for the Q components is used. However, the scattered energy represented by Q_s is merely deflected, not lost from the wavefield. Measurements of Q which examine a substantial window in time of the seismogram, such as coda Q, may include some of this energy. Below we present summaries of three investigations we have carried out or are carrying out that measure Q in different ways. The first interprets the attenuation of the strong motion measure pseudo velocity. Since an integration over the duration of strong motion is carried out in this measure, the total energy in the seismogram including scattered energy is

measured. Our investigation explicitly examines the question of the relative attenuation due to anelasticity and scattering and separates the contribution of each using transport theory. Since the anelastic attenuation has been explicitly separated, we include discussion of possible physical mechanisms. The second investigation examines the Rg phase (fundamental mode Rayleigh wave) in the frequency range 1–10 Hz at distances of 10–30 km. This is a pulse measurement and equation (2) should apply, i. e., the total Q represents the combined effect of anelasticity and attenuation without separating them. Finally we discuss the implications of some previous measurements of coda Q. While this method has become a standard method of measuring Q, the interpretation of the results has not been clear.

RESEARCH ACCOMPLISHED

Attenuation of Pseudo Velocity and Intrinsic Q

The first part of the work summarized in this section is an interpretation of the attenuation of pseudo velocity (PSV) with distance using the compilation of Risk Engineering, Inc. for EPRI (Toksöz et al., 1987). These PSV records cover the northeastern United States and eastern Canada. Data for frequencies of 1 and 5 Hz were analyzed. The theory used is a multiple scattering transport (of energy) equation formalism due to Wu (1984). The theory calculates the total energy density $E(r)$ observed at distance r from a point source in a uniform whole space. Since the PSV includes an integration over the duration of strong motion and is a velocity, it was assumed that $4\pi r^2 E(r) = 4\pi K \cdot (PSV.r)^2$ where the term $4\pi r^2$ corrects for spherical spreading and K is an unknown constant. For this to be justified, the range r must be limited to less than 100 km so that Moho interactions can be excluded. The theory requires that two parameters be specified. One is the extinction coefficient $\eta_e = \omega/(Q_t v)$, or equivalently its reciprocal the extinction length $L_e = 1/\eta_e$. The other parameter is the albedo $B_0 = g/\eta_e$ where g is the turbidity introduced in connection with equation (2). Thus low albedo corresponds to weak scattering and high albedo to strong scattering. The range of albedo is $0 \le B_0 \le 1$. A determination of these two parameters would allow a determination of Q_t, Q_s (through g) and, by (2), Q_i.

The expression for $E(r)$ for a source of unit energy is

$$E(r) = \frac{\eta_e P}{4\pi r} \exp(-\eta_e dr) + \frac{\eta_e}{4\pi r} \int_1^\infty f(s, B_0) \exp(-\eta_e rs)ds \qquad (3)$$

where

$$f(s, B_0) = \left\{ \left[1 - \frac{B_0}{s} \tanh^{-1}(1/s) \right]^2 + \left[\frac{\pi B_0}{2s} \right]^2 \right\}^{-1} \qquad (4)$$

and

$$P = \frac{2d^2(1 - d^2)}{B_0(d^2 + B_0 - 1)} \qquad (5)$$
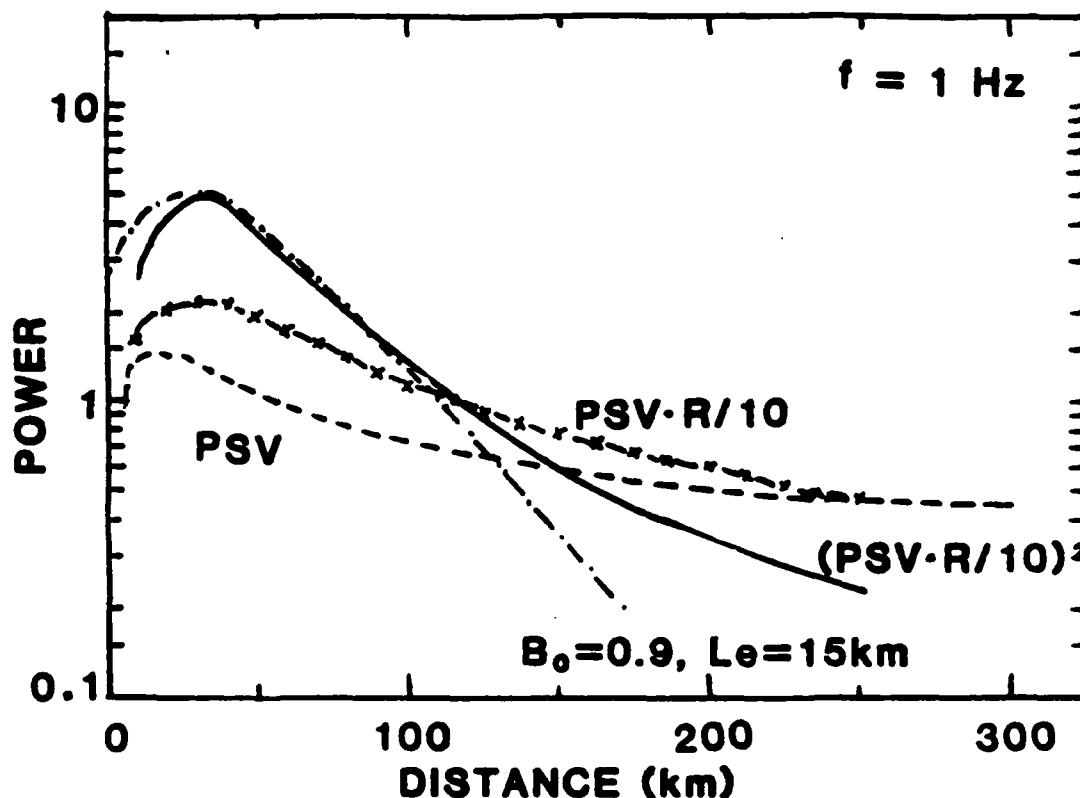
Figure 1: Match between the multiple scattering model (chained curve) and PSV data at 1 Hz. All curves labeled 'PSV' are based on a best fit of the data. Appropriate PSV curve for matching is $(\text{PSV} \cdot \text{R}/10)^2$ in the range 10–100 km.

where d is the solution of

$$\frac{B_0}{2d} \ln\left(\frac{1+d}{1-d}\right) = 1 \tag{6}$$

Figure 1 shows a fit of data at 1 Hz to equations (3–6). Table 1 gives the parameters used to fit both the 1 Hz and 5 Hz data. The results shown in Table 1 represent our first effort to separate the effects of scattering and anelastic attenuation. While they cannot necessarily be compared directly with the Rg and coda results presented below because the same seismic phases may not be involved, they give some strong clues as to the proper interpretation of these results. If the values given in Table 1 are used in equation (2) then the effect of scattering will dominate the attenuation. This appears to be the case for the Rg measurements presented next, where the values of Q are similar to the values of Q_s in Table 1, particularly at 1 Hz. At present we cannot assess the depth dependence in our analysis. An important result, however, of this analysis is the finding that Q_t

Table 1: Results from PSV Analysis.

Parameter	$f = 1$ Hz	$f = 5$ Hz
L_e	15 km	15 km
B_0	0.9	0.9
g	0.06 km^{-1}	0.06 km^{-1}
Q_s	30	150
Q_i	270	1350

given by equation (2) is not the appropriate quantity to define attenuation if the albedo is high and the total energy in the ground motion is considered (equation (3)). This seems to be reflected in the coda Q in the study region, since the values are more typical of the anelastic attenuation Q_i in Table 1.

Since the anelastic Q_i has been isolated and determined by the analysis above, as a second part of the study an interpretation of Q_i in terms of physical mechanisms has been made (Toksöz et al., 1987). Two physical mechanisms were considered, a constant Q due to solid anelasticity and the effects of fluid flow which will produce a frequency dependent Q. To reproduce the values of Q_i in Table 1 a constant Q between 500 and 2000 must be considered along with porosities of the order of 1% and permeabilities of about 100 darcies, values typical of fractured rocks. An interesting result is that for frequencies f greater than 1 Hz, the fluid flow theory gives $Q \propto f^{0.5}$, similar to the coda Q observations.

Attenuation of Rg

The data set used consists of recordings of blasts for a refraction experiment in southeastern Maine conducted by the USGS (Doll et al., 1986). The largest phase from these near surface sources, and hence the phase with the peak amplitude, is Rg, the fundamental mode Rayleigh wave. The frequencies observed on the records for Rg are 1–10 Hz. The Q is calculated by the two station method. First the attenuation coefficient $\gamma(\omega)$ is calculated as

$$\gamma(\omega) = \frac{1}{r_2 - r_1} \cdot \ln\left[\frac{\sqrt{r_2}\, U(r_2, \omega)}{\sqrt{r_1}\, U(r_1, \omega)}\right] \tag{7}$$

where r_1 and r_2 are the source-receiver distances for two records whose Fourier transforms are $U(r_1, \omega)$ and $U(r_2, \omega)$. Since the spectrum window contains the entire Rg wave train, there is no correction for dispersion. The total Q_t in the sense of equation (2) may be calculated from $Q_t = \omega/(2\gamma v)$.

When the measurements were examined, there appeared to be differences between Q values obtained along and across the local Appalachian strike. In Figure 2 we show averages of the Q
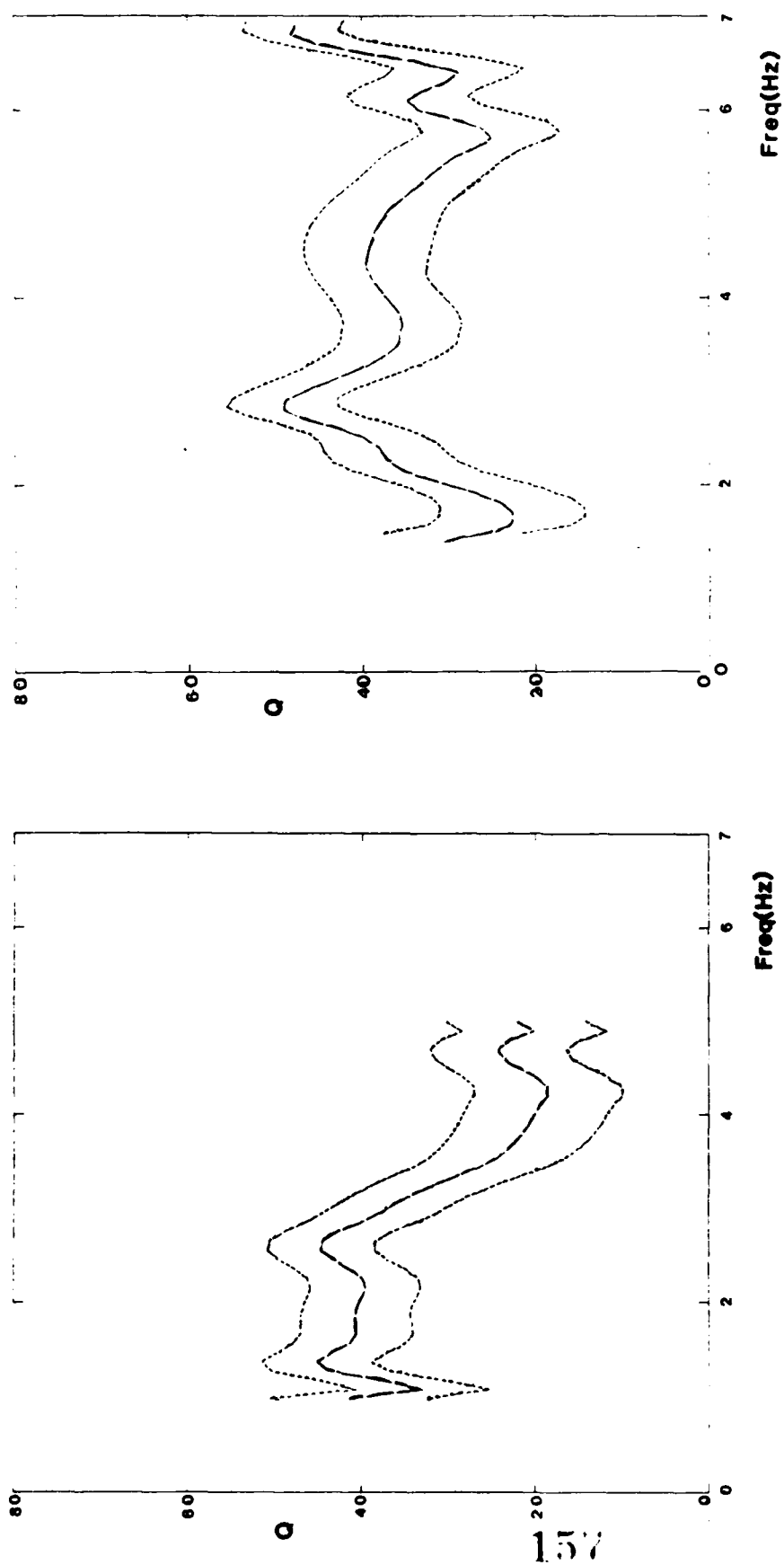
Figure 2: Average values of Rg Q for profiles perpendicular (left) and parallel (right) to strike. Dashed lines are ± one standard deviation.

across and along strike. Note that Q is low in both cases, between 60 and 20. These values explain the rapid disappearance of this phase with distance. They are substantially lower than the values derived by Pulli (1984) from coda discussed below: Pulli obtained a Q of 460 at 1 Hz, increasing with frequency. While it is not possible to separate Q_t into Q_i and Q_s, results presented in the previous section suggest that scattering is important, although Q_i is probably also low, as discussed below. These Q values refer to the upper 2 km of the crust. Azimuthal variation of Rg group velocity has already been noted in the data set we are using (Kafka and Reiter, 1986): Rg is fast along strike (SW–NE) and slow across strike. In Figure 2 we see that attenuation of frequencies above 3 Hz is stronger across strike than along strike. This may explain the common observation that isoseismal contours are often elongated along the structural strike, since these higher frequencies are important in shaking.

Coda Q

In this section we briefly discuss results obtained by Pulli (1984) on coda Q, Q_c, in the northeastern United States. Since this work is in the literature, we quote the following results: for codas at times less than 100 sec after origin

$$Q_c = 140f^{0.95} \tag{8}$$

while at times longer than 100 sec

$$Q_c = 660f^{0.4} \tag{9}$$

In interpreting these results, there has always been a question as to the correspondence of Q_c to other measures of Q. The depth relationships are not known—it is commonly assumed that Q_c is some form of average over the whole crust. In the standard single S scattering theory used to interpret coda, $Q_c = Q_t$ for S waves in equation (2). On the other hand, in the limit of strong scattering $Q_c = Q_i$. Our results in previous sections indicate that for times greater than 100 sec, $Q_c \simeq Q_i$, since the values are approximately equal. Also, the investigation of Q due to fluid flow in fractured rocks gives a similar frequency dependence, suggesting a possible mechanism. The results for coda Q are important because it is an easy measurement to make with routinely available data.

DISCUSSION AND CONCLUSIONS

Our studies of scattering and anelastic attenuation with distance at frequencies of 1–10 Hz indicate that the relative effect of scattering is strong. The result of this is a complex interplay between the type of measurement made and the appropriate attenuation relation. Measurements of quantities such as pulse amplitude will feel the full force of scattering attenuation and will decay rapidly with Q_t dominated by scattering. Measurements such as coda will decay less rapidly because some of the scattered energy is included. A crucial parameter in the description of these effects is the albedo, which is the ratio of attenuation due to scattering to total attenuation. In New England we found an albedo of 0.9, indicating the importance of scattering. This strong scattering

means that coda Q is probably most closely identified with anelastic Q; the frequency dependence suggests that fluid flow in fractured crustal rock is a possible mechanism.

Laboratory data and observations made in the boreholes help to achieve an understanding of the physical mechanisms contributing to the attenuation of seismic waves at regional distances. Laboratory measurements of attenuation in "wet" rocks give relatively low intrinsic Q ($Q \leq 200$) even at pressures of 2 kb, and do not indicate that Q values would increase significantly with pressure. A primary mechanism for this attenuation is the friction along grain boundaries and microcracks (Walsh, 1966; Toksöz and Johnston, 1981). Recent studies indicate that in "wet" rocks microcracks heal at pressures of about 2 kb and temperatures of $400°C$ (Smith and Evans, 1984). Thus, microcracks would not contribute to attenuation in the crust below about 5 km depth, and intrinsic Q below this depth is likely to be very high ($Q \geq 1000$).

Data from well drilled in crystalline rocks shows the presence of both minor and major fractures. The fluid flow in such fractures can contribute significantly to attenuation and give a frequency dependent Q (Toksöz et al., 1987). Above the critical frequency (which could be as low as 1 or 2 Hz), Q is proportional to the square root of frequency. These same factors and other heterogeneities may also enhance scattering, especially of a surface-bound phase such as Rg.

With all these mechanisms included, an attenuation model for the crust can be summarized as:

1. At shallow depth ($h \leq 5$ km) low intrinsic (anelastic) Q with frequency dependence of $f^{0.5}$. A typical value would be $Q = 200f^{0.5}$. Scattering is probably also important in this region.

2. In the lower crust high anelastic Q ($Q_0 \geq 1000$). The influence of scattering remains to be determined in this region.

These values are consistent with models proposed by Campillo et al. (1985) for frequency dependent attenuation in the crust in central France based on Lg waves.

REFERENCES

Aki, K. and P. G. Richards (1980). *Quantitative Seismology Theory and Methods*, W. H. Freeman, San Fransisco.

Campillo, M., J.-L. Plantet and M. Bouchon (1985). Frequency-dependent attenuation in the crust beneath central France from Lg waves: data analysis and numerical modeling. *Bull. Seis. Soc. Am. 75*, 1395–1411.

Dainty, A. M. (1981). A scattering model to explain seismic Q observations in the lithosphere between 1 and 30 Hz. *Geophys. Res. Lett. 8*, 1126–1128.

Doll, W. E., J. H. Luetgert and J. M. Murphy (1986). Seismic refraction and wide-angle reflection in the northern Appalachians; the Chain Lakes Massif, northwest Maine. *EOS 67*, 312.

Kafka, A. L. and E. C. Reiter (1986). Dispersion of Rg waves in southeastern Maine: evidence for lateral anisotropy in the upper crust. *EOS 67*, 312–313.

Pulli, J. J. (1984). Attenuation of coda waves in New England. *Bull. Seis. Soc. Am. 74*, 1149–1166.

Smith, D. L., and B. Evans (1984). Diffusional crack healing in quartz. *J. Geophys. Res. 89*, 4125–4135.

Toksöz, M. N., and D. H. Johnston (eds.) (1981). *Seismic Wave Attenuation*. Geophysics Reprint Series #2, Society of Exploration Geophysicists.

Toksöz, M. N., R. S. Wu and D. P. Schmitt (1987). Physical mechanisms contributing to seismic attenuation in the crust. Submitted to *Proc. NATO ASI 'Strong Ground Motion Seismology', Ankara, Turkey*.

Walsh, J. B. (1966). Seismic wave attenuation in rock due to fracture. *J. Geophys. Res. 71*, 2591–2599.

Wu, R. S. (1984). Seismic wave scattering and the small scale inhomogeneities in the lithosphere. Ph. D. Thesis, Massachusetts Institute of Technology.

COMPARISON OF REGIONAL AND NEAR-FIELD SOURCE PARAMETERS FOR NTS EXPLOSIONS AND REGIONAL DISTANCE BODY WAVES FOR EURASIAN TRAVEL PATHS

Terry C. Wallace
University of Arizona

OBJECTIVE

One of the main consequences of decreasing the yield limit in a threshold test ban is the increased reliance on regional-distance seismograms for monitoring purposes. Most schemes for determining the yield at regional distances are based on measuring the amplitude of phases such as Pn or Lg. It is extremely important to a TTBT to understand the nature of propagation of these phases in different regions, as well as possible sources of bias such as tectonic release. We have continued to study the effects of tectonic release on regional distance waveforms and tying near and regional-distance source parameters together. We have also began studying the propagation of regional phases along Eurasian travel paths.

RESEARCH ACCOMPLISHED

Nearfield modeling of HALFBEAK The teleseismic representation of the tectonic release for most of the Pahute Mesa explosions are inconsistent with the near-field tangential recordings. in general, the near-field records are much more complicated than expected and smaller in amplitude. We feel that to complete our understanding of tectonic release we must develop a single model to explain tangential motions over the entire range of observation. We have modeled the nearfield recordings from HALFBEAK (6/30/66, announced yield of 300 kt). Figure 1 shows the tangential recordings from HALFBEAK and synthetics generated for a distributed shear dislocation source. The velocity structure that was used for the synthetics is that determined by Barker et al. (1985). Green's functions were computed with Kennet-Bouchen numerical integration. The source orientation for the shear dislocations was determined by a constrained moment tensor inversion. It was assumed that the orientation was strike-slip, and the tangential waveforms were inverted for strike. The resulting value, $\theta = N7^\circ E$, is consistent with larger Pahute Mesa events studied teleseismically (Wallace et al., 1985; 1986). The inversion produced a stable estimate of strike, but the quality of fit to the waveforms was quite poor. Since the near-field recordings are only 2-4 times the depth of burial (d = 815 m), tectonic release from a distributed source will produce a very complicated interference pattern. In an attempt to simulate this effect we placed 16 point sources (of equal moment, the total of which was determined by the moment tensor inversion) about the working point at the distance of 1 elastic radius (given by Archambeau, 1972, and a stress drop of 100 bars). Although the fit in figure 1 is not perfect, it does offer a reasonable explanation for the data. In the next step we plan to use this model for tectonic release to fit the vertical and radial near-field observations.

We have also compared the values determined for Ψ_∞ from near-field data to those determined by moment tensor inversion of broadband regional data. Using McEvilly and Johnson's (1986) RDPs for Chancellor and Harzer we calculated a value for Ψ_∞ by fitting a Muller-Murphy source. Using the Livermore National Laboratory's regional network we inverted the Pn and Pnl wavetrains in the frequency band .1 to 1 Hz to obtain the regional estimate for Ψ_∞. The results are summarized in table 1. In both cases the vaule of Ψ_∞ in the near-field is significantly smaller than that determined regionally.

Regional distance propagation in China   Regional distance waveforms are strongly effected by the path of propagation. Although attenuation is the factor which varies most widely, structure can cause dramatic effects, such as "blockage" of particular phases. The digital network which was deployed in 1986 in China (CDSN, see figure 2), and started supplying data to the GDSN in 1987 has been used to study Pn and Pnl propagation across China. Calibration of the travel path effects are very important here not only becasue of the proximity to Several Soviet test sites, but also the stations are idealy situated to study earthquakes from the Hindu Kush-Tien Shan region. We have identified seven events between 1970-1978 in the Pamir region which had anomalous m_b/M_s ratios (these events do not fall in the explosion population, but they are significantly above the mean of the earthquake population). Since these events are enriched in high frequencies we have compared the path "signatures" with more normal events.

Also shown on figure 2 is a regionalization of the southern part of China and crustal thickness and Pn values we have determined using the methodology of Wallace (1986). It is assumed that the average crustal thickness and Pn velocity of a given path is the sum of the percentage of travel path in a given block multiplied by the thickness of the Pn velocity of that block. The blocks were chosen on the basis of surface geology. The results shown in figure 2 are from 12 events recorded at 6 stations (26 travel paths).

CONCLUSIONS AND RECOMMENDATIONS

Near-field modeling continues to provide detailed inofrmation not only about the isotropic part of explosions but also the nature of tectonic release. Much more work needs to be done tying the near-field work to regional distance observations. We intend to model RULSION AND GASBUGGY (using Murphy et al., 1986 as a starting point) in the next year. Regionalization of China for Pn and Pnl propagation will continue, and we also be investigating the presence of a well developed high velocity zone at mid crustal depth for the southwest Chinese paths.

REFERENCES

Archambeau C. (1972). The theory of stress wave radiation from explosions in prestressed media, Geophy. J., 29, 329-366
Barker, J.S., L.J. Burdick and T.C. Wallace (1985). Analysis of nearfield seismic waveforms from underground nuclear explosions, Scientific report No. 1, AFGL-TR-85-0321, Woodwrd Clyde Consultants, Pasadena.

McEvilly, T.V. and L.R. Johnson (1986). Regional studies with broadband data, 8th Annual DARPA/AFGL seismic research symposium, 44-51.

Murphy, J.R. and C.B. Archambeau (1986). Variablility in explosion body wave magnitude: an analysis of the RULISON/GASBUGGY anomaly, Bull. Seism. Soc. Am., 76.

Wallace, T.C. D.V. Helmberger and G.R. Engen (1985). Evidence of tectonic release from underground nuclear explosions in long-period S waves, Bull. Seism. Soc. Am., 75, 157-174.

Wallace, T.C., D.V. Helmberger and T. Lay (1986). Note on the revised moments from Pahute Mesa tectonic release, Bull. Seism. Soc. Am., 76, 313-318.

Wallace, T.C. (1986). The inversion of long-period regional distance Body waves for crustal structure, Geophys. Res. Let., 13, 749-752.

TABLE 1

Comparison of near-field and regional distance source parameters

HARZER	6/6/81	D=637m	nf	0.7×10^9 m^3
			reg	1.1×10^9
CHANCELLOR	9/1/83	D=625	nf	0.34×10^9
			reg	0.55×10^9

DISTANCE (KM)   AZIMUTH (DEG)

1.371   330   MAX. VAL. = 105.70220

2.133   330   MAX. VAL. = 36.13200

3.047   334   MAX. VAL. = 47.16200

                                                         MAX. VAL. = 33.83900

2.132   226

                                                         MAX. VAL. = 22.45200

2.285   80

                        ┌──────────┐
                        0.00   2.00
                        SEC/INCH
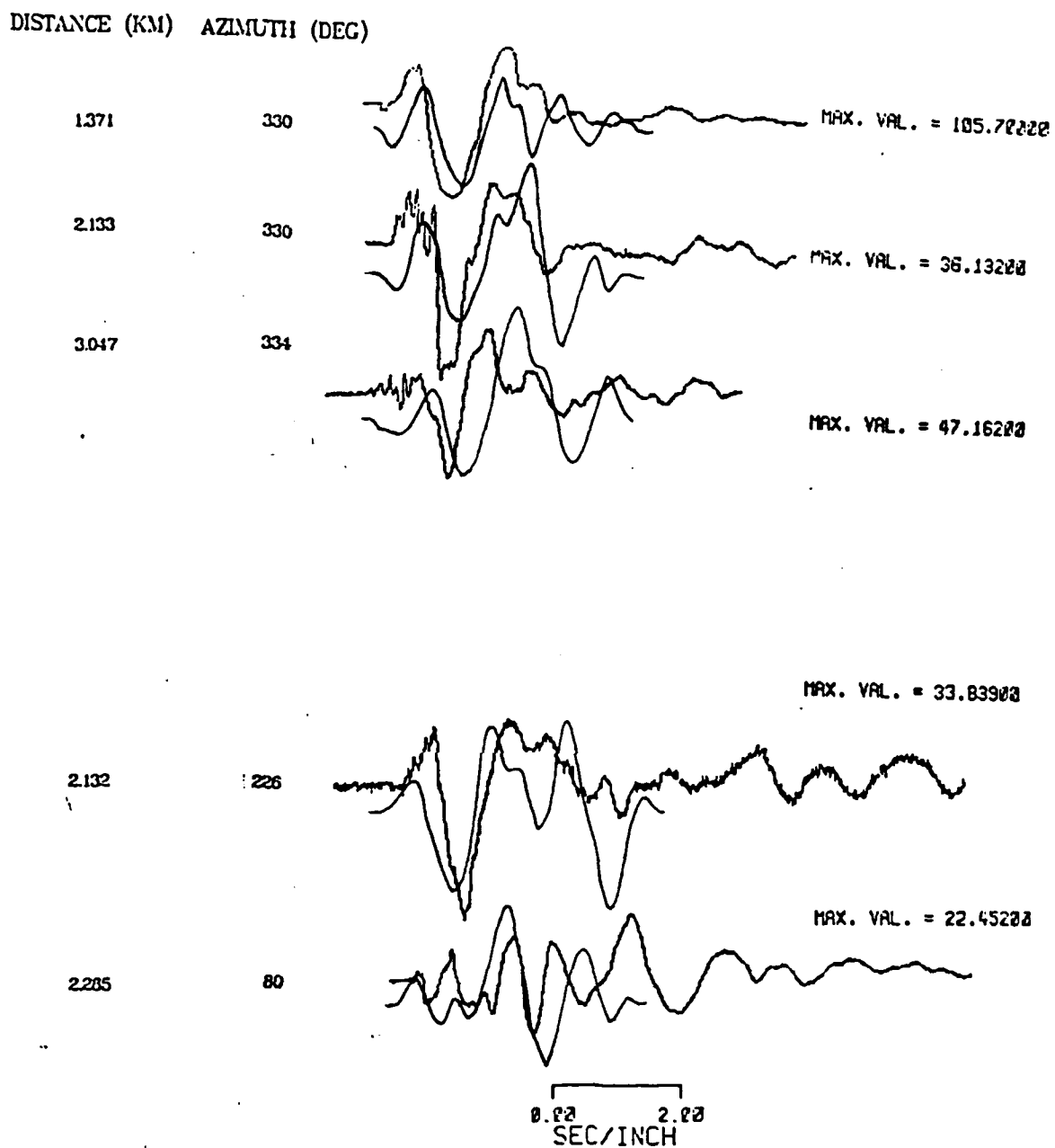
Figure 1: A comparison of the observed and synthetic nearfield records
form HALFBEAK. Top trace is the observed velocity. The synthetics were
calculated with a distributed shear dislocation source.

164
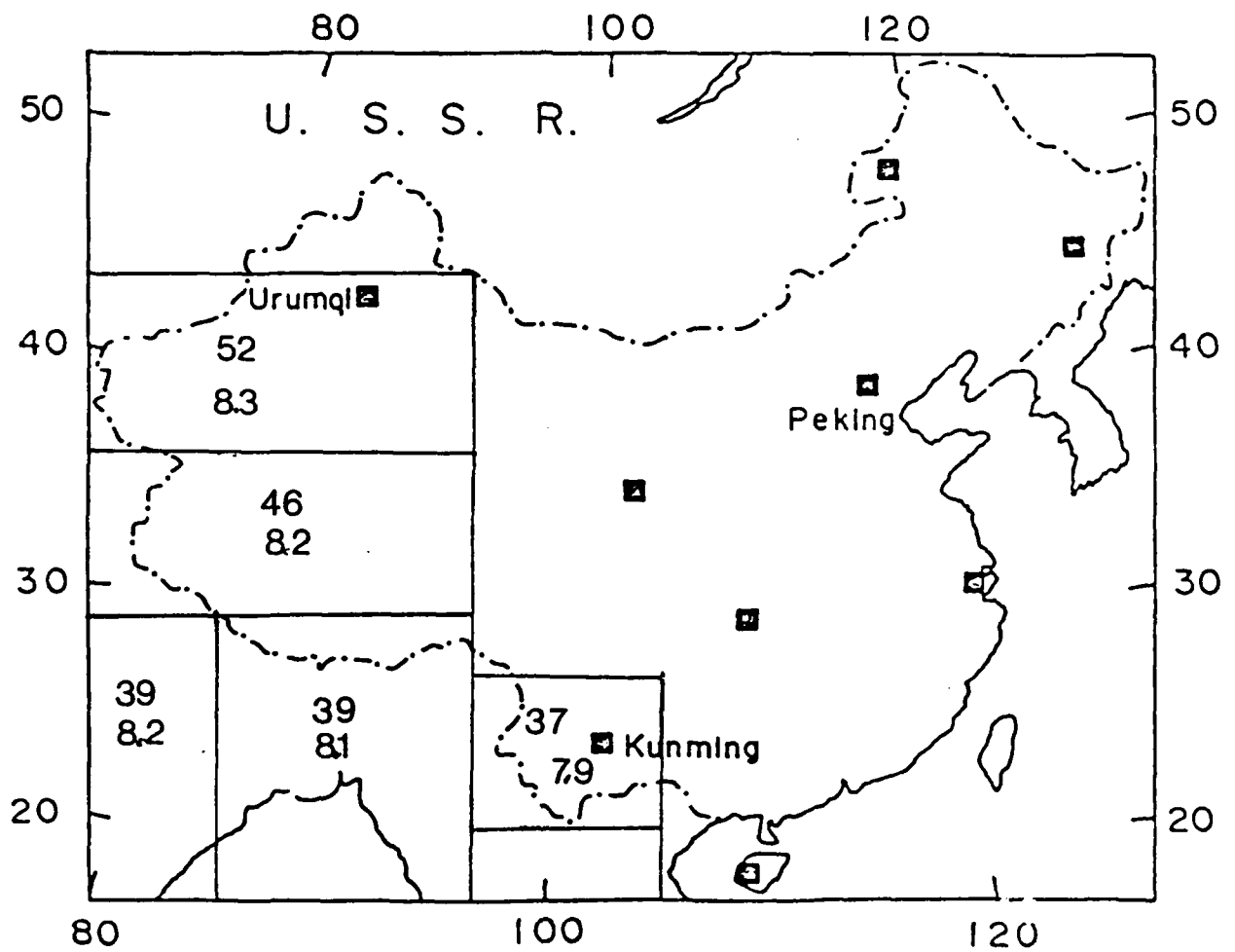
Figure 2: Regionalization of the gross crustal structural of western China. The numbers in the blocks are crustal thickness in km and Pn velocity.

SPECIAL SESSION ON DARPA SMALL ARRAY PROGRAM

Organized by Thomas C. Bache
Science Applications International Corporation

The objective of the DARPA small array program is to demonstrate the capability for monitoring nuclear testing of a network of seismic arrays spaced at regional distances. The program involves: (1) Installation of arrays specifically designed for this task; (2) New analysis procedures to fully exploit the data; (3) Communications and computing facilities to collect and process the data. NORESS has demonstrated the great potential of the small arrays and additional arrays are planned. To fully exploit the data, a computer system incorporating knowledge-based systems technology, together with advanced signal processing and computer graphics technology, is being developed on a distributed network of SUN Workstations and an Alliant computer of the mini-supercomputer class. The system is designed to analyze data from a network of NORESS-type arrays and is being developed by a four-company team including SAIC (prime contractor), Advanced Decision Systems (ADS), Ensco and Teknowledge. The complete system (hardware and documented software) is to be delivered to the Center for Seismic Studies in March, 1989.

This session will feature talks by several speakers, including Ralph Alewine (DARPA), Tom Bache (SAIC), and Doug Baumgardt (Ensco). Dr. Alewine will describe the DARPA objectives for this program and projects now underway or being planned to accomplish these objectives. Dr. Bache is the manager of the analysis system development program and will describe the overall design of this system and the plan for developing it. He will also describe key features of the system being developed by SAIC and ADS. Dr. Baumgardt will describe key features of those elements being developed by Ensco and Teknowledge. Experienced human analysts now interpret seismic data far better than automated procedures. The emphasis in the development is on the exploitation of knowledge-based or 'expert' system technology to close or eliminate this gap. Other major elements of the system include the user-interface for acquiring knowledge and adding it to the system, seismological signal processing for extracting knowledge from the data, and extensive computer graphics for displaying the results of the processing.

A major theme of the talks describing the system is that its advent poses some new research problems for seismology and changes the context for some old problems, like the development of signal processing algorithms. The version to be delivered in two years will be far from complete in the seismological knowledge it embodies and in the techniques being used to extract useful information from seismic signals. Therefore, an important goal is that the software and hardware architecture be designed to facilitate evolution and improvement. Further, this system is intended to serve as a test-bed for new developments, and therefore help focus research on the most relevant issues.

A KNOWLEDGE-BASED SYSTEM FOR ANALYZING DATA FROM A NETWORK OF NORESS-TYPE ARRAYS

Thomas C. Bache
Science Applications International Corporation
10210 Campus Point Drive, San Diego, CA 92121

INTRODUCTION

The NORESS-type arrays provide new opportunities and challenges for test-ban-treaty monitoring seismology. The emphasis is on regional monitoring, and skilled analysts of regional data make extensive use of knowledge of distinctive signal characteristics to help recognize and time regional phases to locate and identify events. Also, the treaty monitoring application requires consistency, reliability and accuracy far beyond that required of networks for monitoring earthquake seismicity. These problem features motivate the need for a new computer system to automate the processing and take advantage of seismological knowledge, much of it region-specific, to analyze the data. The need is not new, but a number of developments in seismology and computer sciences make this an auspicious time for a major program to implement such a system for treaty monitoring.

The major developments include the deployment of the NORESS-type arrays with real-time satellite-link transmission of digital data to a central analysis facility and the demonstration by the NORSAR staff that a bulletin of reasonable quality can be produced automatically from these data (Mykkeltveit and Bungum, 1984). Another major development is that knowledge-based ('expert') systems technology is now sufficiently mature that we can be confident that it can give results significantly better than can be obtained with more traditional methods. The DARPA workstation program has also matured and provides technology for important computer graphics and seismologist interface elements of the system. Finally, current levels of cost/performance for computer hardware essentially eliminate computer speed as a significant limitation on the choice of processing procedures.

DESIGN GOALS

The design goals fall into four somewhat overlapping categories: (1) Operational capabilities of the delivered system; (2) Capability to evolve, improve, and expand; (3) Technology demonstration; (4) Test-bed for future research. The initial implementation is designed for analyzing the data from two arrays, but the hardware/software architecture anticipates expansion to handle more arrays and/or single sensor stations. The system is to take maximum advantage of *knowledge* gained from the data, and to include the capability to efficiently acquire and add the necessary knowledge. Design goal (4) is perhaps most important for the DARPA research community. It is motivated by the perception that evaluation of new concepts has been limited by inadequate capability to test them under realistic conditions. This system is to be a test-bed to provide that capability in two ways. First, the software (and hardware) design emphasizes modularity, anticipating piecewise replacement or upgrading. Second, the system will have the capability for simultaneous processing of multiple data streams (which could be identical), so testing of new modules can be done without compromising the capability for operational processing of the incoming real-time data.

SYSTEM CONCEPT

Experienced human analysts are much better than existing computer systems for analyzing seismic data, not so much for detecting isolated signals (for arrays, automatic detectors are probably just as good or better than humans when many beams are formed), but for interpreting the data in its full context. The human analyst uses heuristics developed with experience and qualitative features of the data such as the envelope shape and duration. Signals that would not be detected in isolation are detected because their presence is suspected from other evidence. Analysts become much more proficient as they gain experience with the character of signals in particular areas. The goal is to match or surpass this human performance, partly by emulating the human thought process, but also by exploiting the superior performance of computers for some tasks. The most difficult skill to emulate is the exceptional human ability to recognize waveform patterns in the presence of varying noise, and there appear to be no reliable techniques for doing so now. However, there are many proven techniques for extracting useful information from discrete waveform segments selected by the triggering of a seismic detector. The NORSAR RONAPP program (Mykkeltveit and Bungum, 1984) is based on this and applies a few simple rules (implemented in FORTRAN) to identify Pn and Lg phases which, together with an azimuth estimate, provide an event location.

The knowledge-based system design builds on traditional seismological algorithms for detection and post-detection processes (e.g., f-k spectrum, Fourier spectrum, polarization, etc.). Attributes of the detections are used together with knowledge about regional signal characteristics to deduce the solution. Knowledge is used in two ways, characterized as model-based and case-based reasoning. The former involves rule-based knowledge representation and reasons from signal detections to a location solution by exploring hypotheses about the identification and association of detected signals. The case-based reasoning uses knowledge represented by scripts and is especially effective for identifying events that are similar to events seen previously (this portion of the design will be discussed by Dr. Baumgardt).

The top level data flow design is shown in Figure 1. The seismological signal processing computations (detection and post-detection) are done on an Alliant FX/8. This machine is networked (Ethernet and Sun Network File System) with six Sun workstations for the knowledge-based processing (called *event processing* in the figure), the graphics, and the user interfaces. The user interface includes two parts. The *analyst review* node has elaborate waveform display and interaction capabilities to facilitate analyst review of solutions determined by the system. *Seismologist review* is for knowledge acquisition and for updating and testing the knowledge base. The capability for parallel processing of test data sets is an important feature under control of the 'seismologist'. The most challenging problem in the system development is implemention of a knowledge acquisition interface that allows a seismologist to alter and expand the knowledge base efficiently and effectively.

The implementation concept is to evolve through a series of prototypes of increasing functionality and software maturity. Some elements of the system are well-understood (particularly the seismological signal processing and the interactive display of digitized maps), and traditional software design-develop-test methods can be used to implement them. On the other hand, many elements of the knowledge-based processing (particularly the knowledge acquisition interface) are only understood conceptually. Also, there are key areas where human (seismological) expertise is inadequate; for example, in the estimation of source depth and in event classification (earthquake, chemical explosion or nuclear explosion) with regional data.
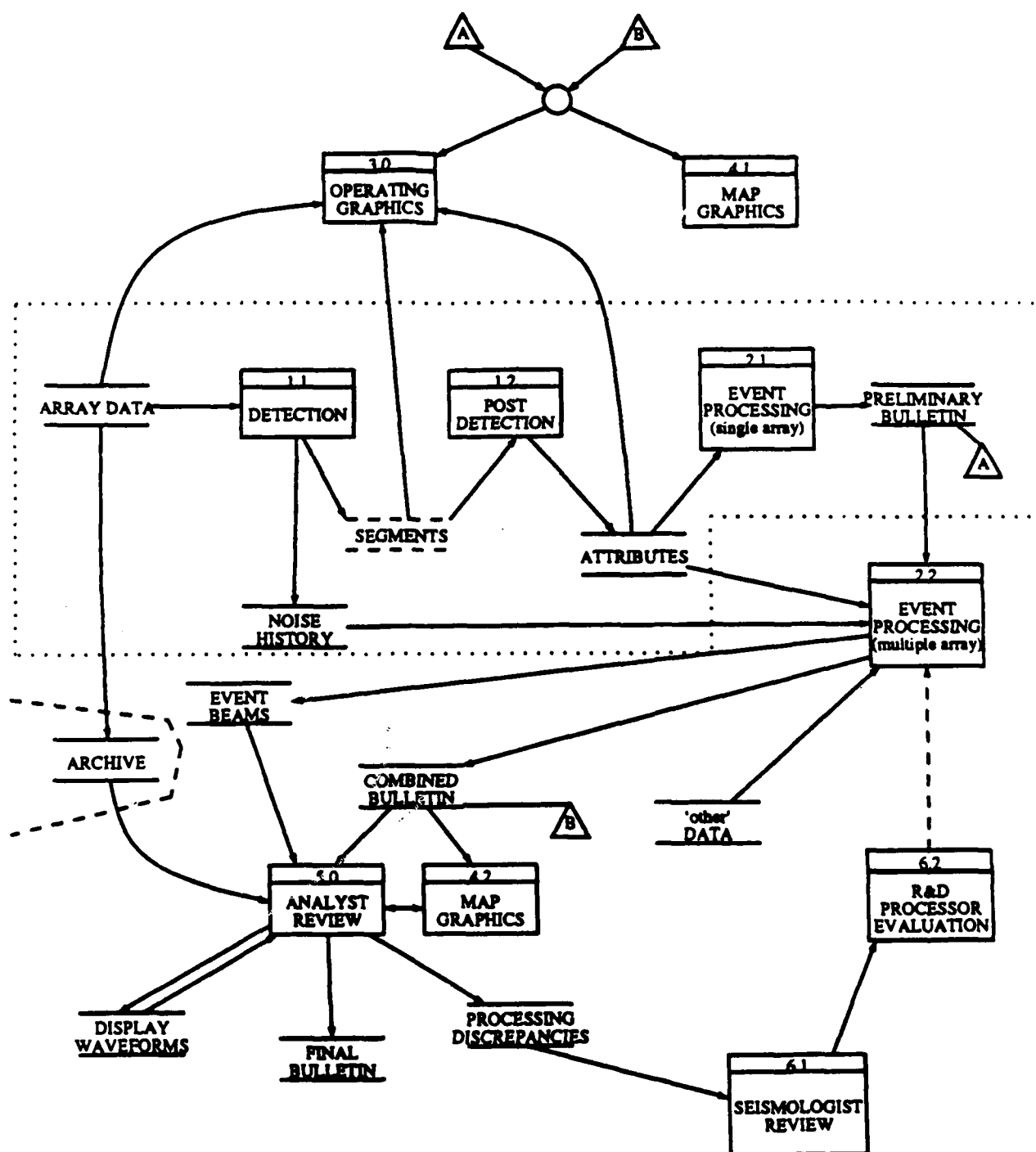
Figure 1   The major functions are shown with the major classes of data objects (enclosed by horizontal lines) passing between them. The hardware design maps closely to this data flow diagram, with each of the functions numbered 1 to 6 having a machine dedicated to it (the *map graphics* functions 4.1 and 4.2 each have a Sun workstation).

169

KNOWLEDGE-BASED SYSTEM DESIGN

In this paper we can only sketch the KBS design. The major steps in the logic flow are indicated in Figure 2. Single array location solutions are formed, and these are then combined to form the network location. The emphasis of the processing is on the latter, since detections from another array easily resolve ambiguities that are very difficult to resolve with the data from a single array. The initial input to the KBS is a list of signal detections and attributes (e.g., phase velocity, azimuth, etc.) from each station. In the *initial phase identification* step, rules are applied to tentatively classify the signals as P, S, teleseism, or noise, with phase velocity being the most powerful classifier. The next step is to group phases that appear to be from the same event, primarily using time separation and azimuth consistency. The grouping is then examined for consistency with the assumption that only a single event contributed phases to the group (e.g., a high confidence P occuring after a high confidence S indicates at least two events). When inconsistencies are found, the system 'backtracks' and regroups the phases. At the *phase association* step, region-specific knowledge is applied to identify the phases as Pn, Pg, etc., which leads immediately to a location estimate and associated confidence bounds (Bratt and Bache, 1987).

The logic for combining single array solutions to obtain the *network location* can be viewed as an expert system implementation of automatic association extended to a network of regional arrays. The process is driven by the location estimate from the array that is apparently closest to the event (earliest P detection), and works outward, searching for corroborating detections or phases from other stations. Inconsistencies cause the system to backtrack to revise earlier hypotheses about phase association or identification. The inference procedure for the *network location* is rather complex and includes reinitiation of signal processing ('recall processing') when there is evidence that it may provide important information. In KBS terminology the control strategy for the inference from detections to a network location estimate may be characterized as a heuristic depth-first search of multiple hypotheses with knowledge-based backtracking which fulfills truth maintenance requirements.

The next step is the *final consistency test* where we check for consistency with expected signal characteristics for events in the vicinity of the estimated location. Up to this point the controlling attributes are expected to be robust signal features such as arrival time, velocity, and azimuth of detected phases, with other attributes taking a secondary role. But once we have a tentative location hypothesis, we can test it against more subtle data features and patterns of features. This suggests case-based reasoning and will be described by Dr. Baumgardt. If inconsistencies are found, the system backtracks to make appropriate revisions. Note that arrival times and azimuths from multiple arrays powerfully constrain the solution, so it would be rare to reject a multiple array solution at this step. However, we expect many events to be detected by only a single array, and for these the case-based reasoning provides a basis for resolving ambiguities that cannot be resolved otherwise.

In *event characterization* we collect the evidence needed to identify the event. The case-based reasoning plays a key role here, especially for mine blasts which are a dominant part of the seismicity in many areas. This step also involves the refinement of location estimates (e.g., master event) and initiation of signal processing tasks for event identification. The final step is *event identification* and involves rule-based reasoning to classify the event.
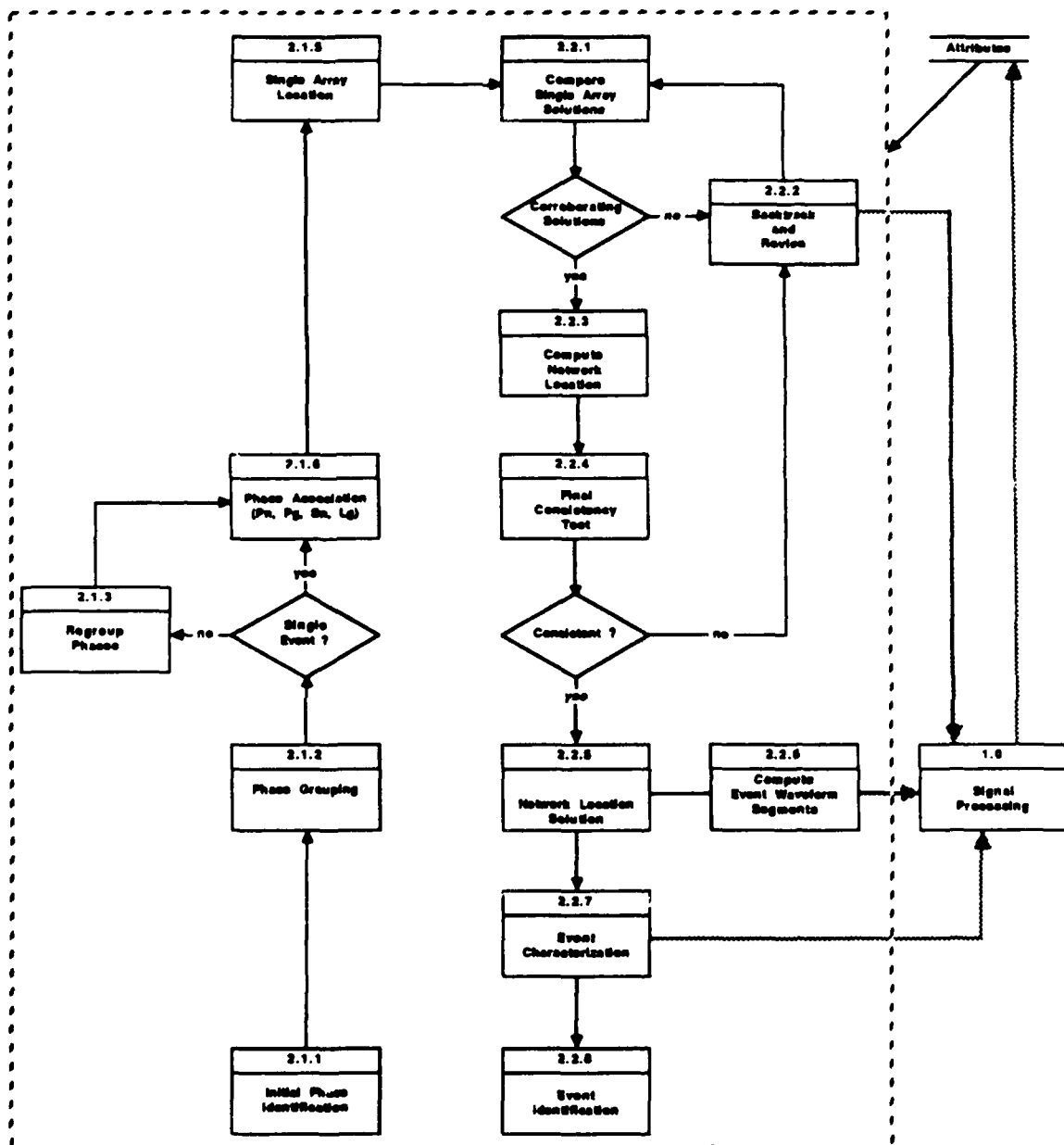
Figure 2   The major steps in the logic flow of the KBS are shown, starting with *initial phase identification* at the lower left and ending with *event identification*. Signal *attributes* are input to the KBS and used throughout. At several steps the KBS can reinitiate signal processing, and this is indicated by arrows extending outside the dashed line encompassing the KBS.

[7]

IMPLEMENTATION PLAN

The development cycle is two years, and the completed system is to be transferred to the Center for Seismic Studies in March, 1989. It will evolve through three major versions. This plan is motivated by the fact that there are many elements of the system that cannot be confidently designed in detail until we gain more experience with processing data in this kind of environment. Thus, the first version (September, 1987) has the integrated functionality to exercise the KBS to learn what knowledge and knowledge acquisition procedures appear to be most effective. Experience with this version is vital for completing the design of the knowledge acquisition interface. The second version (March, 1988) is a better integrated and more complete version of the first, particularly in the graphics display capabilities. The major functionality to be added in the second year is for knowledge acquisition, but the system will be improved and expanded in all areas. Careful attention to modern software engineering practices is emphasized throughout, with the delivered system to be fully documented, tested, and maintainable.

The system is being developed by a four-contractor team, which makes integration of concepts and software unusually difficult for a system of this size. Besides electronic mail, the keys to the integration are early design and implementation of the database structures (based on an extension of the Center for Seismic Studies relational database) and the inter-process communication software (based on Unix sockets with a central dispatcher).

IMPLICATIONS FOR RESEARCH

This system is expected to change the environment for research in test-ban-treaty monitoring. It can efficiently test new concepts on large amounts of data. Perhaps even more important, it provides a basis for assembling data that are especially difficult to analyze. There are many ways to get the right answer from the easy examples; what is needed are new and better ways to deal with the hard ones. Our preliminary impression is that available methods for detecting signals, computing their first-order attributes (e.g., slowness, azimuth, amplitude, etc.), and locating events are quite effective. The payoff is more in using expert system technology to exploit this information than in marginal improvements in capability to extract it. However, seismological capability is weak in several important areas, and we need good ideas to incorporate into the KBS. These include techniques to estimate source depth from regional signals and techniques for regional discrimination. For the latter we note that any regional discriminant must take advantage of the signals from a clandestine nuclear explosion being 'different' from the signals due to 'normal' events. The KBS is designed to collect and organize knowledge about what is normal and note the exceptions, which is a key step toward a regional discriminant.

REFERENCES

Bratt, S.R. and T.C. Bache (1986). "Location estimation using regional array data," Technical Report SAIC-87/1564 submitted to AFGL, December.

Mykkeltveit, S. and H. Bungum (1984). "Processing of regional seismic events using data from small-aperture arrays," *Bull. Seism. Soc. Am.*, **74**, 2313-2333.

Case-Based Reasoning Applied to
Regional Seismic Event Characterization

Douglas R. Baumgardt
Ensco, Inc.
5400 Port Royal Road
Springfield, Virginia 22151 - 2388

Introduction

The overall objective of the NORESS Intelligent Array Processing program is to fully exploit knowledge about seismic signals in regional array processing. The intent is to develop a system which is *revolutionary,* in that it will represent a significant improvement in processing regional array data for testban treaty monitoring. Moreover, the system will be *evolutionary,* in that its performance will change and improve as more knowledge about regional seismic signals and processing is acquired as part of the DARPA seismological research program.

Regional seismograms have very distinctive envelope shapes which an analyst or seismologist easily recognizes and uses to identify specific regional phases, such as Pn, Pg, Sn, and Lg. Many skilled analysts and seismologists can in fact remember past observed patterns in previous seismic events and recognize similar patterns in new data. This capability, of course, degrades as the signal-to-noise ratio decreases. However, even at high signal-to-noise ratios, no automated system has yet been developed which can approximate the analyst's capability for recognizing these distinctive seismic-signal shape patterns. The main *revolutionary* goal which we have set is to develop a knowledge-based system which can recognize signal patterns in data at a level of capability approaching that of a skilled and experienced seismic analyst.

Currently, seismic research has focused extensively on nuclear testban treaty monitoring using regional seismic data. It is anticipated that more knowledge will be forthcoming from the research efforts in regional seismic-event characteristics related to event identification. Thus, the *evolutionary* goal for our system is that new knowledge about regional seismic events can be easily incorporated into the system.

Case-Based Versus Model-Based
Reasoning Paradigms

Most knowledge-based systems fall under one of two general classes, *model-based* and *case-based* reasoning paradigms. In *model-based reasoning,* it is assumed that there exists a model of the application domain which can predict all expected observations about the domain. This model makes predictions about expected observations, based on hypothesized facts about the domain, and reaoning on the truthfulness of the facts consists of comparing the predictions with observations. In essence, *model-based reasoning* attempts to reduce a large number of observations down to a smaller number of knowledge elements, such as rules, obtained from the model. *Model-based* solutions have only been successful in well-understood, highly constrained situations. *Case-based reasoning* uses analogic reasoning by comparing new observations against past observations or cases. No model for the domain is assumed to be known, and the only knowledge of the domain is in the form of remembered observational cases and their interelationships. Generally, the case knowledge, which is often descriptive in nature, is represented in terms of declarative knowledge structures, such as schemas, frames, or scripts, although rules are not precluded.

In regional seismology, *model-based reasoning* would be most appropriate in epicenter determination, which is based on velocity models of the crust and expected travel times of regional phases. Also, reasoning about phase identification can be based on the velocity models, assuming accurate and stable array-parameter measurements (apparent velocity) can be made. However, models have been less successful in predicting the waveform characteristics, such as amplitudes and frequencies, of regional seismic signals. Also, since regional seismic-event identification is not well understood, characterization of regional seismic waveforms would best be accomplished by reasoning

on the similarity of seismic observations from new events to those of previously observed cases. Moreover, seismic analysts seem to recognize signal patterns based on their similarities to prototypical regional seismic patterns observed in the past, which is *case-based reasoning*. Finally, *case-based systems* are designed to learn as more observations are acquired, based on analogies of the incoming patterns to those seen before. Thus, we are currently designing a case-based signal recognition system for the event-characterization part of the system.

Knowledge Representation

There are three general requirements of an effective knowledge-representation scheme:

(1) Completeness - All the knowledge of the domain must be incorporated.
(2) Flexibility - It must be possible to modify the knowledge easily.
(3) Expandability - Aquisition of new knowledge must be facilitated.

The basic knowledge-representational forms we are using for representing knowledge about regional seismic cases are called *scripts*. Scripts are designed to explain and represent under - standing about seismic-event sequencies. Originally, scripts were used in programs for reading and understanding stories. They, in essence, represent a stereotypical sequence of events, like going to a restaurant or driving a car to work. In seismology, scripts consist of temporal patterns of phase attributes, which consist of expected signal-processing parameters for the phase, such as amplitude, frequency, apparent velocity and azimuth across the array, etc. Figure 1 shows an example of a typical script for a mine blast in western Norway. In addition to the actual signal values, there are also associated expected uncertainties or variances for the observations. Reasoning then consists of comparing the observed parameters for incoming data against those stored in the script for specific types of events. The probability of match is determined for each phase, assuming a Gaussian distribution for the errors, and the probabilities of match for each parameter in the phase attributes are then accumulated to yield an overall script-match probability. A match is declared if the parameters fall within the expected range for the parameter at some predefined confidence threshold. If a match is declared, the event is characterized in terms of its similarity to the event or event class represented by the script.

We have defined three different kinds of scripts:

(1) *Single event* - This script is formed from the observations from one event.
(2) *Multiple event* or *cluster* - This script represents a large number of events whose characteristics have been judged to be close enough to be classed together as one type of seismic event.
(3) *Generic* - This script is based on theoretical considerations, not actual observations.

Both *single event* and *multiple event scripts* will be tied directly to observed data, including waveforms and detection records for each of the phases associated with the events. *Multiple event scripts* will be most useful for repeated seismic events occurring at the same place, such as mine explosions or closely spaced earthquakes and earthquake aftershocks. *Single event scripts* will probably be used to represent most earthquakes. *Generic scripts* are not associated with observations but rather represent educated guesses about the characteristics of seismic-event characteristics based on theoretical considerations. *Generic scripts* will be be used when new regional arrays are sited in regions where a historical record of seismic events has not yet been acquired.

The script-representational form illustrated in Figure 1 will be composed of parameter measurements made from actual detections and post-detection processing. This form makes it easy to acquire new scripts. Single-event scripts will also be augmented by the use of signal-parameter templates which include a log-rms incoherent beam and the broad-band fk measurements, F-statistic, apparent velocity, and back azimuth, displayed as a function of time. Templates will be used both for more detailed pattern matching than possible with script matching as well as to help with knowledge acquisition.

The most commonly used representational forms in expert systems are *rules*. Rules can be used

to represent knowledge about regional seismic event cases and scripts may have rules embedded within them. Reasoning with rules is not much different than reasoning with scripts, since the invocation of rules involves a matching process of facts known against the premises of the rules. Rules differ from scripts in that they are more compact and do not usually contain the large concentration of knowledge that can be stored in a script structure. Rules, however, may be better for representing procedural knowledge, which relate to determining what to do next. For example, rules could be used to determine how to interpret the results of a script match and what to do next after script matching.

Procedures constitute another important knowledge-representational form or knowledge source. Procedures include not only procedural rules, discussed above, but also the wide variety of traditional algorithms used in seismic computation, such as frequency-wavenumber analysis or location algorithms. Such procedures frequently have rules embedded within them in the form of if-then type instructions. The unique aspect of knowledge-based systems, which makes them distinct from traditional algorithmic approaches, is that these rules are represented as data structures, rather than as embedded procedures within the code itself. However, in many situations, embedded procedures will be used.

Knowledge Processing

Figure 2 shows schematically the cased-based knowledge processing in the event-characterization part of the system. In general, the knowledge processors utilize two kinds of knowledge: (1) knowledge about signal characteristics and (2) knowledge about signal processing schemes for enhancing these signal characteristics. As shown in Figure 1, scripts contain the constraints on expected values of signal parameters and are used to interpret the results of signal processing. The case-based reasoning approach consists of matching the script parameters against the those measured for a new event. Moreover, scripts will also contain the procedural knowledge which effectively controls the initiation and execution of the signal processors. This kind of processing is called *recall processing.*

As shown in Figure 2, the event-characterization function consists of three subfunctions: (1) *script matching*, (2) *final consistency check*, and (3) *event identification*. *Script matching* opens scripts for historical events located near the hypothesized event location, matches script parameters against those of the new event, and estimates the confidence of match. *Final consistency check* examines the results of the match, determines if any recall processing must be done to pick up undetected phases, for which backtracking to the signal processors would be invoked, determines if the waveform characteristics of the new event are consistent with those of historical events, and, if not, initiates backtracking with alternative hypotheses.

Event identification consists of processors which extract features from the waveforms to be used in event identification. Figure 3 shows a schematic and illustration of a coda-shape matching algorithm to be used for event identification, called dynamic time warping (DTW), which provides a more detailed match between script events and events being characterized. This algorithm, used in speech processing for word recognition, applies a dynamic programming technique to match reference coda shapes in the form of log-rms incoherent beams to those of the events to be processed. The time axes of the reference shapes are stretched or contracted in order to attain the best match in the shapes. The relative distances between the reference and unknown events, in log-rms units, gives the goodness of fit.

Other processing for event *event identification* include spectral analysis, for discrimination, and cepstral analysis, for identification of multiple events or ripple firing in mines and depth characterization. The results of this processing and the script matching results would be examined by rules which would make a determination of the identity of the event, ie, earthquake, explosion, or unknown, with an associated confidence, and then reports the results. The *event identification* part of the system is not well understood because of our limited knowledge of in this field. Hopefully, future research in regional discrimination will produce additional features which can be used at this level to identify seismic events.

EXAMPLE SCRIPT

SCRIPT TYPE	INDIVIDUAL
ARRAY	NORESS
	LATITUDE 60.7353 NORTH
	LONGITUDE 11.5414 EAST
EVENT	TITANIA MINE EXPLOSION (SOUTHWESTERN NORWAY)
ALIASES	EXXON
AUTHOR	DOUG BAUMGARDT
DATE	JULY 19, 1988
COMMENT	This Titania Mine Explosion script was derived from data
COMMENT	collected on APRIL 4, 1986
LATITUDE	58.343 NORTH RANGE 2.5
LONGITUDE	6.456 EAST RANGE 1.8
DEPTH	UNKNOWN
DISTANCE	304 KILOMETERS
AZIMUTH	228 DEGREES
ORIGIN TIME	846949 14:13:24.8
PN TRAVEL TIME	53.8 SEC
TEMPLATE	T6091
ESTIMATED MAGNITUDE	2.7 YIELD 66.7 tns

SOURCE OF INFORMATION University of Bergen reported network bulletin
COMMENT   The event used to define this script was derived from the
           regional bulletins generated by the University of Bergen.

ASSOCIATION   NO PG: RECALL PG (TITA_PG_A TITA_PG_B)
               NO SN: RECALL SN TITA_SN_A;
               PN OPTIONAL PG SN LG: DONE CONFIDENCE 0.9;
               PN OPTIONAL PG LG: DONE CONFIDENCE 0.7
               NO LG: RECALL LG TITA_LG_A
               LG: HELP

PHASE PN			
	RELATIVE TIME	0.0 SEC	ERROR 0.5
	FREQUENCY	6.10 HZ	RANGE 0.1
	VELOCITY	10.0 KPS	ERROR 1.1
	AZIMUTH	218.0	ERROR 10
	SIGNAL-TO-NOISE	12.2	RANGE 5%
	F STATISTIC	6.2	RANGE 3.2
	PN POWER	46.0	RANGE -2.5
	STA	613.5	ERROR 7%
	AMPLITUDE BEAM 6	1312.0	ERROR 10%
	CONFIDENCE	0.9	

PHASE PG			
	RELATIVE TIME	PN + 6.8 SEC	ERROR 0.5
	FREQUENCY	4.7 HZ	RANGE 3.3
	VELOCITY	6.8 KPS	ERROR 1.1
	AZIMUTH	PNAZIMUTH()	ERROR 10
	BEAM	ANY	
	SIGNAL-TO-NOISE	PN/3	ERROR 5%
	CONFIDENCE	0.9	
	RECALL PROCESSING	TITA_PG_A	
	PN POWER	43.5	RANGE 10.5
	STA	224.2	ERROR 30%
	CONFIDENCE	0.7	
	RECALL PROCESSING	TITA_PN_B	
	PN POWER	30.5	RANGE 10.5
	STA	177.2	ERROR 30%
	CONFIDENCE	0.6	

PHASE SN			
	RELATIVE TIME	PN + 44.3 SEC	ERROR 0.5
	FREQUENCY	2.80 HZ	RANGE 3.6
	VELOCITY	5.0 KPS	ERROR 1.1
	AZIMUTH	233.1	ERROR 10
	SNR	3.7	RANGE 0.2
	CONFIDENCE	3.7	
	RECALL PROCESSING	TITA_SN_A	
	FREQUENCY	2.80 HZ	RANGE 3.3
	AZIMUTH	230	ERROR 30
	CONFIDENCE	0.3	

PHASE LG			
	RELATIVE TIME	PN + 73.3 SEC	ERROR 0.5
	FREQUENCY	2.80 HZ	RANGE 0.4
	VELOCITY	3.5 KPS	ERROR 1.1
	AZIMUTH	PNAZIMUTH()	ERROR 30%
	BEAM	13	
	AMPLITUDE	748.4	ERROR 19%
	BEAM GAIN	3.3	RANGE 3.3
	SIGNAL-TO-NOISE	PN/3	ERROR 5%
	CONDITION	PNFSNR() > 2.0	
	CONFIDENCE	0.9	
	RECALL PROCESSING	TITA_LG_A	
	PN POWER	PN/4	
	STA	PN/2	

FIGURE 1:   EXAMPLE OF A SCRIPT KNOWLEDGE STRUCTURE FOR A
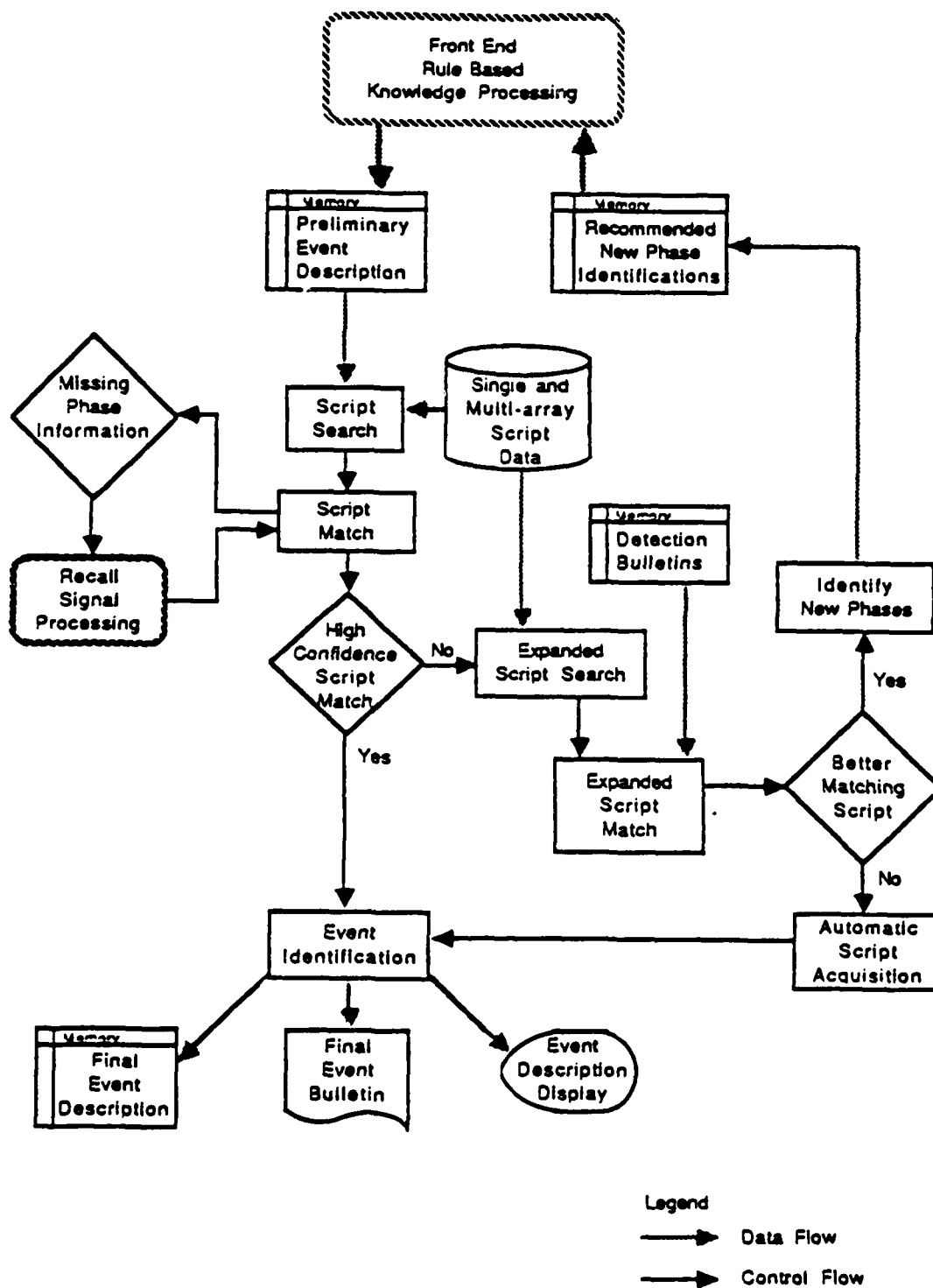WESTERN NORWAY MINE EXPLOSION

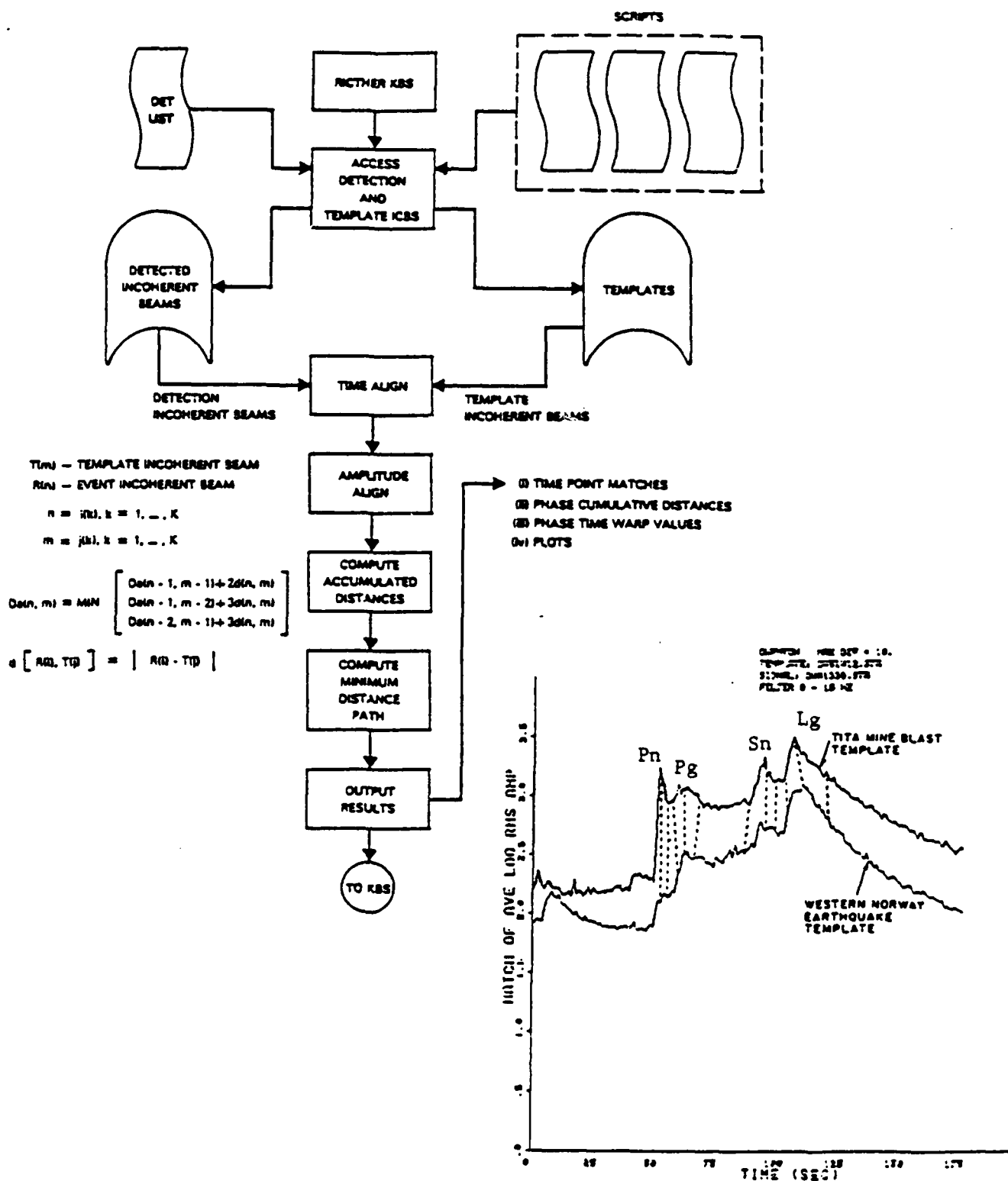FIGURE 2: SCHEMATIC DIAGRAM OF THE EVENT CHARACTERIZATION PROCESS

FIGURE 3: FLOW DIAGRAM AND EXAMPLE OF THE DYNAMIC
TIME WARP PATTERN MATCHES

DETECTION AND LOCATION CAPABILITY OF HYPOTHETICAL MONITORING NETWORKS IN THE SOVIET UNION

Steven R. Bratt, Thomas C. Bache and Donna J. Williams
Science Applications International Corporation

OBJECTIVE

Network simulation provides a framework for organizing empirical experience and for extrapolating that experience to address important treaty monitoring issues. One of the most important applications of network simulations is assessing the capabilities of hypothetical networks for monitoring present and potential test ban treaties. Our research program to simulate seismic monitoring capability is composed of three major efforts: (1) Extension and validation of *SNAPIDX*; a simulation package based on the Seismic Network Assessment Program for Detection (*SNAPID*; Ciervo et al., 1985), (2) Normalization of *SNAPIDX* to the observed performance of existing networks, and (3) Application of the program to simulate the performance of hypothetical treaty monitoring networks. In this paper we summarize our efforts to improve and normalize our simulation program and present examples simulating the detection and location capability of hypothetical networks of arrays and single seismometers in and around the Soviet Union. The results provide insight into the number and quality of stations necessary to monitor a low threshold test ban treaty, but also illustrate the sensitivity of simulations to uncertainty in key elements of the normalization.

RESEARCH ACCOMPLISHED

Simulation Program

We are developing the program *SNAPIDX*, which provides analytical and graphical tools to exploit results from the *SNAPID* simulation of detection and location capabilities of specified networks, including high frequency arrays. *SNAPID* computes detection capability based on assumptions about the detection sensitivity of individual stations and the amplitude of seismic waves as a function of distance. The detection threshold may be defined by complex detection criteria using multiple phases. *SNAPIDX* includes an added option to model detection capability as a function of frequency and a new algorithm for computing location accuracy. The latter is particularly important because epicentral location and depth provide critical information for identifying events. *SNAPID* computes location error using arrival times from all stations, with each datum weighted by the detection probability. A more realistic, though computationally intensive, approach is to compute the location uncertainties from a large number of subsets of detections selected in Monte-Carlo fashion based on their detection probability. *SNAPIDX* can compute both probability-weighted and Monte-Carlo location uncertainties, using arrival times and azimuth estimates from any phase.

Normalization and Assumptions

Normalization of network simulations to empirical experience is crucial to the credibility of the results. We use two sets of amplitude-distance curves to bound P-wave propagation in Eurasia (Figure 1). Curve EVC is composed of the Evernden (1967) Eastern North America (ENA) relation over distances of 0 to 20°, and the Veith and Clawson (1972) teleseismic curve. Curve MBY (Marshall et al., 1986) was derived from data recorded at Soviet stations and, for a given magnitude, produces relatively smaller P-wave amplitudes at regional distances. Nuttli's (1973) ENA Lg curve is used for all simulations, but Lg is not permitted to propagate across structural boundaries known to inhibit Lg propagation. NORESS detection capability is

represented by the detection probability curves of Ringdal (1986) and is simulated by assuming that regional propagation to NORESS is defined by the EVC P and Nuttli Lg curves. This gives station detection thresholds for P and Lg of 0.6 and 1.5 nm. There are substantial uncertainties in these values, and more study is needed to refine them. Arrival time and azimuth uncertainties at NORESS are assigned based on NORESS recordings of location residuals and of predicted versus observed measurements of arrival times of about 90 well-located events in Northern Europe. The total arrival-time standard deviations (σ_t) for P and Lg are 0.5 and 1.5 sec, respectively, and azimuth uncertainty (σ_α) is 8°. These variances assume no bias due to errors in the travel-time model, and so are appropriate for locations with "calibrated" paths.
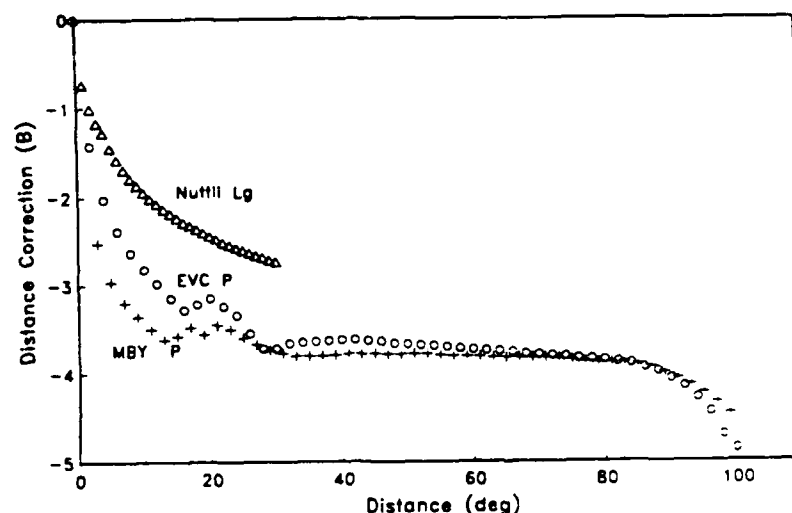
Figure 1.   Amplitude-distance curves ($B(\Delta)$, where $\log_{10}(Amp) = m_b + B(\Delta)$. Curves EVC (Evernden, 1967; Veith and Clawson, 1972) and MBY (Marshall et al., 1986) are used for P-wave attenuation in different simulations. Lg propagation is assumed to follow the curve of Nuttli (1973) in all simulations.

The results presented below are for networks that include 13 NORESS-quality arrays located in the Northern Hemisphere and external to the Soviet Union, and sets of 10 to 50 uniformly-spaced, in-country arrays and single seismometers. We assume that NORESS-type arrays within the USSR have detection thresholds 1.5 times greater than NORESS. The assumption is that the performance of the in-country arrays will be poorer due to the sites being less favorable and/or the clandestine tests of primary interest being conducted during relatively noisy periods. Single stations are assigned detection levels 4 times those of arrays in accordance with preliminary examination of beam gain conducted at SAIC and elsewhere (i.e., Mykkeltveit et al., 1985). The σ_t and σ_α at single stations are assumed to be twice than for arrays.

Application to the USSR

The first set of examples show the effect of varying the number and quality of stations on network detection thresholds throughout the USSR. The event detection criterion is a 90% probability of detecting 3 or more P or Lg phases across the network. Given arrival-time and azimuth information, epicentral and depth constraints may be placed on events meeting this criterion. Events are assumed to be near-surface explosions. Figure 2 shows the detection threshold for a network composed of NORESS-type arrays: 13 outside and 20 inside the Soviet Union. The MBY P-wave amplitude-distance curve is used. The threshold is between m_b 2.5 and 2.8 over most of the USSR. Slightly higher thresholds result when the 20 arrays are replaced by 40 single stations within the USSR (Figure 3). Table 1 summarizes the detection capability for several other combinations of the external network plus internal arrays or

CONTOUR FROM   2.6000   TO   3.4000   CONTOUR INTERVAL OF   0.20000
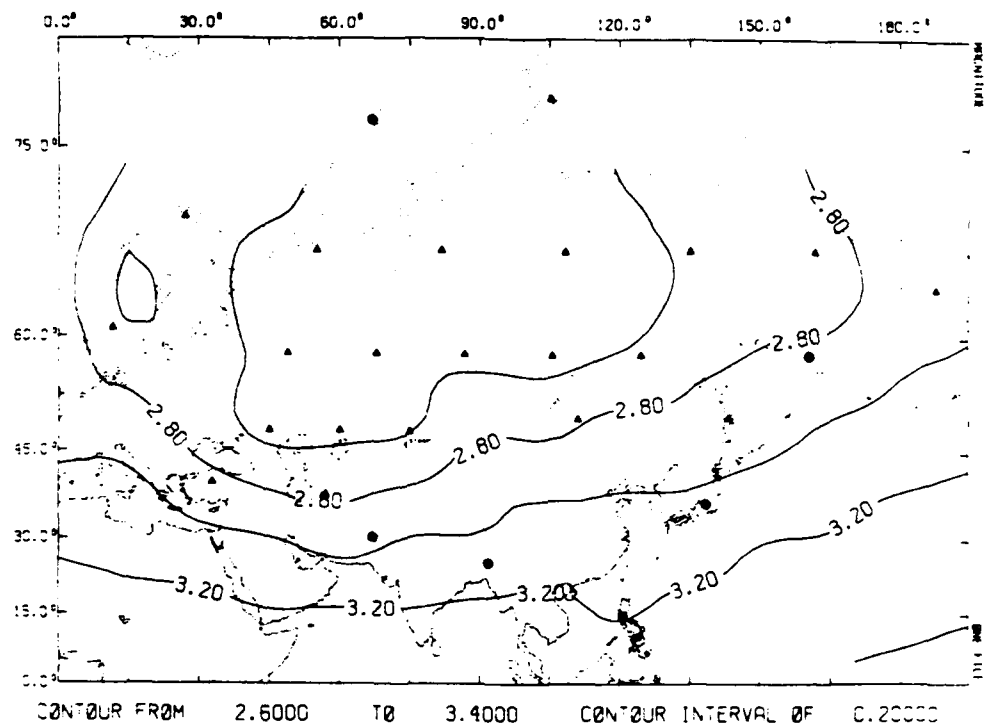
Figure 2.   Magnitude threshold for detection of 3 P or Lg phases from Eurasian events for a network including 13 external and 20 internal NORESS-type arrays. Station are denoted by solid triangles and circles, with Lg propagation blocked to the circle stations. P-wave attenuation was determined from curve MBY (Figure 1).

CONTOUR FROM   2.6000   TO   3.6000   CONTOUR INTERVAL OF   0.20000
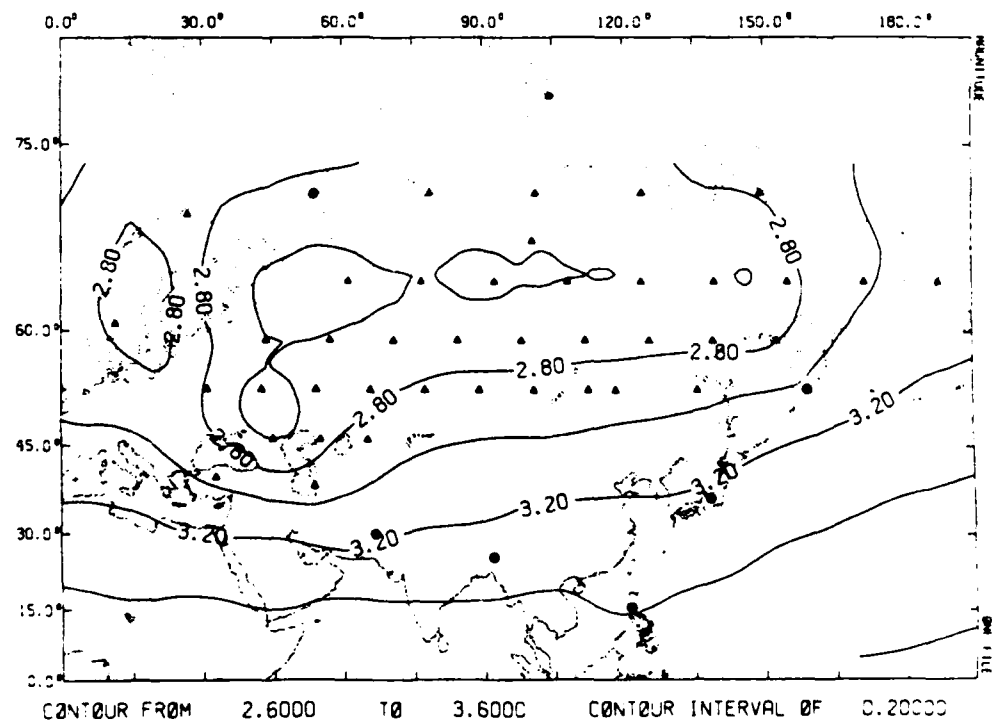
Figure 3.   Detection threshold for network with 13 external arrays and 40 internal single stations.

stations. Because of the large difference in the amplitude at regional distances, replacing MBY by EVC reduces the threshold. For the network of Figure 2, this reduction is about m_b 0.2. It is less than the regional difference between MBY and EVC because of the (unchanged) contributions of regional Lg and of the external arrays to the threshold determination.

Table 1. Summary of Detection Thresholds in the Soviet Union.
(90% Probability of Detecting 3 or more P or Lg Arrivals)

Network	Attenuation Curve	Arrays	Single Stations
13 External	MBY	< 3.2 - 3.4	-
+ 10 Internal	MBY	2.8 - 3.0	3.0 - 3.3
+ 20 Internal	MBY	2.5 - 2.8	2.9 - 3.2
+ 30 Internal	MBY	2.3 - 2.7	2.8 - 3.1
+ 40 Internal	MBY	2.1 - 2.6	2.6 - 3.0
+ 50 Internal	MBY	2.0 - 2.5	2.6 - 3.0
+ 20 Internal	EVC	2.3 - 2.6	2.7 - 3.0

Table 2 gives the median and 90th percentile lengths of the semi-major axis (SMA) for events in the USSR for some of the networks of Table 1. These are determined from 100 Monte-Carlo realizations at each location in a 15° x 15° grid covering the map. All uncertainties were obtained using P and Lg arrival times and azimuths along calibrated paths and with depth left unconstrained. P-wave amplitudes were determined using MBY. Figure 4 shows the median SMA for events at the 3 P or Lg detection threshold located with the network of Figure 2 (13 external and 20 internal arrays). Epicentral uncertainties in the USSR range from 10 to 30 km. Depth uncertainties have similar values. Other examples listed in Table 2 illustrate the dependence of detection capability on event magnitude, and on the difference between arrays and single stations for location of events at a fixed magnitude. The dimensions of all confidence bounds are strongly dependent on the assumed σ_t and σ_α. Additional uncertainty in crustal structure/travel-time curves could more than double the SMA presented in Table 2.

Table 2. Semi-Major Axis of Location Confidence Ellipse
(100 Monte-Carlo Realizations)

Network	Event Magnitude	Median	90th Percentile
13 External Arrays	DT[*]	20 - 45	500 - 700
+ 20 Internal Arrays (probability-weighted)	DT	12 - 30 (8 - 14)	100 - 500
+ 40 Internal Arrays	DT	10 - 30	40 - 300
+ 40 Single Stations	DT	15 - 45	50 - 500
+ 20 Internal Arrays	2.5	10 - 100	50 - 500
+ 20 Internal Arrays	3.0	7 - 20	10 - 50
+ 20 Internal Arrays	3.5	3 - 6	4 - 10
+ 40 Internal Arrays	3.5	3 - 5	3 - 8
+ 40 Internal Stations	3.5	5 - 10	6 - 25

* Semi-major axes computed at the network detection threshold.

CONTOUR FROM   15.000   TO   60.000   CONTOUR INTERVAL OF   15.000
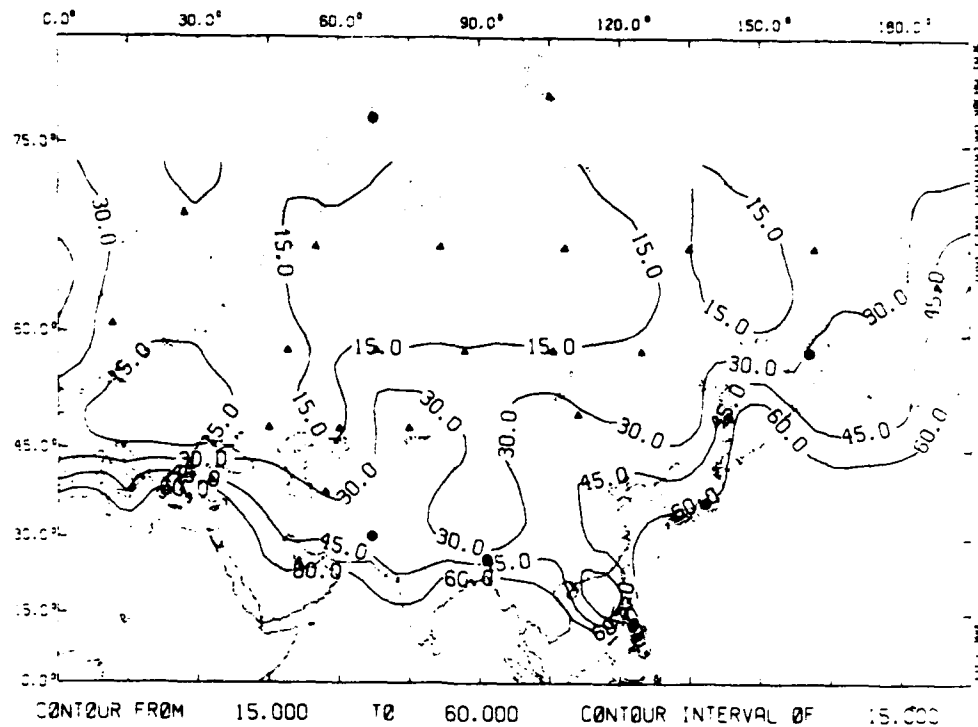
Figure 4. Median length (km) of semi-major axes as determined from 100 Monte-Carlo realizations of location solutions using the network of 13 external and 20 internal arrays. Event magnitudes are at the network detection threshold (Figure 2).

CONTOUR FROM   15.000   TO   60.000   CONTOUR INTERVAL OF   15.000
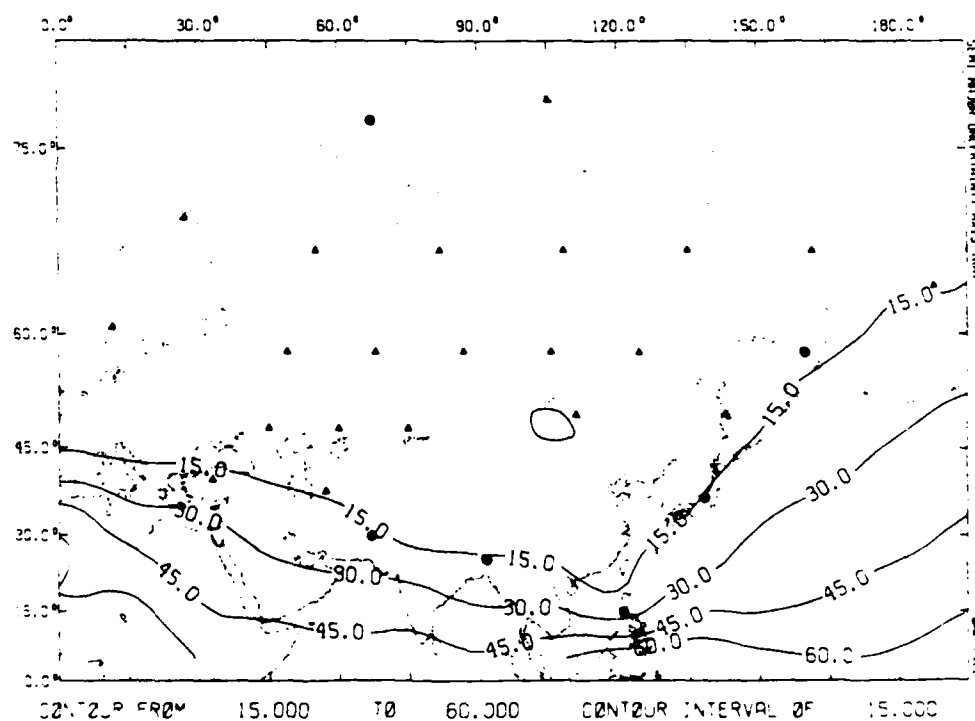
Figure 5. Semi-major axes (km), computed via the *SNAP/D* approach, for events at the detection threshold for the network of Figures 2 and 4. Confidence bounds are determined using all data, with each weighted by the probability of detection.

TS.3

Figure 5 shows the *SNAP/D* probability-weighted SMA computed in a manner otherwise identical to that for Figure 4. Note that for events near the detection threshold, the probability weighted ellipses significantly underestimate the median of epicentral uncertainties expected at any individual location within the USSR. The reason can be seen in the 90th percentile Monte-Carlo SMA which indicate that a significant proportion (> 10%) of events at the detection threshold will be very poorly located.

CONCLUSIONS AND RECOMMENDATIONS

Simulations like these provide a basis for assessing the configuration of networks necessary to meet desired detection and location performance criteria. For example, the simulations suggest that achievement of a detection threshold of m_b 2.5 (about that for a 1 kt decoupled explosion) over most of the USSR would require one or more of the following: (a) more than 20 internal NORESS arrays; (b) propagation more efficient than we observe at NORESS; (c) sites with a lower detection threshold than NORESS; or (d) an improved ability to process array data. About twice as many single stations as arrays are required to provide equivalent detection and location capability. However, our normalization assumptions (e.g.; amplitude versus distance, station detection thresholds, measurement errors, etc.) control the results, and there are substantial uncertainties in these assumptions. We are presently studying the NORESS data to refine our estimates of the parameters that characterize the performance of this station, but it will remain difficult to extrapolate this capability elsewhere until we get data from other sites. We also plan to incorporate regional and frequency-dependent amplitude attenuation into future network simulations.

REFERENCES

Ciervo, A.P., S.K. Sanemitsu, D.E. Snead, R.W. Suey, and A.G. Watson (1985) User's Manual for SNAP/D: Seismic Network Assessment Program for Detection, *Pacific-Sierra Research Corporation, Report* 1027B.

Mykkeltveit, S., D.B. Harris, and T. Kvaerna (1985) Preliminary evaluation of the event detection and location capability of the small-aperture NORESS array, in *NORSAR Scientific Report* 2-84/85, Kjeller, Norway.

Marshall, P.D., J. Bingham and J.B. Young (1986) An analysis of P-wave amplitudes recorded by seismological stations in the USSR, *Geophys. J.R. Astr. Soc.* 84, 71-91.

Nuttli, O.W. (1973) Seismic wave attenuation and magnitude relations for Eastern North America, *J. Geophys. Res.* 78, 876-885.

Ringdal, F. (1986) Regional event detection using the NORESS array, in *NORSAR Scientific Report* 2-85/86, Kjeller, Norway.

Veith, K. and G. Clawson (1972) Magnitude from short-period P-wave data, *Bull. Seismol. Soc. Am.* 62, 435-452.

SPECTRAL CHARACTERISTICS AND ATTENUATION OF REGIONAL PHASES RECORDED AT NORESS

Anne Suteau-Henson, Thomas Sereno, and Thomas C. Bache

Science Applications International Corporation
10210 Campus Point Drive, San Diego, California 92121

OBJECTIVE

Regional events recorded at NORESS are being processed using an automated seismic array processing package which is an extension of the RONAPP program used at NORSAR (Mykkeltveit and Bungum, 1984). The spectrum is calculated automatically for each detected signal, and we have been using these spectra to study the spectral characteristics and attenuation of regional phases. In this paper results are summarized for two studies. In one ' ' compare Pn spectra for various events to evaluate their potential value for characterizing events. In the second we perform a generalized least-square inversion of log amplitude spectra for Pn and Lg attenuation. The data are parameterized by an ω^2 source spectrum with cube-root corner frequency scaling and an assumed geometric spreading function. The spectra are inverted for source moment, a constant relating corner frequency and moment, and apparent attenuation represented by $Q_0 f^\eta$. While Pn amplitude is more variable than Lg, spectra of both phases are well modeled by this simple parameterization.

RESEARCH ACCOMPLISHED

Spectral Characteristics of Pn

We calculate array spectra with the method of Bache et al. (1985), originally developed for teleseismic P waves, but now extended for the analysis of regional phases. For each detection the array spectrum is obtained by averaging "noise-corrected" energy density spectra computed for each vertical channel. We use a five second time window, starting 0.3 seconds before the computed onset time. The power spectrum of a five second noise window taken before Pn is subtracted to correct for the "ambient noise". These "noise-corrected" energy density spectra are then averaged over all array elements, and the square-root of this average is taken, giving the amplitude spectrum for this detection. Bache et al. (1985) show that this spectral estimate converges to the true signal spectrum (as the number of array elements increases) if the noise is random, stationary, and uncorrelated with the signal.

Figure 1 shows the amplitude spectra of Pn for two sets of events. The plot shows only the part of the spectrum above the noise level (averaged across the array elements). The first set includes seven explosions from the Titania mine, located about 400 km from NORESS in S.W. Norway, and the second set includes eight events located in a small area offshore along the same azimuth. Most of these events have M_L between 2.2 and 2.7. The mine blast spectra are rich in high-frequency energy. Their spectral shape is variable, with many having modulations with various periodicities (possibly due to ripple firing). The offshore events may be earthquakes or underwater explosions. They have spectra that are very similar in shape and high-frequency slope, but they differ from the mine blast spectra in having the energy concentrated below 5 Hz and a significant spectral decay at high frequency.

Pulli (1986) first studied this set of events, observed the differences in frequency content, and suggested the use of a spectral ratio to discriminate between them. Following his suggestion, we calculated the ratio of high to low frequency power, using the bands 2 - 5 Hz and 5 - 12 Hz. The results are plotted at the bottom of Figure 1. The spectral ratios for all explosions are greater than 0.3, while those for the offshore events are less than 0.3. Therefore, this spectral ratio successfully separates these two sets of events. However, it is likely that much of the difference is due to path effects (we have noticed that offshore events usually have "different" spectra), and we are not certain whether the offshore events are actually earthquakes or explosions.

We examined a larger suite of events to see how spectral ratios vary. Our data set includes repeated explosions with similar magnitudes (M_L about 2.5) from several mines located in Western USSR at about 1000 km from NORESS. Figure 2 shows spectra for Pn for explosions from two of these mines (Estonia mines E7 and E8) which are located within 25 km. The spectra are similar for events within one of the mines (apart from modulations), but are different between the two, indicating significant differences in source and/or near-source effects. Of particular interest is the peak observed around 3 Hz for E7, but absent from the E8 spectra which are depleted in low frequency energy. At the bottom of Figure 2 are plotted spectral ratios for events in these two mines, and also for events in other mines further north (V2 and V10). E8 has larger spectral ratios than all other mines (the line separates E8 from the others). Overall, the variations are as large as those seen in Figure 1 where this ratio successfully discriminated between two sets of events. Spectra from events at other locations show similar variations for this particular spectral ratio, and we have no evidence that any other ratio will be significantly more consistent. We have no closely matched set of explosions and earthquakes to compare, but a conclusion of the generalized inversion study described next is that there are no consistent distinguishing differences between earthquake and explosion spectra when they are normalized for differences in source size (moment) and path length (Q). However, most of the events used in the inversion had local magnitudes less than 3.0 and Pn spectra band-limited to frequencies near 15 Hz. Because corner frequencies for these small events are near the upper limit of the available bandwidth, the data do not provide firm constraints on possible differences between earthquakes and explosions.

Attenuation of Regional Phases

In order to systematically characterize the spectra of regional phases recorded at NORESS, we have developed a generalized inversion that simultaneously estimates source strength and $Q(f)$. The procedure has been applied to spectra of 150 events at ranges between 300 and 1100 km. At ranges less than about 800 km, the Lg signal/noise ratio is less than one for most of the events above 7 or 8 Hz, while at shorter distances Lg spectra are probably contaminated by Sn coda at high frequency. Therefore, Lg spectra were inverted between 1 and 7 Hz, while Pn spectra were inverted from 1 to 15 Hz (the upper limit for good signal/noise).

The inversion requires a source spectral shape parameterization, and we have adopted an ω^2 model, with corner frequency inversely proportional to the cube root of the long period source level, S_0. Log amplitude spectra are inverted for S_0 for each event and for a single parameter relating S_0 to corner frequency. Spherical spreading is assumed for Pn and cylindrical spreading for Lg beyond a transition distance, $r_0 = 100$ km (Herrmann and Kijko, 1983). The assumed r_0 trades off directly with S_0 and does not affect the Q estimate. However, Q estimates are dependent upon the assumed spreading rate. Attenuation is parameterized by a power law frequency dependence of apparent Q ($Q(f) = Q_0 f^{\eta}$), including the effects of both

scattering and anelasticity.

Spectra computed with the parameters determined by the inversion are compared to observed spectra for a Western USSR mine blast and to a German earthquake in Figure 3. The results of the inversion for L_g are $Q_0 = 300$ and $\eta = 0.44$. For Pn the results are $Q_0 = 250$ and $\eta = 0.50$. The corner frequency for an "average event" with $M_L = 3.0$ is approximately 12 Hz. With these values and S_0 as a function of magnitude, we have parameterized the spectral data and can compute Pn and Lg spectra for an "average event" at any selected range and magnitude. Results for NORESS $M_L = 3.0$ are shown at the bottom of Figure 3, along with an average NORESS noise spectrum estimated from samples taken prior to Pn for many events. The variation of observed Pn spectra about the curves in Figure 3 is greater than for Lg. This is probably because Pn samples a smaller fraction of the focal sphere than Lg, making its amplitude more sensitive to source radiation pattern, focusing and defocusing, and scattering. However, the Pn variations are primarily in absolute amplitude (i.e., in the S_0 for a given M_L) rather than in spectral shape. When only explosions are used in the inversion (to eliminate radiation pattern effects on absolute amplitude), the moment-magnitude scatter is greatly reduced.

CONCLUSIONS AND RECOMMENDATIONS

Spectral ratios are able to discriminate between chemical explosions in S.W. Norway and apparent offshore earthquakes at nearby locations, but path effects may be the cause. We also note that repeated events at the same mine have similar spectral characteristics for Pn, apart from diverse spectral modulations. But these characteristics can be significantly different from those at other mines at the same distance, even when the mines are quite close. These similarities and differences are potentially useful for accurately locating repeated events. However, the observed spectral variations make it difficult to be optimistic that spectral ratios can be used to discriminate between source types with much confidence.

A large suite of regional Pn and Lg spectra were inverted for source moment and apparent attenuation (including both anelasticity and scattering). The results support our tentative conclusion that differences between earthquake and explosion spectra are likely to be overwhelmed by path effects, though our data was restricted to relatively small events and band-limited to frequencies less than 15 Hz. The results of the inversion provide a simple parameterization that can be used to compute representative range-dependent spectra for events of a given magnitude (or assumed source character, such as a decoupled nuclear explosion).

REFERENCES

Bache, T. C., P. D. Marshall, and L. B. Bache (1985), "Q for Teleseismic P waves from Central Asia", *J. Geophys. Res.* **90**, 3575-3587.

Herrmann, R. and A. Kijko (1983), "Modeling Some Empirical Vertical Component L_g Relations," *Bull. Seismol. Soc. Am.* **73**, 157-171.

Mykkeltveit, S. and H. Bungum (1984), "Processing of regional seismic events using data from small-aperture arrays", *Bull. Seism. Soc. Am.* **74**, 2313-2333.

Pulli, J. J. (1986), "Expanded use of computers in regional seismic data analysis", in Technical Report C86-06, Center for Seismic Studies, Arlington, Virginia, 2.29 - 2.38.

TITANIA MINE   OFFSHORE EVENTS

5 - 12 HZ / 2 - 5 HZ
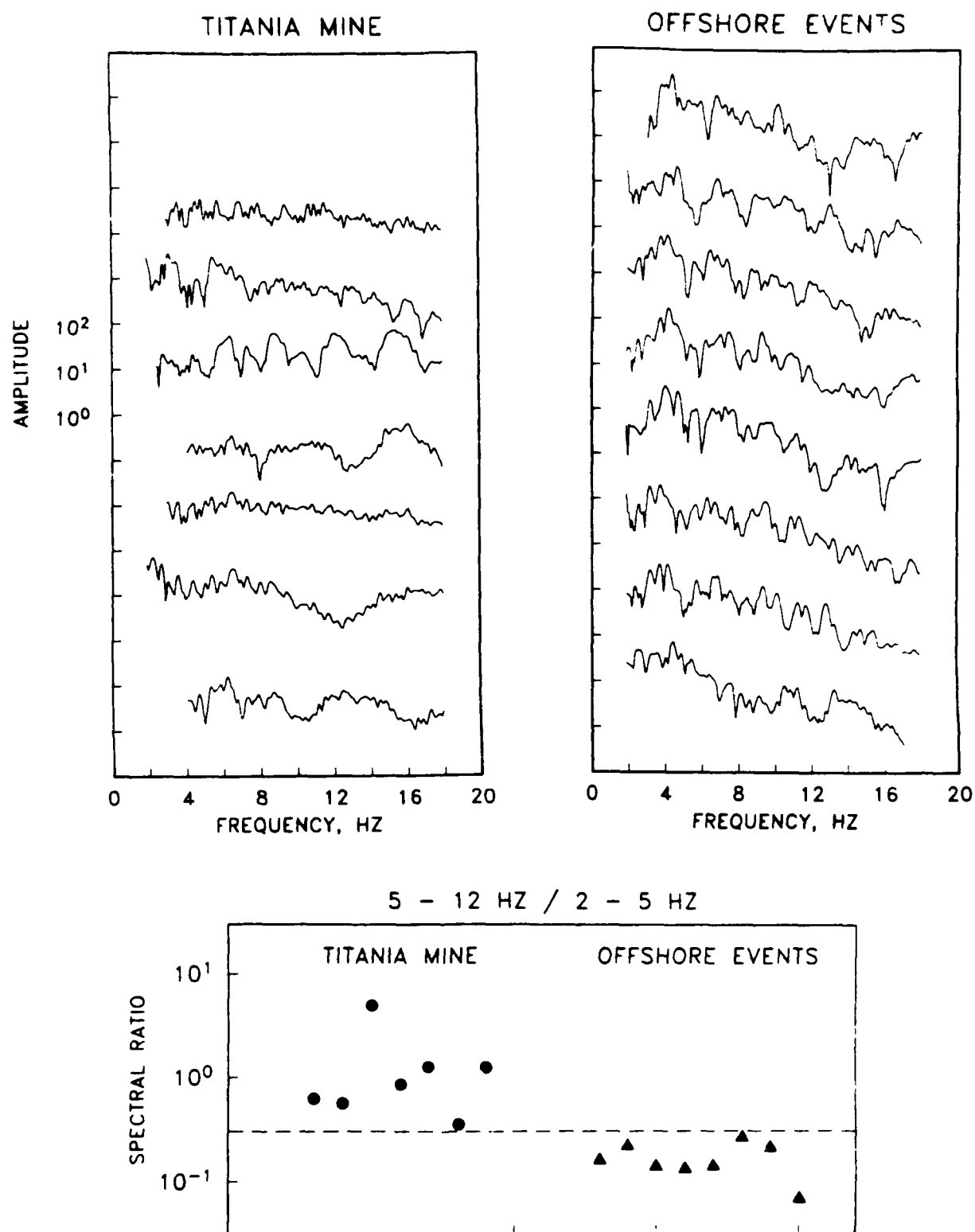
Figure 1:   Instrument-corrected *Pn* amplitude spectra are plotted for a set of events from the
Titania mine in S.W. Norway (left) and a set of nearby offshore events (right).
The amplitude units are arbitrary and a constant vertical offset has been added
between spectra.   Below are power spectral ratios for these two sets of events.
The dashed line corresponds to a value of 0.3.
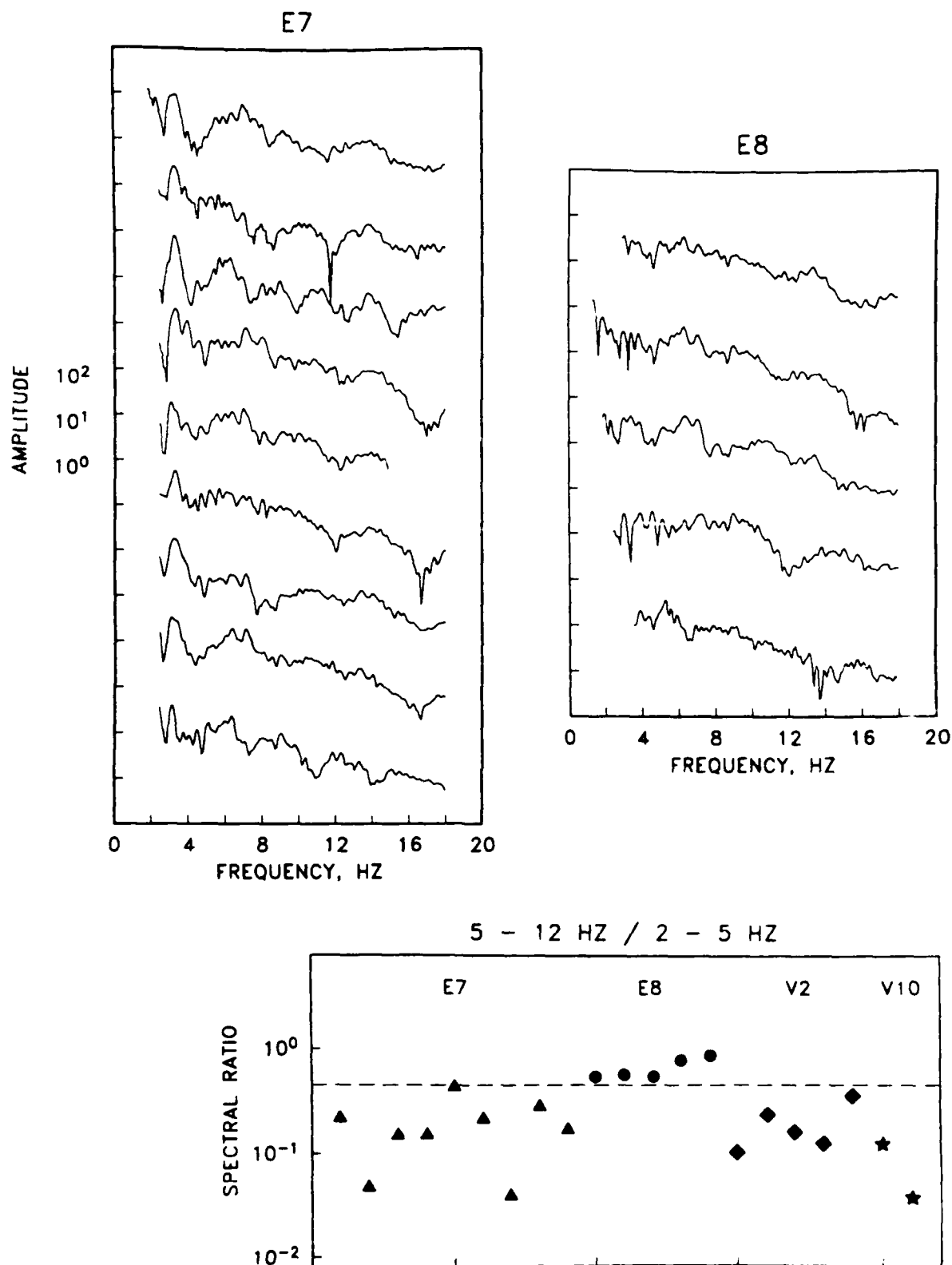
Figure 2: Instrument-corrected *Pn* amplitude spectra are plotted for explosions from Estonia mines E7 (left) and E8 (right). The amplitude units are arbitrary and a constant vertical offset has been added between spectra. Below are power spectral ratios for these two sets of events, and for events from two other Western USSR mines (V2 and V10). The dashed line corresponds to a value of 0.45.
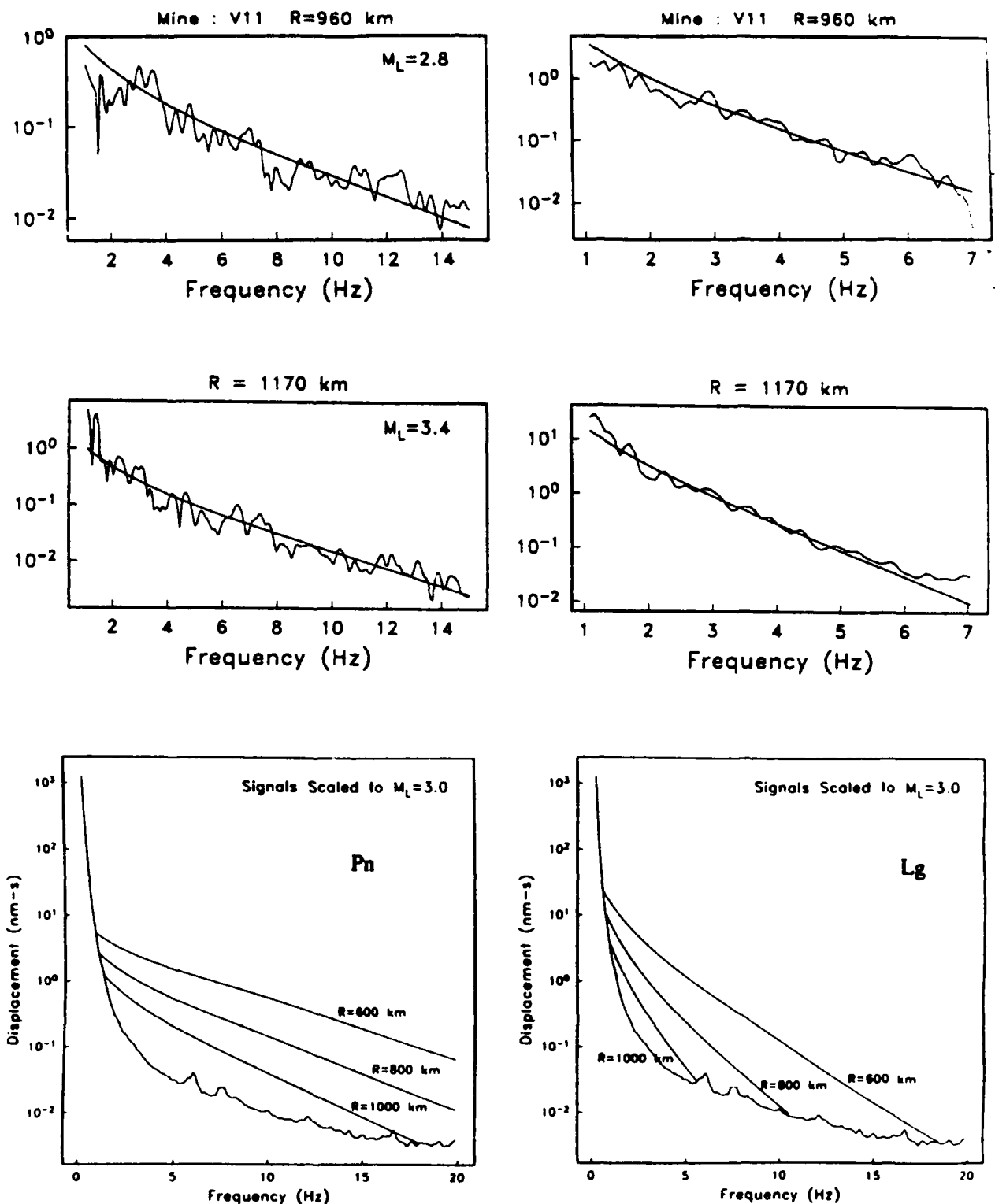
Figure 3: Spectra computed with the parameters determined by the inversion are compared to observed *Pn* (left) and *Lg* (right) spectra for a Western USSR mine blast and a German Earthquake. The inversion extended from 1 to 15 Hz for *Pn* and from 1 to 7 Hz for *Lg*. The bottom panels show predicted range-dependent spectra for an "average event" with NORESS M_L = 3.0. Noise is the average of samples taken before *Pn* for many events.

ARRAY PROCESSING STRATEGIES OF SEISMIC SIGNALS
FROM LOCAL AND REGIONAL EVENTS

EYSTEIN S. HUSEBYE[1,2] and B.O. RUUD[1]

[1] Geological Institute, Box 1047 Blindern, 0316 Oslo 3, Norway

[2] Leave of absence from NORSAR, Kjeller, Norway

1. INTRODUCTION

A variety of array processing schemes have been extensively studied by researchers in different fields like acoustics, radio astronomy, electrical engineering, statistics, geophysics and naturally seismology. In classical array processing, phased beamforming and f-k analysis, it is assumed orthogonality between signals and noise. To enhance resolvability of closely spaced sources, a variety of so-called high resolution techniques have been introduced. In Sec. 2 we examine the performance of a variety of array processing techniques for relatively complex signals. Then we demonstrate the improved array event locations are feasible using interpolated move-out times for extremal points of first cycles (Sec. 3). For events at local and regional distances array records are complex and this is often attributed to scattering contributions of the Chernov type. In Sec. 3 we discuss crustal structural models on the basis of an extensive marine profiling survey in the Skagerrak Sea (ca 200 km SE of NORESS) covering tectonic provinces with an age span of about 300 to 1700 M.y.

2. ARRAY SIGNAL PROCESSING SCHEMES

Array signal processing techniques considered in the context of meritorious features like robustness, stability of estimates and computational efficiencies are as follows:

Phase beamforming and f-k analysis

Weighted beam power $\hat{P}_B = \underline{\omega}^* C(\underline{u}) \underline{\omega}$;   Unweighted beam power $\hat{P}_B = \dfrac{1}{M^2} \underline{\ell}^* C(\underline{\omega}) \underline{\ell}$

where $C(\underline{u})$ = covariance matrix for slowness vector $\underline{u}$; $\underline{\omega}$ = weight function for M sensors, and $\underline{\ell} = (1,1,\ldots,1)$ of length M.

Semblance estimates $\hat{s} = P_B/P_N$

Weighted $\hat{s} = \underline{\omega}^* C\omega / \Sigma \, \omega_i C_{ii}$;   Unweighted $\hat{s} = \underline{\ell}^* C\underline{\ell} / M tr C$

Maximum likelihood methods (MLM)

Here weights are $\underline{\omega} = C^{-1}\underline{\ell} / \underline{\ell}^* C^{-1}\underline{\ell}$.

Beam power and semblance estimates are:

$$\hat{P}_{MLM} = [\underline{\ell}^* C^{-1} \underline{\ell}]^{-1} \quad \text{and} \quad \hat{S}_{MLM} = P_{MLM}/P_{AV}$$

N-th root stack (beamforming)

Firstly, the N-th root stack is formed

$$S_{1/N} = \frac{1}{M} \sum_{i=1}^{T} \text{sign}(y_i) \cdot y_i^{1/N}$$

and then raising to N-th power:

$$S_N = \text{sign}(S_{1/N}) \cdot S_{1/N}^N$$

where y_i = i-th sensor trace and slowness index ignored. Power from the S_N trace is calculated as a function of slowness.

2.1 Result summary

From extensive analysis of many events, major results are:

- The common performance feature of the above techniques is that peak signal power location in the slowness plane is invariant albeit MLM-estimation is best.

- For the complex part of the P-wave train, "short window" techniques like semblance and N-th root stack have the best performance and besides are computationally attractive.

- In general, these techniques are inadequate for parameterizing the coda due to weak signal coherency and/or correlating signals.

- Very different approaches are needed for analyzing the complex part of array records. Particularly, methods based on assumptions of signal/noise orthogonality should be avoided.

3. ARRAY EVENT LOCATION

From Fig. 1 we have that slowness results depend on which part of the signal is actually used in estimation - the very first cycles give "best" results. In consequence, we have experiemented with "point" estimates, that is, pick extremal points of the very first signal cycles using a cubic spline interpolation scheme. For adequate SNRs, extremal points or relative move-out times can consistently be read to nearest 0.002 sec (ca a tenth of sampling rate), which is equivalent to errors of ca 1 deg in azimuth an 0.1 km s^{-1} for P_n-velocity signal. For event location per se bias errors have to be removed via "master event" techniques.

4. CRUSTAL STRUCTURE MAPPING

During Jan/Feb 1987 the eminent ship M/V Mobil Search completed 1730 km of deep seismic profiling lines in the Skagerrak Sea (16 sec twt or ca 50 km depth range). A few examples of preliminary structural results derived from these data are shown in Fig. 2; the outstanding features here are the strong lamination of the crust. These characteristics appear to be independent of the geological ages of the tectonic provinces sampled; old shield structures in Swedish waters (1700 M.y.) to Permian crust in the southward extension of the Oslo graben (300 M.y.). The ship's air gun signals were recorded at mobile 3-component land stations and also by the NORESS array 2-300 km to the north. In a special experiment 40 sec twt recordings were used, which is equivalent to a depth range of ca 150 km, or the entire lithosphere. We consider these profiling experiments particularly relevant in a seismic monitoring context as such laminated structures would provide a relatively <u>deterministic</u> explanation of complex seismograms (coda waves) at local and regional distances. Furthermore, crustal laminations of the kind displayed in Fig. 2 appear to be a rather universal feature of the continental crust (e.g., see Matthews and Smith, 1987). Finally, we will attempt to compute synthetic seismograms on the basis of the derived crustal structures (numerical problems are severe) which may be a more realistic alternative to scattering hyptheses in modelling P-signal codas.

5. CONCLUDING REMARKS

We have made a comparison between common array signal processing techniques and find that differences in performances are modest. An essential point here is that we have to compromise between adequate bandwidth and short signal windows because wavelet slownesses may vary considerably through a P-signal wave train. A weakness of these processing schemes (beamforming, f-k, semblance, MLM and N-th root stack) is the general inability to properly handle interfering, presumably correlating signals. Analyzing techniques for handling such cases are very complicated requiring multiwavelet parameterization models. A parallel problem here is that more extensive array signal parameterization requires new schemes for objectively using this information for event location and source identification.

Local and regional seismogram complexities are generally attributed to randomly distributed scattering contributions. We give evidence on the basis of extensive vertical seismic profiling of an area south of NORESS that the principal crustal feature is structural lamination, apparently independent og ages of geological provinces.

REFERENCE:

Matthews, D. & C. Smith (eds.) (1987): Deep Seismic Reflection Profiling of the Continental Lithosphere, Geophys. J. Roy. Astr. Soc., 89. 1-447.

Fig. 1   MLM-Semblance analysis of NORESS recordings from an underground
Novaya Zemlya explosion. Traces, that of AOZ displayed, are
unfiltered and signal window of 0.75 sec used. (a) Looping over
azimuth; velocity fixed at 9.5 km s^{-1}; (b) Looping over velocity;
azimuth fixed at 30 deg. Note the dispersiveness in the slowness
parameters with time, and also that semblance is relatively weak
in the most energetic part of the record, presumably due to
interference.   194

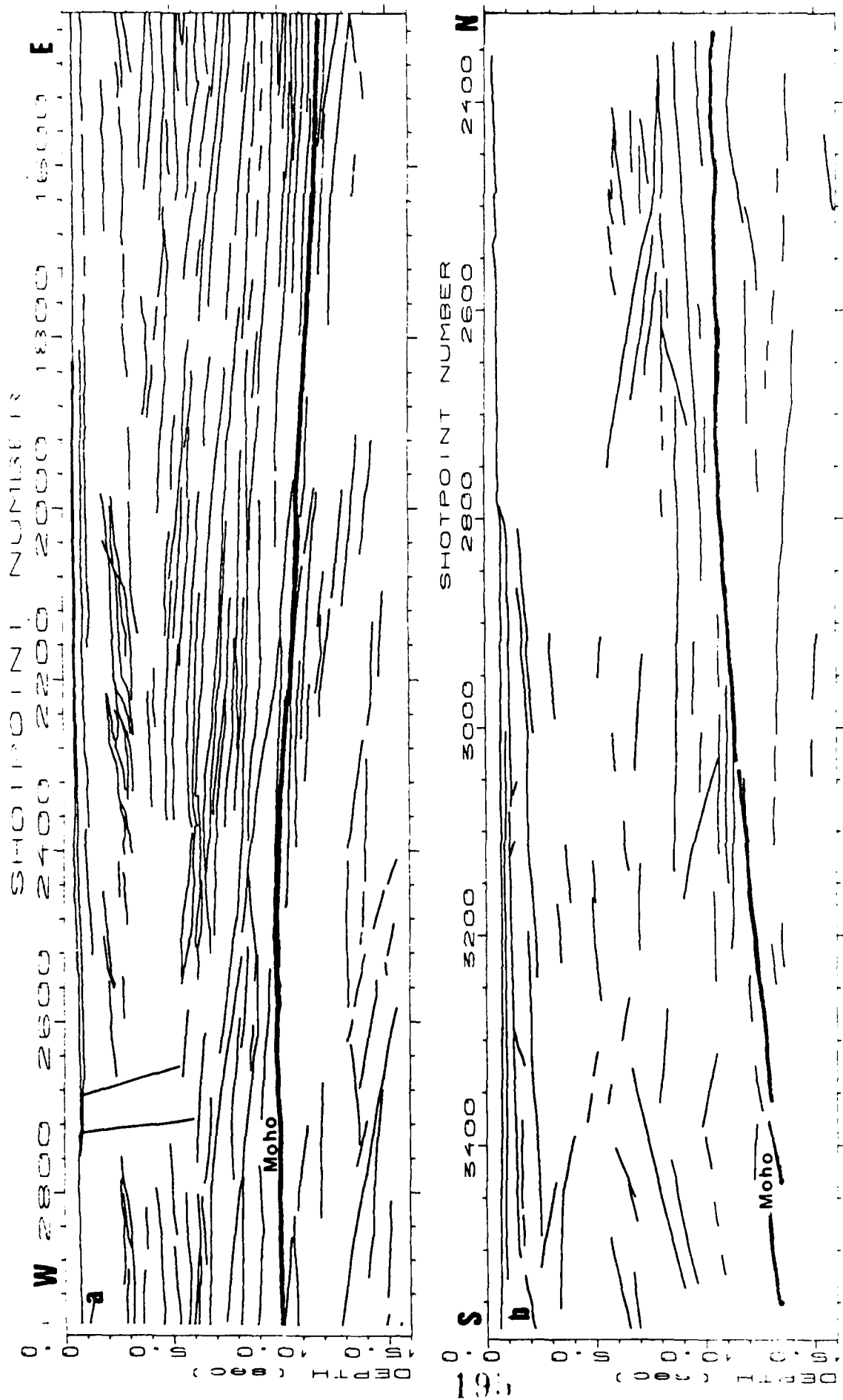Fig. 2   Crustal structural results on the basis of vertical profiling. Shot point spacing is 50 meters and depth in sec (twt). (a) East-west profile running towards Sweden, just north of Jutland, Denmark; (b) North-south profile parallel (offshore ca 20 km) to the Norwegian coast. The apparent upper crust transparency to the north may be due to hard (rocky) sea floor. Notice that laminated structures can be seen below Moho.

WIDE-BAND SLOWNESS ESTIMATION USING A SMALL APERTURE SEISMIC ARRAY

TORMOD KVÆRNA

NTNF/NORSAR, P.O. Box 51, N-2007 Kjeller, Norway

OBJECTIVE

In order to evaluate the location potential of the NORESS array, the slowness of events of known origins have been estimated applying different approaches. The objective of this investigation is to develop methods and rules that can be applied in real-time processing of regional array data and to give an idea of the uncertainty of automatic location estimates.

RESEARCH ACCOMPLISHED

Kværna and Doornbos (1986) described a method to estimate the slowness vector using arrays of either vertical or three-component seismometers. Their conclusion was that conventional frequency-domain beamforming of vertical sensor data provided more stable estimates than estimates obtained by similar processing of three-component arrays or sensors.

In this study we pursue this investigation further, by concentrating on conventional slowness estimation (narrow-band and wide-band) for a suite of reference events of known origin.

Blåsjø

We have selected a set of ten quarry blasts at a dam construction site in southwestern Norway (Blåsjø).

Site coordinates:	59.31 N 6.95 E
True azimuth from NORESS:	240.2 degrees
Distance from NORESS:	301.2 km

The size of the explosions is typically 50 tons TNT. All of the events have a high signal-to-noise ratio (SNR) at NORESS; thus noise interference in the slowness estimates is minimal.

Fig. 1 shows the results from processing the Pn phase for each of the ten events. Four different methods have been chosen for frequency selection:

a) Narrow band - variable frequency

   The analysis frequency f selected for each event is the dominant frequency of the signal as determined by the cycle count method of the real-time processor.

b) Wide band - variable frequencies

   Processing is done in the band ($f_0 - f_0/4$, $f_0 + f_0/4$) where f_0 is the dominant frequency.

c) Narrow band - 7.0 Hz

   In this case the frequency has been kept fixed (f_0 = 7.0 Hz) for all
   events.

d) Wide band 5.0 - 9.0 Hz

   This is analogous to b) but with f_0 = 7.0 Hz kept fixed for all events.

It is clear from the figure that by far the most stable result is obtained
by method d). The mean azimuth is estimated at 242.19 degrees, and the
maximum spread around the mean is only ± 1 degree.

We also conducted slowness estimation of the Sn and Lg phases of the ten
events, using the fixed frequency approach, i.e., corresponding to c) and
d). Fig. 2a shows the results for the single frequency case (f_0 = 4.0 Hz),
plotted together with the Pn results from c) above. We notice that the
azimuth spread is larger for the two secondary phases. There is a clear
distinction between the estimated phase velocities of the primary and
secondary phases, and the Sn phase velocities tend to be larger than those
of Lg.

In fig. 2b, a similar plot is presented corresponding to the wide band,
fixed frequency approach (cf. d) above). We now see a clear phase velocity
separation among all three phase types. In addition, estimated azimuths are
generally consistent, although the scatter is somewhat larger for Sn than
for Lg. The mean azimuth for the Lg phase is estimated at 238.85 degrees,
and the maximum spread around the mean is ± 2 degrees.

All processing results in this study are based on a 3 sec. long time inter-
val. We also conducted some experiments, changing slightly the positioning
of the analysis window, but it did not produce any significant changes in
the overall results. Correct determination of the start time and length of
the analysis window may become more important for events with lower SNR,
and rules for automatic picking of these variables should be further
investigated.

Semipalatinsk

P-wave recordings from sixteen presumed nuclear explosions at Semipalatinsk
have been analyzed by the wide band, fixed frequencies approach. A fre-
quency range of 1.5-3.5 Hz was selected. This is for all events close to
the optimum filter band for SNR gain on the array beam.

Site coordinates: 50 N 79 E
True azimuth from NORESS: 75 degrees
Distance from NORESS: 4200 km

All events, except one, had a very high SNR. As shown in fig. 3, the sta-
bility of the Semipalatinsk slowness estimates is as good as in the Blåsjø
case. The mean azimuth is 78.10 degrees and the maximum spread around the
mean is ± 1 degree.

Estonia

As a third data base for testing of the location algoritnms, NURESS recordings of ten mining explosions in the Estonian region of USSR were chosen. These events were located by the network in Finland, and reported by the University of Helsinki.

Site coordinates: 59.5 N   28.5 E
True azimuth from NORESS: 92 degrees
Distance from NORESS: 950 km

In the 5.0-7.0 Hz band, the Pn phases of these events had a single channel SNR ranging from 2.7 to 12.6, which is much lower than for the Blåsjø and Semipalatinsk events. The University of Helsinki reported duration magnitudes (Md) in the range 2.5 to 2.9.

Results from wide band slowness estimation of the Pn phases are shown in figure 3. They were all processed in the frequency band 5.0-7.0 Hz. The mean azimuth is 81.38 degrees and the maximum spread around the mean is nine degrees. This is significantly larger than for the two other sites. In addition the mean azimuth has a bias of almost ten degrees from the true azimuth of 92 degrees.

Automatic estimation of slowness

It is difficult to predetermine fixed frequency bands for slowness estimation, because of the large variation in signal and noise spectra, see figure 4b. A bad choice of frequency may lead to processing in the band with lowest SNR rather than best SNR. A real-time detection processor will use several filter bands and array sub-geometries to get the best SNR for different categories of signals. The detection report will therefore contain information about which frequency band and array sub-geometry that give the best SNR. By using this information we may stabilize the slowness estimates in various ways. If the SNR is above a given limit, we may if possible, expand the array geometry and thereby making the estimates more stable. We can also stabilize the estimates by increasing the processing bandwidth to higher frequencies, provided the SNR is sufficently high.

We have tested this idea by processing the ten Estonian events with the same array sub-geometry and filter band as for the beam with maximum SNR. The results are shown in figure 4a. The Pn and Sn estimates show a large scatter in both azimuth and velocity, but the Lg estimates are more consistent. The mean of the Lg azimuths is 92.98 degrees with a maximum spread around the mean of 6 degrees. We were not able to separate the Sn and Lg phases on the basis of velocity as in the Blåsjø case, probably due to lower SNR and a narrower usable bandwidth.

CONCLUSIONS AND RECOMMENDATIONS

This study has shown that employing a wider frequency band clearly tends to increase the stability of the slowness estimates, provided the signal-to-noise ratio is adequate over the band of interest. The stability was found, particularly for Pn, to be remarkably good for the western Norway quarry blasts when using a fixed frequency band for all ten events. The same apply to the teleseismic P-phases from Semipalatinsk.

If the processing band for slowness estimation is selected from the detection processor information, we should apply the estimated Lg azimuth for location purposes, see figure 4a and figure 2b.

From figure 4b, we can see that the Lg spectra show a more uniform pattern than the Pn spectra. The best frequency band for detection of Lg phases will for this suite of events be 1.0-3.0 Hz, whereas the optimum Pn filter bands will range from 2.5-4.5 Hz to 6.0-8.0 Hz.

The robustness and stability of the Lg azimuth estimates using the detector information is due to the fact that the detection processor for all ten events report 1.0-3.0 as the filter band with optimum SNR.

REFERENCES

Kværna, T and D.J. Doornbos (1986): An integrated approach to slowness analysis with arrays and three-component stations. Semiann. Tech. Summary, 1 Oct - 31 Mar 1986, NORSAR Sci. Rep. No. 2-85/86 Kjeller, Norway

Kværna, T and F. Ringdal (1986): Stability of various f-k estimation methods. Semiann. Tech. Summary, 1 Apr - 30 Sep 1986, NORSAR Sci. Rep. No. 1-86/87 Kjeller, Norway
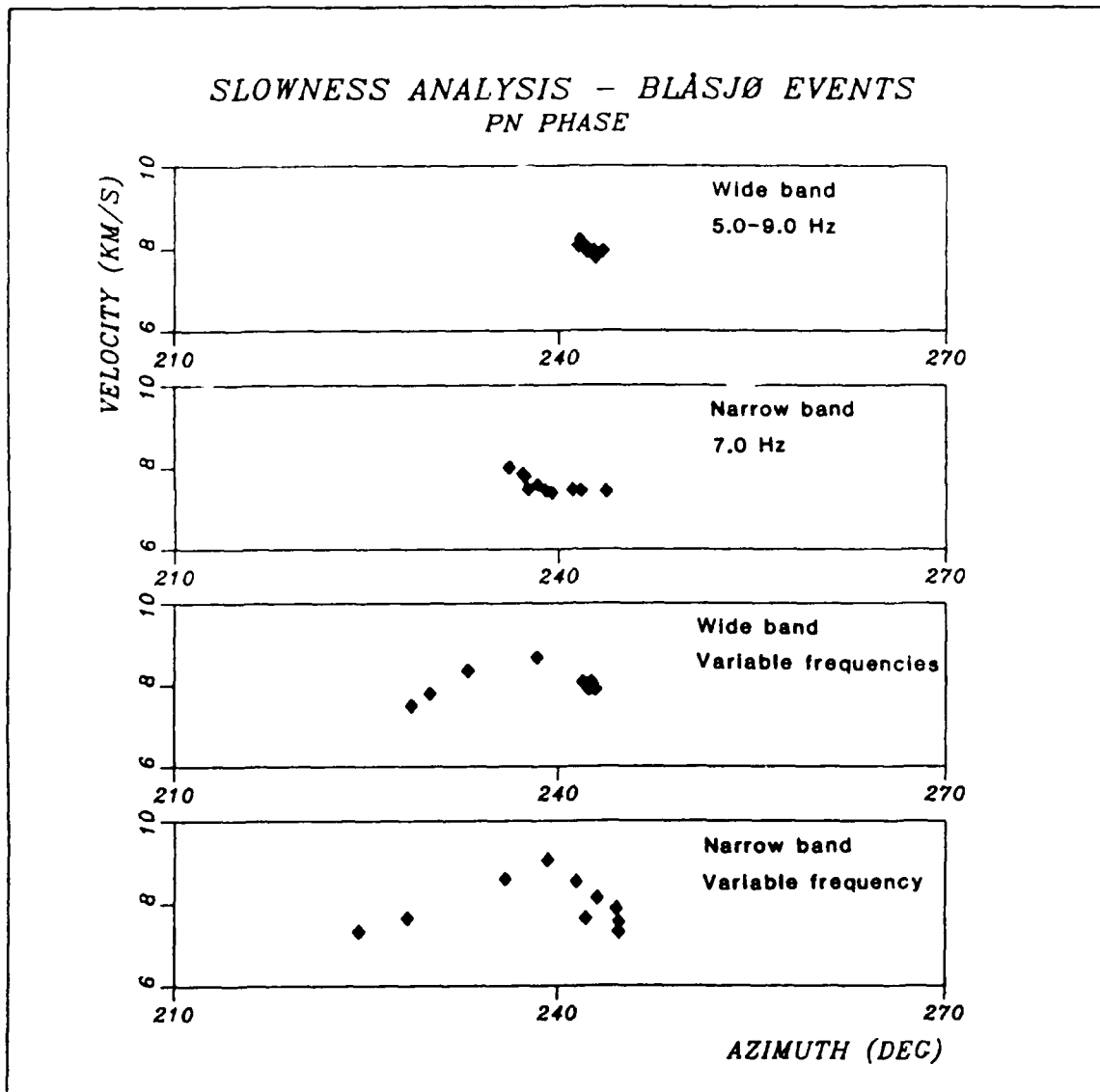
SLOWNESS ANALYSIS - BLÅSJØ EVENTS
PN PHASE

Fig. 1 Processing results (azimuth and velocity) for the Pn phase of the
ten Blåsjø events in the data base. Results using four different
approaches, as described in the text, are shown. Note the
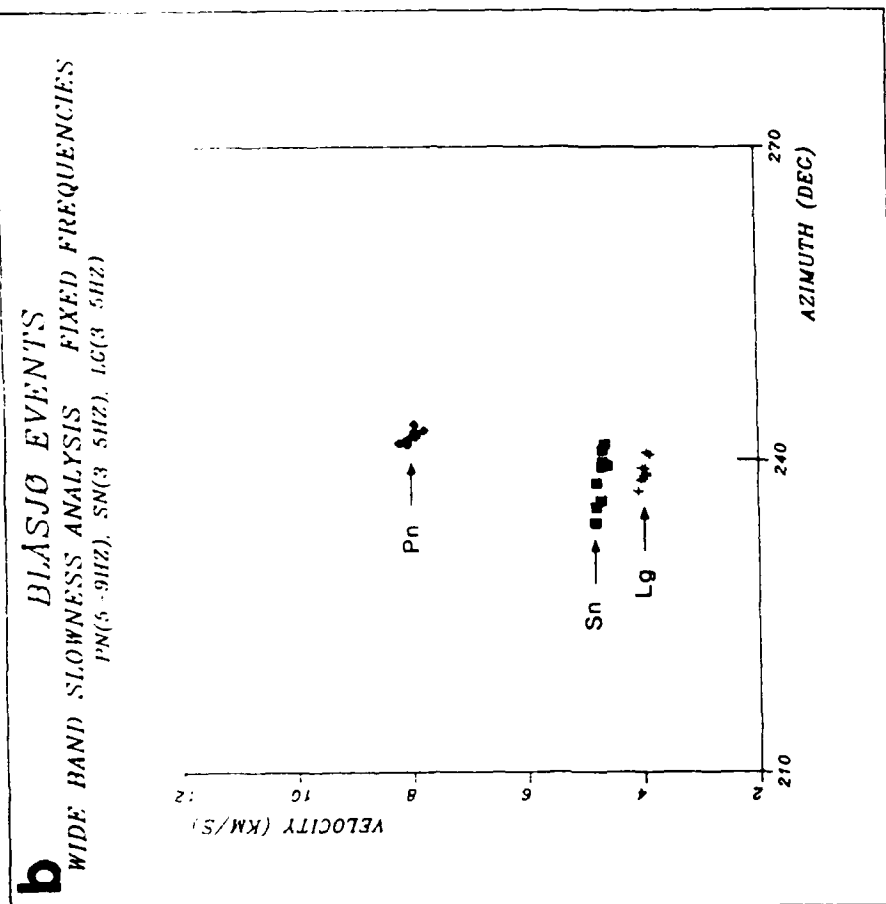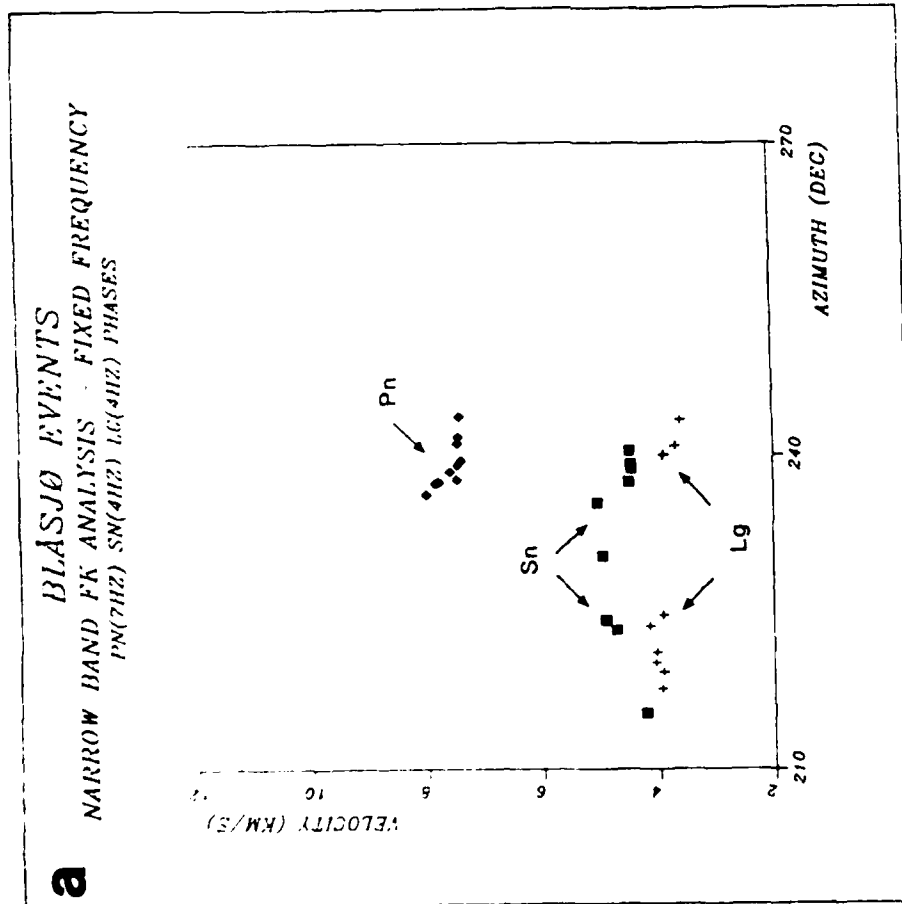excellent consistency of the results for the wideband case on top.

Fig. 2 (a) Results using narrow band f-k analysis of Pn, Sn and Lg phases of the ten Blåsjø events. The processing frequency has been kept fixed for all events, but is higher (7 Hz) for Pn than for Sn and Lg (4 Hz).
(b) Results using wide band slowness analysis of Pn, Sn and Lg phases of the ten Blåsjø events. The processing frequency band has been kept fixed, as indicated in the plot. Note in particular that there is a clear phase velocity separation between each of the three phase types.

P-WAVE SLOWNESS ESTIMATES
SEMIPALATINSK, ESTONIA AND BLÅSJØ
FIXED FREQUENCY BANDS

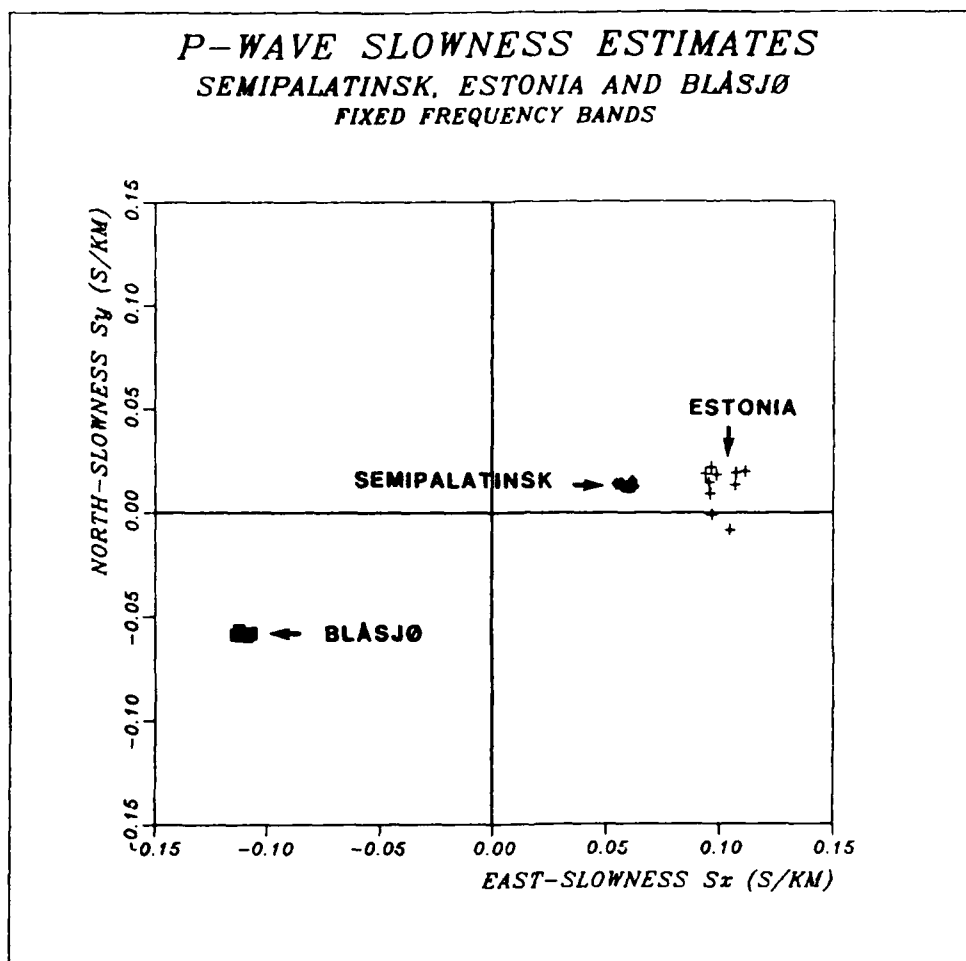Fig. 3 Wide band slowness estimates of the P phase for a suite of
events from the following sites:

i) Sixteen presumed nuclear explosions from Semipalatinsk,
    processed in the 1.5-3-5 Hz band.
ii) Ten explosions from a mining area in Estonia, USSR,
    processed in the 5.0-7.0 Hz band.
iii) Ten quarry blasts at the dam construction site Blåsjø
    in southwestern Norway, processed in the 5.0-9.0 Hz band.

ESTONIAN EVENTS P-PHASES

POWER DENSITY (QU×QU / HZ)

1.0E+08
1.0E+07
1.0E+06
1.0E+05
1.0E+04
1.0E+03
1.0E+02
1.0E+01
1.0E+00
1.0E-01

FREQUENCY

0.1 1.0 10.0 100.0

ESTONIAN EVENTS LG-PHASES

POWER DENSITY (QU×QU / HZ)

1.0E+08
1.0E+07
1.0E+06
1.0E+05
1.0E+04
1.0E+03
1.0E+02
1.0E+01
1.0E+00
1.0E-01

Noise

FREQUENCY

0.1 1.0 10.0 100.0

b

ESTONIAN EVENTS
AZIMUTH: 92 DEGREES
FREQUENCY BAND OF THE BEST DETECTION BEAM

VELOCITY (KM/S)

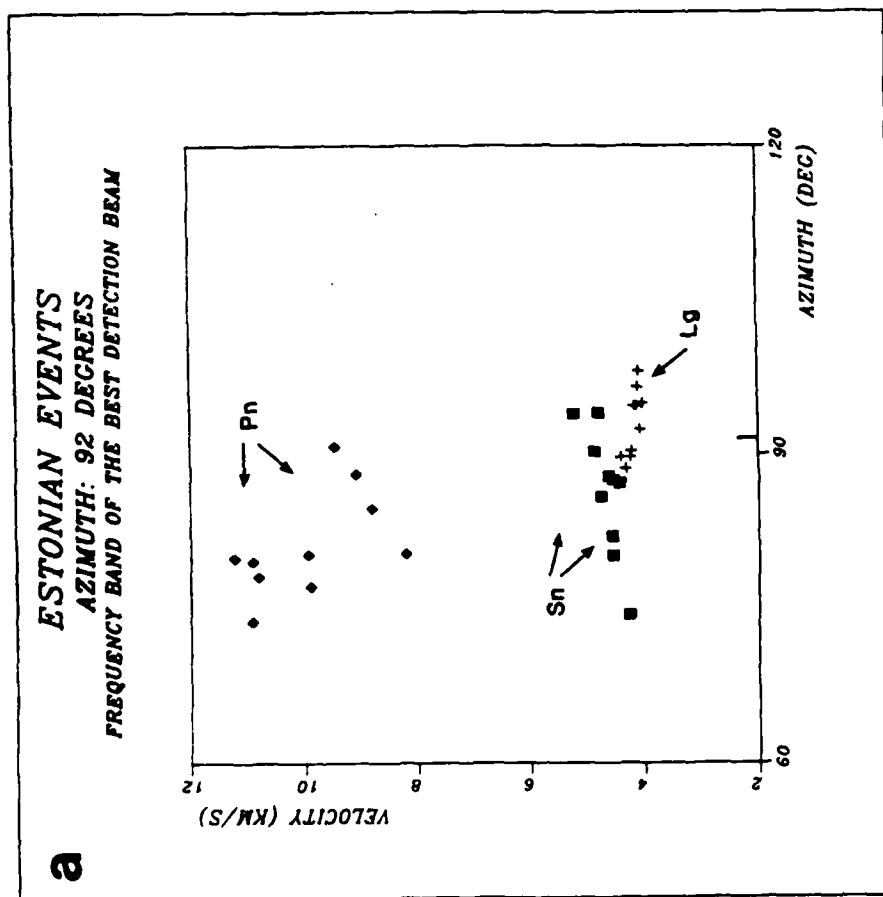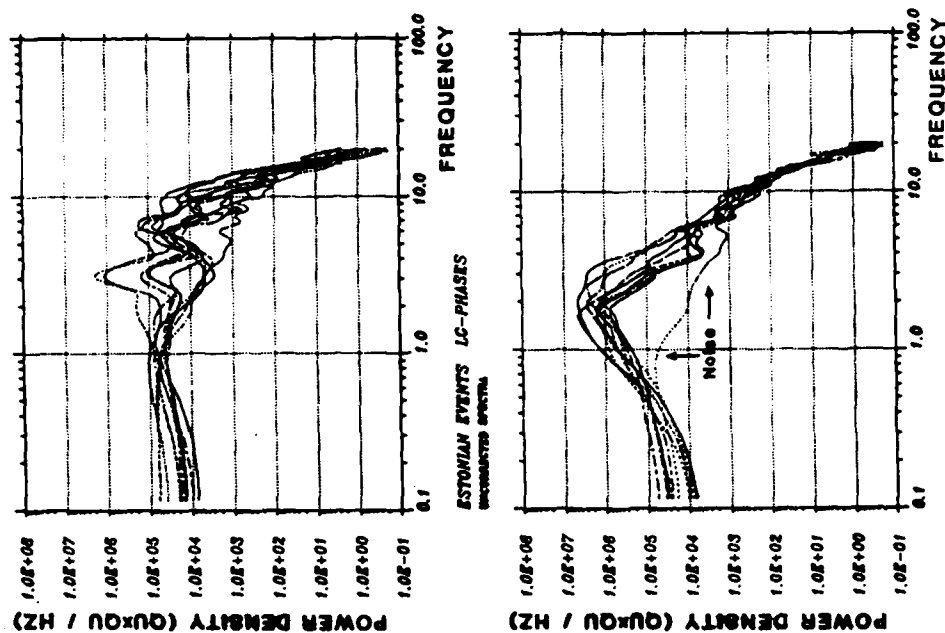12 10 8 6 4 2

Pn

Sn

Lg

AZIMUTH (DEG)

60 90 120

a

Fig. 4 (a) Results using wide band slowness analysis of the Pn, Sn and Lg phases from the ten Estonian explosions. The analysis frequency band has been chosen to be the same as the band of the best detection beam. Note the relatively small spread of the Lg estimates centered around the true azimuth.

(b) Pn and Lg spectra for the same events as described in fig. 4a. Note the large variation in the Pn spectra of the upper figure with two peaks at about 3 Hz and 6 Hz. The Lg spectra of the lower figure show a more uniform pattern with a peak at about 2 Hz.

INVESTIGATION OF EXPLOSION GENERATED SV Lg WAVES
IN 2-D HETEROGENEOUS CRUSTAL MODELS BY LFD SIMULATION

K. L. McLaughlin, R.-S. Jih, and Z. A. Der
Teledyne Geotech Alexandria Laboratories
314 Montgomery Street, Alexandria, Va 22314

Nuttli (1987) has recently reported that $m_{b(P)} - m_{b(Lg)}$ varies from 0.036(0.015) for the eastern portion of the Eastern Kazakh test site (EEKTS) to 0.27(0.03) for the central portion of the Eastern Kazakh test site (CEKTS). Nuttli argues that the teleseismic P wave magnitudes, $m_{b(P)}$ in the central portion of the test site are systematically larger. We have investigated Nuttli's individual station $m_{b(Lg)}$ readings (personal communication, 1986) and determined that his results are not caused by censoring, noise contamination, or biases in station corrections.

An alternative to Nuttli's hypothesis is that Lg excitation may be smaller at the CEKTS than the EEKTS. CEKTS has considerable topographic relief (Rodean, 1979) while EEKTS consists of folded sedimentary rocks (Nordyke, 1973). We have investigated several 2-D models for the excitation of SV Lg using linear elastic finite difference calculations. These simplistic models simulate the excitation of far field SV waves from dilatational line sources imbeded in 2-D heterogeneous models with and without free surface topography. The results from these simulations are presented for the 0.5-1.0 Hz bandwidth in Table I. The results for each model are referenced to the excitation for a uniform layer over a uniform half space model. The models are arranged in order of decreasing SV Lg excitation relative to the reference model (j=0).

Calculations are performed using reciprocity by directing an SV plane wave from a uniform half space upon the model. See Figures 1, 2, and 3 for snapshots of a SV plane waves with apparent velocities of 4.5 km/s incident upon three models. The dilatational strain is recorded at an array of locations with an average depth of 0.5 km in the grid. The average spectral level of the dilatational strain history in the 0.5-1.0 Hz bandwidth from the array of locations is determined relative to a reference model, $Log(\frac{Lg_j}{Lg_0})$. Our reference model (j=0) is a uniform 2 km layer ($\alpha=5.0km/s,\beta=2.74km/s$) over a uniform half space ($\alpha=6.0km/s,\beta=3.55km/s$). The test models have included combinations of topographic profiles, 10% rms random velocity variation in the layer, as well as folded layers with random velocities.

While we continue to experiment with various models, our preliminary results indicate that P to SV conversion is strongly enhanced by velocity variation in the vicinity of rough topography and the introduction of low velocity layers near the surface. The introduction of interfaces alone does not of itself increase SV excitation with the required slowness range. We continue to experiment with the geometry of heterogeneity, and the scale lengths of the heterogeneity. Although we can not presently explain Nuttli's results, we predict substantial variations in SV Lg excitation by explosions imbedded in crustal heterogeneity.

REFERENCES

Nuttli, O. W. (1987). *Bull. Seism. Soc. Am.* 77, 679-681.

Rodean, H. C. (1979). UCRL-52856, *Lawrence Livermore Laboratory.*

Nordyde, M. D. (1973). UCRL-51414, *Lawrence Livermore Laboratory.*

TABLE I. COMPARISON OF EXPLOSION SV Lg EXCITATION 0.5-1.0 Hz

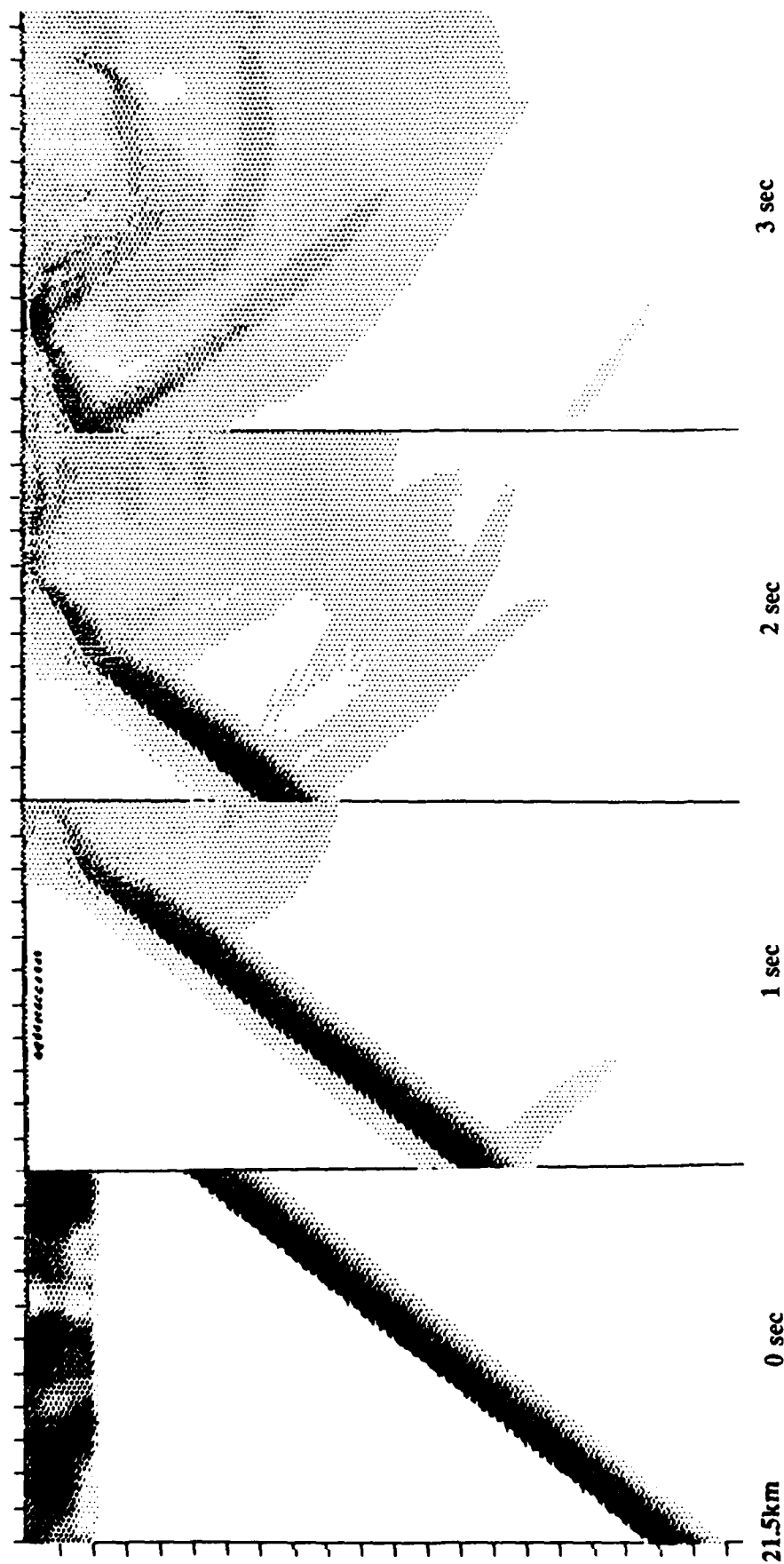| j	DESCRIPTION	v	$\bar{\alpha}_0$	h(km)	$Log(\frac{Lg_j}{Lg_0})$
0	1-LAYER	0%	5.0	2.0	0.000
1	1-LAYER TOPO	10%	4.5	2.0	0.127
2	1-LAYER TOPO	10%	5.0	2.0	0.063
3	2-LAYER	0%	4.5/5.0	1.0/1.0	0.037
4	2-LAYER	10%	4.5/5.0	1.0/1.0	0.001
5	1-LAYER	10%	4.5	2.0	-0.014
6	1-LAYER	10%	5.0	2.0	-0.032
7	0-LAYER TOPO	0%	6.0	2.0	-0.107
8	7 FOLDED LAYERS	10%	5.0	3.0	-0.163
9	11 FOLDED LAYERS	10%	5.0	3.0	-0.173

Figure 1. Model 6. SV wave in a half space ($\alpha=6.0km/s,\beta=3.55km/s$) incident upon a 2 km layer with average P-wave velocity of 5 km/s and a Gaussian 10% rms velocity variation. The S-wave velocity is assumed to be proportional to the P-wave velocity (indicated in the 0 sec frame). Snapshots of the displacement field are shown at 1 second intervals. The dilatational strain is recorded at 32 locations (indicated in the 1 sec frame) at a depth of 0.5 km in order to infer the excitation of far-field SV waves from explosion sources. Although absorbing boundary conditions are used care must be taken to avoid residual reflections from the sides of the grid.
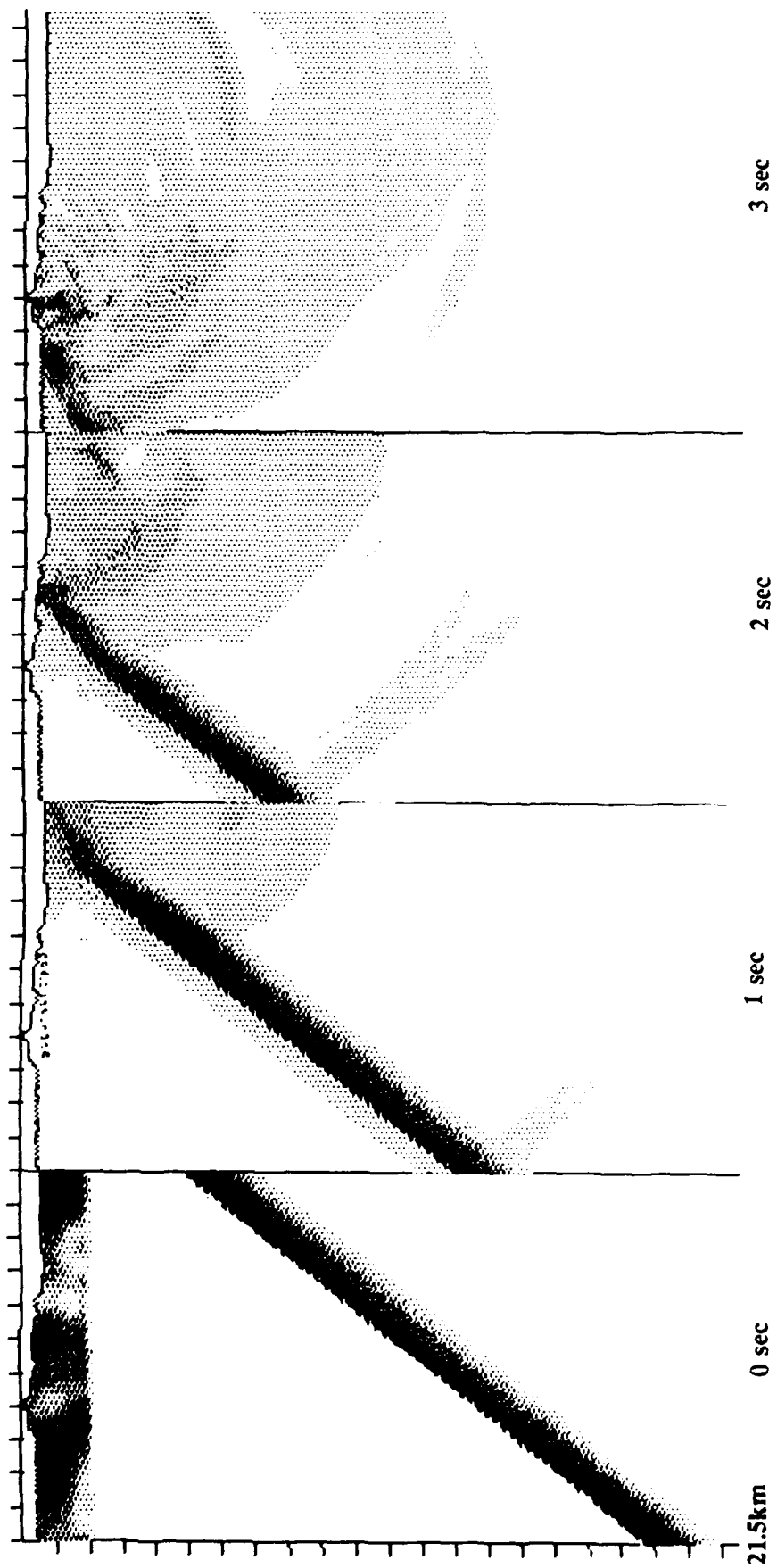
Figure 2. Model 2. Same as in Figure 1, except that the model has a random free-surface topographic profile.

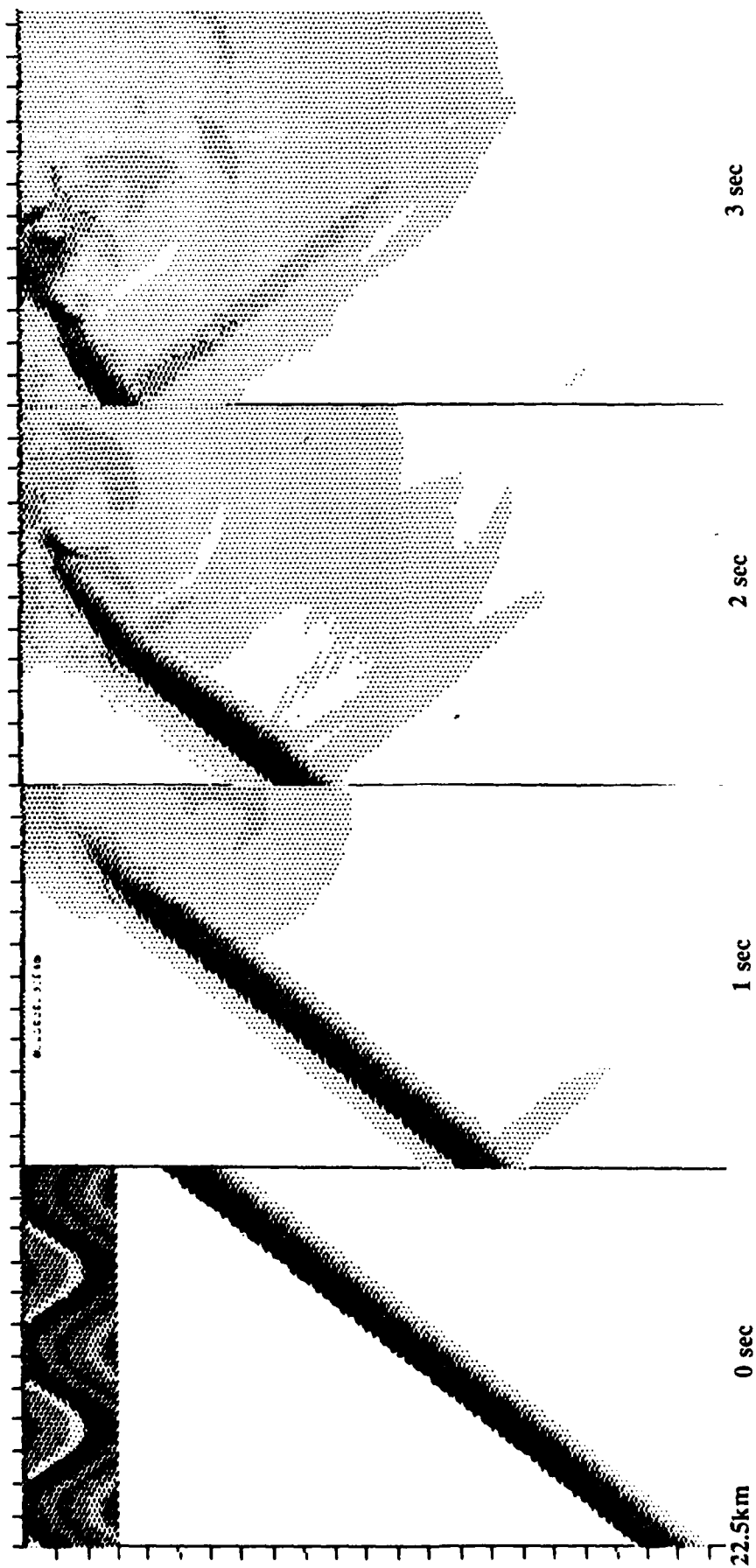0 sec   1 sec   2 sec   3 sec

21.5km

Figure 3. Model 9. Same as Figure 1 except that the 3 km thick low velocity layer consists of lightly folded (5 km wavelength, 2.5 km amplitude) 0.5 km thick layers with 10% rms velocity variation with respect to an average velocity of 5 km/s.
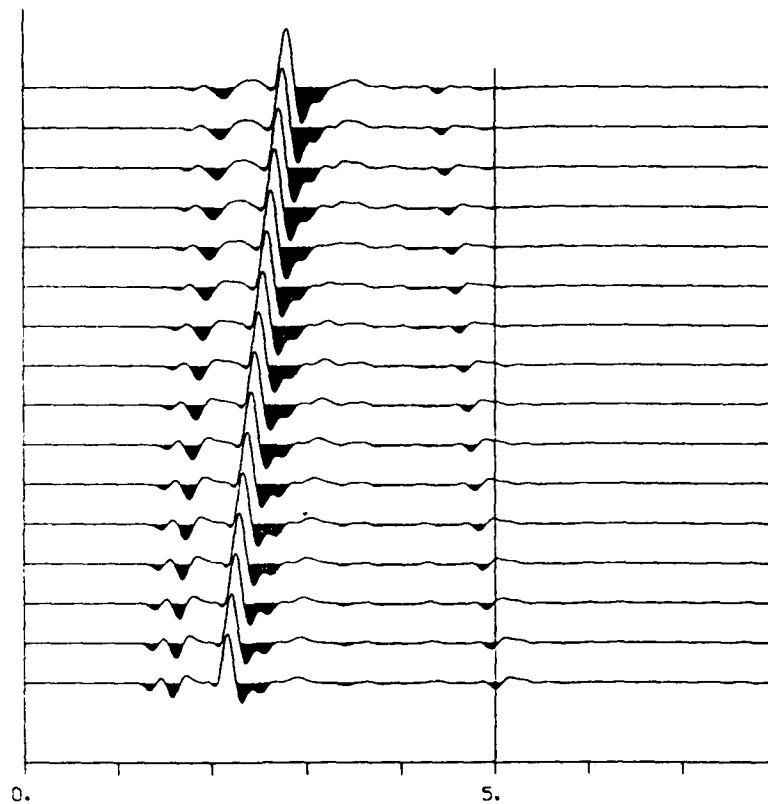
Figure 4. Model 0. Dilatational strain history (5 Hz low-pass) from incident broadband SV plane wave recorded at 16 locations at 0.5 km depth in the reference model. SV-to-P conversions are evident from layer interface and free surface as well as a later residual side boundary reflection. Only the portion of the response uncontaminated by the side reflections are used in analysis.

Figure 5. Model 7. Dilatational strain history (5 Hz low-pass) from incident broadband SV plane wave recorded at 16 locations under the topographic profile. The model consists of a uniform velocity layer ($\alpha=5km/s,\beta=2.74km/s$) with a topographic profile over a uniform velocity half space. SV-to-P conversion is evident from the layer interface, but the bulk of the conversion and coda is generated by the free-surface.
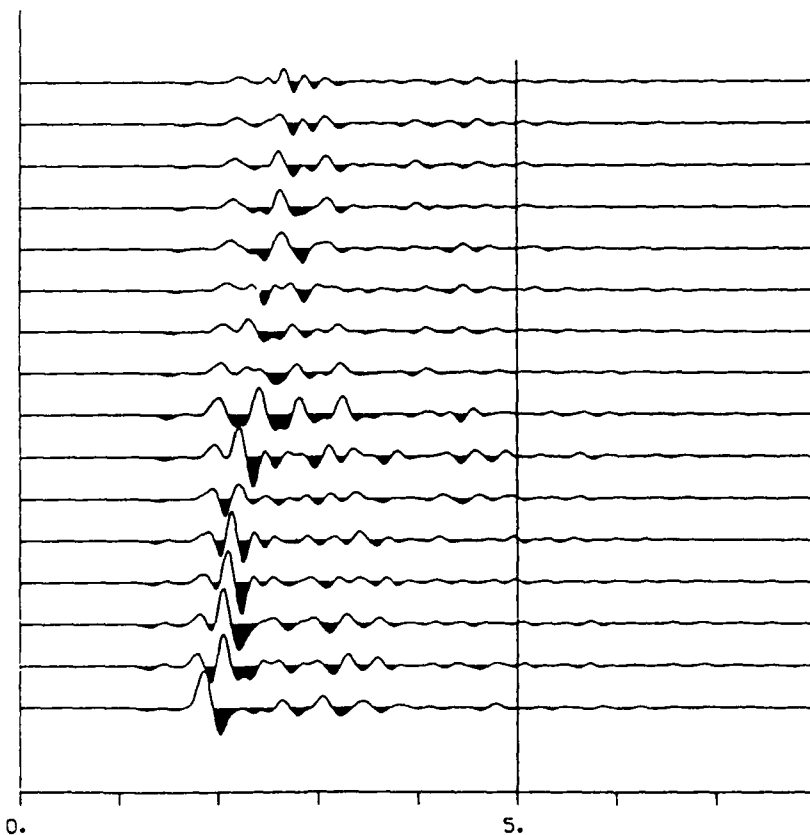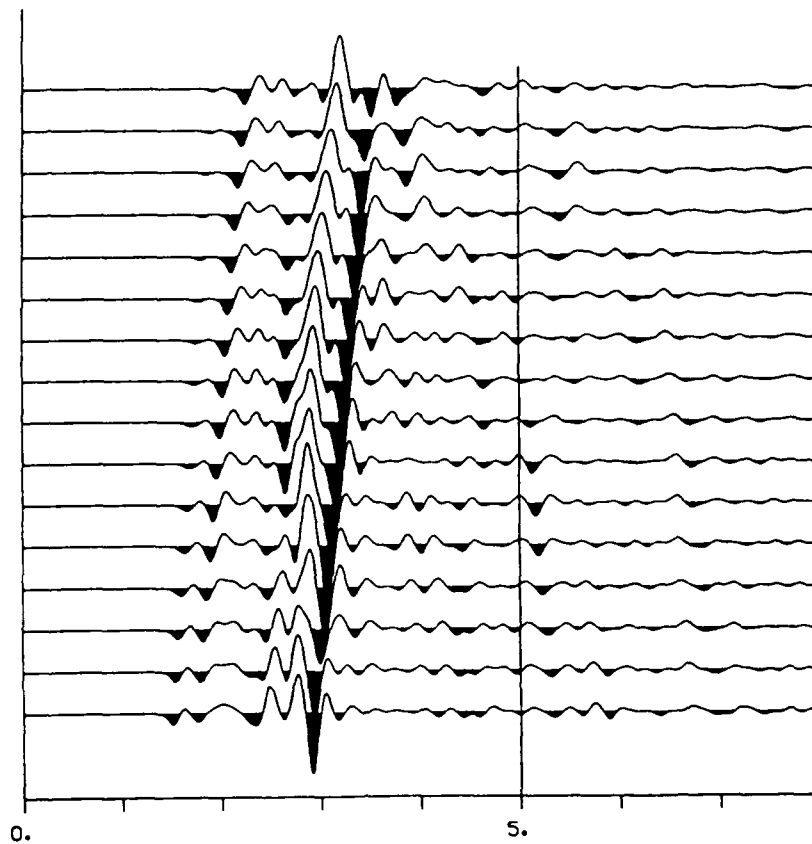
Figure 6. Model 9. Dilatational strain history (5 Hz low-pass) from incident broadband SV plane wave recorded at 16 locations at a depth of 0.5 km in model 9. The model consists of a layer (average $\alpha=5km/s, \beta=2.74km/s$) with folded layers of random velocity with a 10% velocity variation (see Figure 3). SV-to-P conversion is evident from the layer interface, but the bulk of the conversion is still generated by interaction with the free-surface.
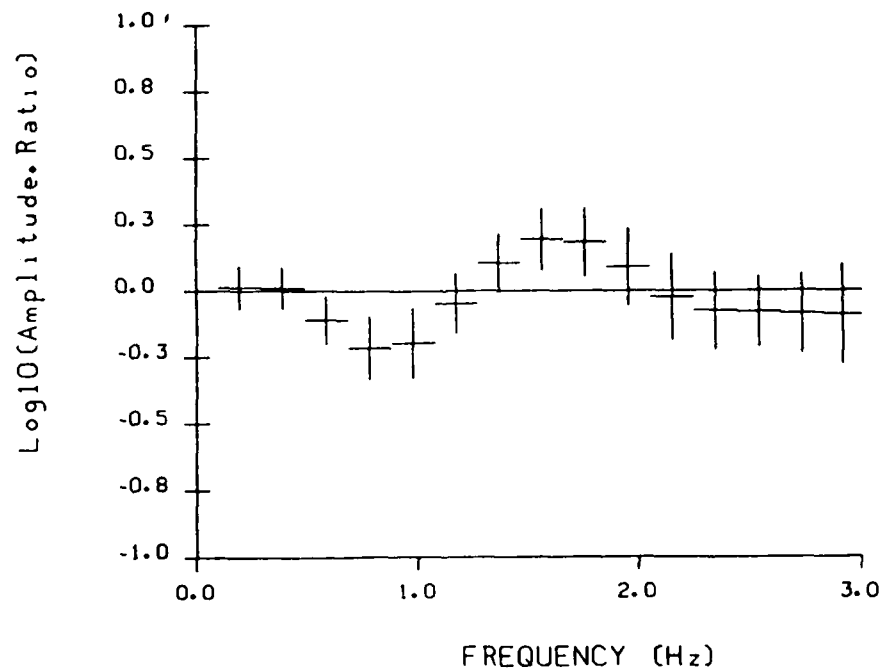

FREQUENCY (Hz)

Figure 7. Average spectral ratio as a function of frequency, $Log(\frac{Lg_9}{Lg_0})$, of the Model 9 responses shown in Figure 6 relative to the reference model. Model 9 response in the 0.5 to 1.0 Hz range is defficient with respect to the reference model by 0.173 log units. Vertical bars represent the standard error of a single observation.

STUDY OF HIGH FREQUENCY SEISMIC RECORDINGS IN FENNOSCANDIA

FRODE RINGDAL, JAN FYEN, TORMOD KVÆRNA AND SVEIN MYKKELTVEIT
NTNF/NORSAR
P.O. Box 51, N-2007 Kjeller, Norway

OBJECTIVE

The objective of this study is to assess the characteristics of seismic signals and noise at high frequencies, and in this context develop methods for improved detection and characterization of regional and teleseismic phases. In particular, processing techniques exploiting the potential of high-frequency arrays are emphasized.

RESEARCH ACCOMPLISHED

Data sources for this study have included tie NORESS array and the associated High Frequency Seismic Element (HFSE) in Norway and an experimental small-aperture array (FINESA) in Finland.

A description of NORESS may be found in Mykkeltveit et al (1985). The array diameter is 3 km, with 25 seismometer sites arranged in four concentric circles. The HFSE is a three-component system located at the NORESS center. The sampling rate is 125 Hz, which permits a much greater bandwidth to be recorded than for the NORESS system which has 40 Hz sampling.

The FINESA array has been described by Korhonen et al (1987). This experimental array, which is located at 61.4°N, 26.1°E near the town of Heinola, Finland, currently comprises 10 seismometer sites over an area approximately 1.5 km in diameter. Data are normally recorded in an event-triggered mode, with a sampling rate of 40 Hz.

NORESS-FINESA comparison

An important part of our research program has been to determine whether the excellent array processing results documented from the NORESS deployment can be duplicated at other array sites in Fennoscandia. To this end, we have analyzed in detail recordings from the FINESA array, and made comparison to NORESS.

As an example, Fig. 1 shows the respective NORESS and FINESA spatial correlations of noise as a function of sensor separation in 4 selected frequency bands. We note that the correlation characteristics are similar, in particular the strong negative correlation at selected distance/frequency combinations is present also at FINESA, and appears to be at least as pronounced as for NORESS. The noise level at FINESA is similar to that of NORESS in the 0-2 Hz band, and slightly higher in the 2-15 Hz band.

The signal frequency contents at FINESA are comparable to those observed at NORESS, given similar epicentral distance. Signal correlation across the array is high, as expected, except at very high frequencies. A noteworthy feature at FINESA is the presence of strong, coherent Rg waves (1 second period) for explosions out to more than 200 km distance. In contrast, NORESS does not observe Rg beyond 50-60 km.

The phase identification capability of the initial FINESA deployment has been evaluated using both single frequency and broadband f-k analysis. The estimated phase velocities are generally reliable indicators of phase type (primary or secondary), although the separation is not 100 per cent. The resolution is not sufficient to separate Sn from Lg on phase velocity alone, a result also found at NORESS. Azimuth estimates are sufficiently accurate for successful phase association; median error was found to be about 5 degrees both for P and S, using automatic, single frequency f-k estimation.

NORESS noise suppression capability

Earlier case studies have shown that the spatial noise correlation proper-ties at NORESS can be exploited to achieve better than $\sqrt{N}$ gain in beam-forming (N = no. of sensors). We have conducted a systematic study of this topic over the past year, by regularly computing noise suppression charac-teristics for various NORESS subgeometries, using an automatic aLgorithm that is activated once per hour.

The study has shown that NORESS noise suppression characteristics are remarkably stable over time, and show no strong dependency on the noise level (e.g., suppression during nighttime and daytime is similar, even though the actual noise level is quite variable). We have found that (a) better than $\sqrt{N}$ suppression can be consistently achieved at selected fre-quencies and subconfigurations and (b) at selected frequencies a sub-geometry can outperform the full array.

Examples of the results for a typical one-week period are shown in Fig. 2. Noise suppression is here defined as the ratio between the power spectrum of an infinite velocity beam and the average single sensor power spectrum. The upper part of the figure shows results when forming a beam from all 25 NORESS SPZ instruments, the bottom part corresponds to selecting the 17 element subarray (TELEV) consisting of A0 plus the C and D rings. It is evident that the TELEV subarray in comparison to the full array provides a much improved noise suppression at frequencies below 3 Hz (typical of tele-seismic events), in particular near 2.0 Hz.

Noise spectral studies

Using data recorded both by NORESS and the HFSE, the variability of seismic noise spectra as a function of time has been studied, using an automatic hourly computational procedure. Fig. 3 shows in the upper half the results

from a typical week, plotting spectral level at selected frequencies as a
function of time. Note that diurnal variations are prominent especially
during weekdays at frequencies above 2 Hz, whereas such variations are
modest at lower frequencies.

In the lower half of Fig. 3, the spectral levels at a fixed time of day (02
hours local time) are plotted for an approximately one-year period. Again,
we see a difference between no.se at low (0.5 Hz) and higher frequencies.
The noise level at 0.5 Hz is clearly seasonally dependent, and is con-
sistently high during winter months. A noteworthy feature is the strong
rise in high frequency noise during April/May, this appears to be a sea-
sonal feature attributable to strongly increased water flow in nearby rivers.

High_frequency_signal_spectra

We have analyzed HFSE recordings for recent Soviet underground nuclear
explosions in order to determine the amount of high frequency contents that
can be observed at NORESS. Fig. 4 shows spectra of the Semipalatinsk explo-
sions of Feb 26 (Degelen Mountains) and March 12 (Shagan River) 1987. Both
events were assigned m_b = 5.4 by PDE, whereas the NORESS measurements were
5.8 and 6.3, respectively. The spectrum of the Shagan River event is higher
in the band 0-10 Hz, whereas the two spectra are similar above 10 Hz. The
signal stays above the noise level up to about 20 Hz.

CONCLUSIONS AND RECOMMENDATIONS

The FINESA-NORESS comparison has shown that many of the signal and noise
chararcteristics that contribute to the impressive NORESS performance may
be found also at other sites in Fennoscandia.

Extensive analysis of NORESS data over a one-year period has demonstrated
that better than √N gain can be obtained consistently in selected fre-
quency bands, using special subgeometries of the array.

Both on a diurnal and seasonal basis, the variations in NORESS noise level
are significant, and this must be taken into account when using the array
in a network capability assessment context.

Underground nuclear explosions at teleseismic distances recorded at NORESS
show considerable amounts of high frequency energy. For Semipalatinsk
explosions, signal energy exceeds the noise level up to about 20 Hz for
magnitude 5 events.

Therefore, in a geological and tectonic environment similar to that of the
NORESS site, high frequency recording systems (with a sampling rate of at
least 40 Hz) will be important not only for local and regional events, but
also for the teleseismic monitoring.

REFERENCES

Bungum, H., S. Mykkeltveit & T. Kværna (1986): Seismic noise in Fenno-
scandia with emphasis on high frequencies. Bull. Seism. Soc. Am., 75
1489-1513.

Korhonen, H., S. Pirhonen, F. Ringdal, S. Mykkeltveit, T. Kværna, P.W.
Larsen and R. Paulsen (1987): The FINESA array and preliminary
results of data analysis, Report S-16, Inst. of Seismology, Univ. of
Helsinki.

Mykkeltveit, S., D.B. Harris & T. Kværna (1985): Preliminary evaluation
of event detection and location capability of the small aperture
NORESS array. NORSAR Semiannual Technical Summary, 1 Oct 84 - 31 Mar
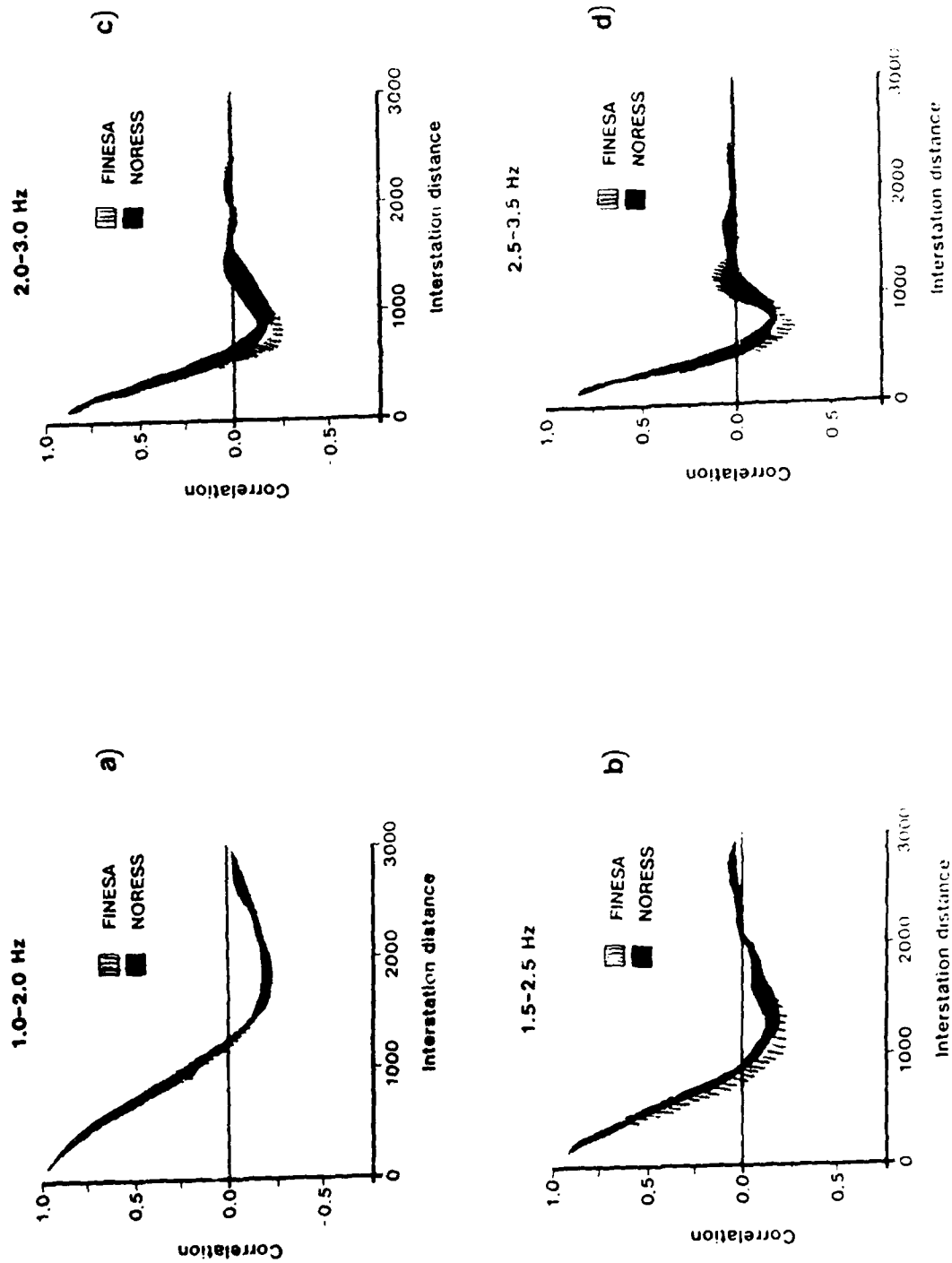85, NORSAR, Kjeller, Norway.

Fig. 1 Comparison between NORESS and FINESA of average noise correlation as a function of intersensor distance. Four frequency bands are shown. The plots indicate the range of correlation curves for the two arrays based on six noise samples each of 110 sec length. Note the similarity for the two arrays.
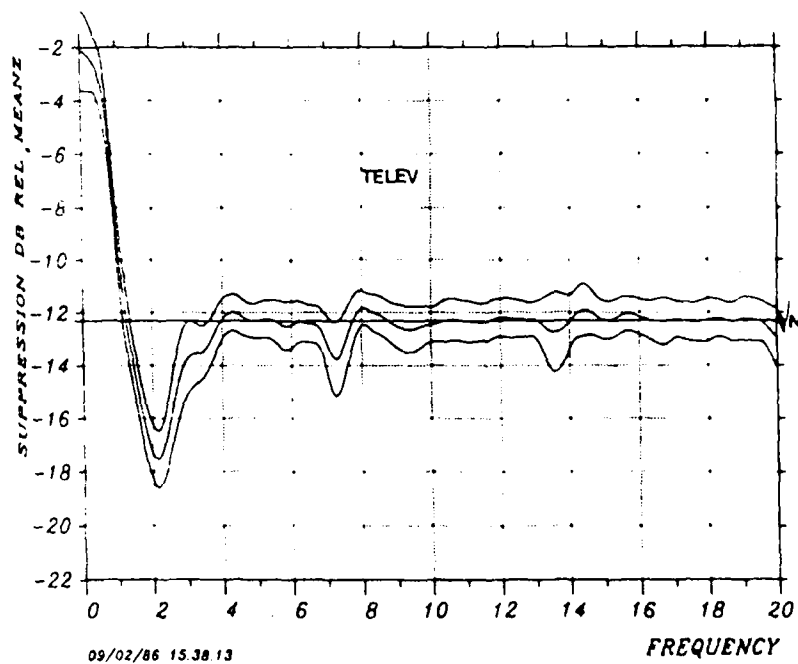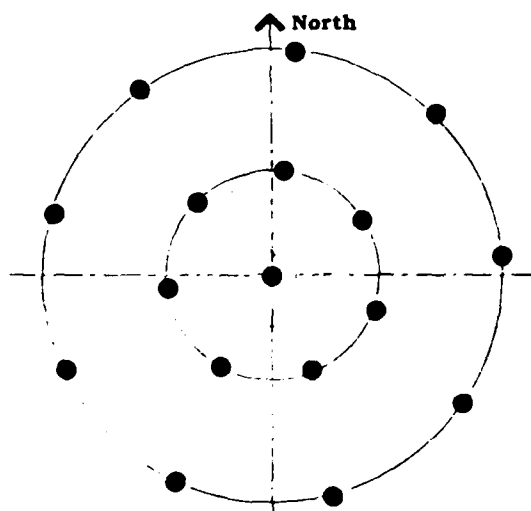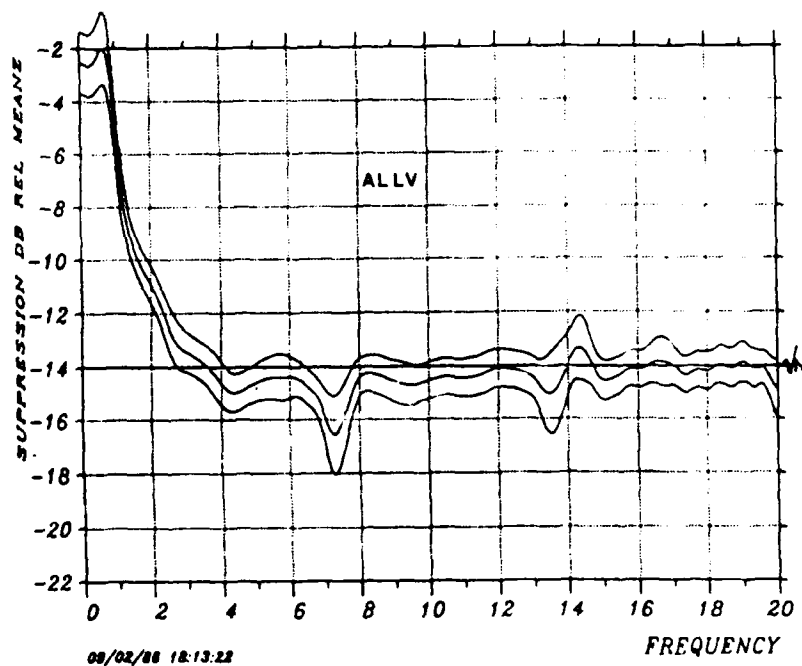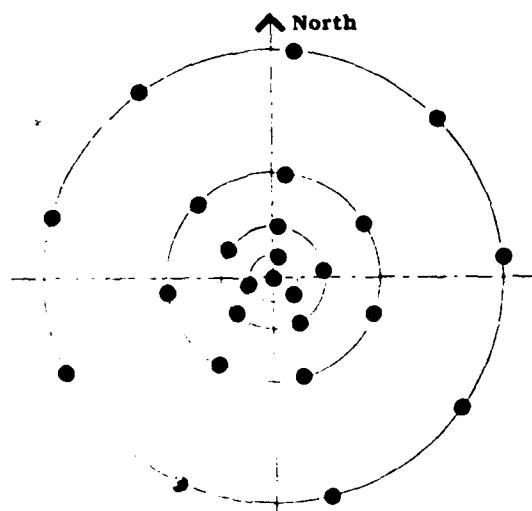
Fig. 2   NORESS noise suppression for the full 25 element SPZ array (top)
and the 17 element TELEV subgeometry (bottom). The respective
geometries are shown to the left (array diameter is 3 km). The
curves plotted are average noise suppression over a one-week
period, together with plus and minus one standard deviation.
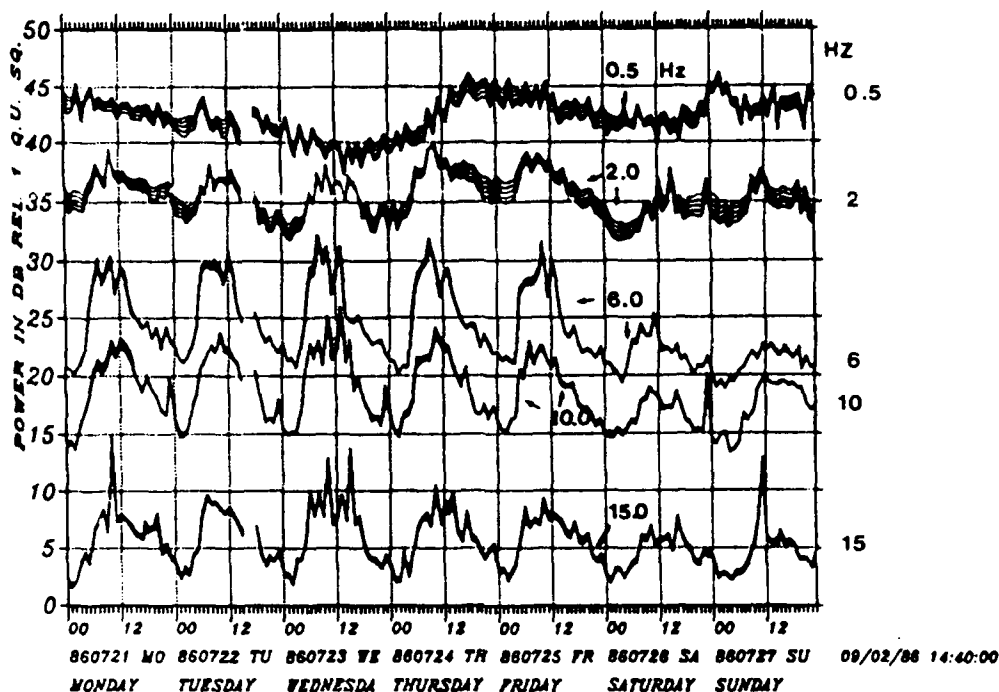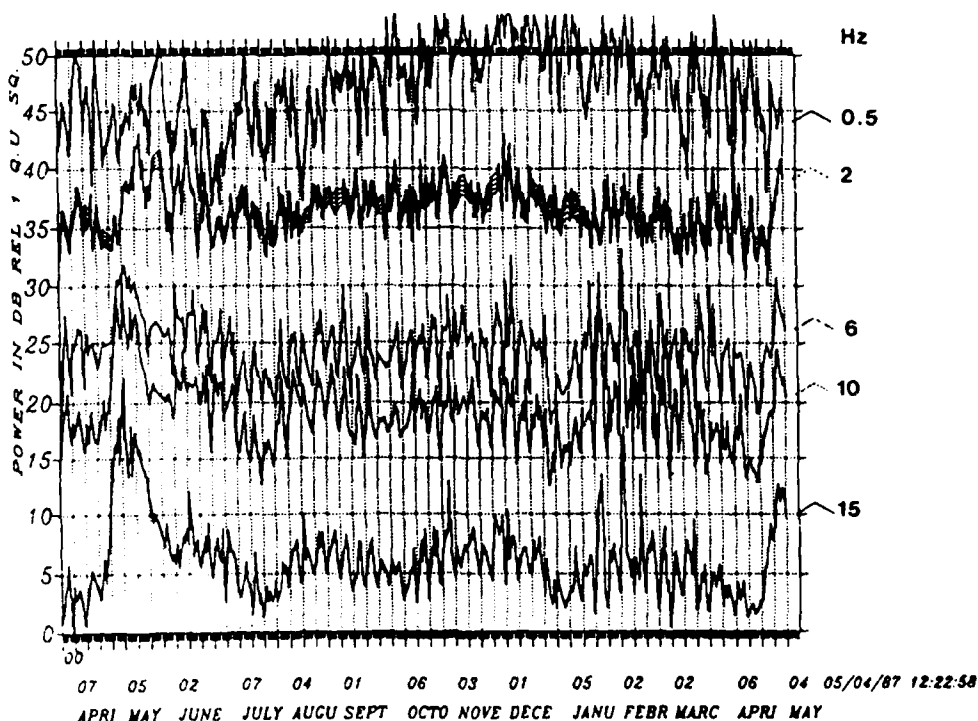
Fig. 3 The top part shows variations in noise levels (averaged across NORESS) at five selected frequencies for a one-week period. Note the significant diurnal variations during workdays at high frequencies. The bottom part shows noise levels at the same five frequencies sampled at 02 hours local time only, for a one-year period.

216

SPECTRAL PLOT
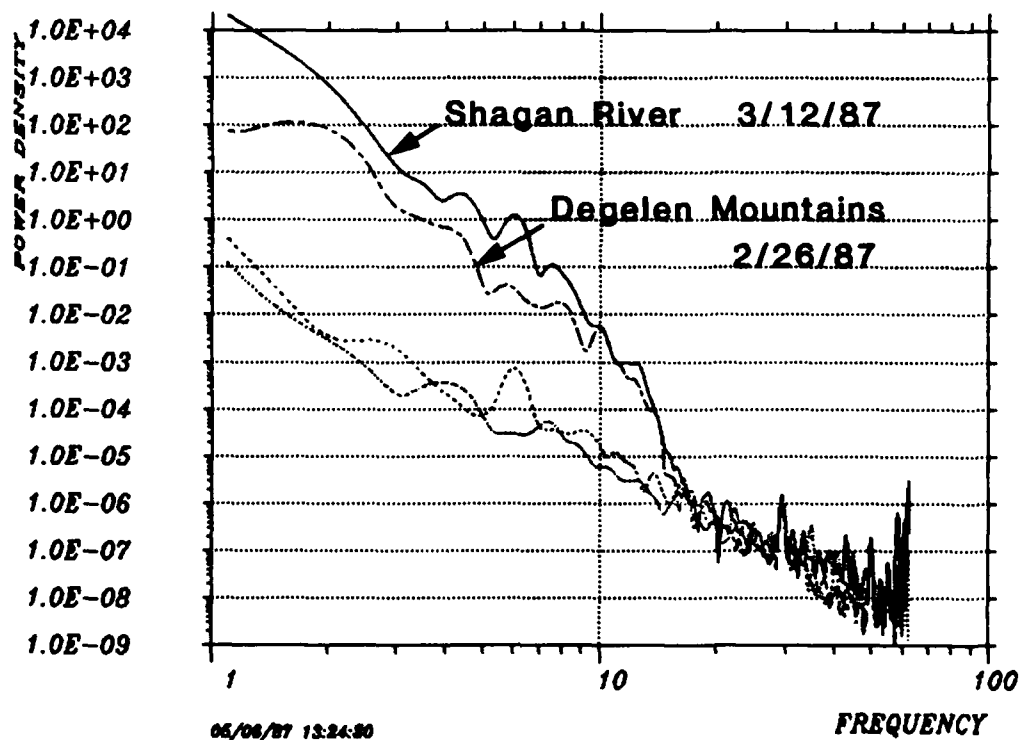
Fig. 4 Ground motion power spectra (nm²/Hz) for two nuclear explosions at Semipalatinsk, recorded at the NORESS High Frequency Seismic Element. Corresponding noise spectra are also shown. Note the presence of high frequency signal energy exceeding the noise level up to about 20 Hz.

CHARACTERISTICS OF REGIONAL SEISMIC SIGNALS

A.S. RYALL, A. JURKEVICS, P. DYSART and J.J. PULLI

Center for Seismic Studies
1300 N. 17th St., Suite 1450
Arlington, VA 22209

INTRODUCTION

The Center for Seismic Studies has been using NORESS data to test a number of seismic analysis techniques as DARPA workstation tools, with the overall aim of increasing information derived from regional seismic data. Work to date has included the extraction of frequency-domain spectral parameters, time-domain autoregressive parameters, and particle-motion information. The data set being used for testing includes NORESS recordings of approximately 100 events (primarily quarry blasts and small earthquakes) in Scandanavia and the western Soviet Union, generally at distance ranges of 1,000 km or less.

Of these techniques, polarization analysis has been given the most attention, and the first part of this report focuses on that method. A second section illustrates all the techniques by application of the various analysis tools in an attempt to identify an event more than 2,000 km from the NORESS array.

PARTICLE-MOTION ANALYSIS

Objectives.

Objectives in the research on seismic-wave particle motions have been the following:

- Develop robust and versatile algorithms for processing three-component seismic data and extracting quantitative polarization information using both single-stations (i.e., networks) and arrays of three-component sensors.

- Determine what type of information can be extracted from three-component seismograms and under what circumstances. For example, what are the best algorithms to use, how does particle-motion information behave as a function of the signal-to-noise level, what frequency bands to use, how to select the time windows, and what parameters should be extracted in order to provide the most useful polarization information?

- Implement the polarization analyses in both interactive seismic workstation mode and automatic on-line "post-detection" mode. The processing modules need to be computationally efficient and straightforward to implement in order to accomplish this.

- Evaluate the usefulness of polarization processing of short-period and high-frequency data for identifying regional seismic phases, discriminating explosions from earthquakes, and constructing particle-motion "signatures" to identify events from repeated sources.

Research Accomplished.

After considering numerous polarization algorithms available in the literature, a time-domain method is being used which is based on the work of Flinn (1965). This approach, which is based on least squares, is robust, efficient and versatile. Modifications to the original algorithm were made to estimate polarization in discrete frequency bands, and particle-motion parameters are extracted from the data as a function of time and frequency with no attempt at actually performing polarization filtering. An important feature of the underlying approach is that it can be easily extended to an array of three-component sensors by the method of covariance-matrix averaging (Jurkevics, 1986a,b). Theory, synthetic tests and analyses of real data all show that the advantage gained by using an array of three-component sensors is $1/N$ in estimation variance, where N is the number of stations in the array. The time windows are generally sufficiently long that a time shifting between array elements is not needed during the averaging. Thus polarization is estimated in a consistent manner using both single stations in a regional network or multiple stations in an array.

Software has been developed for performing interactive polarization analysis on a SUN graphics workstation using either single-station networks or array data. Various polarization characteristics can be extracted and displayed in different frequency bands and time resolutions using short-period, long-period or high-frequency data.

Two empirical studies of polarization characteristics of regional waves have been conducted. The first study by Antoinette Campanella entails more than 60 recordings from RSTN stations during the 1985 GSETT. This analysis evaluates the capability of estimating the source back azimuths using a network of three-component stations. Both short-period P waves and long-period Rayleigh waves are used. The second study involves 95 regional events recorded on the multiple three-component set of the NORESS array. Here, emphasis is placed on distinguishing regional seismic phases, estimating source azimuths and identifying source and propagation characteristics.

An important consideration in these empirical analyses is to determine the optimum manner for implementing the polarization algorithm in an automatic mode in a processor such as RONAPP or the one being developed by SAIC for the new expert system. For example, the polarization results for detection are sensitive to the choice of extraction window and frequency, so a fixed set of frequency bands and a time window based on the envelope shape are recommended.

The concept of using seismic "signatures" of particle motions for identifying events from fixed, known sources is being evaluated. This has been done using repeated blasts from several mines as well as nearby earthquakes recorded at NORESS. The particle-motion signatures consist of the six elements of the particle-motion covariance matrix as a function of time in several bands. Experiments show that using the covariance-matrix cross-terms provide important signature information not available in just the auto-terms (i.e., in just the signal envelopes).

Three-component analysis of high-frequency data was begun but has been postphoned due to apparent distortions in the horizontal channels in the high-frequency records from NORESS. Since the high-frequency sensor has been redeployed, an analysis will be carried out soon to determine applicability of the high-frequency horizonatal components to the topics listed above.

Conclusions and Recommendations

Preliminary results of the RSTN data study show that the azimuth error varies between stations. P waves give better azimuths than Rayleigh waves. All of the events taken together show that one standard deviation of the P azimuth error varies from 21° at RSON to 55° at RSSD, while Rayleigh waves have standard deviations of around 55° at all the stations (many of these events were teleseisms).

The analysis using NORESS data indicates that the regional phases can be well distinguished by polarization characteristics. P_n and P_g particle motions are rectilinear, while S_n and L_g motions tend to be planar by nature. P_n can be separated from P_g by the orientation of rectilinear motion and S_n from L_g by the orientation of planar motion, with a confidence of better than about 80%. This result is by strictly using polarization information and does not include the relative spectral exitation or F-K velocities. P_n particle-motions have a more steeply-incident orientation than of P_g waves, which is consistent with their propagation characteristics. S_n waves have approximately equal radial and transverse components and vertical components which are smaller than the horizontals. This implies that the steeply-incident S_n waves contain both S_H and S_V components. S_n particle motions are very well-defined across the entire short-period band when there is signal above the noise (noise for S_n usually means the level of the late P coda). L_g waves have approximately equal vertical and transverse components and smaller radial components. L_g waves generally have useful particle-motion information only below 6-8 Hz.

When the signal-to-noise ratio is greater than about 1.0, the accuracy of source back azimuths from P_n particle motions using the multiple three-component sensors at NORESS are very similar to the F-K results using all 25 vertical channels. When the S/N goes below 1.0, the quality of the polarization estimates degrade. The errors in source azimuth using the minimum horizontal component of L_g waves are about twice as large as the errors from the P_n waves. S_n phases do not appear useful for estimating source azimuth.

The analyses done so far have utilized particle-motion information for source discrimination in indirect rather than direct ways. Particle-motion signatures are used to identify events from fixed known sources and the use of horizontal as well as vertical components for computing the amplitudes of regional phases gives more stable estimates. Polarization attributes computed for P coda are useful for identifying arrivals of reflected and depth phases, which may remain hidden by simply plotting amplitudes.

Preliminary results indicate that three-component information above 15 Hz is important, particularly since S_n as well as P_n signals are present at these higher frequencies. More research is being planned to evaluate the use of particle-motion information at frequencies above 15 Hz and to apply particle-motion information more directly to the problem of source identification.

Experience in particle-motion analysis of regional events to date suggests the following additional points:

- For signal-to-noise levels greater than 1.0, an array of about 4 three-component sensors gives location and phase identification capabilities which are comparable to a full array of 25 vertical channels.

- Horizontal components are important in regional analysis and should be included in

detection and phase identification.

- Polarization analysis can be very efficient and automated and should be included in any on-line processing scheme.

- Particle-motion information is valuable for phase identification and augments F-K analysis for this.

THE DISCRIMINATION PROBLEM

As an example of the regional discrimination problem we analyzed an m_b(NEIS) 4.6 event that occurred on 1 August 1986, during the recent Soviet nuclear testing moratorium. A master-event relocation of the event gave a location at 73.02° N, 56.50° E, south of Matochkin Shar strait on the eastern shore of Novaya Zemlya, USSR. Both the NEIS and Moscow Data Center locations were farther inland. Of 34 events that occurred within 200 km of this event during a 20-year period prior to 1986, all except four appear to have been underground nuclear tests and the others were probably aftershocks of one of the explosions.

Objective.

Our analysis of this event was motivated by three considerations: (1) At a distance range of 22.7° from NORESS, it offered the opportunity to extend previous research on discriminants to larger distance. In a CTBT the ability to utilize data at such ranges for identification of small events would be extremely useful. (2) It provided a possible way to evaluate recent claims by Evernden et al. (1986), that explosion source functions are richer in high frequencies than those of earthquakes, and that high-frequency signals propagate extremely efficiently over much of the USSR. (3) It presented a unique opportunity to compare signals of a small underground explosion at the Novaya Zemlya test site in 1977 with those of a presumed tectonic event within about 50 miles of the test site. Most identification studies in the literature have combined tests in one area with earthquakes in different areas.

Results.

Figure 1 shows a comparison of NORSAR recordings of the 1 August event with a magnitude (m_b) 4.6 presumed explosion at the nearby test site, on 9 October 1977. The top part of the figure indicates more variation in signal character between the different subarrays for a single event, than between the two events recorded on the same instrument. Maximum amplitudes vary by about a factor of three across the array for the 1977 shot and by a factor of about two for the 1986 event. The bottom of the figure indicates that the envelope of the events was essentially identical for the P through Lg phases, in contrast to an expectation by Evernden et al. that a tectonic event should have large high-frequency shear waves.

The 1986 event was also compared with an announced PNE in the Ural Mountains on 28 March 1987, and a number of techniques being tested as seismic workstation tools at the Center failed to discriminate these two events. Spectral ratios at frequencies of 0.4 and 4 Hz for the PNE and the Novaya Zemlya event were very similar, and different from earthquakes at the same distance range in southern Europe. Parameters determined from polarization analysis did not discriminate between the PNE and Novaya Zemlya event,

nor could they be separated on the basis of signal complexity or first motion. Results of autoregressive spectral analysis (Dysart, 1986) were compared for these events and a number of earthquakes, and were not diagnostic. In terms of the AR parameters, the 1986 and 1977 Novaya Zemlya events were indistinguishable. The only analysis suggesting that the 1986 event was earthquake-like was the $M_s:m_b$ ratio (3.4:4.3), a type of analysis that could not be used for smaller events of interest to a CTBT.

Conclusions and Recommendations.

These results suggest that path effects are more important than source effects in determining the character of signals at distances around 2,000 km. They also illustrate the difficulty of identifying a well-recorded seismic event, with magnitude equivalent to a tamped underground nuclear explosion of a few kilotons, located near a well-studied test site, in a stable geologic region. Far greater difficulties would be encountered in attempting to use a limited number of seismic stations to detect, locate and identify much smaller earthquakes, mine blasts and possible decoupled nuclear explosions in all parts of the USSR.

Evaluation of proposed regional discrimination techniques should emphasize recordings earthquakes and explosions located in the same area, and should concentrate on distance ranges of 1,000-2,000 km -- i.e., distances that will be of primary interest to verification of a CTBT.

REFERENCES

Dysart, P. S., 1986. "Autoregressive Analysis of Regional Seismograms from Earthquakes and Explosions," *SAIC/Center for Seismic Studies Technical Report for the Period 1 July - 30 September 1986*, C86-07, dated November 1986.

Flinn, E.A., 1965. "Signal Analysis Using Rectilinearity and Direction of Particle Motion," *Proc. IEEE, 53*, 1874.

Jurkevics, A., 1986. "Polarization Analysis Using an Array of Three-Component Sensors: Part I -- Theory," *SAIC/Center for Seismic Studies Technical Report for the Period 1 July - 30 September 1986*, C86-07, dated November 1986.

Jurkevics, A., 1986. "Polarization Analysis Using an Array of Three-Component Sensors: Part II -- Application to NORESS," *SAIC/Center for Seismic Studies Technical Report for the Period 1 July - 30 September 1986*, C86-07, dated November 1986.

Smart, E. and H. Sproules, 1981. "Regional Phase Processors," *Teledyne Geotech Report*, VSC-TR-81-19.

1977282

N01A0		240
N01B0		146
N02C0		503
N03C0		519
N04C0		287
N06C0		265

1986213

		137
		115
		146
		246
		219
		146

0.0   10.0   20.0   30.0   40.0

Time (sec)
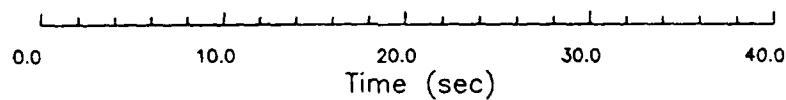
Date: 1977282

Start time: 11:04:13.8   272 nm
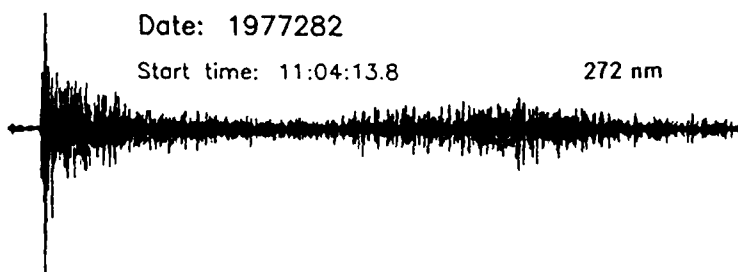
Date: 1986213

Start time: 14:00:56.3   182 nm

N04C0   0.8 to 8.0 Hz

0.0   50.0 100.0 150.0 200.0 250.0 300.0 350.0 400.0 450.0

Time (sec)
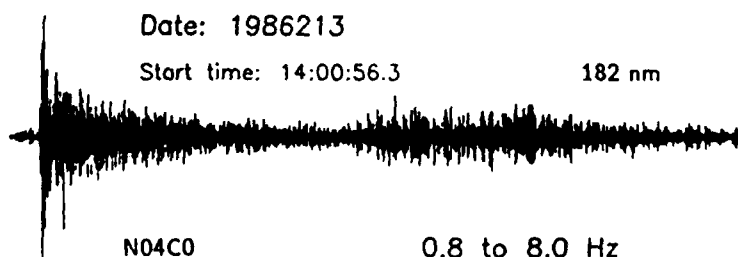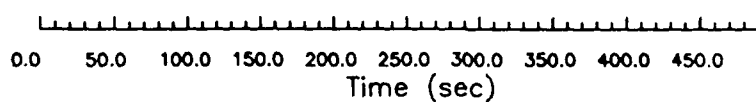
Spectral Determination of Regional and Teleseismic Lg Attenuation and Source Multiplicity in Explosions

Douglas R. Baumgardt
ENSCO, Inc.
5400 Port Royal Road
Springfield, Virginia 22151 - 2388

Objectives

This study has addressed the problem of measuring the anelastic attenuation of Lg phases, recorded at regional and teleseismic distances, and the spectral characterization of explosion sources using regionally recorded crustal phases. These two studies are related in that source-receiver propagation effects, in particular, attenuation, must be corrected for before seismic events can be identified on the basis of their signal characteristics.

The study of Lg attenuation has been motivated by studies by Nuttli (1986,a,b) of absolute yield estimation of nuclear explosions using magnitude measurements of Lg waves. The estimation of $m_b(Lg)$ requires that Lg amplitudes be corrected for distance-dependent attenuation. Nuttli (1986, a,b) used frequency measurements in the Lg coda to make a single-station estimation of Lg Q. Nuttli (1986a) showed how spectral measurements could be used to constrain the frequency-dependence of Lg. In this study, two spectral methods for estimating Lg Q have been investigated, both of which fit attenuation models to the spectral shape of Lg spectra, after correction for noise, instrument, and source. These techniques were then applied to digital high-frequency data for events at NTS and at the Eastern Kazakh test site in the USSR, and the resulting Lg attenuation values compared to those estimated by the coda method. Because Lg waves have higher signal-to-noise ratios than coda waves, the spectral method may be more useful for estimating Lg attenuation for smaller and more distant explosions than the coda method if it can be shown that the spectral Q estimates are comparable to the coda estimates for larger explosions.

The second study followed up on results of an earlier study of teleseismic Lg waves from PNE's in the USSR that indicated that these explosions may have been multiple events (Baumgardt, 1986). Source multiplicity was revealed by the presence of modulation patterns or "scalloping" in spectra computed for P-codas, Sn and Lg waves. These spectral modulation patterns biased the determination of attenuation of Lg by the spectral method. The purpose of this study was to determine if such spectral characteristics can be found in known multiple explosions, such as mine blasts with "ripple fire". We also investigated the application of homomorphic deconvolution (cepstral analysis) for studying multiple explosions and for removing the scalloping effects from regional phase spectra so as not to bias spectral Q estimation.

Research Accomplished

Lg Attenuation. Spectral-shape estimation procedure procedure has been developed to invert for average whole-path crustal attenuation. Smooth Lg spectra were determined by two methods: multiple Gaussian bandpass filtering for single-channel data and multichannel stacking of Fourier spectra of array data. The spectra were corrected for noise, instrument, and source effects. For the source correction , the von Seggern and Blandford (1972) source model

was assumed, using a hardrock potential. The resulting spectra were then fit to an attenuation model in the form of

$$A = A_0 \exp(\frac{-\pi f \Delta}{QU})$$

(1)

The frequency dependence of Q was assumed to be $Q = Q_0(\frac{f}{f_0})^\zeta$. For frequency independent attenuation, the spectral shape of log A versus f is linear and Q was determined by linear least squares. For the frequency-dependent case, substituting in for Q in (1) and taking the log gives

$$\log A = \log A_0 - (\frac{\pi f^{1-\zeta}\Delta}{2.3Q_0 U}).$$

(2)

Equation 2 gives a power-law relation between the log A and linear frequency. Nonlinear inversion of Lg spectra for log A_0, Q_0, and ζ using (2) is difficult because of strong tradeoffs between Q_0 and ζ. Stable estimates of Q_0 and ζ were obtained by inverting for Q_0 by least squares, assuming a range of values for ζ (between 0 and 1) and log A, and searching for the values that give the minimum variance.

Lg attenuation estimates were made for 15 NTS explosions recorded at the 4 Lawrence-Livermore network stations, MNV, KNB, LAC, and ELK. Examples of spectral fits are shown in Figure 1 and the average results are given in Table 1. Also shown in Table 1 are the results of Nuttli (1986 a) for the Basin and Range stations, BKS, DUG, and TUC. We find that the values of attenuation are, on average, comparable although the spectral Lg-Q_0 estimates seem to be smaller than those for estimated Nuttli by the coda method. Table 2 compares estimates of Lg attenuation at NORESS with those of Nuttli (1986b) for the Scandinavian stations, COP, KEV, KON, NUR, and UME. Again, our results are comparable to those Nuttli, although the Q_0 values for the spectral method are slightly lower than those of the coda method.

Multiple Explosions. The spectral stacking method was used to compute smooth spectra for mine blasts and earthquakes in western Norway recorded at the NORESS array. Spectra were computed for the crustal phases, *Pn*, *Pg*, *Sn*, and *Lg* and compared on offset plots, such as those shown in Figure 2. Cepstra were computed by Fourier transforming each of the spectra for the phases, and are also shown in Figure 2. The cepstral analysis approach is described in more detail in Baumgardt and Ziegler (1987). Comparison of the spectra and cepstra cf the explosions and earthquakes shows that many mine blasts have consistent modulation patterns for each phase. These patterns are not seen in the earthquake spectra. The cepstral analysis technique shows that the delay times for the multiple explosions are between 80 and 150 ms, which are consistent with the millisecond or "fast" type delays commonly used in mine blasting. Similar analysis has also been applied to the PNE explosions, recorded at the NORSAR array, which indicate delays on the order of 0.5 to 1.0 s. Using homomorphic deconvolution, or cepstral liftering, the modulations in the mine-blast and PNE spectra can be removed. We found that the deconvolved spectra of the mine blasts closely resembled those of the earthquakes. Also, the deconvolved PNE spectra more closely resembled those of nearby PNE's, in terms of their high-frequency spectral slopes, which do not appear to be multiple events.

Conclusions and Recommendations

This study has resulted in the following conclusions:

(1) The least-squares spectral-shape fitting method produces consistent values of Lg attenuation which are reasonably consistent with those estimated by other methods.

(2) For the LLNL data, narrowband (0 to 5 Hz) estimates of Lg attenuation give lower values of Q_0 and higher values of ζ than broadband (0 to 10 Hz) estimates. This indicates that, in addition to Q being frequency dependent, with Q increasing with frequency, the frequency dependence itself, ζ, is also frequency dependent, with Q becoming less frequency dependent at higher frequencies.

(3) All our spectral Q estimates were made using the hard rock potential in the von Seggern and Blandford source correction, even for events in tuff. Using the tuff potential results in unreasonably high values of Q for events in tuff. This suggests that Lg spectra are relatively insensitive to explosion media rock types, or that depth of burial may result in Lg spectra in tuff which resemble those in harder rock.

(4) Source multiplicity can easily be identified in explosions using broadband data. NORESS can resolve delay times as short as 50 ms. This may provide a method for distinguishing between mine blasts and earthquakes. The fact that many PNEs in Russia are multiple explosions should be taken into account when estimating yields of these events.

(5) After removing the spectral modulations from the mine-blast spectra, they more closely resembled the spectra of nearby earthquakes which occurred on land.

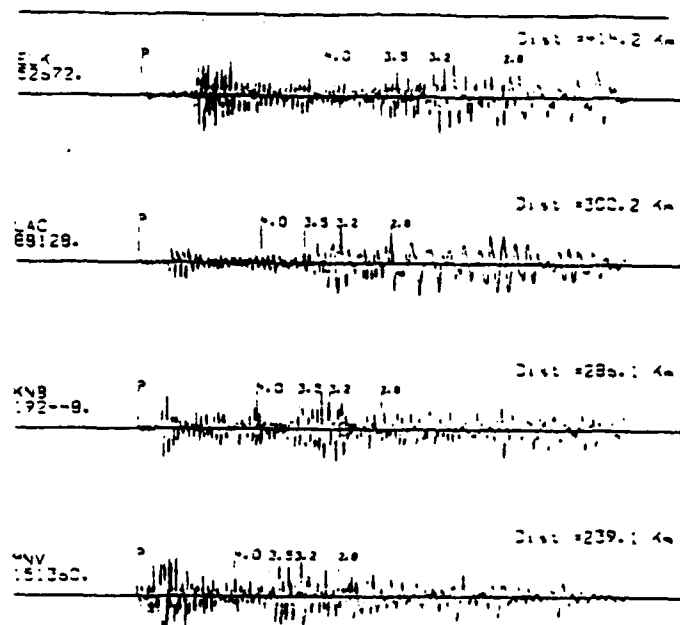These studies suggest the following additional studies:

(1) Using data from stations in the LRSM and VELA networks, joint inversions for source potential and attenuation of Lg should be accomplished using spectral magnitudes and constraining the attenuation model to fit the spectral shapes.

(2) Using higher-frequency broadband data from the new HFSE recording element at NORESS, try to resolve multiple explosion delays smaller than 50 ms.

References

Baumgardt, D.R.(1985). Attenuation, blockage, and scattering of teleseismic Lg from Underground nuclear explosions in Eurasia, *AFGL-TR-0332*, ENSCO, Inc., Springfield, Virginia.

Baumgardt, D.R. and K.A. Ziegler(1987). Spectral evidence for source multiplicity in explosions, Semiannual Report, *SAS-TR-87-01*, Submitted to AFGL.

Nuttli, O.W.(1986a). Yield estimates of Nevada test site explosions obtained from seismic Lg waves, *J. Geophys. Res.*, 91 ,2137-2151.

Nuttli, O.W.(1986b). Lg magnitudes of selected East Kazakhstan underground explosions, *Bull. Seism. Soc. Am.*, 76 ,1241-1251.

Von Seggern, D.H., and R.R. Blandford(1972). Source time functions and spectra for underground nuclear explosions, *Geophys. J. R. astr. Soc.*, 31 ,83-97.
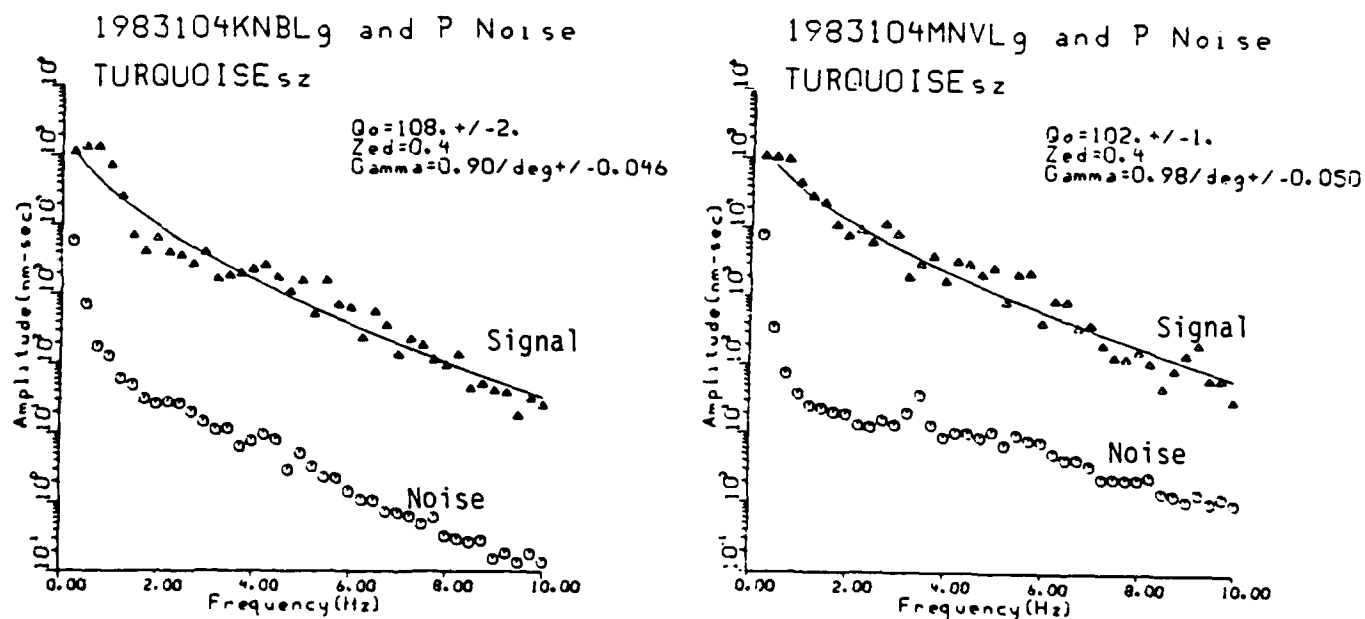
TABLE 1				
BASIN AND RANGE LG Q ESTIMATES					
Station	Delta (Km)	Azimuth (Deg.)	Q (Frequency Independent)	Q_0	ζ
LLNL SPECTRAL ESTIMATES					
KNB	285	90	371± 53 (0-10Hz)	111± 54	0.5± .16
			280± 42 (0-5Hz)	58± 21	0.7± .13
ELK	415	9	484± 42 (0-10Hz)	262± 58	0.3± .05
			529± 92 (0-5Hz)	117± 45	0.6± .13
LAC	298	187	374± 41 (0-10Hz)	161± 57	0.3± .12
			338± 72 (0-5Hz)	56± 39	0.7± .09
MNV	242	310	305± 54 (0-10Hz)	111± 63	0.4± .10
			240± 38 (0-5Hz)	81± 27	0.5± .11
NUTTLI CODA ESTIMATES					
BKS	557	281	-	139	0.6
DUG	446	38	-	155	0.6
TUG	712	136	-	162	0.6

TABLE 2			
SHAGAN RIVER LG Q ESTIMATES			
Event	Q (Frequency Independent)	Q_0	ζ
NORESS SPECTRAL ESTIMATES			
1	1328	455	0.6
2	1358	463	0.6
3	1399	423	0.6
4	1533	509	0.6
5	1307	436	0.6
6	1333	426	0.6
NUTTLI CODA ESTIMATES			
Station				
COP	-	700	0.4
KEV	-	554	0.4
KON	-	700	0.4
NUR	-	580	0.4

(a)

1983104KNBLg and P Noise
TURQUOISEsz

$Q_o = 108. +/-2.$
$Zed = 0.4$
$Gamma = 0.90/deg +/-0.046$

Signal

Noise

1983104MNVLg and P Noise
TURQUOISEsz

$Q_o = 102. +/-1.$
$Zed = 0.4$
$Gamma = 0.98/deg +/-0.050$

Signal

Noise

(b)

FIGURE 1(a) LLNL WAVEFORMS FOR NTS EXPLOSION TURQUOISE.

(b) Lg ATTENUATION ESTIMATES FOR KNB AND MNV IN 3.5 TO 3.2 KM/SEC
WINDOW. PRE-Pn NOISE AND Lg SPECTRA COMPUTED BY BANDPASS FILTER
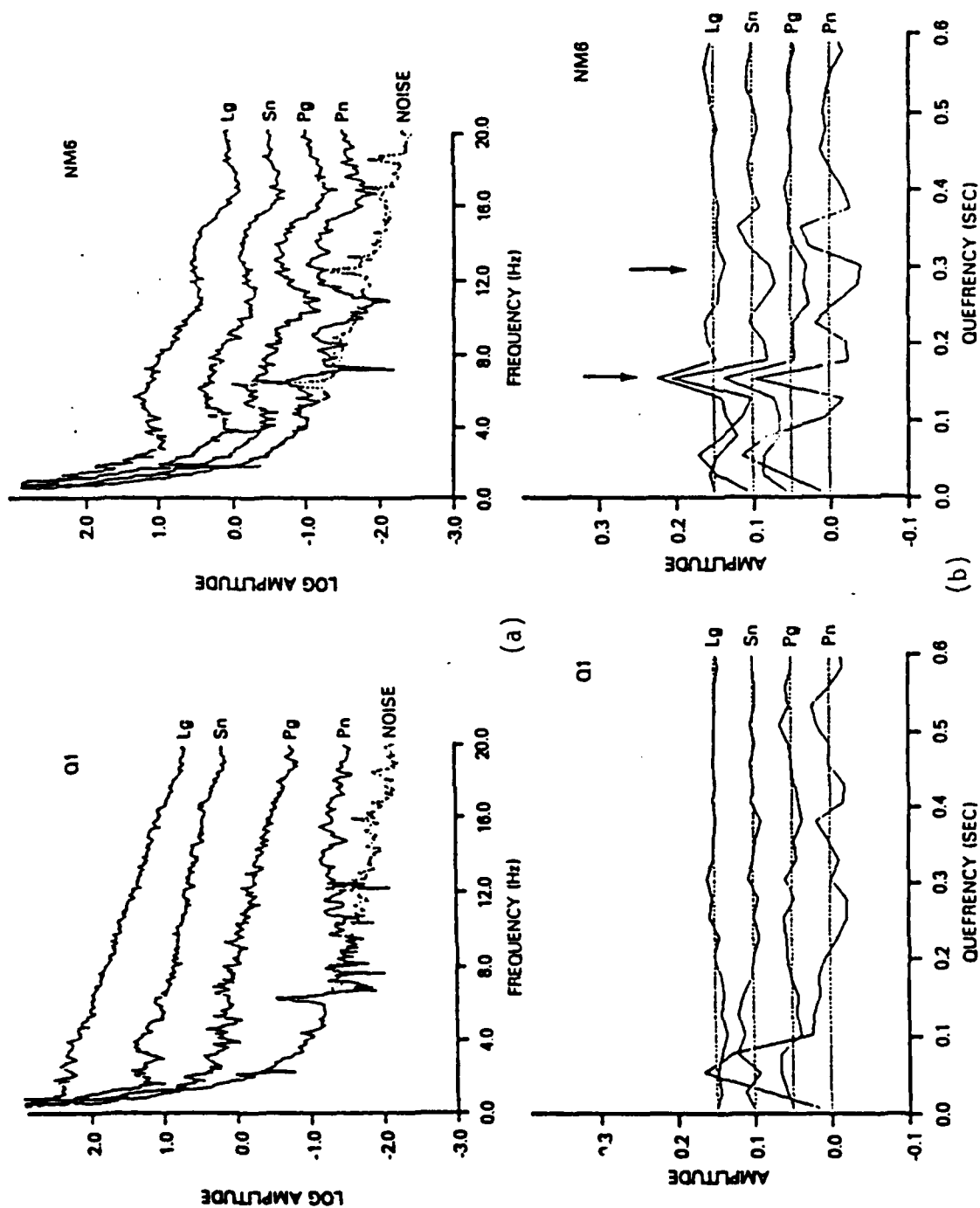METHOD.

FIGURE 2(a) SPECTRA FOR WESTERN NORWAY EARTHQUAKE (LEFT) AND MINE BLAST (RIGHT) RECORDED AT NORESS (b). CEPSTRA COMPUTED BY FOURIER TRANSFORMING SPECTRA ARROW SHOWS 150 ms PEAK FROM MINE BLAST DELAYED SHOT.

FREQUENCY VARIABLE FILTERS AND
SURFACE-WAVE AMPLITUDE ANALYSIS

Robert B. Herrmann, David R. Russell and Horng-Jye Hwang
Department of Earth and Atmospheric Sciences
Saint Louis University

OBJECTIVE

In order to better estimate phase velocities and spectral amplitudes of surface waves, the relative merits of different techniques are examined. We are specifically interested in a comparison between multiple filter analysis estimates of spectral amplitude and phase matched filters.

RESEARCH ACCOMPLISHED

For surface-wave studies, the objective is to process $s(t)$, the raw surface-wave time history, by a series of convolutional filters designed for modal isolation. In the context of this discussion, the definition of "convolution" is extended to include the general case of frequency varying filters, that is, filters that have a changing bandwidth during the convolution operation. This will produce a time signal (or spectrum) which can be used for further analysis.

Most surface-wave filters can be expressed by the following relations:

$$\psi(t) = \frac{1}{2\pi} \int_{-\infty}^{\infty} P(\omega) \ W_r(t,\omega) \ S(\omega) \ e^{i\omega t} \ d\omega \tag{1}$$

$$\Psi(\omega) = \int_{-\infty}^{\infty} \psi(t) \ e^{-i\omega t} \ dt \tag{2}$$

$$h(t,\omega_0) = \frac{1}{2\pi} \int_{0}^{\infty} \Psi(\omega) \ H(\omega-\omega_0) \ e^{i\omega t} \ d\omega \tag{3}$$

where

$$S(\omega) = \sum_j |S_j(\omega)| \ e^{-ik_j(\omega)x}$$

$$P(\omega) = e^{ik_j(\omega)x}$$

$W_r(t,\omega) = $ time and frequency variable window

$H(\omega - \omega_0) = $ frequency domain convolution filter.

$S(\omega)$ is the total spectrum of the seismogram, $s(t)$, and is composed of a sum of normal modes, multi-pathed signals, possible interfering events and phases, and incoherent noise. The purpose of the above filters is to isolate the j'th mode of interest so the amplitude spectrum $|S_j(\omega)|$ and wavenumber spectrum $k_j(\omega)$ can be recovered. This is probably too idealistic a goal in some cases, as pointed out by Der (1986). Due to scattering and reflections, there may not be a pure isolated mode to recover. A more

accurate statement is that the purpose of such filters is to isolate seismic energy propagating in the vicinity of desired modes of interest.

$P(\omega)$ is a phase-matched filter. The wavenumber estimate $\bar{k}_j$ should be near the true modal wavenumber, in order to compress the energy of the desired signal about zero-lag in the time domain, forming a "pseudo-autocorrelation function" $\psi(t)$. Herrin and Goforth (1977) discussed this in detail.

$W_\tau(t,\omega)$ is a time and frequency variable window used to isolate modes of interest and improve signal to noise ratios. It is symmetric about position τ in the time domain, with a width controlled by the frequency ω.

Various combinations of the above filters have been used for modal isolation, three of which will be detailed below.

Case 1: $P(\omega) \equiv 1$, $W_\tau(t,\omega) \equiv 1$

This is the basis for the multiple filter technique (MFT) (Dziewonski et $al.$, 1969). Equations (1) and (2) are simply Fourier transforms, so the raw spectrum $S(\omega)$ is input into (3), which is the MFT evaluated at ω_0. $H(\omega)$ is a narrow bandpass filter (usually a band-limited Gaussian), symmetrically about ω_0. The non-negative integral limits cause the time signal $h(t,\omega_0)$ to be complex, with the modulus having maxima at the group velocities of the signal modes. Herrmann (1973) showed that under the condition of an approximately flat amplitude spectrum and linear phase delay of the j'th mode across the width of $H(\omega)$,

$$h(t_j,\omega_0) \approx A \ |S_j(\omega_0)| \ e^{i[\omega_0 t_j - k_j(\omega_0)x]} \tag{4}$$

where A is a constant of proportionality determined by the frequency and the width of the Gaussian filter $H(\omega)$, and t_j is the group delay of the j'th mode. Evaluating (3) at multiple frequencies will extract the spectrum of the j'th mode, if it is suitably smooth.

Case 2: $W_\tau(t,\omega) = W_0(t)$

This is the phase-matched filter method of Herrin and Goforth (1977). Wavenumbers are found for the phase-matched filter $P(\omega)$ by integrating the group delay found in MFT. The window $W_0(t)$ is not frequency dependent, so it can be factored from the integral in (1). It is centered about zero-lag in the time domain. Equation (1) is now the windowed pseudo-autocorrelation function, and (2) is the phase-matched spectrum of the isolated mode of interest.

The above methods attempt to isolate spectral modes of interest via frequency domain convolutions. As Dziewonski and Hales (1972) pointed out, the process of convolution will distort the signal spectrum unless the prescribed filters are Dirac impulses in the frequency domain. By removing the phase of the signal, PMF can reduce phase distortion, but neither MFT or PMF address the problem of amplitude distortion due to the convolution operation. The method presented in this paper will utilize a frequency variable window which will allow the analyst to place maximum error bounds on the amount of tolerable amplitude bias.

Case 3: $W_\tau(t,\omega) = W_0(t,\omega)$

This is the method of frequency variable filtering (FVF). The raw spectrum $S(\omega)$ is phase-matched filtered to compress the energy of the signal of interest about zero-lag in the time domain. Then, each harmonic component of this pseudo-autocorrelation function is windowed about zero-lag with $W_0(t,\omega)$, with the width of the window proportional to the period of the individual harmonic. These operations are done in equation (1), which is then Fourier transformed by equation (2) to give the isolated modal spectrum of interest.

An advantage of FVF is that the time window $W_0(t,\omega)$ can be constructed at each frequency to correct the bias due to windowing. In designing the FVF, we prefer to use Parzen windows to window the pseudo-autocorrelation function for calculating phase residuals, and a frequency variable cosine window to

correct the amplitude spectrum. The width of the window is proportional to:

$$|\Psi''|^{1/2}$$

where $|\Psi''|$ is the modulus of the complex second derivative of the Parzen windowed pseudo-autocorrelation function. The constant of proportionality is determined by the maximum level of acceptable bias.

As a comparative test, we present a typical oceanic surface wave, which, for purposes of demonstration, is to be considered as pure signal. Figure 1 shows the raw seismogram, its amplitude spectrum and the group velocity dispersion contours from MFT. Figure 2 shows the results of filtering the signal, with linear scaled residuals at the bottom.

The signal demonstrates the limits of spectral resolution for the filters. All of them miss the sharply varying spectral peak at 17 seconds, and the null at 25 seconds. The FVF can be designed to be sensitive to this curvature, but this would require time domain cosine windows with widths that would make the filter essentially all-pass, reducing the effectiveness in the presence of noise.

At all other periods, both PMF and FVF adequately resolve the spectrum. However, notice from the residual plots that the MFT fails to pick the secondary peak at 25 seconds. This is due to the low resolution of the Gaussian filter at that period.

Figure 3 shows the raw waveform and the isolated fundamental mode using the PMF and FVF techniques. Note that neither can duplicate the notch in the original time series. This is due to the inability to resolve the 17 second spectral peak.

CONCLUSIONS

The method of FVF is a viable alternative to both MFT and PMF. It has the advantage of explicitly addressing spectral bias, which is an unavoidable side effect of any type of convolutional smoothing. As a result, it can be designed to be more selective than either PMF or MFT, except at points where signal curvature requires a wider time window.

FVF is not always successful, as seen in the example. To successfully extract the 17 second peak, the time windows would have to be so wide that the filter would become all-pass.

FVF and PMF have the advantage over MFT in that processing results can be seen in both the time and frequency domains. It is recommended that FVF, and in some cases PMF, be preferred over MFT as filters for isolating surface-wave normal mode amplitude spectra.

REFERENCES

Der, Z. A. (1986). Comments on the paper "Estimation of scalar moments from explosion-generated surface waves" by Jeffry L. Stevens, *Bull. Seism. Soc. Am. 76*, 1822-1824.

Dziewonski, A., S. Bloch, and M. Landisman (1969). A technique for the analysis of transient seismic signals, *Bull. Seism. Soc. Am. 59*, 427-444.

Dziewonski, A., and A. Hales (1972). Numerical analysis of dispersed seismic waves, *in* B. A. Bolt (editor), *Methods of computational physics, vol. 11*, Academic Press, New York, 39-85.

Herrin, E. and T. Goforth (1977). Phase-matched filters: application to the study of Rayleigh waves, *Bull. Seis. Soc. Am. 67*, 1259-1275.

Herrmann, R. B. (1973). Some aspects of band-pass filtering of surface waves, *Bull. Seism. Soc. Am. 63*, 663-671.
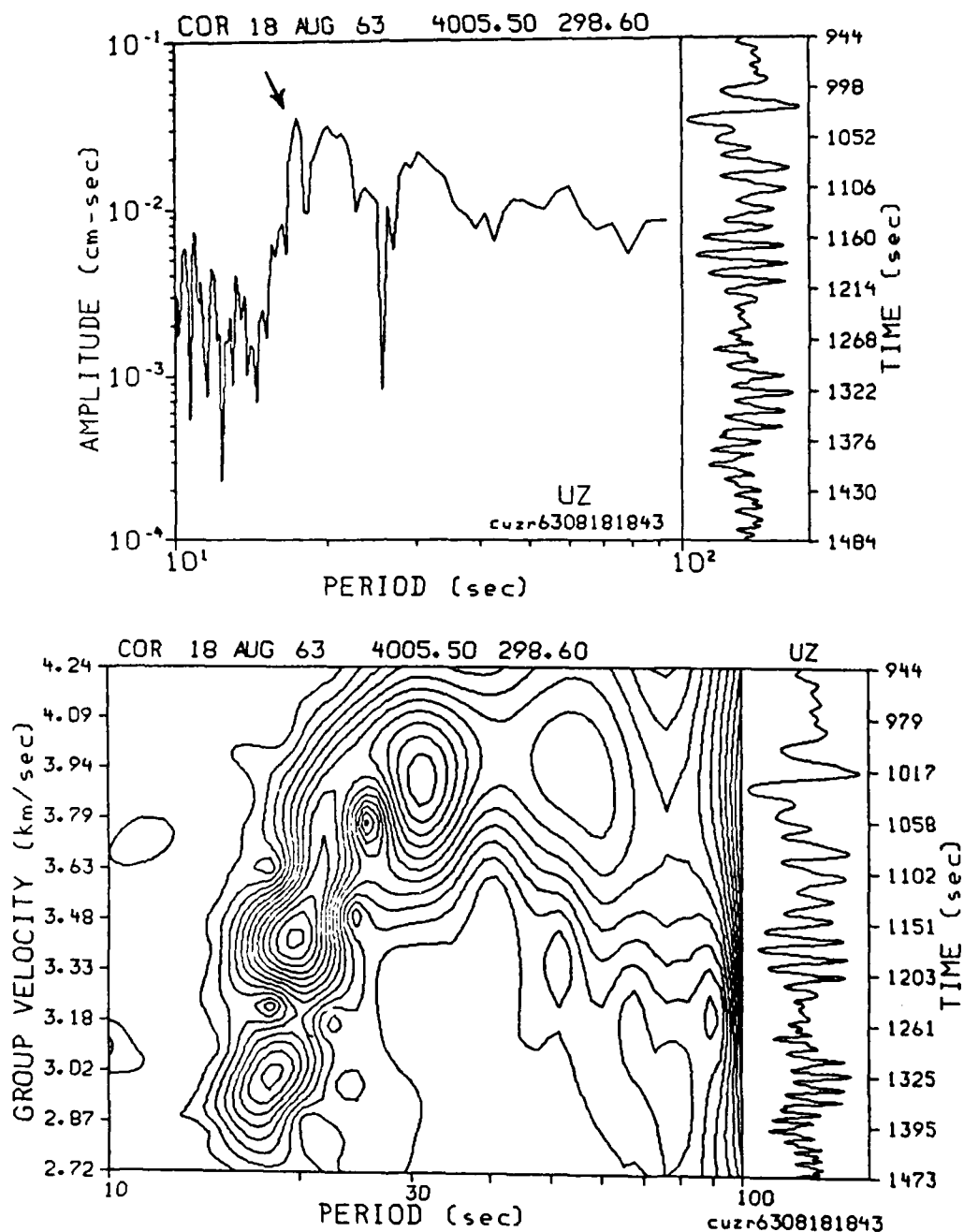
Fig. 1. Spectrum (top) and MFT group velocity contours (bottom). Time domain seismograms are plotted to the right. Notice the non-linear time scale for the MFT plot. The arrow indicates the 17 second spectral peak.
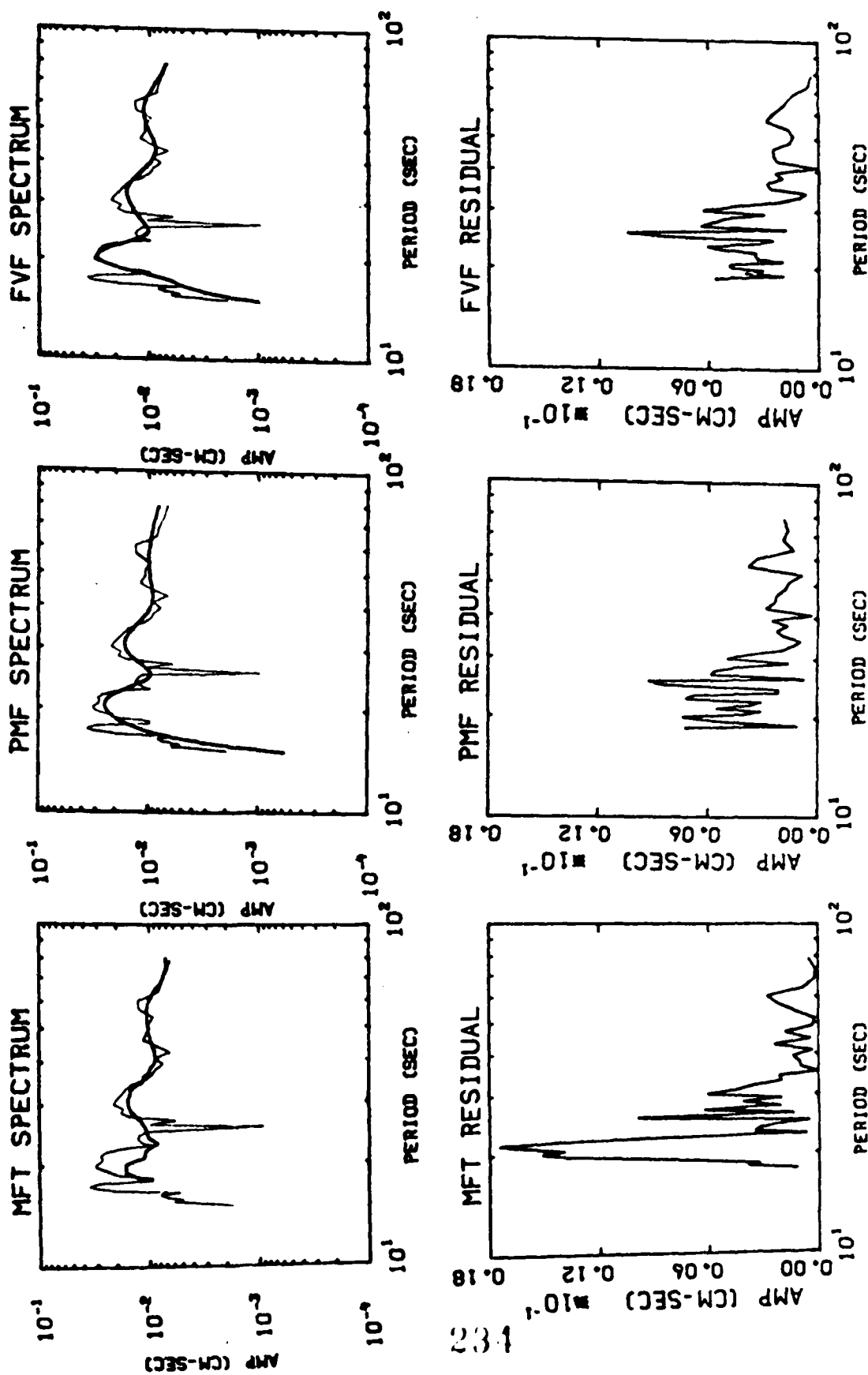
Fig 2. Amplitude spectra. Top) comparison of the original spectra (light line) with the isolated fundamental mode spectra (smooth line) using the MFT, PMF, and FVF techniques. Bottom) residuals between the original spectrum and the isolated modes. The 17 second residual is NOT plotted. Notice the linear amplitude scale.
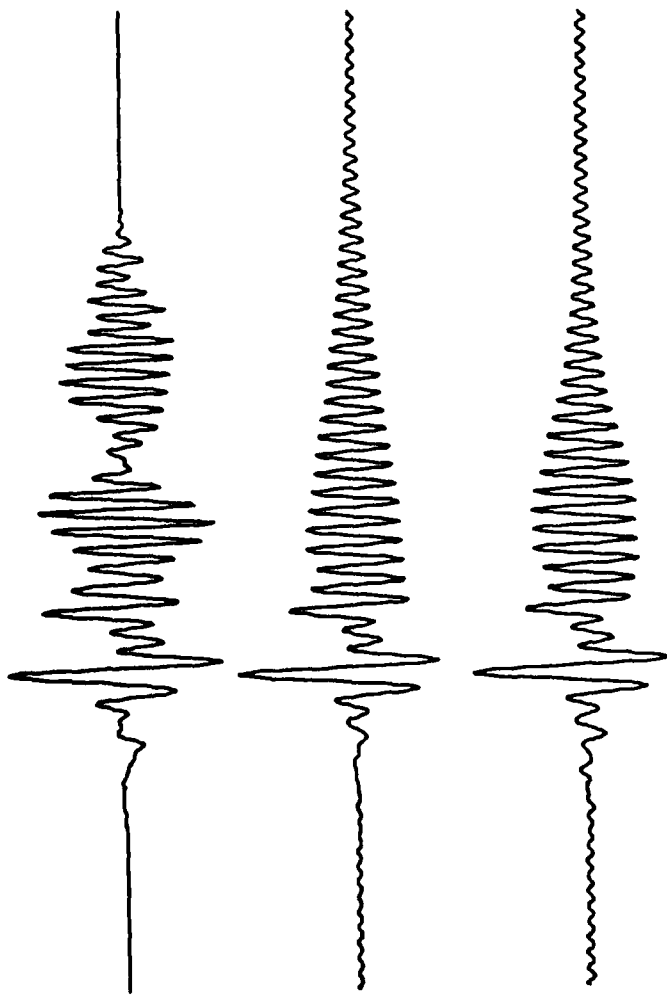
Fig. 3. Raw seismogram (top), fundamental mode isolated by PMF (center), and fundamental mode isolated by FVF (bottom).

Rg WAVES AS A DEPTH DISCRIMINANT
FOR EARTHQUAKES AND EXPLOSIONS IN NEW ENGLAND

Alan L. Kafka
Weston Observatory
Dept. of Geology and Geophysics
Boston College

OBJECTIVE

Regionally recorded seismograms from small earthquakes and explosions in New England are generally very complex, and it is usually difficult to identify specific phases other than the initial P wave and/or the onset of the S wave. One phase that can often be identified by its waveform and spectral content is the Rg phase. Rg is a fundamental mode Rayleigh wave generated by shallow focus earthquakes and explosions. These waves are recorded by short-period seismic stations in New England, and they are particularly prominent on seismograms of quarry blasts (Figure 1). The period range of the Rg waves recorded in New England is about 0.2 to 2.5 sec. Source depth is probably the most significant factor affecting the amplitude of Rg relative to the other phases on seismograms, although distance from the source is also an important factor since Rg appears to be more highly attenuated than other recorded phases. The objectives of this research are to investigate the propagation properties of Rg waves recorded in New England and to evaluate Rg as a depth discriminant. The seismograms of small earthquakes and explosions analyzed in this study are recorded at stations of the New England Seismic Network (NESN) operated by Weston Observatory.

RESEARCH ACCOMPLISHED

Many of the sources used in this study are quarry blasts. One of the first steps in this research was to estimate the size of these blasts so that the results of this study could be compared with results from other studies of explosions and earthquakes. An extensive analysis of source and path properties of the various recorded phases (Pg, Sg, Lg, etc.) would be necessary to accurately determine magnitudes from the high-frequency seismograms. However, such a procedure would be a diversion from the main goal of this study; i.e. to study the Rg phase. For the purposes of this report, I therefore chose a simple approach that provides a crude estimate of the magnitudes of these events. In Figure 3, I compare signal durations measured from NESN seismograms of quarry blasts with signal durations measured from NESN seismograms of earthquakes that were large enough to calculate mbL_g magnitudes. The sample of quarry blasts used for this comparison is from a study by Fowler (1985). Signal duration (measured in sec) is the amount of time from the first arrival of the P wave to the time when the signal decays into the background noise. The mbL_g magnitudes were determined primarily from WWSSN stations located at Weston, MA (WES) and Palisades, NY (PAL), but for some of the larger events other WWSSN stations were used. In some cases only one station was used for an mbL_g calculation. Based on the results shown in Figure 3, quarry blasts recorded by the NESN were generally found to range in magnitude from about 1.0 to 1.6.

In addition to these magnitude estimates, observed amplitudes of Rg waves were used to estimate seismic moments of the quarry blasts. Preliminary results suggest that the seismic moment of a typical quarry blast in this study is on the order of 10^{18} to 10^{19} dyne-cm.

For the larger quarry blasts, Rg can sometimes be identified at distances up to about 100-150 km from the source, although at those distances the Rg signals are usually not very strong. Only the largest quarry blasts generate strong Rg signals at stations beyond about 70-80 km. The

strongest Rg signals are generally in the period range of about 0.5 to 1.5 sec. In that period range Rg displacement is essentially confined to depths of about 1 to 5 km, with most of the Rayleigh wave energy in the upper 2 or 3 km (e.g. Bath, 1975; Kafka and Reiter, 1987). Thus, sources deeper than about 4 km would not be expected to generate strong Rg signals; and so, if Rg can be clearly identified on a seismogram, the source is most likely very shallow. Observed Rg waves could, therefore, be used to discriminate between very shallow events and deeper events, provided that the Rg phase can be identified on seismograms and distinguished from other recorded phases.

One distinguishing characteristic of the Rg phase is its arrival time. Arrival times of Rg waves can be predicted if group velocity dispersion is known (or can at least be approximated). In New England, Rg is normally dispersive and travels with group velocities between about 2.0 and 3.2 km/sec (Kafka and Dollin, 1985; Kafka and Reiter, 1987).

Analysis of amplitude spectra of Rg and other phases provides additional information for identifying Rg. For a sample of five quarry blasts and two earthquakes, amplitude spectra were calculated for portions of seismograms between the arrival of the S-wave and the end of the coda. The stations used for this analysis were at distances ranging from 17 to 100 km from the sources. Since the recording instruments all have similar responses that enhance the frequency range of the signals, the seismograms used in this analysis were not corrected for instrument response. The seismograms and spectra are, of course, very complex since the propagation paths traverse various geological structures. Nonetheless, preliminary analysis of the amplitude spectra suggests some general patterns.

Amplitude spectra of the seismograms in Figure 1 are shown in Figure 4. The energy in the S-to-coda part of the seismograms was generally in the frequency range of about 0.3 to 15.0 Hz. Within that frequency range there appear to be three somewhat distinct frequency bands. A large portion of the energy generated by background noise appears to be concentrated between about 0.3 and 1.0 Hz. (However, the background noise spectrum is not obvious in the four examples shown here since the signals are generally quite strong.) Energy associated with the Rg phase appears to be concentrated between about 0.5 and 3.0 Hz, and energy from other phases (presumably Sg and Lg) appear to be concentrated in the frequency range of about 5-12 Hz. Using these preliminary observations as a guide, I am investigating the relative amounts of seismic energy in those three frequency bands.

Since Rg appears to be the primary contributor to energy in the 1.0 to 3.0 Hz frequency band, the ratio of spectral amplitudes in that band to spectral amplitudes in higher frequency bands might prove useful as a depth discriminant. For the sample of quarry blasts and earthquakes discussed above, the average spectral amplitude was calculated for a low frequeny range (1.0 to 3.0 Hz) and for a high frequency range (5.0 to 12.0 Hz). Figure 4 shows a histogram of ratios of the low frequency to high frequency averages calculated from the sample of quarry blasts and earthquakes. The two earthquakes in that sample are a foreshock and aftershock of the mbL_g 3.8 earthquake that occurred on October 21, 1985 near Ardsley, NY. Those events were well recorded by nearby stations operated by Lamont-Doherty Geological Observatory and Woodward-Clyde Consultants, and the depths of both events are fairly well constrained to be about 5 km. Thus, if Rg is being identified by the low frequency to high frequency ratio, the earthquakes should have a lower ratio than the quarry blasts. For the sample shown in Figure 4, the earthquakes can be distinguished from the blasts based on this low frequency to high frequency ratio.

CONCLUSIONS AND RECOMMENDATIONS

The results of this low frequency to high frequency ratio method for identifying Rg are very preliminary at this point. It is clear that, for the sample shown in this report, the earthquakes can be distinguished from the blasts using this ratio, and indeed the results look encouraging There are, however, a number of additional lines of investigation that must be considered First, the seismograms of quarry blasts chosen for this example, were initially chosen because of their clearly identifiable Rg waves and because they were generated by quarries that are well known at Weston Observatory. To what extent, then, would this method work for less "ideal" seismograms of quarry blasts? Second, the two earthquakes were chosen because they occurred very close to stations of the Northeast United States Seismic Network. Thus, the locations and depths of the earthquakes are better constrained than the "typical" small earthquake occurring in the northeastern United States. Third, while this amplitude ratio method is a simple and straight-forward procedure, it doesn't exploit the known differences in arrival time between Rg and other phases. It may be possible to identify Rg more clearly and to separate it from other recorded phases by measuring amplitudes at particular periods and arrival times for the entire seismogram using a narrow-band pass filter anlaysis Such an approach will be taken in the next phase of this research. Finally, the differences in attenuation between Rg and other phases were only roughly considered in this analysis by restricting the distance range for seismograms used in this example. A more thorough analysis of attenuation is planned as part of this research.

REFERENCES

Bath, M., Short-period Rayleigh waves from near-surface events, Phys of Earth and Planet. Int., 10, 369-376, 1975.

Fowler, R.V., Attenuation of Rg waves in southern New England, M.S. Thesis, Boston College. 92 p., 1985.

Kafka, A.L. and Dollin. M.F. Constraints on lateral variation in upper crustal structure beneath southern New England from dispersion of Rg waves, Geophys. Res Letters, 12, 5, 235-238, 1985

Kafka, A.L and Reiter, E.C., Dispersion of Rg waves in southeastern Maine Evidence for lateral anisotropy in the shallow crust, Bull. Seis Soc. Am., (in press), 1987
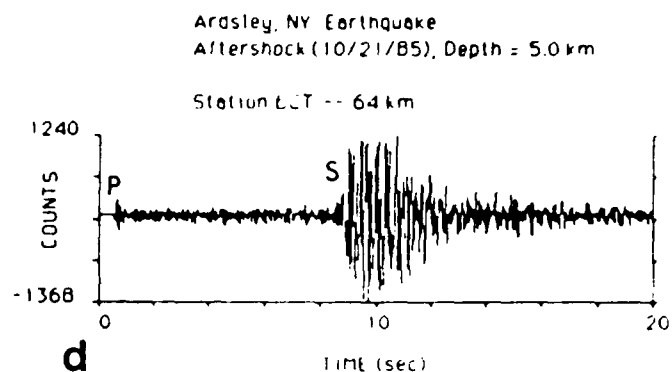
North Branford, CT Quarry Blast

Station MDI -- 36 km

Reed Gap, CT Quarry Blast

Station UCT -- 57 km

Reed Gap, CT Quarry Blast

Station NSC -- 74 km

Ardsley, NY Earthquake
Aftershock (10/21/85), Depth = 5.0 km
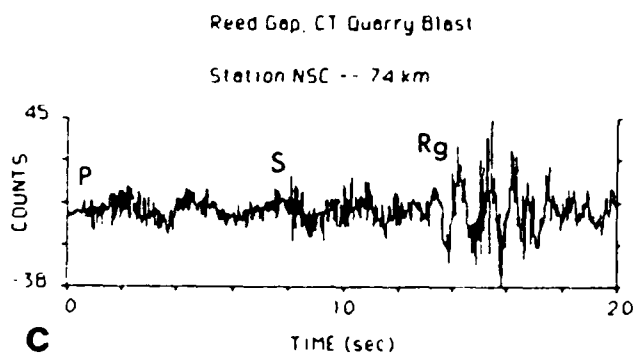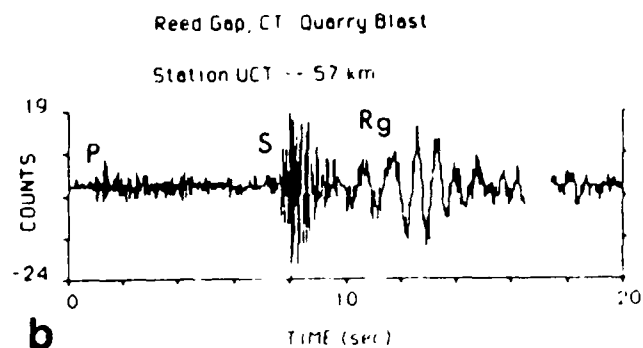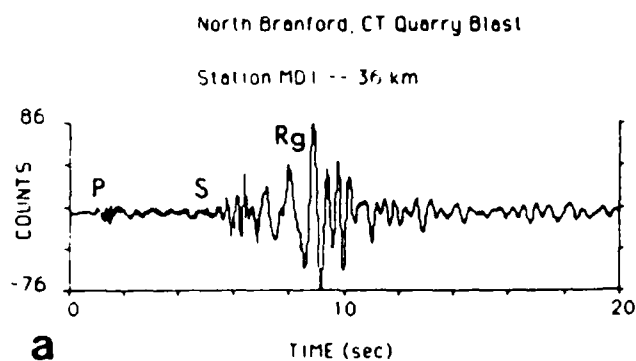
Station ECT -- 64 km

Figure 1 Examples of seismograms used in this study. Locations of sources and stations are shown in Figure 2. Paths corresponding to seismograms a, b, c and d in this figure are labelled A, B, C and D respectively in Figure 2.
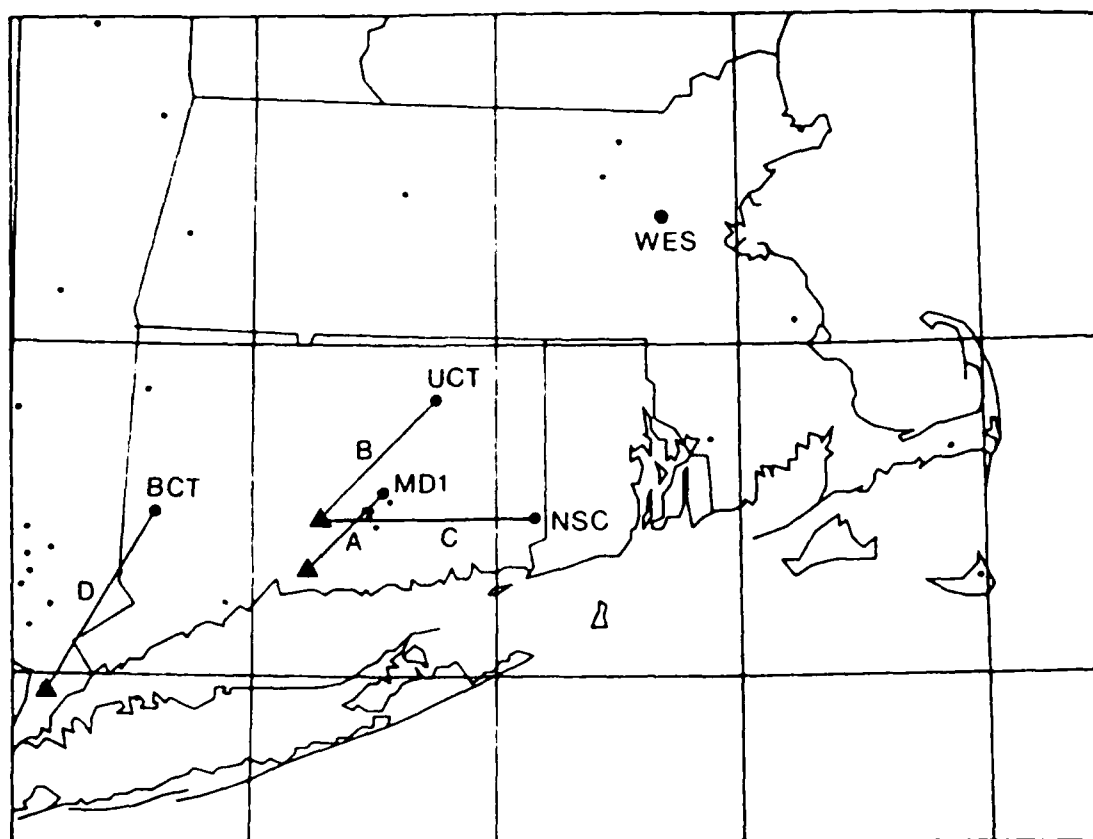
239

Figure 2 Map of southern New England and adjacent areas showing locations of sources (closed triangles) and stations (closed circles) for seismograms shown in Figure 1. WES indicates the location of Weston Observatory where the short-peiod seismograms from this study are recorded. Small dots indicate locations of other short-period stations that are part of the Northeast United States Seismic Network.
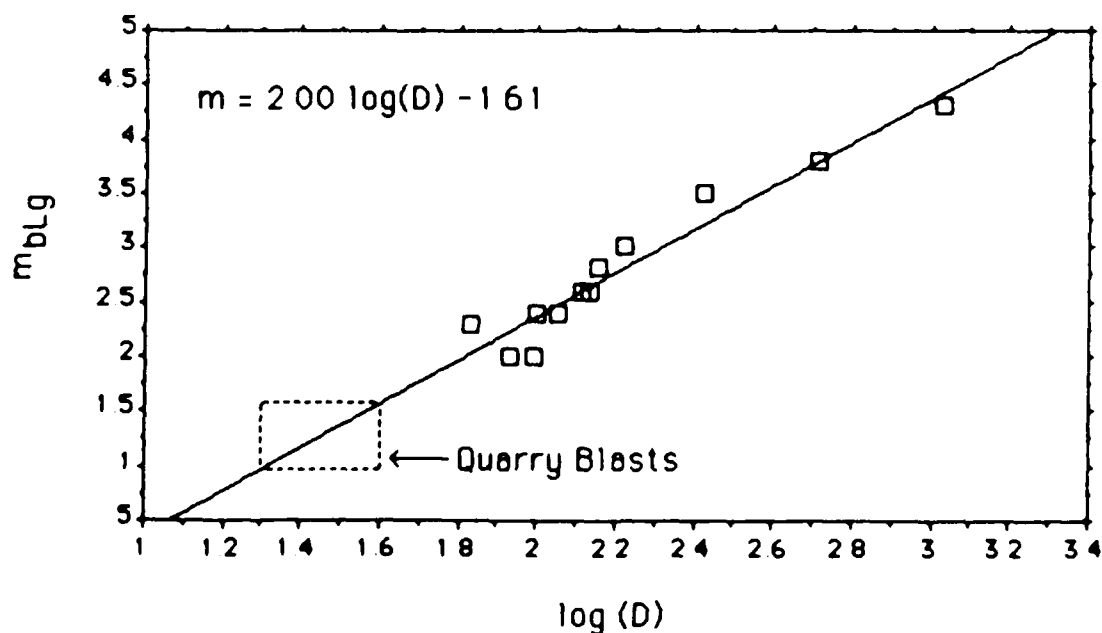

$$m = 2.00 \log(D) - 1.61$$

Figure 3 Signal duration (D, sec) versus magnitude for a sample of earthquakes recorded by the NESN. The dashed line rectangle shows the range of signal durations and inferred magnitude estimates for a sample of quarry blasts in southern New England studied by Fowler (1985)
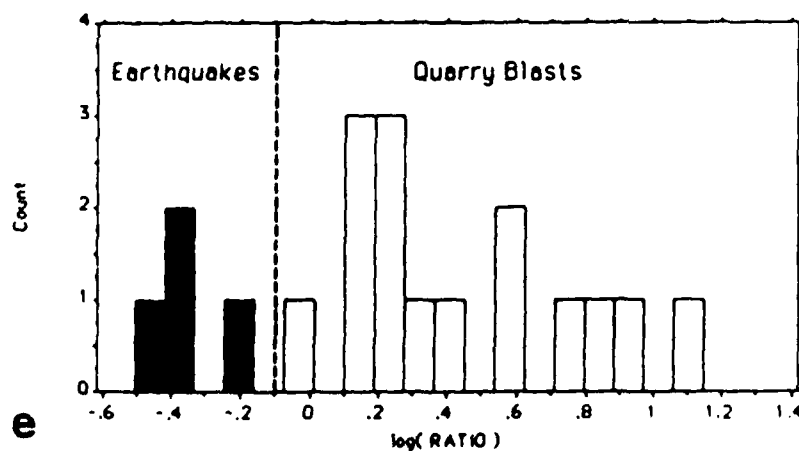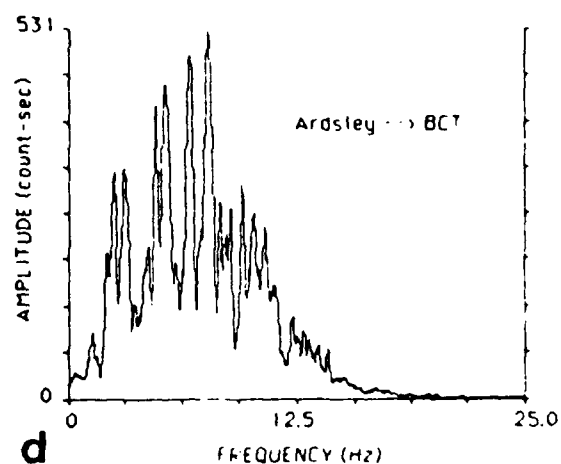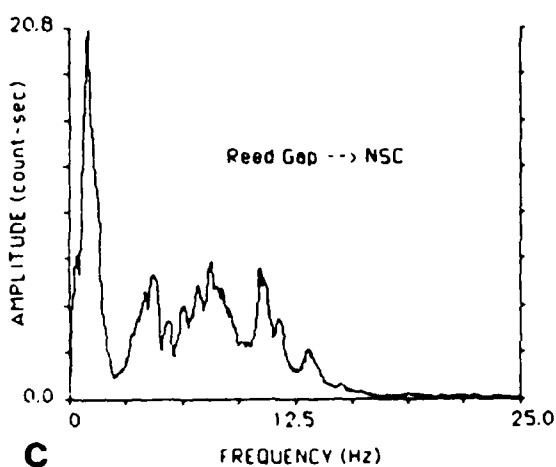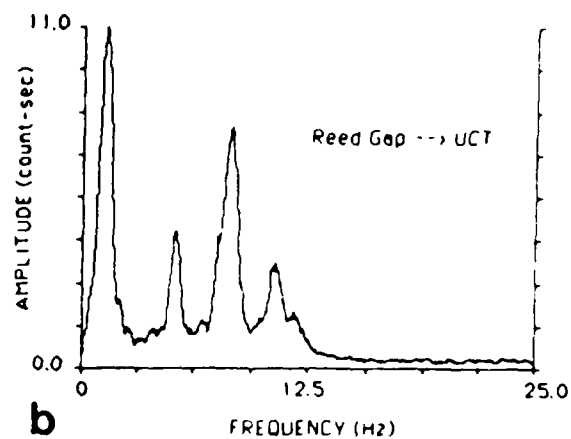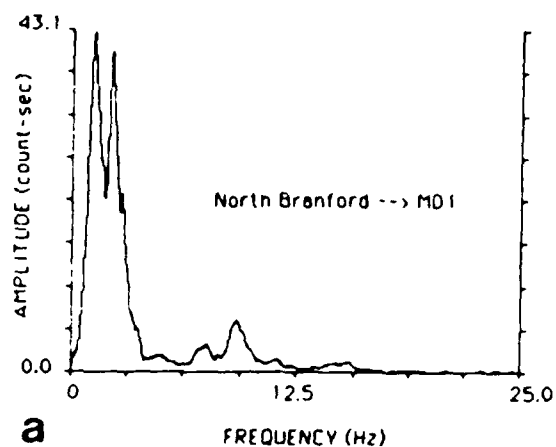
Figure 4 (a) - (d) Amplitude spectra of seismograms shown in Figure 1. These spectra were smoothed with a moving average filter. (e) Histogram of the logarithm of the low-frequency (1-3 Hz) to high-frequency (5-12 Hz) amplitude ratio for a sample of five quarry blasts and two earthquakes.

241

INVESTIGATIONS ON LOCAL SEISMIC PHASES AND EVALUATION OF BODY WAVES MAGNITUDE
(Western Europe)

By B. Massinon and P. Mechler
Radiomana, 27 rue Claude Bernard, 75005 Paris, France

Objective :

The main objective of our contribution to the Darpa Research Program is to optimize methods to extract from seismic records at local,regional and teleseismic epicentral distances, information concerning the nature of the source (earthquake, chemical blast, rockburst) and its principal characteristics.(magnitude, seismic moment, corner frequency, depth etc).

A second objective necessary to approach the first one is to better understand the radiation and propagation of the seismic source within the crust and to evaluate the influence of the crust in term of attenuation and wave form modeling.
Our fields of investigation have been both :

  - theoretical : numerical simulation
  - empirical   : processing of seismic data recorded on the LDG networks.

Research accomplished :

1°) Local epicentral distances :

a) Source depth evaluation by numerical simulation :

Our purpose is to evaluate the influence of focal depth on seismograms recorded at local distances, with the help of synthetics.
By using a method of modelisation of seismograms based on an exact discrete wavenumbers computation (Bouchon 1982), we have computed the waveforms at epicentral distances ranging from 10 to 60 km, every 10 km.
The source function s (ω) is a Brune source. The propagation model is the crust model currently used for France area. (Darpa Annual Report 1984). No anelastic attenuation is taken into account. For each epicentral distance, different seismograms have been computed for different focal depths : 1, 3, 6, 9, 12 and 27 km, all focus situated within the crust.

The evolution of each seismogram versus depth is clearly observed : very complicated with a source near the earth level, essentially composed of guided waves with a source within the first layers, it becomes simpler and simpler when the focal depth increases. At a depth of 27 km, only direct P_g and S_g still exist. The R_g waves (surface waves in sedimentary layers) are the most sensitive to focal depth effect with maximum (1 km depth) to minimum (27 km depth) spectral ratio ranging from 100 to 1000.

Besides the depth influence, the effect of epicentral distance is clearly seen.

In order to let the seismograms be independant from distance we deconvolve them from geometrical attenuation. For that purpose an inversion technique is applied in the frequency domain of the synthetics to obtain simultaneously the source spectrum and the geometrical attenuation. This inversion is done on each focal depth previously selected.

Large differences exist between the computed source spectra for each phase and the original sources (Brune source) specially in their low frequency part.

Nevertheless if we compute the ratio of low frequency amplitudes of these sources (S_g / R_g , P_g / R_g, P_g / S_g) it shows clear variations versus focal depth.(Fig.1)

Although different points are still not solved as the absence of flat frequency response of each computed source spectrum, we might expect determine source depth ranges at local epicentral distance by a careful analysis of the relative importance of each seismic phase.
We intend to test this method on real cases.

b) Seismic sources evaluation at local distances :
During a period of six months we have set up a seismic network (10 SP stations) surrounding a coal mine exploitation. Epicentral distances varying from 1 km to 6 km.

Rockbursts are recorded with magnitudes M_L within the range of $M_L=1$ to $M_L=3.2$. Besides the aim of locating these events in three dimensions, we have started to compute source spectra.
As an example,Fig. 2 shows a serie of 12 displacement source spectra recorded at the same seismic station distant of 6 km from both source area "a" and "b". No attenuation correction has been applied. The lower displacement spectrum when visible is the corresponding seismic noise spectrum.

The data are sampled at 50 samples/sec. and the recorded band width is defined between 0.5 and 16 Hz. Corner frequencies are generally well defined and inferior to 10 Hz.

Among these first examples is one chemical blast ("tir") recorded at the same epicentral distance. Arbitrary ordinates unities are the same for the 12 spectra and so it is possible to compare the blast spectrum with rockburst spectra with $M_L = 1.6$, $M_L = 1.7$, and $M_L = 1.8$.

The four cases have a low frequency displacement value around one unit . The blast corner frequency $F_c = 6.2$ Hz, $F_c = 3.4$ Hz, and $F_c = 1.8$ Hz.

Such comparisons between rockbursts, chemical blasts, and earthquakes sources if any,are going to be the main part of our future work in this field.

2°) Regional epicentral distances:

a) Data base for source studies at regional distances :
We have achieved in 1986 a regional seismic data base which includes the seismic data, of some 431 western european earthquakes recorded in the french LDG network from 1984 to 1986.
These quakes are located within thecrust with M_L magnitudes ranging from 2.4 to 5.7. The data base contains the seismic records (50 samples/S) as short period seismograms (0.5 Hz - 16 Hz) corresponding to vertical component for the 28 seismic stations. It also contains the displacement source spectra of each quake computed on L_g waves train, more precisely on the maximum amplitude part (L_{g1}), the coda (L_{g2}) and the end of the coda (L_{g3}). This beeing done after attenuation correction versus distance. One example is given on Fig. 3 corresponding to an earthquake which occured in the Ossau valley (Pyrenees), the 19 04 86 ($H_o = 22$ h 5' TU; lat.=43°06N long.=0°45'E ; $M_L = 3.3$) where the three spectra are given with their main characteristics. Seismic moments M_o systematically computed are related to magnitudes M_L as follows :

$$M_{oL_{g1}} = 15.0 + 1.4 \ M_L$$
$$M_{oL_{g2}} = 15.5 + 1.3 \ M_L$$
$$M_{oL_{g3}} = 15.6 + 1.2 \ M_L$$

Or for the whole set of $\quad M_{oL_g}$:

$$M_{oL_g} = 15.1 + 1.4 \ M_L$$

Any attempt to regionalize earthquakes by peculiar $M_o = F (M_L)$ relationship did not lead to positive results up to now.
Nevertheless, Q tomography might bring more accurate attenuation factors and consequently might lead to some quakes regionalization if any.

b) <u>Theoretical studies on regional waves radiation and propagation</u> :
Two studies have been undertaken which concern the effect of irregular layering
and topography on the generation and propagation of seismic waves radiated by
a superficial seismic event.

<u>Diffraction and conversion of elastic waves at a corrugated interface</u>
We evaluate the efficiency of P to S conversion in the region of the source to
understand the high amplitude of the regional phases L emitted by a superficial seismic.
event.
We have considered an interface between two media which elastic parameters correspond
to crust and upper mantle. In the case of an incident P wave, the P to P reflexion
is nearly specular while P to S reflexion is very different from the perfectly
flat case. Even for small values of the incident angle. S waves are diffracted
in direction above the critical angles of these waves with significant amplitudes.

S waves incident with this angle present a quasi specular reflexion and this
contributes to L_g.
As a result this phenomenon can be invoked to explain the large amplitude of
L_g radiation for superficial seismic event.

<u>Numerical simulation of the radiation and propagation of seismic waves in</u>
<u>a laterally varying crust</u> :

The effect of irregular layering and topography on the generation and propagation
of seismic waves radiated by a superficial seismic event as a blast is formulated
in term of a boundary integral equation-discrete wavenumber method.

The source is located in a geological structure with complex geometry such as
a sediment and alluvion field basin or rough topography.

A resulting enhancement in shear waves radiation and the effect of a laterally
varying crust on the propagation of regional phases are observed.

A strong effect of irregular layering on the amplitude and coda duration of the
seismic phases is also clearly seen.

<u>Conclusions and recommendations</u> :

Our study on seismic sources at local epicentral distances by recording events
in a coal mine has just started.

The quality of data we have obtained encourage us to carefully compute the main
source parameters and look at possible differences between rockbursts, chemical
blasts and earthquakes.

The method to obtain a source depth information we have studied on synthetics
should also be tested on these empirical data.

At regional distances, we are able now to compute the displacement spectrum
of any seismic source which occurs in France and the vicinity for reasonable
M_L (M_L $>$ 2.0).

Nevertheless our attenuation model for L_g waves is not yet adapted to each peculiar
propagation path due to crustal heterogeneities and a Q tomography study over
France should improve our results on source evaluation.

We also try to evaluate the influence of these crustal lateral heterogeneities
and irregular layering on synthetics and particularly on L_g phases. We plan
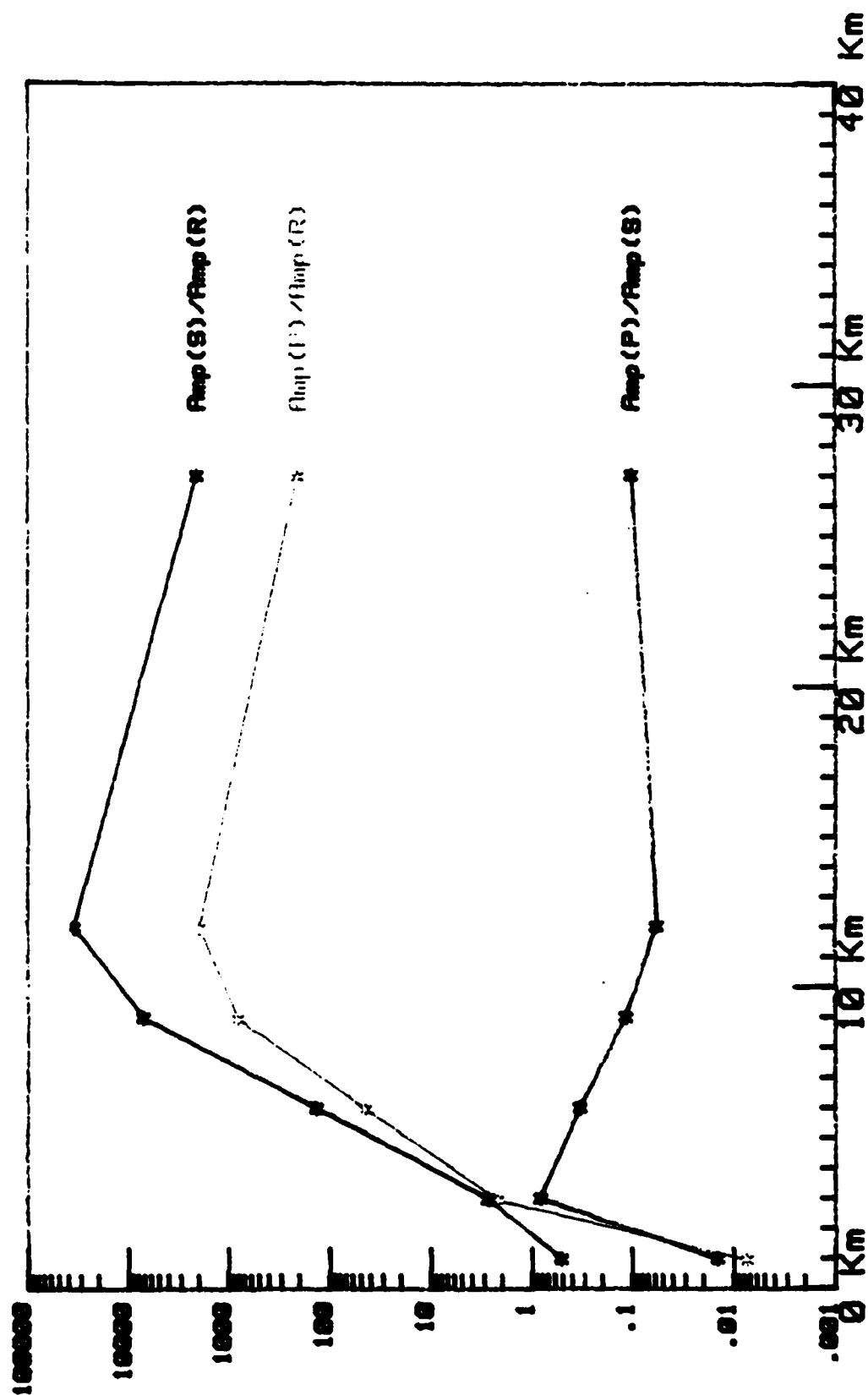to continue this study and extend it to teleseism distances.

FIG. 1 -- LOW FREQUENCY SPECTRAL RATIO VERSUS FOCAL DEPTH

FIG. 2 : ROCKBURST DISPLACEMENT SPECTRA AND ASSOCIATED SEISMIC NOISE SPECTRA RECORDED

AT 6 KM FROM THE TWO SOURCE AREA NAMED a AND b
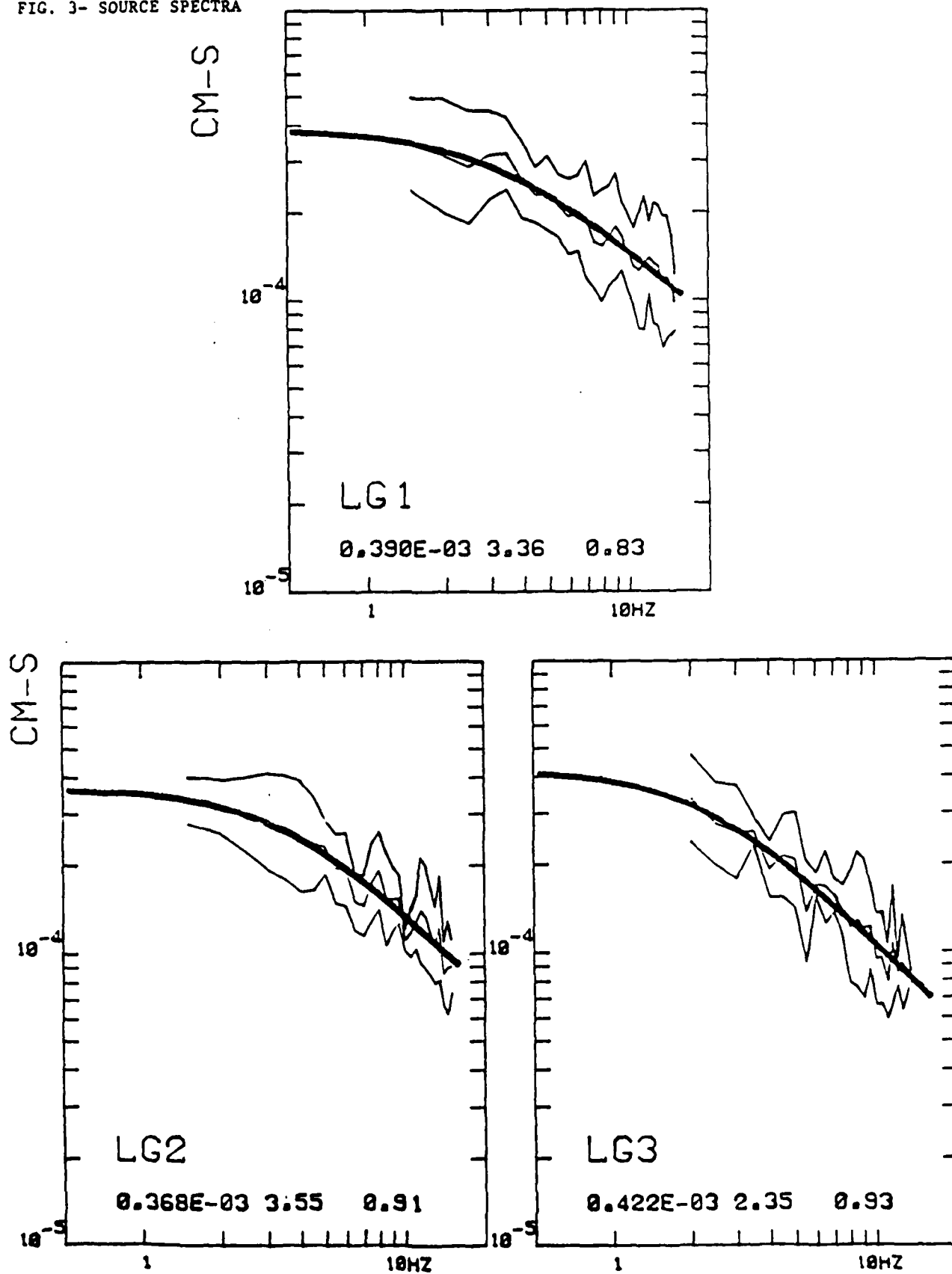
One spectrum corresponds to a chemical blast at the same epicentral distance (see tir)

For each figure are given :
the spot : a, b or tir
the day and origin time : 283 9 58 56
the station code : G 05 and corner frequency F_c

246
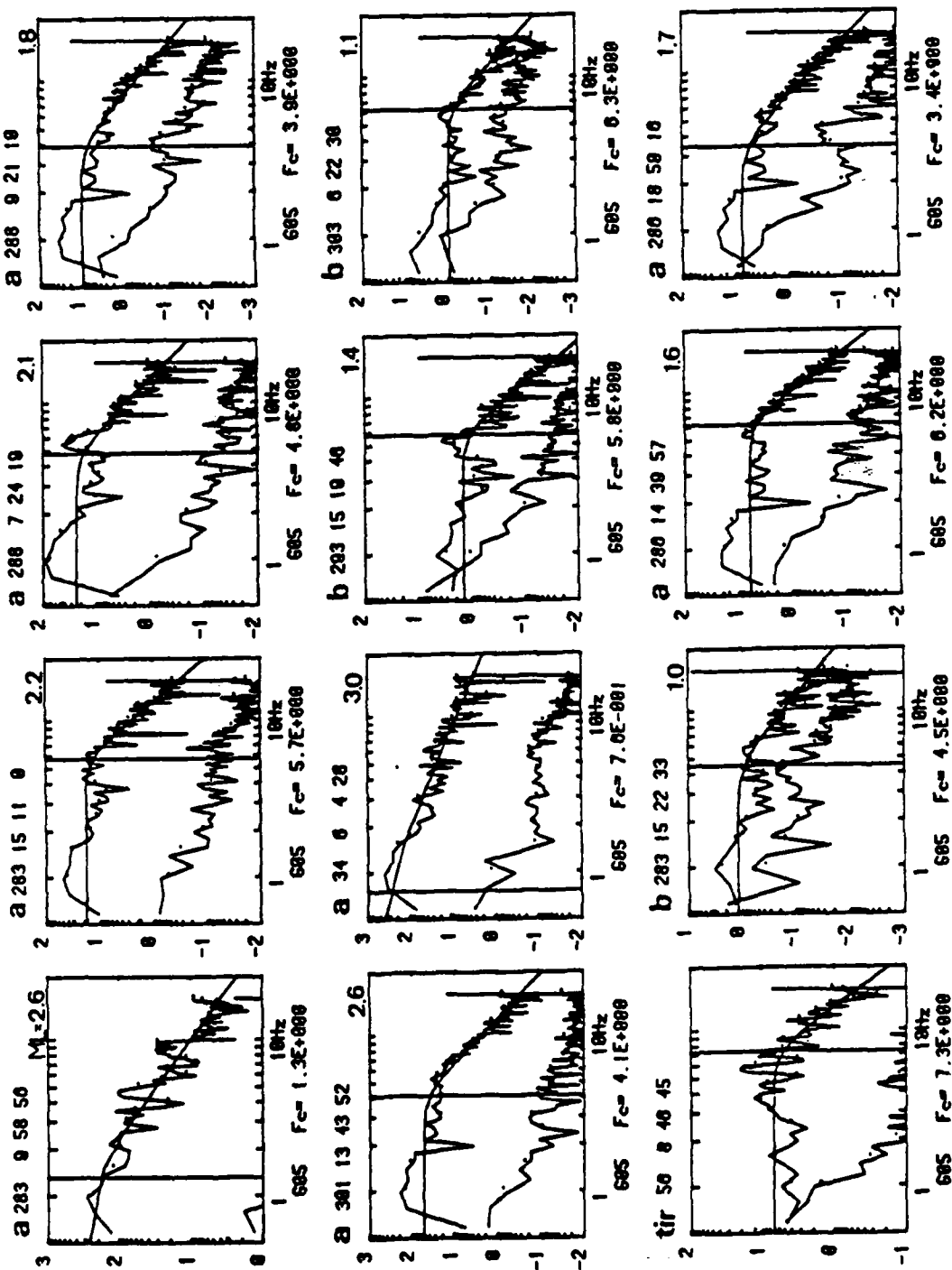
OSSAU

190486 22 5 13.6   43.06   -0.45 3.3

FIG. 3- SOURCE SPECTRA

LG1

0.390E-03 3.36   0.83

LG2

0.368E-03 3.55   0.91

LG3

0.422E-03 2.35   0.93

LIST OF PARTICIPANTS

Ralph Alewine
Geophysical Sciences Division
Defense Advanced Research Projects Agency
1400 Wilson Boulevard
Arlington, VA 22209-2308

Shelton S. Alexander
Geosciences Department
403 Deike Building
The Pennsylvania State University
University Park, PA 16802

Charles B. Archambeau
Cooperative Institute for Research in
  Environmental Sciences
University of Colorado
Boulder, CO 80309

Thomas C. Bache Jr.
Science Applications Int'l Corp.
10210 Campus Point Drive
San Diego, CA 92121

Jeffrey Barker
Woodward-Clyde Consultants
566 El Dorado Street
Pasadena, CA 91101

Noel Barstow
Rondout Associates, Inc.
P.O. Box 224
Stone Ridge, NY 12484

Peter Basham
Geological Survey of Canada
1 Observatory Crescent
Ottawa, Ontario
CANADA K1A 0Y3

James Battis
AFGL/LWH
Hanscom AFB, MA 01731-5000

Douglas R. Baumgardt
Signal Analysis and Systems Division
ENSCO, Inc.
5400 Port Royal Road
Springfield, VA 22151

Robert Blandford
Geophysical Sciences Division
Defense Advanced Research Projects Agency
1400 Wilson Boulevard
Arlington, VA 22209-2308

Michel Bouchon
I.R.I.G.M.-B.P. 68
38402 St. Martin D'Heres
Cedex, FRANCE

Steve Bratt
Science Applications Int'l Corp
10210 Campus Point Drive
San Diego, CA 92121

Lawrence J. Burdick
Woodward-Clyde Consultants
566 El Dorado Street
Pasadena, CA 91101

Michel Campillo
I.R.I.G.M.-B.P. 68
38402 St. Martin D'Heres
Cedex, FRANCE

Jerry Carter
Rondout Associates, Inc.
P.O. Box 224
Stone Ridge, NY 12484

Kin-Yip Chun
Geophysics Division
Physics Department
University of Toronto
Ontario, CANADA M5S 1A7

John Cipar
AFGL/LWH
Hanscom AFB, MA 01731-5000

Dean Clauter
HQ AFTAC/TGR
Patrick AFB, FL 32925-6001

Vernon F. Cormier
Earth Resources Laboratory
Department of Earth, Atmospheric and
  Planetary Sciences
Massachusetts Institute of Technology
42 Carleton Street
Cambridge, MA 02142

Anton M. Dainty
Earth Resources Laboratory
Department of Earth, Atmospheric and
    Planetary Sciences
Massachusetts Institute of Technology
42 Carleton Street
Cambridge, MA   02142

Steven Day
S-CUBED
3398 Carmel Mountain Road
San Diego, CA   92121

H.B. Durham
Sandia National Laboratory
Albuquerque, NM   87185

John F. Ferguson
Center for Lithospheric Studies
The University of Texas at Dallas
P.O. Box 688
Richardson, TX 75083-0688

Glenn Fezie
HQ AFTAC/TGR
Patrick AFB, FL   32925-6001

Stanley Flatté
Applied Sciences Building
University of California, Santa Cruz
Santa Cruz, CA   95064

Alexander Florence
SRI International
333 Ravenswood Avenue
Menlo Park, CA   94025-3493

Lind Gee
Department of Earth, Atmospheric and
    Planetary Sciences
Massachusetts Institute of Technology
Cambridge, MA   02139

Jeffrey Given
Sierra Geophysics
11255 Kirkland Way
Kirkland, WA   98033

Steve Grand
University of Illinois
Department of Geology
245 Natural History Building
1301 West Green Street
Urbana, IL   61801

Roy Greenfield
441 Deike Building
Pennsylvania State University
University Park, PA   16802

Peter Harjes
Institute for Geophysik
Ruhr University
Bochum
P.O. Box 102148
4630 Bochum 1
FEDERAL REPUBLIC OF GERMANY

David G. Harkrider
Seismological Laboratory
Div. of Geological & Planetary Sci.
California Institute of Technology
Pasadena, CA   91125

Donald V. Helmberger
Seismological Laboratory
Div. of Geological & Planetary Sci.
California Institute of Technology
Pasadena, CA 91125

Manfred Henger
Fed. Inst. for Geosciences & Nat'l Res.
Postfach 510153
D-3000 Hannover 51
FEDERAL REPUBLIC OF GERMANY

Anne Henson
Science Applications Int'l Corp
10210 Campus Point Drive
San Diego, CA   02121

Eugene Herrin
Institute for the Study of Earth & Man
Geophysical Laboratory
Southern Methodist University
Dallas, TX 75275

Robert B. Herrmann
Dept. of Earth & Atmospheric Sci.
Saint Louis University
Saint Louis, MO 63156

Eystein Husebye
NTNF/NORSAR
P.O. Box 51
N-2007 Kjeller, NORWAY

Hans Israelsson
Center for Seismic Studies
1300 North 17th Street
Suite 1450
Arlington, VA 22209-3871

Rong Song Jih
Teledyne Geotech
314 Montgomery Street
Alexandria, VA 22314

Lane R. Johnson
Seismographic Station
University of California
Berkeley, CA 94720

Paul Johnson
ESS-4, Mail Stop J979
Los Alamos National Laboratory
Los Alamos, NM 87545

Thomas H. Jordan
Department of Earth, Atmospheric and
    Planetary Sciences
Massachusetts Institute of Technology
Cambridge, MA 02139

Katharine Kadinsky-Cade
Earth Resources Laboratory
Department of Earth, Atmospheric
  & Planetary Sciences
Massachusetts Institute of Technology
Cambridge, MA 02139

Alan L. Kafka
Weston Observatory
Department of Geology & Geophysics
Boston College
381 Concord Road
Weston, MA 02193

Brian L.N. Kennett
Research School of Earth Sciences
Institute of Advanced Studies
G.P.O. Box 4
Canberra 2601
AUSTRALIA

Ann Kerr
Defense Advanced Research Projects Agency
1400 Wilson Boulevard
Arlington, VA 22209-2308

Tormod Kvaerna
NTNF/NORSAR
P.O. Box 51
N-2007 Kjeller, NORWAY

Thorne Lay
Department of Geological Sciences
1006 C.C. Little Building
University of Michigan
Ann Arbor, MI 48109-1063

William Leith
USGS
Mail Stop 928
Reston, VA 22092

James Lewkowicz
AFGL/LWH
Hanscom AFB, MA 01731-5000

Christopher Lynnes
Department of Geological Sciences
1006 C.C. Little Building
University of Michigan
Ann Arbor, MI 48109-1063

Randolph Martin
New England Research
P.O. Box 857
Norwich, VT 05055

Robert Masse
Box 25046, Mail Stop 967
Denver Federal Center
Denver, CO 80225

Bernard Massinon
Societe Radiomana
27, Rue Claude Bernard
75005, Paris, FRANCE

Gary McCartor
Mission Research Corp
735 State Street
P. O. Drawer 719
Santa Barbara, CA 93102

Keith L. McLaughlin
Teledyne Geotech
314 Montgomery Street
Alexandria, VA 22314

Pierre Mechler
Societe Radiomana
27, Rue Claude Bernard
75005 Paris, FRANCE

George Mellman
Sierra Geophysics
11255 Kirkland Way
Kirkland, WA 98033

William Menke
Lamont-Doherty Geological Observatory
  of Columbia University
Palisades, NY 10964

Brian J. Mitchell
Dept. of Earth & Atmospheric Sci.
Saint Louis University
Saint Louis, MO 63156

Jack Murphy
S-CUBED
Reston Geophysics Office
11800 Sunrise Valley Drive
Suite 1212
Reston, VA 22091

Geza Nagy
SRI International
333 Ravenswood Avenue
Menlo Park, CA 94025-3493

Keith Nakanishi
Lawrence Livermore National Laboratory
P.O. Box 808, L-205
Livermore, CA 94550

Carl Newton
Los Alamos National Laboratory
P.O. Box 1663
Mail Stop C 335
Group ESS3
Los Alamos, NM 87545

Robert North
Geophysics Division
Geological Survey of Canada
1 Observatory Crescent
Ottawa, Ontario
CANADA, K1A 0Y3

Henry A. Ossing
AFGL/LWH
Hanscom AFB, MA 01731-5000

Howard J. Patton
Lawrence Livermore National Laboratory
P.O. Box 808, L-205
Livermore, CA 94550

Frank F. Pilotte
Director of Geophysics
Headquarters Air Force Technical
  Applications Center
Patrick AFB, Florida 32925-6001

Keith Priestley
Seismological Laboratory
Mackay School of Mines
University of Nevada
Reno, NV 89557

Robert Reinke
AFWL/NTESG
Kirtland AFB, NM 87117-6008

Frode Ringdal
NTNF/NORSAR
P.O. Box 51
N-2007 Kjeller, NORWAY

George H. Rothe
HQ AFTAC/TGR
Patrick AFB, Florida 32925-6001

Alan S. Ryall, Jr.
Center for Seismic Studies
1300 North 17th Street
Suite 1450
Arlington, VA 22209-3871

Chandan Saikia
Woodward-Clyde Consultants
566 El Dorado Street
Pasadena, CA 91101

Charles G. Sammis
Center for Earth Sciences
University of Southern California
University Park
Los Angeles, CA   90069-0741

Jörg Schlittenhardt
Federal Inst. for Geosciences & Nat'l Res.
Postfach 510153
D-3000 Hannover 51
FEDERAL REPUBLIC OF GERMANY

Donald L. Springer
Lawrence Livermore National Lab.
P.O. Box 808, L-205
Livermore, CA   94550

Brian Stump
Institute for the Study of Earth & Man
Geophysical Laboratory
Southern Methodist University
Dallas, TX   75275

Ta-liang Teng
Center for Earth Sciences
University of Southern California
University Park
Los Angeles, CA   90089-0741

M. Nafi Toksoz
Earth Resources Laboratory
Department of Earth, Atmospheric and
    Planetary Sciences
Massachusetts Institute of Technology
42 Carleton Street
Cambridge, MA   02142

Kenneth Toy
IGPP, A-025
Scripps Institution of Oceanography
Inst. of Geophysics & Planetary Physics
La Jolla, CA   92093

Marios Vassiliou
Rockwell International Science Center
1049 Camino Dos Rios
P.O. Box 1085
Thousand Oaks, CA   91360

Terry C. Wallace
Department of Geosciences
Building #11
University of Arizona
Tucson, AZ   85721

Greg Wojcik
Weidlinger Associates
620 Hansen Way, Suite 100
Palo Alto, CA   94304

William Wortman
Mission Research Corp
735 State Street
P.O. Drawer 719
Santa Barbara, CA   93102

Francis T. Wu
Department of Geological Sciences
State University of New York
   at Binghamton
Vestal, NY   13901